ADVANCED FUNCTIONAL MATERIALS FOR NEXT GENERATION GAS SENSING APPLICATIONS

Ph.D. Thesis

By

MANISH KUMAR TIWARI

DEPARTMENT OF METALLURGICAL ENGINEERING AND MATERIALS SCIENCE

INDIAN INSTITUTE OF TECHNOLOGY INDORE

APRIL 2025

ADVANCED FUNCTIONAL MATERIALS FOR NEXT GENERATION GAS SENSING APPLICATIONS

A THESIS

Submitted in partial fulfillment of the
requirements for the award of the degree
of
DOCTOR OF PHILOSOPHY

by
MANISH KUMAR TIWARI

DEPARTMENT OF METALLURGICAL ENGINEERING AND MATERIALS SCIENCE
INDIAN INSTITUTE OF TECHNOLOGY INDORE
APRIL 2025

INDIAN INSTITUTE OF TECHNOLOGY INDORE

CANDIDATE'S DECLARATION

I hereby certify that the work which is being presented in the thesis entitled **ADVANCED FUNCTIONAL MATERIALS FOR NEXT GENERATION GAS SENSING APPLICATIONS** in the partial fulfillment of the requirements for the award of the degree of **DOCTOR OF PHILOSOPHY** and submitted in the **DEPARTMENT OF METALLURGICAL ENGINEERING AND MATERIALS SCIENCE, Indian Institute of Technology Indore**, is an authentic record of my own work carried out during the time period from August 2020 to March 2025 under the supervision of Prof. Parasharam M. Shirage, Professor, Department of Metallurgical Engineering and Materials Science.

The matter presented in this thesis has not been submitted by me for the award of any other degree of this or any other institute.

Manish
24/05/2025
Signature of the student with date
MANISH KUMAR TIWARI

This is to certify that the above statement made by the candidate is correct to the best of my/our knowledge.

Signature of Thesis Supervisor with date
Prof. PARASHARAM M. SHIRAGE

MANISH KUMAR TIWARI has successfully given his Ph.D. Oral Examination held on **May 22, 2025**.

May 22, 2025
Signature of Thesis Supervisor with date
Prof. PARASHARAM M. SHIRAGE

ACKNOWLEDGEMENTS

First and foremost, I would like to express my deepest gratitude to **Prof. Parasharam M. Shirage**, Professor, Department of Metallurgical Engineering and Materials Science, IIT Indore. His invaluable mentorship, insightful guidance, and unwavering support have been instrumental in the successful completion of this research. I am sincerely indebted to him for his constant encouragement and for devoting his precious time to critically reviewing my work, providing thoughtful suggestions, and helping refine the manuscript in its final form. His dedication and passion for research have been a source of immense motivation for me throughout my Ph.D. journey.

I extend my heartfelt thanks to the members of my Ph.D. Student Progress Committee (PSPC), **Prof. Shaibal Mukherjee, Prof. Shaikh M. Mobin** and **Prof. Sunil Kumar**, for their consistent evaluation of my progress and their invaluable suggestions that shaped the course of my research. Their constructive criticisms helped refine the technical aspects of my work.

I am also grateful to Prof. Pradeep Mathur, the founding director of IIT Indore, and **Prof. Suhash S. Joshi**, the current director, for providing an excellent research environment and the necessary facilities.

I acknowledge **IIT Indore** for providing me **fellowship under Teaching Assistant (TA) category,** providing expenses towards attending the international conference during my Ph.D. tenure, and for providing all the necessary characterization facilities for pursuing this research work. I am also thankful to the **Department of Metallurgical Engineering and Materials Science** and the **Sophisticated Instruments Center (SIC)** at IIT Indore for providing access to state-of-the-art experimental and characterization facilities.

I would like to express my sincere thanks to **Dr. Sawanta S. Mali, Dr. Jyoti V. Patil, Dr. Chang Kook Hong** (Department of Advanced Chemical Engineering, Chonnam National University, Gwangju, South Korea), **Dr. Hyunju Lee, Dr. Yoshio Ohshita and Dr. Atsushi Ogura** (Toyota Technological Institute, Nagoya, Japan) for conducting XPS, HRTEM characterization.

I would like to express my appreciation to all the technical staff at IIT Indore for their assistance with various technical and non-technical matters. Their contributions were crucial to overcoming several challenges encountered during this research.

My heartfelt thanks extend to my colleagues from the **Advanced Functional Materials Research Group**, including **Dr. Subhash Chand Yadav**, Archana Rajendra Kanwade, Abhishek Srivastava, Shraddhha M. Rajore, Jena Akash Kumar Satrughna. Their companionship, insights, and shared experiences have been invaluable, providing both technical assistance and much-needed moral support.

I am also grateful to my peers, **Dr. Chandrabhan Patel** and others, for their camaraderie and help during my Ph.D. days. The discussions and shared experiences with them have been a vital part of my academic life.

Their constant encouragement and emotional support have been my pillars of strength during both the highs and lows of this journey. I am especially thankful for their unwavering compassion and assistance in my most trying times.

I am very grateful to my wife **Maya** for her immense support and selfless services in the last three and half years of my PhD. Lastly, and most importantly, I owe my deepest thanks to **my parents, and siblings**, whose unconditional love, patience, and belief in me have been my greatest sources of strength. Their sacrifices, constant support, and endless encouragement have been the foundation upon which this achievement stands. Without their blessings and steadfast motivation, this journey would not have been possible.

Date: 2nd April 2025 Manish Kumar Tiwari

Dedicated

To

My family

LIST OF PUBLICATIONS

(From the Thesis Work)

Journal Publications:

Paper-1: M. K. Tiwari, S. C. Yadav, A. R. Kanwade, J. A. K. Satrughna, S. M. Rajore and P. M. Shirage, Advancements in lanthanide-based perovskite oxide semiconductors for gas sensing applications: a focus on doping effects and development, *Anal. Methods*, 2023, 15, 5754-5787. **(IF = 2.7)**. DOI: https://doi.org/10.1039/D3AY01420G.

Paper-2: M. K. Tiwari, S. C. Yadav, A. Srivastava, A. R. Kanwade, J. A. K. Satrughna, S. S. Mali, J. V. Patil, C. K. Hong, and P. M. Shirage, Enhancement of CO gas sensing performance by Mn-doped porous $ZnSnO_3$ microspheres, *RSC Adv.*, 2022, 12, 32249–32261. **(IF = 4.036).** DOI:10.1039/d2ra06785d**.**

Paper-3: M. K. Tiwari, A. R. Kanwade, S. C. Yadav, A. Srivastava, J. A. K. Satrughna, and P. M. Shirage, NASICON-type $Na_3Fe_2(PO_4)_3$ material for an excellent room temperature CO sensor, *J. Mater. Chem. C*, 2023, 11, 5469-5480. **(IF = 8.067).** DOI:10.1039/d3tc00300k.

Paper-4: M. K. Tiwari, A. R. Kanwade, S. M. Rajore, J. A. K. Satrughna, H. Lee, Y. Ohshita, A. Ogura, S. S. Mali, J. V. Patil, C. K. Hong, and P. M. Shirage, $W_{18}O_{49}$ Nanofibers Functionalized with Graphene as a Selective Sensing of NO_2 gas at Room Temperature, *ACS Appl. Mater. Interfaces*, 2024, 16, 49520-49532. **(IF = 8.3)**. DOI: https://doi.org/10.1021/acsami.4c10014.

Paper-5: M. K. Tiwari, J. A. K. Satrughna, A. R. Kanwade, S. M. Rajore, S. S. Mali, J. V. Patil, C. K. Hong, and P. M. Shirage, Interlinked $W_{18}O_{49}$ Nanowires Network on FTO: An Advanced Sensing Architecture for Selective NO_2 Gas Sensing. (Under Review)

LIST OF PUBLICATIONS (OTHER THAN THESIS WORK):

1. A. Kanwade, S. Gupta, A. Kankane, **M. K. Tiwari**, A. Srivastava, J. A. Kumar Satrughna, S. Chand Yadav and P. M. Shirage, Transition metal oxides as a cathode for indispensable Na-ion batteries, *RSC Adv.*, 2022, 12, 23284–23310. DOI:10.1039/d2ra03601k.

2. A. Srivastava, B. S. Chauhan, S. C. Yadav, **M. K. Tiwari**, J. A. K. Satrughna, A. Kanwade, K. Bala and P. M. Shirage, Performance of dye-sensitized solar cells by utilizing Codiaeum Variegatum Leaf and Delonix Regia Flower as natural sensitizers, *Chem. Phys. Lett.*, 2022, 807, 140087. DOI:10.1016/j.cplett.2022.140087.

3. A. Srivastava, J. A. K. Satrughna, **M. K. Tiwari**, A. Kanwade, S. C. Yadav, K. Bala and P. M. Shirage, Effect of $Ti_{1-x}Fe_xO_2$ photoanodes on the performance of dye-sensitized solar cells utilizing natural betalain pigments extracted from Beta vulgaris (BV), *Energy Adv.*, 2023, 2, 148–160. DOI:10.1039/d2ya00197g.

4. A. S. Teja, A. Srivastava, J. A. K. Satrughna, M. K. Tiwari, A. Kanwade, S. C. Yadav and P. M. Shirage, Optimal processing methodology for futuristic natural dye-sensitized solar cells and novel applications, *Dye. Pigment.*, 2023, 210, 110997. DOI:10.1016/j.dyepig.2022.110997.

5. S. C. Yadav, **M. K. Tiwari**, A. Kanwade, H. Lee, A. Ogura and P. M. Shirage, Butea monosperma, crown of thorns, red lantana camara and royal poinciana flowers extract as natural dyes for dye sensitized solar cells with improved efficiency, *Electrochim. Acta*, 2023, 441, 141793. DOI:https://doi.org/10.1016/j.electacta.2022.141793.

6. J. A. K. Satrughna, A. Kanwade, A. Srivastava, **M. K. Tiwari**, S. C. Yadav, A. S. Teja and P. M. Shirage, Experimental and computational advancement of cathode materials for futuristic sodium ion batteries, *Mater. Today*, 2023, 65, 107371. DOI: https://doi.org/10.1016/j.mattod.2023.06.013.

7. A. Srivastava, J. A. K. Satrughna, M. K. Tiwari, A. Kanwade, S. C. Yadav, K. Bala and P. M. Shirage, Lead metal halide perovskite solar cells: Fabrication, advancement strategies, alternatives, and future perspectives, *Mater. Today Commun.*, 2023, 35, 105686. **DOI**: https://doi.org/10.1016/j.mtcomm.2023.105686.

8. A. S. Teja, A. Srivastava, J. A. K. Satrughna, **M. K. Tiwari**, A. Kanwade, H. Lee, A. Ogura and P. M. Shirage, Synergistic co-sensitization of environment-friendly chlorophyll and anthocyanin-based natural dye-sensitized solar cells: An effective approach towards enhanced efficiency and stability, *Solar Energy*, 2023, 261, 112-124. DOI: https://doi.org/10.1016/j.solener.2023.06.004.

9. A. S. Shaikh, S. C. Yadav, A. Srivastava, A. Kanwade, **M. K. Tiwari,** S. M. Rajore, J. A. K. Satrughna, M. Dhonde, and P. M. Shirage, Dynamic synergy of tin in the electron-transfer layer and absorber layer for advancing perovskite solar cells: a comprehensive review, *Energy Adv.*, 2024. DOI: https://doi.org/10.1039/D4YA00204K

10. S. M. Rajore, A. R. Kanwade, J. A. K. Satrughna, **M. K. Tiwari,** and P. M. Shirage, A comprehensive review on advancements in catalysts for aluminum-air batteries, *J. Power Sources*, 2024, 616, 235101. DOI: https://doi.org/10.1016/j.jpowsour.2024.235101

11. J. A. K. Satrughna, A. Kanwade, S. M. Rajore, **M. K. Tiwari**, Y. Ito, A. Ogura, H. Lee, Y. Ohshita and P. M. Shirage, Sol-gel based synthesis of high-capacity-$NaCoO_2$ cathode for advanced sodium-

ion batteries, *Electrochim. Acta*, 2024, 507, 145201. DOI: https://doi.org/10.1016/j.electacta.2024.145201

12. J. A. K. Satrughna, A. Kanwade, S. M. Rajore, **M. K. Tiwari**, Y. Ito, A. Ogura, H. Lee, Y. Ohshita, S. S. Mali, J. V. Patil, C. K. Hong, and P. M. Shirage, Unveiling the physicochemical and electrochemical features of sodium deficient-$Na_{0.8}Fe(SO_4)_2$ as cathode for sodium-ion batteries, *Next Research*, 2025, 100210. DOI: https://doi.org/10.1016/j.nexres.2025.100210

LIST OF CONFERENCE/WORKSHOP/COURSES ATTENDED

1. Oral presentation at “Student Research Symposium 2024 (SRS’24)” by IEEE Madhya Pradesh Section Electron Devices Society Chapter, IEEE Sensors Council IIT Indore, Indian Institute of Technology Indore, India, 3rd-4th October, 2024.
2. Oral presentation at “*4th Ineternational Conference on Advanced Materials Synthesis, Characterisation and Applications-2024 (AMSCA-2024)*”, Queensland University of Technology, Brisbane, Australia, 25th-27th September, 2024.
3. Workshop: "Empowering Women in Sensor Technology (EWST’22)", IEEE Sensors Council, Indian Institute of Technology Indore, India, December 2022.
4. Participated in Distinguished Lecture on "2D Magnetic TMDs for Spintronics and Quantum Sensing", by IEEE Sensors Council Student Chapter Indian Institute of Technology Indore, India, June 22, 2023.
5. Oral presentation at “*Ineternational Conference on Advanced Materials Synthesis, Characterization and Applications (AMSCA Maverick-2022)*”, Department of Physics, Savitribai Phule Pune University, Pune-07, Maharashtra, India, 18th-20th October, 2022.
6. QIP Short-term course (AICTE) on "Synthesis and Characterization of Thin Films", Indian Institute of Technology Indore, India, March 2022.
7. QIP Short-term course, AICTE, on "Advanced Materials for Environmental Sensors", Indian Institute of Technology Indore, India, 07-12 March 2022.

8. QIP Short-term course, AICTE, on "Materials Engineering from Synthesis to Applications", Indian Institute of Technology Indore, India, February 2022.

9. Workshop on "Workshop on Sensors" organized by Indo-South Korea joint Network Center for Environmental Cyber Physical Systems- JNC Node1, November 2021, Department of Physics, Indian Institute of Technology Roorkee jointly with Indian Institute of Technology Indore and Gauhati University.

10. Workshop on "Nanotechnology Enabled Memristive Devices and Systems for Neuromorphic Computation and its Associate Applications", IEEE Nanotechnology Council (NTC), Indian Institute of Technology Indore, India, November 2021.

TABLE OF CONTENTS

LIST OF FIGURES

Chapter 1

Chapter 2

Chapter 3

Chapter 4

Chapter 5

Chapter 6

LIST OF TABLES

ACRONYMS/ABBREVIATIONS

1D	One-dimensional
2D	Two-dimensional
ACGIH	American Conference of Governmental Industrial Hygienists
AQG	Air Quality Guideline
BAW	Bulk Acoustic Wave
BE	Binding Energy
BET	Brunauer–Emmett–Teller
BJH	Barrett-Joyner-Halenda
BSEs	Backscattered Electrons
C	Concentration of gases
DC	Direct Current
DI	De-Ionized
DTG	Derivative Thermogravimetric
EDL	Electron Depletion Layer
EDS	Energy Dispersive X-ray Spectroscopy
FEG	Field Emission Gun
FESEM	Field Emission Scanning Electron Microscopy
FTO	Fluorine-doped Tin Oxide
Gr	Graphene
HAL	Hole Accumulation Layer
HRTEM	High Resolution Transmission Electron Microscopy
ICDD	International Centre for Diffraction Data
IDE	Interdigitated Electrode
IR	Infrared
JCPDS	Joint Committee on Powder Diffraction Standards
LoD	Limit of Detection
MFC	Mass Flow Controller
MOS	Metal Oxide Semiconductor
NF	Nanofiber
NFP	$Na_3Fe_2(PO_4)_3$
NIOSH	National Institute for Occupational Safety and Health
O_C	Chemisorbed Oxygen
O_L	Lattice Oxygen
O_V	Oxygen Vacancies
OSHA	Occupational Safety and Health Administration
PEL	Permissible Exposure Limit
ppm	parts per million
ppb	parts per billion
PVD	Physical Vapor Deposition
R	Response of the gas sensor
R_a	Resistance of Sensor in Absence of Test Gas

R_g	Resistance of Sensor in Presence of Test Gas
RH	Relative Humidity
RF	Radio Frequency
SAED	Selected Area Electron Diffraction
SAW	Surface Acoustic Wave
SEs	Secondary Electrons
TEM	Transmission Electron Microscopy
TGA	Thermogravimetric Analysis
WHO	World Health Organization
XPS	X-Ray Photoelectron Spectroscopy
XRD	X-Ray Diffraction
VOCs	Volatile Organic Compounds

Chapter 1

Introduction

This chapter provides a comprehensive overview of gas sensors, their historical development, and their vital role in various applications, including environmental monitoring and industrial safety. It introduces different types of gas sensors and their working principles, with a focus on chemiresistive sensors due to their simplicity and high sensitivity. The chapter highlights key factors affecting gas sensing performance, such as temperature, humidity, and material properties. Specific hazardous gases and their permissible exposure limits are discussed, emphasizing the need for reliable gas sensors. The chapter also outlines the importance of material selection, introducing $ZnSnO_3$, $Na_3Fe_2(PO_4)_3$, $W_{18}O_{49}$, *and graphene/g-*C_3N_4 *composites.*

1.1 Introduction of Gas Sensors

Gas sensors have become integral to modern technology, finding applications across various fields such as environmental monitoring, industrial safety, medical diagnostics, and even household appliances. These *sensors play a vital role in detecting harmful gases, ensuring human safety, and enhancing the quality of life by monitoring air quality and pollution levels*. The growing concerns around climate change, urbanization, and industrial emissions have further driven the demand for reliable and efficient gas sensing technologies [1].

The fundamental principle behind gas sensors is their *ability to detect specific gases in the environment and convert that detection into measurable electrical signals*. Over the years, the technological advancements in gas sensors have resulted in smaller, more sensitive, and energy-efficient devices capable of detecting gases at very low concentrations (ppm or ppb levels) [2].

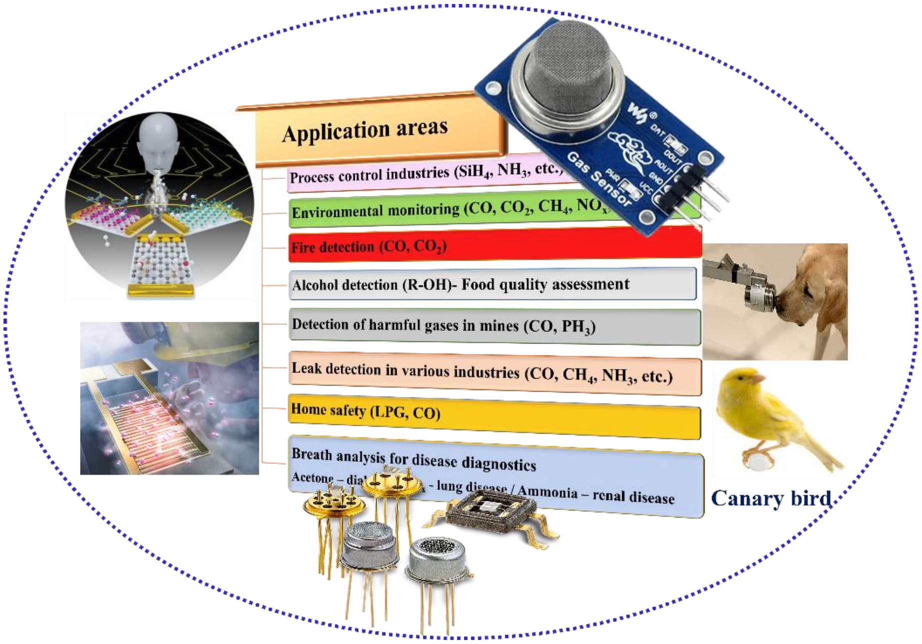

Figure 1.1. Schematic of Gas sensors and its application areas.

In response to the ever-increasing need for precise and stable gas sensing, researchers have explored a wide range of materials, with metal oxide semiconductors (MOS) emerging as one of the most prominent candidates. These materials are particularly well-suited for resistive gas sensors due to their ability to undergo changes in electrical conductivity when exposed to target gases. This interaction is typically facilitated through adsorption and surface reactions, making MOS-based sensors highly sensitive to gases like CO, NO_2, and others.

With continuous innovation, new nanostructured materials, composites, and hybrid systems are being developed, offering enhanced sensitivity, selectivity, and stability. As a result, the field of gas sensing has seen remarkable progress, opening doors to more versatile and robust sensors that meet the demands of diverse applications.

1.2 History of Gas Sensor Development

The journey of gas sensors began in the early 19th century with rudimentary gas detection methods, primarily used for safety in mining operations. The earliest forms of gas detection techniques were manual and relied on basic chemical reactions, such as using canaries to warn miners of dangerous gases like methane or carbon monoxide. However, as industrialization progressed, the need for more reliable and automated systems grew significantly.

By the mid-20th century, the development of solid-state gas sensors marked a significant leap forward. These sensors, particularly MOS-based sensors, brought about a revolution in gas detection due to their robustness, sensitivity, and relative ease of fabrication. The first notable advancement in this domain was the discovery of the semiconducting properties of metal oxides such as SnO_2 (tin oxide), which could detect reducing gases like carbon monoxide (CO) through changes in electrical resistance. In 1962, the SnO_2-based gas sensor was commercialized, laying the foundation for widespread use in industrial and domestic applications [3].

The 1980s and 1990s saw rapid advancements in gas sensing technologies, driven by the miniaturization of electronic components and the rise of nanotechnology. Researchers began exploring new materials, such as doped metal oxides, nanostructures, and composite materials, which offered enhanced gas sensing capabilities, including lower detection limits and improved selectivity. Notable among these were the use of noble metal catalysts (e.g., Pt, Pd) to enhance the response of sensors, as well as the introduction of optical and acoustic wave sensors that broadened the scope of gas detection mechanisms.

In recent years, the emergence of nanomaterials has opened new frontiers in gas sensing. Materials like graphene, carbon nanotubes, and metal oxide nanostructures have dramatically improved the sensitivity and selectivity of gas sensors. These nanomaterials offer a high surface area-to-volume ratio, which enhances their interaction with gas molecules, leading to faster and more sensitive detection [4]. The shift towards flexible, wearable, and low-power gas sensors has also become a major focus in current research, particularly for applications in environmental monitoring and health diagnostics.

Overall, the history of gas sensors reflects a constant push towards more efficient, sensitive, and versatile technologies. As the demand for better air quality monitoring and industrial safety grows, the field continues to evolve with innovations in materials and sensor designs.

1.3 Types of Gas Sensors

Gas sensors can be classified into several types based on their working principles, the nature of the gases they detect, and the technology used. Each type of gas sensor is suited for specific applications depending on factors such as sensitivity, selectivity, response time, and operating conditions. Following are the primary types of gas sensors commonly used today.

MOS gas sensors are among the most widely used for detecting gases like CO, NO_2, and H_2. These sensors operate based on the change in electrical resistance when the target gas interacts with the sensor material, usually a metal oxide like SnO_2, ZnO, or WO_3. When exposed to reducing or oxidizing gases, the surface of the metal oxide undergoes chemical reactions, altering the number of charge carriers (electrons or holes) and thereby changing the sensor's conductivity. One of the advantages of MOS sensors is their high sensitivity, especially at low gas concentrations (ppm or even ppb levels). However, they require elevated temperatures (typically 200–400°C) to function effectively, which increases power consumption. Recent advancements have focused on reducing the operating temperature by incorporating dopants or nanostructured materials, which improve sensitivity and lower the energy requirement.

Electrochemical gas sensors detect gases by means of an electrochemical reaction. The gas of interest diffuses into the sensor and reacts at an electrode, generating an electrical current proportional to the gas concentration. Electrochemical sensors are known for their high specificity and low power consumption, making them ideal for portable or battery-operated devices. However, they may have limitations such as shorter lifespans due to electrode degradation over time [5]. **Catalytic gas sensors**, also known as catalytic bead sensors, are typically used to detect combustible gases like methane, propane, and hydrogen. The working principle involves the oxidation of the target gas on the surface of a catalytic element, which causes a temperature increase that alters the resistance of the sensor. However, catalytic gas sensors require oxygen to function properly and may suffer from poisoning by certain chemicals like silicones or sulfides, which deactivates the catalyst [6]. **Optical gas sensors** utilize the interaction of light with the target gas to detect its presence. The most common technique is infrared (IR) absorption, where the sensor measures the absorption of IR light at specific wavelengths corresponding to the gas's molecular vibrations. While optical sensors offer high selectivity and long-term stability, they tend to be more expensive and complex compared to MOS or electrochemical sensors [7]. **Acoustic wave gas sensors**, including surface acoustic wave (SAW) and bulk acoustic wave (BAW) sensors, detect gases by monitoring changes in acoustic wave propagation. When gas molecules adsorb onto the sensor's surface, they affect the mass and viscoelastic properties of the sensing layer, altering the velocity and amplitude of the acoustic waves. However, their operation may be influenced by environmental factors such as humidity and temperature [8].

Table 1.1 Comparison of Different Gas Sensors

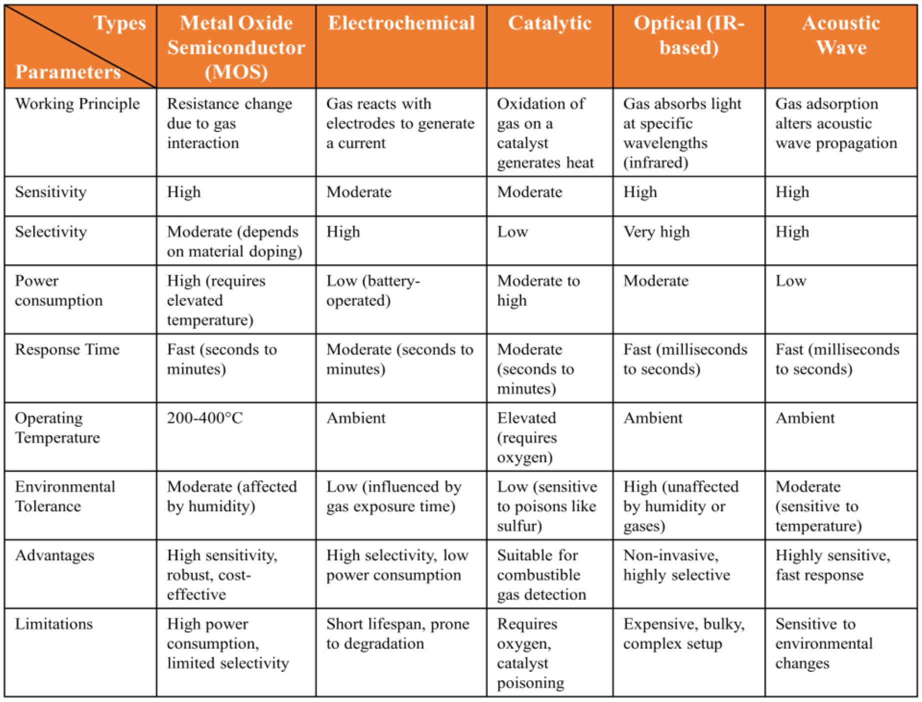

Types Parameters	Metal Oxide Semiconductor (MOS)	Electrochemical	Catalytic	Optical (IR-based)	Acoustic Wave
Working Principle	Resistance change due to gas interaction	Gas reacts with electrodes to generate a current	Oxidation of gas on a catalyst generates heat	Gas absorbs light at specific wavelengths (infrared)	Gas adsorption alters acoustic wave propagation
Sensitivity	High	Moderate	Moderate	High	High
Selectivity	Moderate (depends on material doping)	High	Low	Very high	High
Power consumption	High (requires elevated temperature)	Low (battery-operated)	Moderate to high	Moderate	Low
Response Time	Fast (seconds to minutes)	Moderate (seconds to minutes)	Moderate (seconds to minutes)	Fast (milliseconds to seconds)	Fast (milliseconds to seconds)
Operating Temperature	200-400°C	Ambient	Elevated (requires oxygen)	Ambient	Ambient
Environmental Tolerance	Moderate (affected by humidity)	Low (influenced by gas exposure time)	Low (sensitive to poisons like sulfur)	High (unaffected by humidity or gases)	Moderate (sensitive to temperature)
Advantages	High sensitivity, robust, cost-effective	High selectivity, low power consumption	Suitable for combustible gas detection	Non-invasive, highly selective	Highly sensitive, fast response
Limitations	High power consumption, limited selectivity	Short lifespan, prone to degradation	Requires oxygen, catalyst poisoning	Expensive, bulky, complex setup	Sensitive to environmental changes

Key Points Favoring Chemi resistive Sensors:

- **High Sensitivity**: MOS sensors are particularly sensitive to low concentrations of gases, making them ideal for detecting trace amounts of harmful gases like NO_2 and CO.
- **Cost-Effective**: Compared to other types, MOS sensors are relatively inexpensive to produce, especially when implemented in bulk for large-scale applications.
- **Robust and Simple Design**: MOS sensors have a relatively simple design, which enhances their durability and makes them suitable for various applications, including industrial and environmental monitoring.
- **Faster Response Time**: While not the fastest (optical and acoustic sensors can respond faster), MOS sensors still offer relatively quick

response times in the range of seconds to minutes, making them effective for real-time monitoring.

- **Compatibility with Nanomaterials**: The performance of MOS sensors can be significantly enhanced with the incorporation of nanostructures like $W_{18}O_{49}$ nanowires and g-C_3N_4 composites. These materials improve the sensitivity and response at lower operating temperatures, making them an attractive choice for developing efficient gas sensors with advanced functionalities.

1.4 Key Gas Sensor Terminology

In the field of gas sensing, various technical terms are used to describe the properties and performance of sensors (Figure 1.2). A solid understanding of this terminology is crucial to interpreting sensor behavior and selecting the appropriate sensor for specific applications. Below are key terms commonly encountered in gas sensing literature [9–12].

Sensitivity or Response: Sensitivity refers to the degree to which a sensor's output signal changes in response to a given concentration of gas. It is typically defined as the ratio of the change in the electrical signal, such as resistance, in the presence and absence of target gas. It is often expressed as:

$$R = \frac{R_g}{R_a} \quad (n\text{-type MOS in presence of oxidizing gas}) \qquad (1.1)$$

$$R = \frac{R_a}{R_g} \quad (n\text{-type MOS in presence of reducing gas}) \qquad (1.2)$$

Where, R_g and R_a represent the resistance of the sensor in the presence and absence of the test gas, respectively.

Selectivity: Selectivity refers to a sensor's ability to differentiate between target gases and other interfering gases in the environment. A highly selective sensor will respond predominantly to the gas of interest, with minimal interference from other substances. Achieving high selectivity is often one of the greatest challenges in gas sensor design, particularly in environments where multiple gases are present.

Response Time is the time taken by a sensor to reach a specific percentage (typically 90%) of its final value after being exposed to the target gas. Faster response times are important for real-time monitoring applications. **Recovery Time**, on the other hand, is the time required for the sensor to return to its baseline value after the removal of the target gas. Both response and recovery times depend on factors such as the sensor material, operating temperature, and the nature of the target gas.

Limit of Detection Limit (LoD): The Limit of Detection (LoD) is the minimum concentration of gas that a sensor can detect reliably. Below this limit, the sensor's output may become indistinguishable from noise, leading to inaccurate or unreliable readings. Sensors with a low LoD are essential for applications that require the detection of trace gas concentrations, such as environmental monitoring.

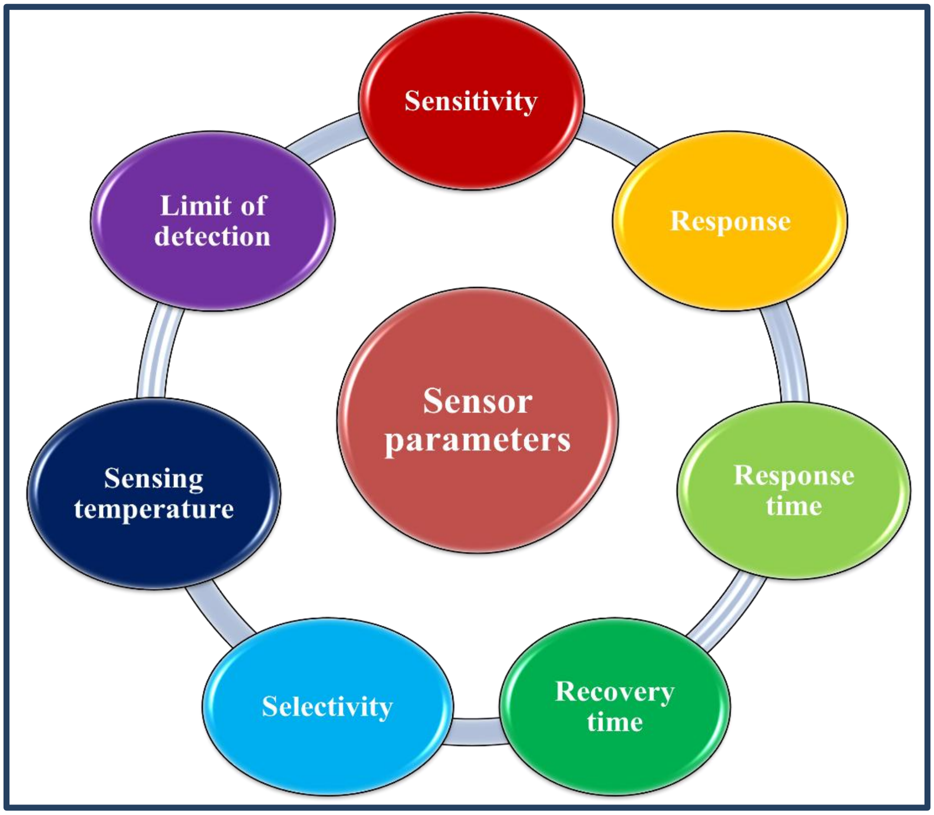

Figure 1.2. Important sensing parameters for measurement.

Stability refers to the ability of a sensor to maintain consistent performance over time, without significant drift in its output signal. Long-term stability is essential for applications where the sensor is expected to operate for extended periods without recalibration.

Repeatability is the ability of the sensor to provide the same output for repeated exposures to the same concentration of gas under identical conditions. High repeatability ensures that the sensor can be relied upon for accurate measurements in multiple use cases.

Operating Temperature: Operating temperature is the temperature at which a gas sensor functions optimally. Different types of gas sensors operate at varying temperatures, with MOS-based sensors typically requiring elevated temperatures (200-400°C) to achieve high sensitivity. Reducing the operating temperature while maintaining sensor performance is a major research focus, particularly in the development of nanostructured materials.

1.5 Overview of Common Hazardous Gases and Their Exposure Limits

Gas sensors are critical for monitoring various hazardous gases in industrial, environmental, and indoor settings to ensure human safety and health. Understanding the toxicity, permissible exposure limits (PELs), and health effects of these gases is essential for designing effective gas sensing systems. Regulatory bodies such as the Occupational Safety and Health Administration (OSHA), the National Institute for Occupational Safety and Health (NIOSH), and the American Conference of Governmental Industrial Hygienists (ACGIH) have established guidelines for safe exposure levels to protect human health. This section highlights some commonly monitored hazardous gases and their impact (Figure 1.3), followed by a summary table of their exposure limits.

1.5.1 Common Hazardous Gases

- **Ammonia (NH_3)**: A colorless gas with a pungent odor, widely used in fertilizers and industrial processes. It is corrosive to the skin, eyes, and respiratory system at high concentrations [13–15].
- **Carbon Monoxide (CO)**: A colorless, odorless gas produced by incomplete combustion of carbon-containing fuels. It is highly toxic, leading to headaches, dizziness, and even death at high levels due to its strong affinity for hemoglobin [16].
- **Carbon Dioxide (CO_2)**: While not toxic at normal levels, elevated concentrations of CO_2 can lead to respiratory issues, headaches, and impaired cognitive function. It is commonly monitored in indoor air quality assessments [17].
- **Hydrogen Sulfide (H_2S)**: Recognized by its characteristic rotten egg smell, H_2S is highly toxic and can cause eye irritation, respiratory distress, and even sudden death at high concentrations [18].
- **Nitrogen Dioxide (NO_2)**: A reddish-brown gas with a sharp, biting odor, commonly produced by vehicle emissions and industrial processes. NO_2 is a potent respiratory irritant and a significant contributor to air pollution [19,20].
- **Ethanol (C_2H_5OH)**: A volatile organic compound (VOC) widely used in industrial solvents, disinfectants, and beverages. Prolonged exposure to high concentrations can cause dizziness, headaches, and respiratory issues [21,22].
- **Volatile Organic Compounds (VOCs)**: This broad category includes numerous organic chemicals that evaporate at room temperature, contributing to indoor and outdoor air pollution. Examples include formaldehyde, benzene, and toluene, which are known to cause various health issues ranging from mild irritation to cancer [23,24].

Figure 1.3. Primary sources and health effects of common hazardous gases.

1.5.2 Exposure Limits for Common Gases

To mitigate health risks, regulatory authorities have established guidelines for maximum permissible exposure levels. The table below summarizes the exposure limits set by OSHA, NIOSH, and ACGIH for some of the most common hazardous gases [25,26].

Table 1.2. Exposure limits for several gases set by OSHA, NIOSH and ACGIH

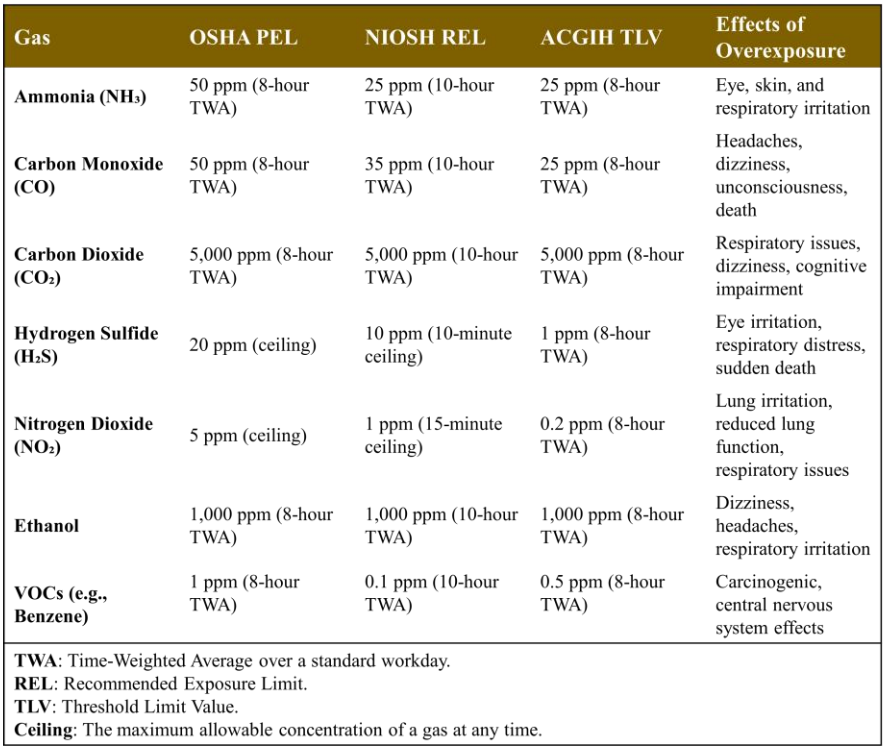

Gas	OSHA PEL	NIOSH REL	ACGIH TLV	Effects of Overexposure
Ammonia (NH_3)	50 ppm (8-hour TWA)	25 ppm (10-hour TWA)	25 ppm (8-hour TWA)	Eye, skin, and respiratory irritation
Carbon Monoxide (CO)	50 ppm (8-hour TWA)	35 ppm (10-hour TWA)	25 ppm (8-hour TWA)	Headaches, dizziness, unconsciousness, death
Carbon Dioxide (CO_2)	5,000 ppm (8-hour TWA)	5,000 ppm (10-hour TWA)	5,000 ppm (8-hour TWA)	Respiratory issues, dizziness, cognitive impairment
Hydrogen Sulfide (H_2S)	20 ppm (ceiling)	10 ppm (10-minute ceiling)	1 ppm (8-hour TWA)	Eye irritation, respiratory distress, sudden death
Nitrogen Dioxide (NO_2)	5 ppm (ceiling)	1 ppm (15-minute ceiling)	0.2 ppm (8-hour TWA)	Lung irritation, reduced lung function, respiratory issues
Ethanol	1,000 ppm (8-hour TWA)	1,000 ppm (10-hour TWA)	1,000 ppm (8-hour TWA)	Dizziness, headaches, respiratory irritation
VOCs (e.g., Benzene)	1 ppm (8-hour TWA)	0.1 ppm (10-hour TWA)	0.5 ppm (8-hour TWA)	Carcinogenic, central nervous system effects

TWA: Time-Weighted Average over a standard workday.
REL: Recommended Exposure Limit.
TLV: Threshold Limit Value.
Ceiling: The maximum allowable concentration of a gas at any time.

1.6 General Gas Sensing Mechanism

The effectiveness of gas sensors largely depends on their ability to detect and quantify specific gas molecules in the surrounding environment. The sensing mechanism is a complex interplay of physical and chemical interactions between the target gas molecules and the sensor's active material. Understanding this mechanism is crucial for optimizing sensor performance, such as sensitivity, selectivity, response time, and recovery time. This section will discuss the general principles underlying the gas sensing process, particularly focusing on chemiresistive sensors, which are widely used due to their simplicity, low cost, and high sensitivity.

1.6.1 Basic Principle of Gas Sensing

At the core of any gas sensing mechanism is the interaction between the gas molecules and the surface of the sensor material**.** When a sensor material is exposed to a target gas, various processes occur that lead to a change in the material's electrical properties. The key principle behind most chemiresistive sensors is the **change in electrical resistance** of the sensing material in response to the adsorption of gas molecules.

In general, the gas sensing process can be broken down into the following steps:

1. **Adsorption**: Gas molecules from the environment come into contact with the sensor surface, and they are adsorbed onto the material’s surface.
2. **Surface Reactions and Charge Transfer**: The adsorbed gas molecules undergo chemical reactions with the sensor material, resulting in charge transfer between the gas and the material.
3. **Conductivity Changes**: The transfer of charge modifies the carrier concentration in the material, leading to a measurable change in its electrical resistance.

These changes in resistance are typically monitored in real-time, with sensors exhibiting a higher or lower resistance depending on the type of gas, the concentration of the gas, and the properties of the sensor material [27,28].

1.6.2 Working Principle of Chemi-resistive Gas Sensors

Chemi-resistive sensors, commonly based on **MOS**, detect gases by monitoring changes in the **resistance** of the semiconductor material. These sensors rely on the interaction between the adsorbed gas molecules and the electrons in the conduction band of the semiconductor material [29–31].

1.6.2.1 Adsorption-Desorption Processes

The **adsorption-desorption process** is the first step in the gas sensing mechanism. When the sensor is exposed to gas molecules, the molecules are adsorbed onto the surface of the sensing material. The rate of adsorption depends on factors such as the concentration of gas molecules, the surface area of the sensor, and the temperature.

- **Physisorption**: This involves weak, reversible adsorption of molecules onto the sensor surface *via* van der Waals forces.
- **Chemisorption**: In this case, gas molecules form strong, often irreversible, bonds with the surface atoms of the sensor material.

After adsorption, the gas molecules may eventually desorb from the surface, which is influenced by temperature, pressure, and the nature of the interaction. **Desorption** plays a crucial role in ensuring the sensor can reset between measurements, which is important for continuous monitoring.

1.6.2.2 Surface Reactions and Charge Transfer

Once gas molecules are adsorbed on the sensor surface, **surface reactions** occur, resulting in **charge transfer**. These reactions involve the exchange of electrons between the gas molecules and the sensor material, and they are crucial for the change in electrical conductivity.

- **Oxidizing Gases (e.g., NO_2)**: These gases tend to **capture electrons** from the conduction band of the sensor material, which **increases the resistance** of the sensor, especially in *n*-type semiconductors. The captured electrons are transferred to oxygen species on the surface, resulting in a more significant electron depletion zone.

$$NO_2 + e^- \rightarrow NO_2^-$$

- **Reducing Gases (e.g., CO, H_2)**: Reducing gases **donate electrons** to the conduction band of the sensor material, which **decreases the resistance** by reducing the electron depletion layer and increasing the number of free charge carriers.

$$CO + O^-(adsorbed) \rightarrow CO_2 + e^-$$

These surface reactions and charge transfer mechanisms determine the type and magnitude of the resistance change, which is critical for detecting and quantifying the presence of target gases.

1.6.2.3 Conductivity Changes in Chemi-resistive Sensors

The changes in conductivity of a chemi-resistive sensor are primarily driven by the formation of an **electron depletion layer** in the material (Figure 1.4), particularly in metal oxide semiconductors. This depletion layer is a result of the adsorbed oxygen species (or other gas molecules), which capture free electrons from the semiconductor's conduction band.

- **In *n*-type Semiconductors** (e.g., SnO_2, WO_3): When the sensor is exposed to air, oxygen molecules adsorb onto the surface and capture electrons, forming an electron-depleted region. This region has fewer charge carriers, which leads to an increase in the sensor's resistance.

$$O_2(gas) + 2e^- \rightarrow O^-(adsorbed)$$

- **In the presence of reducing gases**, these adsorbed oxygen ions react with the reducing gases, releasing the trapped electrons back into the conduction band, thus decreasing the resistance.

$$CO(gas) + O^-(adsorbed) \rightarrow CO_2(gas) + e^-$$

- **In *p*-type Semiconductors** (e.g., CuO, NiO): The electron depletion layer forms in the opposite direction, and oxidizing gases lead to a decrease in resistance, while reducing gases increase it.

Table 1.3. Comparison of Oxidizing *vs*. Reducing Gases in Chemi resistive Sensors.

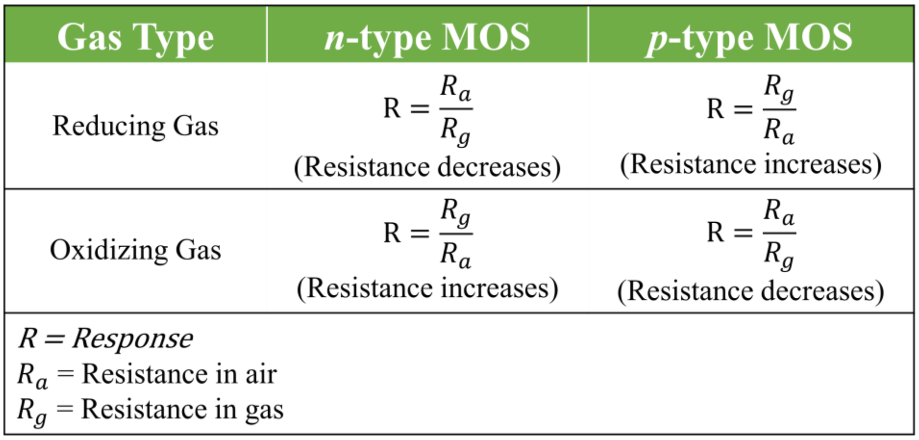

Gas Type	*n*-type MOS	*p*-type MOS
Reducing Gas	$R = \frac{R_a}{R_g}$ (Resistance decreases)	$R = \frac{R_g}{R_a}$ (Resistance increases)
Oxidizing Gas	$R = \frac{R_g}{R_a}$ (Resistance increases)	$R = \frac{R_a}{R_g}$ (Resistance decreases)
$R = Response$ R_a = Resistance in air R_g = Resistance in gas		

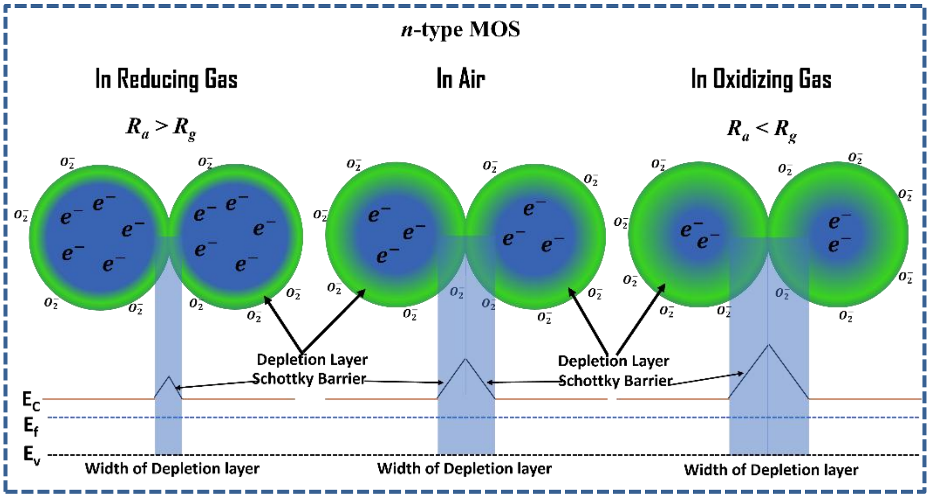

Figure 1.4. Schematic of general gas-sensing mechanism for *n*-type MOS.

1.7 Factors Affecting Gas Sensing Performance

The performance of gas sensors, especially Chemi resistive types, is influenced by a range of factors that determine their sensitivity, selectivity, response time, and overall stability. Understanding these factors is crucial for optimizing the design and functionality of gas sensors for specific applications.

1.7.1 Role of Temperature

Temperature is one of the most significant factors influencing gas sensing performance, particularly for chemi-resistive sensors. The sensing mechanism often involves surface adsorption-desorption processes, which are highly temperature-dependent [32].

Temperature and Gas Adsorption:

- At low temperatures, gas adsorption dominates, but the reaction rates may be insufficient for electron transfer or surface reactions.
- At higher temperatures, the desorption of gases increases, reducing the amount of adsorbed gas on the sensor surface.

Optimal Operating Temperature:

- Every sensor material has an **optimal operating temperature**, which ensures a balance between adsorption and reaction rates.
- For example, *n*-type semiconductors like SnO_2 exhibit maximum sensitivity at specific temperatures depending on the target gas.

Thermal Activation of Surface Species:

- Temperature can activate adsorbed oxygen species such as O_2^-, O^-, or O^{2-}, which play a vital role in the sensing mechanism.
- For example:
    - Below 150°C: O_2^- is predominant.
    - 150–300°C: O^- is the dominant species.
    - Above 300°C: O^{2-} becomes more significant.

1.7.2 Humidity Influence

Humidity is a significant environmental factor that can influence the gas sensing properties. Water molecules compete with target gas molecules for adsorption sites on the sensing surface, which can interfere with the sensor's response [4].

Competitive Adsorption:

- Water molecules can occupy active sites on the sensor surface, reducing the effective adsorption of target gas molecules.

- This often results in reduced sensitivity.

Electrical Effects:

- Adsorbed water layers can alter the conductivity of the sensor. For instance, in *n*-type semiconductors, water tends to decrease resistance by increasing surface conductivity.

Long-Term Stability:

- Prolonged exposure to high humidity can lead to material degradation, impacting the sensor's long-term performance.

1.7.3 Gas Concentration and Flow Rate

The concentration and flow rate of the target gas are crucial parameters affecting the sensor's response.

Gas Concentration: The sensor response is often proportional to the gas concentration within a specific range. This relationship can be expressed using the power-law equation:

$$R = A.C^n$$

where R is the sensor response, C is the gas concentration, and n is a material-dependent constant.

Flow Rate: Higher flow rates can reduce the residence time of gas molecules near the sensor surface, impacting adsorption-desorption dynamics. Thus, the controlled flow rates are essential for reproducible measurements [33,34].

1.7.4 Surface Area, Morphology, and Doping Effects

The structural and compositional characteristics of the sensing material play a decisive role in determining the sensitivity, selectivity, and overall efficiency of gas sensors. These attributes directly influence the interaction between gas molecules and the sensing surface, which is the foundation of the sensing mechanism.

High Surface Area: A high surface area is crucial for enhancing gas sensing performance. It increases the number of active sites available for gas adsorption, which directly correlates with higher sensitivity. Nanostructured materials, such as nanowires, nanorods, nanosheets, and nanoparticles, are particularly effective due to their large surface-to-volume ratios. For example, $W_{18}O_{49}$ nanowires provide an extensive surface area along their length, ensuring higher interaction with gas molecules compared to bulk materials. Similarly, graphene, a 2D material, offers an enormous surface area with excellent electrical conductivity, making it ideal for hybrid sensors.

- **Advantages of High Surface Area:**
    - Enhanced adsorption of target gas molecules.
    - Improved response times due to faster gas diffusion.
    - Increased active interaction sites, enabling lower detection limits.

Morphology and Porosity: The morphology of the sensing material significantly influences gas diffusion and adsorption efficiency. Materials with tailored structures, such as porous, hollow, or hierarchical configurations, exhibit superior gas sensing performance. **Porous nanomaterials** allow gases to diffuse efficiently through their framework, increasing the interaction between the gas molecules and the active sensing sites. For example, porous SnO_2 exhibits better sensitivity to CO compared to its non-porous counterpart. **Hollow spheres** or nanotubes provide an internal void where gas molecules can penetrate and interact with active sites on both the inner and outer surfaces, improving sensitivity and response time. **Hierarchical structures**, such as flower-like or networked architectures, combine the advantages of high surface area and porosity, allowing for superior gas diffusion and multiple interaction pathways.

Doping Effects: Doping, the intentional introduction of impurities into the sensing material, is a widely used strategy to enhance gas sensing properties. It affects the electronic structure, surface activity, and chemical affinity of the sensing material, influencing sensitivity, selectivity, and stability. Dopants introduce new energy levels or modify existing ones within the band structure of the sensing material. This alteration can increase the availability of charge carriers or reduce the activation energy required for gas sensing. For instance, Mn-doped SnO_2 improves sensitivity to CO due to enhanced charge carrier concentration and optimized oxygen adsorption. Certain dopants, such as noble metals (*e.g.*, Pt, Au), act as catalysts, promoting faster reaction rates between the gas molecules and the surface oxygen species. These dopants also lower the sensor's operating temperature, making the sensor more energy-efficient. Doping can create specific sites on the surface that have a higher affinity for particular gases [35]. For example:

- Fe-doped WO_3 shows selective sensitivity to NO_2.
- Ag-doped ZnO enhances ethanol sensing while reducing interference from other gases.

Dopants can stabilize the crystal structure of the sensing material, reducing material degradation over time and improving long-term stability [36,37].

1.8 Research Gaps and Challenges – Motivation

Despite significant advancements in gas sensor technology, several challenges persist, limiting their widespread application. The key research gaps and motivation for this study are outlined below:

High Operating Temperature:

- Most metal oxide-based gas sensors require elevated temperatures (>200°C) for optimal performance, leading to high power consumption.
- This limits their applicability in portable, wearable, and battery-operated devices.

Poor Selectivity:

- Many gas sensors lack selectivity and respond to multiple gases, making accurate detection difficult.
- Cross-sensitivity to interfering gases affects reliability in real-world applications.

Slow Response and Recovery Times:

- Conventional sensors often exhibit delayed response and recovery times, reducing their effectiveness in detecting rapid gas exposure.
- This is particularly problematic for real-time monitoring and emergency applications.

Stability and Durability Issues:

- Sensor performance degrades over time due to exposure to humidity, temperature fluctuations, and repeated gas exposure cycles.
- Long-term stability is a critical requirement for industrial and environmental monitoring applications.

Scalability and Reproducibility Challenges:

- The synthesis and fabrication of nanomaterial-based sensors often lead to batch-to-batch variations.
- Ensuring reproducible performance across large-scale production remains a challenge.

1.9 Materials of Choice

The selection of materials for this research was guided by the unique requirements of gas sensing applications, including sensitivity, selectivity, stability, and the ability to operate under specific environmental conditions. The materials investigated in this work—$ZnSnO_3$, $Na_3Fe_2(PO_4)_3$, $W_{18}O_{49}$, and graphene — exhibit remarkable gas sensing properties, making them ideal candidates for the proposed studies (Figure 1.5). This section provides an overview of these materials and highlights their relevance for gas sensing.

1.9.1 $ZnSnO_3$

$ZnSnO_3$, a ternary metal oxide, has garnered significant attention in gas sensing applications due to its unique physicochemical properties. Its perovskite-like structure and large surface area provide abundant active sites for gas adsorption and surface reactions, which are critical for efficient gas sensing. $ZnSnO_3$ is a semiconducting material with a suitable bandgap (typically ~3.6 eV), making it highly responsive to changes in surface chemistry caused by gas molecules.

The high mobility of charge carriers in $ZnSnO_3$ ensures rapid signal transduction, while its thermal and chemical stability enable reliable operation in varying environmental conditions. The material's porosity and ability to form nanostructures such as microspheres, nanowires, and nanosheets further enhance its sensing performance by increasing the surface-to-volume ratio and facilitating gas diffusion.

$ZnSnO_3$ is particularly effective for detecting reducing gases like CO due to its strong interaction with such molecules, leading to significant resistance changes. When doped with elements like manganese (Mn), the gas sensing performance is further enhanced through increased oxygen vacancy concentrations and improved catalytic activity, allowing for greater sensitivity, selectivity, and lower operating temperatures [38].

1.9.2 $Na_3Fe_2(PO_4)_3$

$Na_3Fe_2(PO_4)_3$, a NASICON-type material, has emerged as a promising candidate for gas sensing due to its unique structural and electrochemical properties. The material’s crystalline framework offers high ionic conductivity, which facilitates efficient charge transport during gas sensing processes. Its large lattice structure allows for the incorporation of various gas molecules, enabling strong interactions between the gas species and the material surface.

One of the key advantages of $Na_3Fe_2(PO_4)_3$ is its exceptional stability under ambient conditions, making it suitable for room-temperature gas sensing applications. Unlike many conventional semiconducting metal oxides, which require elevated operating temperatures, $Na_3Fe_2(PO_4)_3$ exhibits significant sensing responses at room temperature, reducing energy consumption and improving operational safety.

The presence of iron (Fe) in the material's composition plays a vital role in its catalytic activity. Fe ions can facilitate the redox reactions of target gas molecules, leading to changes in electrical conductivity. This feature is particularly advantageous for detecting gases like CO, where oxidation or reduction reactions on the material's surface are key to sensing. Additionally, the porous structure of $Na_3Fe_2(PO_4)_3$ contributes to a higher surface area, which enhances gas adsorption and improves sensitivity [39].

1.9.3 $W_{18}O_{49}$

$W_{18}O_{49}$, a sub-stoichiometric phase of tungsten oxide (WO_{3-X}), is a highly promising material for gas sensing due to its unique electronic and structural properties. This material exhibits an oxygen-deficient, monoclinic crystal structure, which creates a high density of oxygen vacancies. These vacancies act as active sites for gas adsorption and surface reactions, making $W_{18}O_{49}$ highly sensitive to changes in the surrounding gas atmosphere.

The semiconducting nature of $W_{18}O_{49}$, with its *n*-type conductivity, allows it to respond effectively to oxidizing and reducing gases through changes in resistance. Its narrow bandgap (~2.8–3.2 eV) facilitates the easy transfer of charge carriers during gas sensing processes, enabling a rapid and significant response to gas adsorption.

One of $W_{18}O_{49}$'s standout features is its ability to form one-dimensional nanostructures, such as nanowires and nanorods. These structures enhance gas sensing performance by providing a high surface-to-volume ratio, facilitating gas diffusion, and improving the interaction between gas molecules and the material surface. Furthermore, the interconnected nature of $W_{18}O_{49}$ nanowires supports efficient charge transport, which improves signal stability and sensor reliability. $W_{18}O_{49}$ is particularly effective for detecting oxidizing gases like NO_2, as the interaction between NO_2 and the oxygen vacancies on its surface leads to a significant change in resistance. Its excellent thermal and chemical stability ensures consistent performance even under harsh environmental conditions, while its ability to operate at low temperatures reduces power consumption [40].

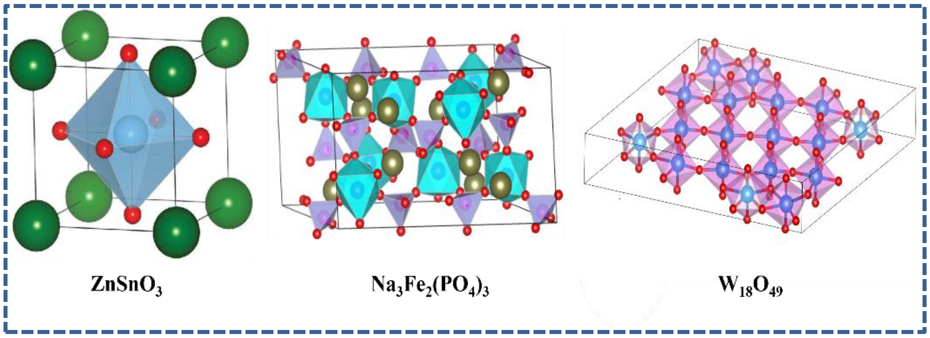

Figure 1.5. Schematic of crystal structure of $ZnSnO_3$, $Na_3Fe_2(PO_4)_3$, and $W_{18}O_{49}$.

1.10 Scope and Goals of the Thesis

The main aspiration of this thesis is to develop advanced functional materials for next-generation gas sensors with high sensitivity, selectivity, and stability under diverse environmental conditions. This thesis addresses the challenges mentioned in **Section 1.8** by exploring novel materials and their composites to design efficient gas sensing devices. The research focuses on the synthesis, characterization, and performance evaluation of materials like $ZnSnO_3$, $Na_3Fe_2(PO_4)_3$, $W_{18}O_{49}$, and graphene. Special emphasis is given to improving gas sensing mechanisms and understanding the role of material properties, such as morphology, surface area, and doping, in enhancing sensing performance. The overall aim is to contribute to the development of sustainable, energy-efficient gas sensors for the detection of hazardous gases like CO, NO_2, and NH_3.

1.10.1 Thesis Objectives

The primary objectives of this thesis are as follows:

- **Achieving Room-Temperature or Low-Temperature Operation:** Develop gas sensors capable of detecting target gases at room temperature or significantly lower temperatures compared to conventional metal oxide-based sensors.
- **Enhancing Sensitivity for Ultra-Low Gas Concentrations:** Improve the sensor response to sense trace levels of gases with high accuracy and reliability.

- **Improving Selectivity for Specific Gases in Mixed Environments:** Optimize material properties to achieve high selectivity, ensuring the sensor effectively differentiates target gases from interfering species.
- **Ensuring Long-Term Stability and Repeatability:** Develop sensors with excellent stability over extended operational periods, maintaining consistent performance under varying environmental conditions.
- **Reducing Power Consumption for Energy-Efficient Sensors:** Design sensors with low power requirements, making them suitable for portable and battery-operated applications.
- **Enhancing Sensor Response and Recovery Time:** Improve the kinetics of gas adsorption and desorption to achieve fast response and recovery times, ensuring real-time monitoring capabilities.
- **Developing Sensors Operable in Harsh Environmental Conditions:** Ensure sensor functionality in harsh environment conditions such as high humidity and pollutant-rich environments, expanding their applicability in industrial and outdoor settings.

1.10.2 Thesis Outlines

The work has been divided into seven chapters circumscribed between the introduction (Chapter 1) and the conclusions and future scope (Chapter 7). The chapter-wise organization is summarized as follows:

***Chapter 1: Introduction*.** This chapter provides a comprehensive introduction to gas sensors, including their history, types, general sensing mechanisms, and factors affecting their performance. It also discusses the rationale for material selection and outlines the scope and goals of the research.

Chapter 2: Materials Synthesis and Experimental Techniques. This chapter describes the synthesis methods adopted for the selected materials and the experimental techniques used for material characterization and gas sensing measurements.

Chapter 3: Mn-doped $ZnSnO_3$ for Enhanced CO Sensing Performance. This chapter presents the synthesis of Mn-doped $ZnSnO_3$ microspheres using a co-precipitation method, followed by detailed structural and morphological characterizations. The gas sensing performance for CO is evaluated, focusing on the effects of Mn doping on sensitivity, response time, and operating temperature. The chapter also includes a discussion on the role of Mn as a dopant in enhancing the gas sensing mechanism.

Chapter 4: NASICON-type $Na_3Fe_2(PO_4)_3$ for an Excellent Room-Temperature CO Sensing. This chapter discusses the synthesis of NASICON-type $Na_3Fe_2(PO_4)_3$ material and its application in CO sensing at room temperature. The unique ionic conductivity of $Na_3Fe_2(PO_4)_3$ is explored to understand its role in facilitating CO adsorption and detection.

Chapter 5: $W_{18}O_{49}$ Nanofibers Functionalized with Graphene as a Selective Sensing of NO_2 Gas at Room Temperature. This chapter focuses on the synthesis of $W_{18}O_{49}$ nanowires functionalized with graphene to create a composite material for the selective sensing of NO_2 gas at room temperature. The chapter delves into the synergistic effects of the graphene's high surface area on improving sensitivity and selectivity.

Chapter 6: Interlinked $W_{18}O_{49}$ Nanowires Network on FTO for Selective NO_2 Gas Sensing. This chapter focuses on the development of a unique interlinked $W_{18}O_{49}$ nanowire network grown on FTO substrates. The chapter delves into the fabrication process, material characterization, and gas sensing performance, highlighting the enhanced selectivity and sensitivity towards NO_2 gas.

Chapter 7: Conclusions and Future Scope. This chapter summarizes the key findings of the thesis and highlights the future directions for research in the field of gas sensors.

By addressing the outlined objectives, this thesis aims to contribute to the field of gas sensing through the development of innovative materials and advanced sensing technologies. The work aligns with global efforts to enhance environmental safety and industrial efficiency, making it highly relevant to current scientific and societal needs.

References

[1] G. Korotcenkov, Metal oxides for solid-state gas sensors: What determines our choice?, Mater. Sci. Eng. B 139 (2007) 1–23. https://doi.org/10.1016/j.mseb.2007.01.044.

[2] R. WENGER, D. DONEFF, K. MOSER, Die diagnostische Bedeutung des Vektorkardiogramms für die Erkennung unvollständiger Rechts- und Linksschenkelblockformen., Z. Kreislaufforsch. 42 (1953) 161–173.

[3] P.T. Moseley, Progress in the development of semiconducting metal oxide gas sensors: A review, Meas. Sci. Technol. 28 (2017). https://doi.org/10.1088/1361-6501/aa7443.

[4] C. Wang, L. Yin, L. Zhang, D. Xiang, R. Gao, Metal oxide gas sensors: Sensitivity and influencing factors, Sensors 10 (2010) 2088–2106. https://doi.org/10.3390/s100302088.

[5] M. Righettoni, A. Tricoli, S. Gass, A. Schmid, A. Amann, S.E. Pratsinis, Breath acetone monitoring by portable Si:WO_3 gas sensors, Anal. Chim. Acta 738 (2012) 69–75. https://doi.org/10.1016/j.aca.2012.06.002.

[6] P. Wang, X. Tian, M. Yan, B. Yang, Z. Hua, A low temperature catalytic-type combustible gas sensor based on Pt supported zeolite catalyst films, J. Mater. Sci. 56 (2021) 4666–4676. https://doi.org/10.1007/s10853-020-05563-w.

[7] J. Hodgkinson, R.P. Tatam, Optical gas sensing: A review, Meas. Sci. Technol. 24 (2013). https://doi.org/10.1088/0957-0233/24/1/012004.

[8] W.P. Jakubik, Surface acoustic wave-based gas sensors, Thin Solid Films 520 (2011) 986–993. https://doi.org/10.1016/j.tsf.2011.04.174.

[9] J.B.A. Gomes, J.J.P.C. Rodrigues, R.A.L. Rabêlo, N. Kumar, S. Kozlov, IoT-enabled gas sensors: Technologies, applications, and opportunities, J. Sens. Actuator Networks 8 (2019). https://doi.org/10.3390/jsan8040057.

[10] X. Liu, S. Cheng, H. Liu, S. Hu, D. Zhang, H. Ning, A survey on gas sensing technology, Sensors (Switzerland) 12 (2012) 9635–9665. https://doi.org/10.3390/s120709635.

[11] M.V. Nikolic, V. Milovanovic, Z.Z. Vasiljevic, Z. Stamenkovic, Semiconductor gas sensors: Materials, technology, design, and application, Sensors (Switzerland) 20 (2020) 1–31. https://doi.org/10.3390/s20226694.

[12] S. Feng, F. Farha, Q. Li, Y. Wan, Y. Xu, T. Zhang, H. Ning, Review on smart gas sensing technology, Sensors (Switzerland) 19 (2019) 1–22. https://doi.org/10.3390/s19173760.

[13] D.J. Kearney, T. Hubbard, D. Putnam, Breath ammonia measurement in Helicobacter pylori infection, Dig. Dis. Sci. 47 (2002) 2523–2530. https://doi.org/10.1023/A:1020568227868.

[14] B. Timmer, W. Olthuis, A. Van Den Berg, Ammonia sensors and their applications - A review, Sensors Actuators, B Chem. 107 (2005) 666–677. https://doi.org/10.1016/j.snb.2004.11.054.

[15] G.H. Mount, B. Rumburg, J. Havig, B. Lamb, H. Westberg, D. Yonge, K. Johnson, R. Kincaid, Measurement of atmospheric ammonia at a dairy using differential optical absorption spectroscopy in the mid-ultraviolet, Atmos. Environ. 36 (2002) 1799–1810. https://doi.org/10.1016/S1352-2310(02)00158-9.

[16] T. Nandy, R.A. Coutu, C. Ababei, Carbon monoxide sensing technologies for next-generation cyber-physical systems, Sensors (Switzerland) 18 (2018). https://doi.org/10.3390/s18103443.

[17] R.J. Rath, S. Naficy, J. Giaretta, F. Oveissi, J. Yun, F. Dehghani, S. Farajikhah, Chemiresistive Sensor for Enhanced CO_2 Gas Monitoring, ACS Sensors 9 (2024) 1735–1742. https://doi.org/10.1021/acssensors.3c01779.

[18] F.I.M. Ali, F. Awwad, Y.E. Greish, S.T. Mahmoud, Hydrogen Sulfide (H_2S) Gas Sensor: A Review, IEEE Sens. J. 19 (2019) 2394–2407. https://doi.org/10.1109/JSEN.2018.2886131.

[19] A. Azizi, M. Dogan, H. Long, J.D. Cain, K. Lee, R. Eskandari, A. Varieschi, E.C. Glazer, M.L. Cohen, A. Zettl, High-Performance Atomically-Thin Room-Temperature NO_2 Sensor, Nano Lett. 20 (2020) 6120–6127. https://doi.org/10.1021/acs.nanolett.0c02221.

[20] K.W. Huang, C. Sivakumar, C.H. Wu, C.W. Lee, W.E. Lee, F.Y. Tsai, M.S. Ho, Highly Efficient Room Temperature NO_2 Sensor Using Two-Phase TiOx Heterogeneous Nanoparticles, ACS Appl. Mater. Interfaces 16 (2024) 10485–10495. https://doi.org/10.1021/acsami.3c15770.

[21] S. Duangmanee, Y. Poo-arporn, N. Senamart, P. Kamonpha, P. Leuasoongnoen, P. Janphuang, N. Chanlek, P. Kidkhunthod, K. Subannajui, R. P. Poo-arporn, Vertically Aligned ZnO-WO_3 Nanorods with Core–Shell Heterostructure for Ethanol Sensing at Low Temperature: In Situ XAS Study , ACS Appl. Nano Mater. (2024). https://doi.org/10.1021/acsanm.4c03545.

[22] S. Kumar, S.D. Lawaniya, S.R. Nelamarri, M. Kumar, P.K. Dwivedi, Y.K. Mishra, K. Awasthi, ZnO Nanosheets Decorated with Ag-Pt Nanoparticles for Selective Detection of Ethanol, ACS Appl. Nano Mater. 6 (2023) 15479–15489. https://doi.org/10.1021/acsanm.3c02035.

[23] W. Rosario, P.K. Singh, A. Tiwari, U. Jain, D.K. Avasthi, N. Chauhan, Nanomaterial-based VOC sensing applications and a deep dive into their developmental trends, J. Mater. Chem. A 12 (2024) 9979–10011. https://doi.org/10.1039/d3ta07171e.

[24] P. Srinivasan, S. Samanta, A. Krishnakumar, J.B.B. Rayappan, K. Kailasam, Insights into g-C_3N_4as a chemi-resistive gas sensor for VOCs and humidity-a review of the state of the art and recent advancements, J. Mater. Chem. A 9 (2021) 10612–10651. https://doi.org/10.1039/d0ta12500h.

[25] M. Yusuf, Jabirian Journal of Biointerface Research in Pharmaceutics and Applied Chemistry, SSRN Electron. J. (2024) 7–12. https://doi.org/10.2139/ssrn.4878775.

[26] K. Lambrini, I. Christos, O. Petros, M. Alexandros, Dangerous Gases and Poisoning: A Literature Review, J. Healthc. Commun. 03 (2018) 1–4. https://doi.org/10.4172/2472-1654.100136.

[27] V.S. Bhati, M. Kumar, R. Banerjee, Gas sensing performance of 2D nanomaterials/metal oxide nanocomposites: a review, J. Mater. Chem. C 9 (2021) 8776–8808. https://doi.org/10.1039/d1tc01857d.

[28] S. Ma, J. Xu, Nanostructured metal oxide heterojunctions for chemiresistive gas sensors, J. Mater. Chem. A 11 (2023) 23742–23771. https://doi.org/10.1039/d3ta04953a.

[29] A. Sharma, C.S. Rout, Advances in understanding the gas sensing mechanisms byin situandoperandospectroscopy, J. Mater. Chem. A 9 (2021) 18175–18207. https://doi.org/10.1039/d1ta05054k.

[30] C. Wang, Y. Song, M. Zhao, H. Lu, J. Wang, X. Zou, Material design and mechanism interpretation of metal oxide nanofibers for improving gas sensitivity, Coord. Chem. Rev. 531 (2025) 216492. https://doi.org/10.1016/j.ccr.2025.216492.

[31] S. Panda, S. Mehlawat, N. Dhariwal, A. Sanger, A. Kumar, Comprehensive review on gas sensors: Unveiling recent developments and addressing challenges, Mater. Sci. Eng. B 308 (2024) 117616. https://doi.org/10.1016/j.mseb.2024.117616.

[32] T. Ravikumar, L. Thirumalaisamy, A. Thomas, S. Nallakumar, S. Pandiaraj, M. Mr, A.N. Alodhayb, S. Pitchaimuthu, V. Dananjaya, C. Abeykoon, K. Sivaperuman, A.N. Grace, Impact of annealing temperature on the response and sensitivity of spinel $ZnFe_2O_4$ thin film to ammonia gas sensing at room temperature, Mater. Today Chem. 43 (2025) 102515. https://doi.org/10.1016/j.mtchem.2025.102515.

[33] J. Yi, H. Han, Analysis of factors affecting response for mixed potential gas sensors, Electrochim. Acta 379 (2021) 138129. https://doi.org/10.1016/j.electacta.2021.138129.

[34] D.Y. Nadargi, A. Umar, J.D. Nadargi, S.A. Lokare, S. Akbar, I.S. Mulla, S.S. Suryavanshi, N.L. Bhandari, M.G. Chaskar, Gas sensors and factors influencing sensing mechanism with a special focus on MOS sensors, J. Mater. Sci. 58 (2023) 559–582. https://doi.org/10.1007/s10853-022-08072-0.

[35] M.K. Tiwari, S. Chand Yadav, A. Kanwade, J.A. Kumar Satrughna, S.M. Rajore, P.M. Shirage, Advancements in lanthanide-based perovskite oxide semiconductors for gas sensing applications: a

focus on doping effects and development, Anal. Methods 15 (2023) 5754–5787. https://doi.org/10.1039/d3ay01420g.

[36] A. Dey, Semiconductor metal oxide gas sensors: A review, Mater. Sci. Eng. B 229 (2018) 206–217. https://doi.org/10.1016/j.mseb.2017.12.036.

[37] M. Rastgou, Y. He, Q. Jiang, An Analytical Comparison of the Performance of Various Sensing Materials and Mechanisms for Efficient Detection Capability of, Engineering (2024). https://doi.org/10.1016/j.eng.2024.11.008.

[38] M.K. Tiwari, S.C. Yadav, A. Srivastava, A. Kanwade, J.A.K. Satrughna, S.S. Mali, J. V. Patil, C.K. Hong, P.M. Shirage, Enhancement of CO gas sensing performance by Mn-doped porous $ZnSnO_3$ microspheres, RSC Adv. 12 (2022) 32249–32261. https://doi.org/10.1039/d2ra06785d.

[39] M.K. Tiwari, A. Kanwade, C. Yadav, NASICON-type $Na_3Fe_2(PO_4)_3$ material for an excellent room temperature CO sensor, J. Mater. Chem. C 11 (2023). https://doi.org/10.1039/d3tc00300k.

[40] M.K. Tiwari, A.R. Kanwade, S.M. Rajore, J.A.K. Satrughna, Y. Ito, H. Lee, Y. Ohshita, A. Ogura, S.S. Mali, J. V. Patil, C.K. Hong, P.M. Shirage, $W_{18}O_{49}$ Nanofibers Functionalized with Graphene as a Selective Sensing of NO_2 Gas at Room Temperature, ACS Appl. Mater. Interfaces (2024). https://doi.org/10.1021/acsami.4c10014.

Chapter 2

Experimental and Characterization Techniques

This chapter presents the synthesis methods and characterization techniques employed in this research. Nanomaterials were synthesized using hydrothermal, solvothermal, sol-gel, and co-precipitation methods, followed by deposition through doctor-blade coating and DC magnetron sputtering. The structural, morphological, compositional, and surface properties were analyzed using X-ray diffraction (XRD), field emission scanning electron microscopy (FESEM) with energy-dispersive X-ray spectroscopy (EDS), transmission electron microscopy (TEM), X-ray photoelectron spectroscopy (XPS), nitrogen adsorption/desorption (BET) analysis, and thermogravimetric analysis (TGA). The sensing performance of the materials was evaluated using a dynamic flow-through gas sensing system and a humidity sensing system with precisely controlled environmental conditions. This chapter provides a comprehensive understanding of the experimental workflow and analytical techniques used in the study.

2.1 Introduction

Gas sensors play a vital role in detecting and monitoring hazardous gases in various industrial, environmental, and domestic applications. The performance of gas sensors depends significantly on the properties of the sensing material, which are influenced by the synthesis and deposition techniques used. Advanced functional materials, particularly metal oxide semiconductors, have garnered considerable attention due to their high sensitivity, stability, and tunable surface properties.

This chapter outlines the various synthesis and deposition methods employed in fabricating gas sensors, highlighting their advantages and limitations. A systematic approach to material synthesis ensures reproducibility, control over nanostructure morphology, and enhancement in gas sensing characteristics. Among these, wet chemical synthesis methods, such as sol-gel, hydrothermal, and co-precipitation techniques, offer significant advantages in controlling particle size, morphology, and composition. These methods enable the fabrication of nanostructured materials with high surface area and active sites, which are essential for improving gas sensor performance. Additionally, wet chemical methods allow for doping, composite formation, and surface functionalization, which further enhance selectivity and sensitivity.

In this chapter, different characterization techniques such as X-ray diffraction (XRD), field emission scanning electron microscopy (FESEM), transmission electron microscopy (TEM), high resolution transmission electron microscopy (HRTEM), Thermogravimetric analysis (TGA), X-ray photoelectron spectroscopy (XPS) and Brunauer–Emmett–Teller (BET) surface area analysis technique are discussed. These techniques provide insights into the crystallinity, phase purity, surface morphology, deep analysis of the structures, chemical composition and surface area analysis of the synthesized materials. Furthermore, gas and humidity sensing measurement systems are described, explaining their role in assessing sensitivity, selectivity, response time, and stability of the sensors

The experimental methodologies detailed in this chapter lay the foundation for understanding material behavior, optimizing sensor fabrication processes, and ultimately enhancing gas sensor performance for real-world applications.

2.2 Synthesis *via* Wet Chemical Method and Deposition Techniques

Both the chemical and physical deposition methods are used in the present thesis work. Chemical method mainly co-precipitation and hydrothermal synthesis method are employed for the growth of nanostructured materials, which are the active layer or sensing layer of the sensor. DC reactive magnetron sputtering technique is employed for the growth of metal electrodes on glass substrates in a desired pattern. Doctor-blade coating technique is employed for the deposition of obtained nanostructured materials powder on the prepared electrode patterns. All the systems mentioned above are explained concisely in the following section.

2.2.1 Synthesis of Sensing Material by Co-precipitation Method

The co-precipitation method is a widely used wet-chemical synthesis technique for producing homogeneous nanomaterials. In this method, metal precursors are dissolved in an aqueous solution, and a precipitating agent is added to induce nucleation and growth. The obtained precipitate is washed, dried, and calcined to achieve the desired phase and morphology. This technique offers advantages such as simplicity, scalability, and control over particle size and composition. The co-precipitation method is highly effective for synthesizing mixed metal oxides, doped semiconductors, and composite materials. Controlling parameters such as pH, temperature, and stirring rate enables fine-tuning of particle size and crystallinity, which is crucial for enhancing gas sensor properties. However, this method may sometimes result in agglomeration, which can be mitigated by using surfactants or dispersing agents [1,2].

In this thesis work, co-precipitation method was used to synthesize **pure and Mn-doped $ZnSnO_3$ microspheres**. All the precursors, reagents, and solvents were used as received without further purification. Zinc sulfate heptahydrate ($ZnSO_4.7H_2O$, >99.5%), Sodium stannate trihydrate ($Na_2SnO_3.3H_2O$, >99%), Manganese sulfate monohydrate ($MnSO_4.H_2O$, >99%), and Ammonia solution (NH_3,~25%) were of analytical grade and purchased from Sigma-Aldrich Co. Ltd. In a standard procedure, 0.1M $ZnSO_4.7H_2O$ was dissolved in 50 mL of DI water and stirred vigorously at room temperature until a clear, transparent solution was obtained. Similarly, 0.1M $Na_2SnO_3.3H_2O$ was dissolved in 50 mL of DI water and stirred separately. To maintain a pH of ~10, an appropriate amount of aqueous NH_3 solution was gradually added dropwise to the $ZnSO_4$ solution under continuous stirring. Subsequently, a measured quantity of $MnSO_4 \cdot H_2O$ was introduced into the $ZnSO_4$ solution, followed by the addition of the sodium stannate solution in a [Zn]/[Sn] molar ratio of 1:1. The resulting mixture was stirred rigorously at 60 ºC for 2 hours. After the reaction, the precipitate was collected through centrifugation at 5,000 rpm and repeatedly washed with deionized water to eliminate impurities. The final product was dried at 100 ºC for 10 hours in a hot air oven. To obtain pure and Mn-doped $ZnSnO_3$ spherical particles, the as-prepared $ZnSn(OH)_6$ powders were subjected to heat treatment at 500 ºC for 4 hours in a muffle furnace.

2.2.2 Synthesis of Sensing Material by Sol-gel method

The sol-gel method is another wet-chemical synthesis technique that allows the fabrication of highly porous and uniform nanostructured materials. This method involves the hydrolysis and condensation of metal alkoxides or inorganic salts in a solvent, forming a colloidal sol that gradually transforms into a gel. The gel is then dried and calcined to obtain the final nanomaterial. The sol-gel process offers precise control over composition, homogeneity, and porosity. By modifying the precursor solution composition, the morphology and surface properties can be tailored to enhance gas adsorption and reaction kinetics. Furthermore, sol-gel-derived materials exhibit high surface area and tunable porosity, which directly impact sensor sensitivity and response time. However, this method requires careful control of synthesis parameters such as precursor concentration, reaction temperature, and aging time to achieve desired material characteristics [3,4].

Here, we have optimized the sol-gel synthesis protocol to gain the **NASICON-type $Na_3Fe_2(PO_4)_3$ (NFP) porous material**. For the synthesis of NFP, chemicals required such as Sodium nitrate ($NaNO_3$) (Merk; 99%), Iron nitrate nonahydrate ($Fe(NO_3)_3.9H_2O$) (Alfa Aesar; 98%-101%), Ammonium dihydrogen phosphate ($NH_4H_2PO_4$) (Alfa Aesar; 98%), and Citric acid monohydrate ($C_6H_8O_7.H_2O$) (Alfa Aesar; 99%) were purchased of analytical grade. All the chemicals were directly used without any further purification. The procedure adopted is as shown in Figure 2.1. The stoichiometric amount of $NaNO_3$, $Fe(NO_3)_3.9H_2O$, $NH_4H_2PO_4$ and $C_6H_8O_7.H_2O$ were dissolved in 50 ml of DI water where $C_6H_8O_7.H_2O$ was engrossed as a chelating agent. The mixed solution was kept for continous magnetic stirring and the temperature was set to 80 ℃. After the continous reaction of 9 hours, the water get evaporated to form the gel precursor and the gel precursor was then further dried in furnace at 100 ℃. The obtained black colored material was ground into very fine particles using mortar pestle and annealed at 700 ℃ for 10 hours in muffle furnace at the heating rate of 5 ℃ min^{-1} to obtain the brown porous NFP as the final product.

Both co-precipitation and sol-gel methods provide effective routes for synthesizing advanced functional materials for gas sensing applications. Their ability to control nanostructure properties, composition, and surface area makes them promising techniques for developing next-generation gas sensors with high sensitivity, selectivity, and stability.

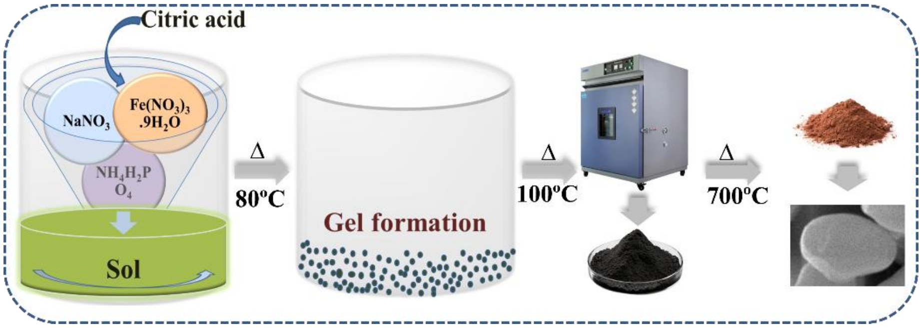

Figure 2.1. Schematic illustartion of the synthesis of $Na_3Fe_2(PO_4)_3$ sensing material.

2.2.3 Synthesis of Sensing Material by Hydrothermal method

The hydrothermal and solvothermal methods are widely used for synthesizing nanomaterials with controlled morphology, crystallinity, and phase purity. Both techniques involve chemical reactions occurring in a sealed autoclave under high temperature and pressure conditions, with the key difference being the solvent used. The hydrothermal method utilizes water as the reaction medium, whereas the solvothermal method employs organic solvents such as alcohols, ethylene glycol, or amines [5,6]. These methods are particularly useful for producing nanostructures, complex oxides, and hybrid materials with tailored structural properties. The solution is transferred into a Teflon-lined stainless-steel autoclave (Figure 2.2(a)), which is filled to 50–80% of its total volume to maintain a balance between liquid and vapor phases [7]. The sealed autoclave is heated to temperatures typically ranging from 100 to 350°C, depending on the desired material properties. Under these conditions, high pressure builds up inside the vessel due to the solvent's vapor pressure, promoting enhanced solubility, reaction kinetics, and controlled nucleation and crystal growth (Figure 2.2(b)). For instance, in a hydrothermal system at **180°C** with **50–60 mL of water in a 100 mL autoclave, the estimated pressure is 1.0–1.2 MPa**, as determined using steam tables and the Antoine equation ($\log P = A - (B/(T+C))$, where P is vapor pressure of the substance in bar, T is temperature in °C, and A, B, C are empirical constants specific to the substance found in steam tables).

For example, the Antoine constants for water in the range 99–374 °C are as ***A* = 8.07131**, ***B* = 1730.63**, **C = 233.426** [8]. By carefully optimizing synthesis parameters, these methods enable the fabrication of advanced functional materials for applications in gas sensors.

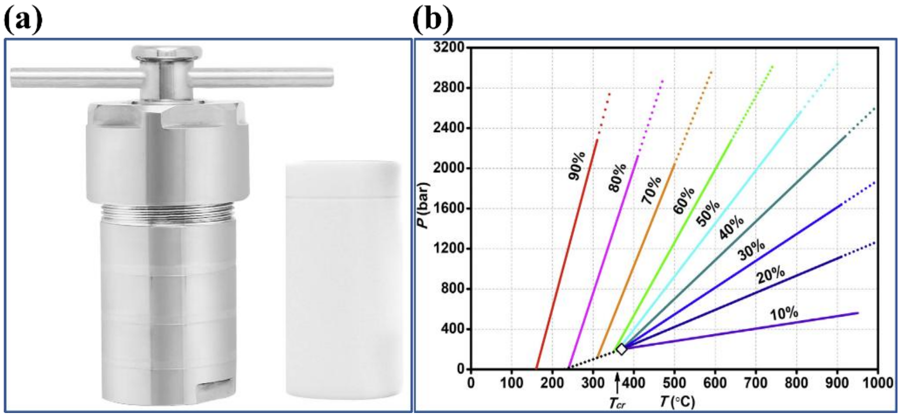

Figure 2.2. (a) General purpose autoclave for hydrothermal or solvothermal synthesis, and (b) Correlation of pressure and temperature for water under different degree of vessel filling.

Here, we have optimized the hydrothermal and solvothermal synthesis protocol to gain the **WO_3 and $W_{18}O_{49}$ nanofibers or nanowires** as well as to form their composite structure with graphene material to obtain **1D-2D composite nanostructures**.

(a) Synthesis of WO_3 or $W_{18}O_{49}$ nanofibers

All the chemicals and reagents were of analytical grade, which were used as received without any further purification. Sodium tungsten dyhydrate ($Na_2WO_4.2H_2O$) was procured from Sisco Research Laboratories Pvt. Ltd., India. Sodium sulfate (Na_2SO_4), Potassium sulfate (K_2SO_4), and Ethanol (C_2H_5OH, EMSURE, ACS, ISO, absolute for analysis) were procured from Merck KGaA, Germany. WO_3 NFs self-assembled bundles were synthesized by a facile hydrothermal method. Initially, 0.15 mol of $Na_2WO_4.2H_2O$ was dissolved into 4:1 mixture of DI water and ethanol under vigorous stirring, and then 2M HCl was added dropwise into the solution to adjust the pH of the solution from 8.5 to about 1.25. In the solution of pH 1.25, 0.035 M Na_2SO_4 and 0.035 M K_2SO_4 were added frequently and the solution is magnetically stirred at room temperature for 1 hour. Then the obtained light-yellow solution was transferred into a 100 ml Teflon-lined stainless-steel autoclave and reacted for 16 h at a temperature of 180 °C. The resultant bluish products were collected and washed with DI water and ethanol several times, then dried at 80 °C for 10 h under vacuum. The $W_{18}O_{49}$ NFs self-assembled bundles were obtained under the same conditions as for WO_3, except that the amount of Na_2SO_4 and K_2SO_4 were doubled i.e. 0.07 M each was added into the pH 1.25 solution.

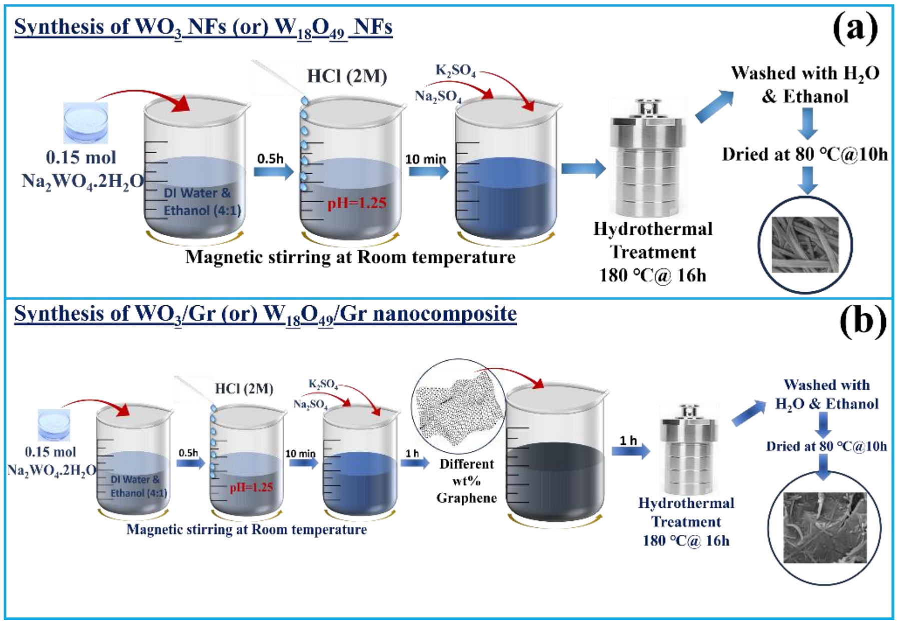

Figure 2.3. Schematic illustration of the synthesis process for (a) WO_3 or $W_{18}O_{49}$, and (b) WO_3/Gr or $W_{18}O_{49}$/Gr nanocomposite.

(b) Synthesis of WO_3/Gr or $W_{18}O_{49}$/Gr nanocomposite

The nanocomposites of WO_3 or $W_{18}O_{49}$ with graphene were formed by slight alteration in step 1 (Figure 2.3(a)). Step 2 is illustrated in Figure 2.3(b), where a 0.5 to 3 wt % of Gr was dispersed to 50 ml solution (1 h after the addition of Na_2SO_4 and K_2SO_4). The above solution was ultrasonicated for 1 h and followed by vigorous stirring of 1 h at room temperature, hydrothermal treatment at 180 ℃ for 16 h, centrifuged and dried in vacuum at 80 ℃ for 10 h to obtain WO_3/Gr or $W_{18}O_{49}$/Gr composites.

2.2.3 Doctor-blade coating method

The doctor-blade coating method, also known as blade coating or tape casting, is a widely used technique for depositing thin films of functional materials onto substrates (Figure 2.4). This method is particularly effective for fabricating uniform coatings of ceramic slurries, metal oxides, perovskites, and polymer-based films for applications in gas sensors, solar cells, and batteries. The doctor-blade method involves spreading a viscous slurry or precursor solution over a substrate using a sharp-edged blade. The blade is positioned at a fixed height, controlling the thickness of the deposited film (5 µm, 10 µm, 15 µm, 20 µm). The coated substrate is then dried and, if necessary, thermally treated to remove solvents and enhance film adhesion [9,10].

In this thesis research, after synthesizing nanomaterials *via* wet chemical methods, the obtained powder is processed into a viscous paste using DI water or ethanol as the dispersing medium. This paste is then deposited onto a substrate with pre-patterned electrodes using the doctor-blade coating method. The controlled spreading ensures a uniform and well-adhered film, which is essential for achieving consistent electrical response in sensor applications. Following deposition, the coated substrates undergo drying and thermal treatment to remove residual solvents, enhance material stability, and optimize interfacial contact between the active layer and electrodes. This approach ensures reproducible and high-performance coatings suitable for gas sensing and other functional applications.

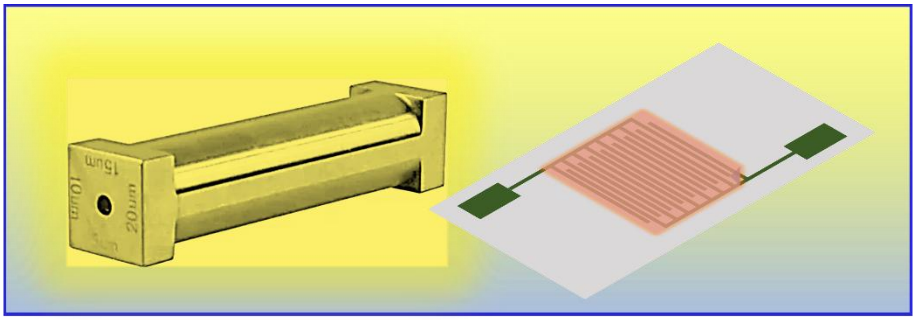

Figure 2.4. Schematic of doctor-blade method coating tool and after-coating sample image.

2.2.4 DC Magnetron Sputtering

Sputtering is a physical vapor deposition (PVD) technique used to deposit thin films of metals, oxides, and other materials onto substrates. The process involves bombarding a target material with energetic ions, causing atoms to be ejected and deposited as a thin film on a substrate. Sputtering is widely used in semiconductor fabrication, optical coatings, and sensor applications due to its ability to produce highly uniform and adhesive coatings with precise thickness control. Sputtering techniques are classified based on the energy source and deposition mechanism:

1. DC Sputtering – Uses a direct current (DC) power supply to generate plasma for metallic target deposition.
2. RF Sputtering – Uses radio frequency (RF) power, suitable for insulating and non-conductive targets.
3. Magnetron Sputtering – Enhances the sputtering process using magnetic fields to increase ionization efficiency.
4. Reactive Sputtering – Involves introducing reactive gases (*e.g.*, O_2, N_2) to form compound films like oxides or nitrides.

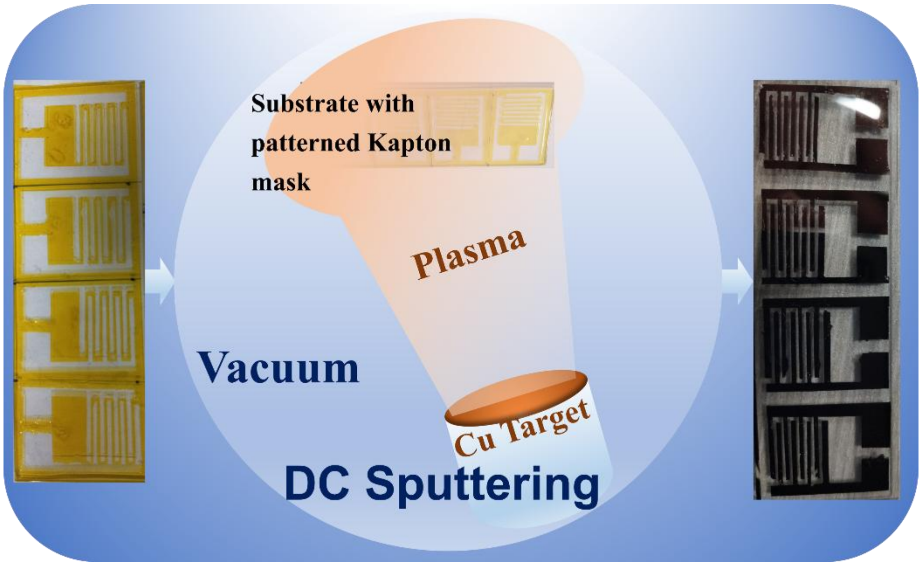

Figure 2.5. Schematic illustration of application of DC magnetron sputtering for the formation of Cu-based IDE pattern.

DC magnetron sputtering operates by applying a negative DC voltage to the target material (cathode), which is placed in a vacuum chamber filled with argon gas. When a high voltage is applied, the argon gas is ionized into Ar^+ ions and free electrons. The positively charged Ar^+ ions accelerate towards the negatively charged target, bombarding it and ejecting atoms via momentum transfer. These sputtered atoms then travel through the chamber and deposit onto the substrate, forming a thin film. The addition of a magnetic field near the target surface traps electrons, increasing the plasma density and improving sputtering efficiency. This allows for higher deposition rates, better film uniformity, and lower substrate heating, making magnetron sputtering ideal for high-quality coatings [11–13].

In our work, we utilized DC magnetron sputtering to deposit copper (Cu), as shown in Figure 2.5, and silver (Ag) thin films onto glass substrates, forming interdigitated electrode (IDE) patterns for sensor applications. The process enabled precise control over film thickness, adhesion, and electrical conductivity, which are critical for ensuring efficient charge transport and sensor response. By optimizing the sputtering parameters, we achieved well-defined and conductive IDE patterns, essential for enhancing the performance of our gas sensors.

2.3 Materials Characterization Techniques

To analyze the gas and VOC sensing properties influenced by the morphology of the nanomaterial, it is essential to characterize the synthesized material using various techniques. These characterization methods help examine the surface structure, crystal morphology, phase composition, and elemental distribution of the material. In this thesis, different material characterization techniques have been employed to gain a comprehensive understanding of the synthesized nanomaterials, which are discussed in the following sections.

2.3.1 X-Ray Diffraction

XRD is a powerful non-destructive characterization technique used to analyze the structural properties and phase purity of crystalline materials. It is widely employed in materials to identify the crystal structure, lattice parameters, and phase composition of synthesized materials. The technique provides crucial insights into the material's crystallinity, helping to confirm the successful synthesis of the desired phases [14].

XRD operates on the principle of **Bragg's Law**, which describes the diffraction of X-rays by the periodic arrangement of atoms in a crystal. When an X-ray beam interacts with a crystalline material, it gets scattered by the atomic planes, producing a diffraction pattern based on the following equation (Figure 2.6):

$$n\lambda = 2d\,(\mathrm{Sin}\ \theta) \qquad (2.1)$$

where, n = order of diffraction (integer), λ = 1.5406 Å, X-ray wavelength, d = interplanar spacing, θ = diffraction angle. When the diffraction condition is met, constructive interference occurs, resulting in characteristic diffraction peaks. The position, intensity, and width of these peaks provide insight into the crystal structure, phase composition, and structural defects of the material.

During an XRD experiment, a monochromatic X-ray beam is directed at the sample, and the detector records the intensity of the diffracted X-rays as a function of the diffraction angle (2θ). The obtained XRD pattern consists of peaks corresponding to different crystallographic planes. By comparing these peaks with reference databases, the crystal structure and phase composition of the material can be identified.

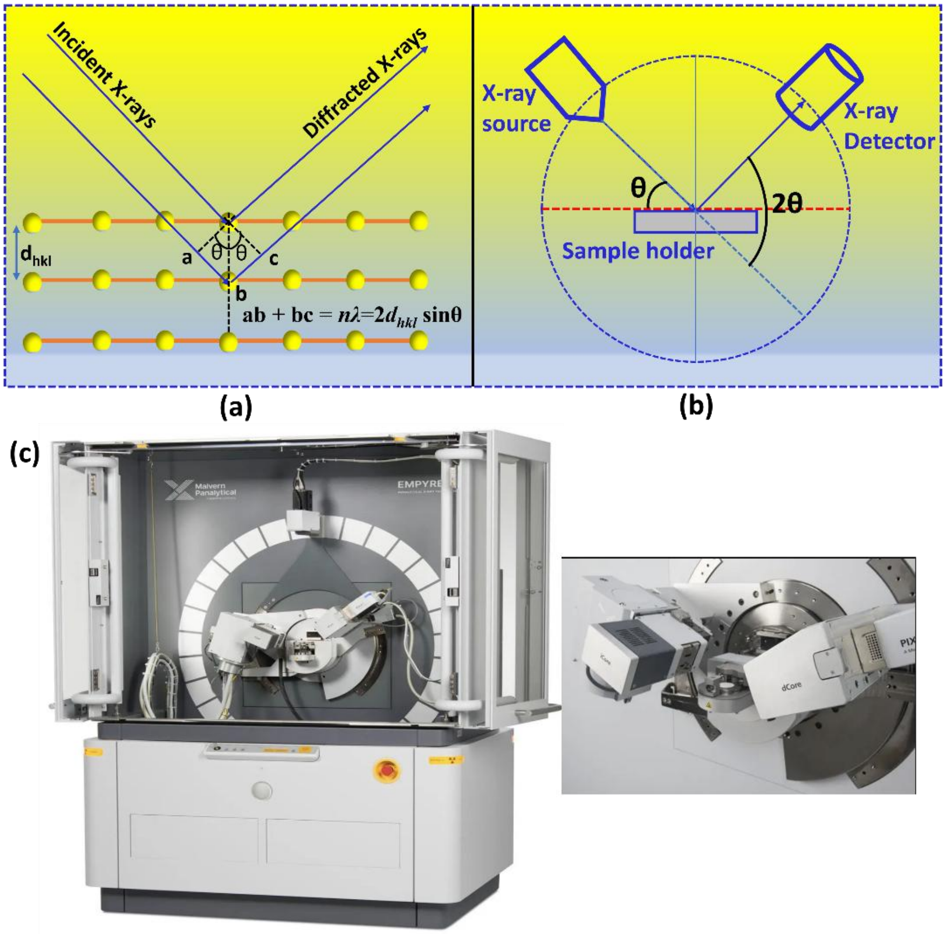

Figure 2.6. Schematic illustration of (a) diffraction of X-rays by a set of crystal planes based on Bragg’s law, (b) XRD diffractometer system, and (c) image of the third generation Empyrean, Malvern Panalytical X-ray diffractometer.

The *Joint Committee on Powder Diffraction Standards* (JCPDS), now known as the *International Centre for Diffraction Data* (ICDD), provides a database of standard diffraction patterns. Each material has a unique JCPDS card that includes 2θ values, *d*-spacing, relative intensities, and crystal structure information. By comparing the experimental XRD pattern with JCPDS data, the phase purity and crystallographic structure of the material can be confirmed. To achieve a more precise structural determination, **Rietveld refinement** is performed using **FullProf software**. This method involves fitting the experimental XRD pattern with a theoretical model by adjusting parameters such as: *Lattice parameters* (unit cell dimensions), *Atomic positions and occupancies*, *Peak broadening factors* (instrumental and sample-related), and *Phase fraction* (for multiphase materials). The refinement process minimizes the difference between the observed and calculated diffraction patterns, ensuring an accurate determination of the crystal structure and phase composition of the synthesized nanomaterials [15,16].

In this thesis work, **third generation Empyrean, Malvern Panalytical X-ray Diffractometer** (Cu-Kα radiation, λ = 1.5406 Å) is used to perform the X-ray diffraction analysis of developed materials. Figure 2.6(c) shows the actual image of the Empyrean, Malvern Panalytical X-ray Diffractometer used in this thesis work.

2.3.2 Field Emission Scanning Electron Microscopy/Energy Dispersive X-ray Spectroscopy

FESEM is an advanced imaging technique used for high-resolution morphological and microstructural analysis of materials. It operates on the same fundamental principle as conventional Scanning Electron Microscopy (SEM) but employs a field emission gun (FEG) as the electron source. The FEG provides a highly focused and coherent electron beam, leading to improved resolution and enhanced imaging capabilities, making FESEM a crucial tool for nanomaterials research.

The working of FESEM is based on the interaction between a finely focused electron beam and the sample surface. The sample is placed inside a vacuum-sealed chamber, as FESEM requires a high-vacuum environment to prevent electron scattering due to air molecules. The electron column contains electromagnetic lenses that focus and direct the electron beam onto the sample with high precision. The electron beam is then rastered across the sample using a scanning system controlled by deflector coils. Upon interaction with the sample surface, various signals such as secondary electrons (SEs), backscattered electrons (BSEs), and characteristic X-rays are emitted (Figure 2.7). These are collected by respective detectors, including the SE detector for topographical contrast and the BSE detector for compositional contrast [17,18].

To complement morphological studies, FESEM is also equipped with Energy Dispersive X-ray Spectroscopy (EDS), which enables elemental analysis of the material. EDS detects characteristic X-rays emitted from the sample when excited by the electron beam, allowing for qualitative and semi-quantitative elemental composition analysis. The combination of FESEM and EDS provides a comprehensive understanding of a material's morphology, composition, and uniformity, making it an indispensable tool for materials science research [19].

In this research, **FESEM (JSM-7610 F Plus JEOL)**, as shown in Figure 2.7 (c,d), was employed to analyze the surface morphology, particle size, and microstructure of the synthesized materials, providing crucial insights into their physical properties. The nanostructured materials were examined for uniformity, porosity, and interconnectivity, which directly influence gas sensing performance. Additionally, the EDS analysis was used to verify the elemental composition of the synthesized materials, ensuring phase purity and confirming the presence of intended elements in the samples.

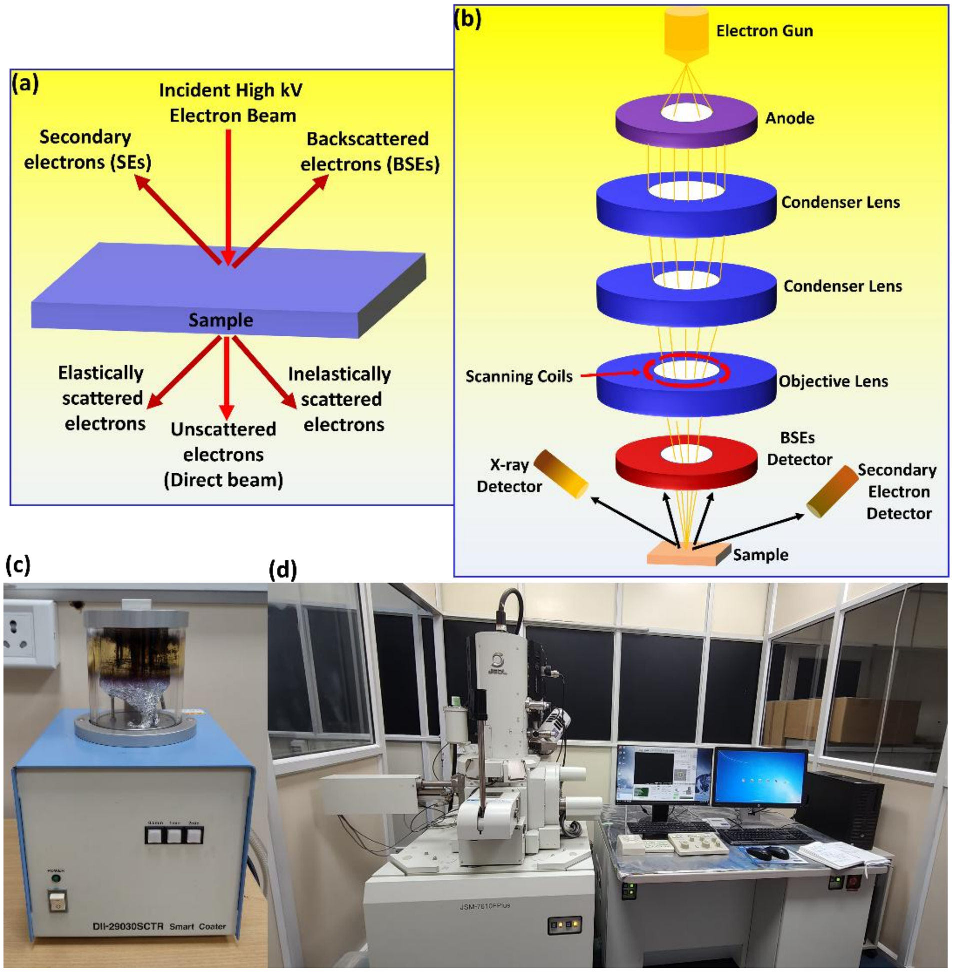

Figure 2.7. (a) Schematic of electron scattering from a specimen, (b) Schematic illustration of FESEM/EDS working principle, real images of the (c) smart coater and (d) JSM-7610F Plus JEOL FESEM.

2.3.3 Transmission Electron Microscopy

TEM is a powerful characterization technique that enables the study of materials at atomic resolution by transmitting a high-energy electron beam through an ultra-thin specimen. Unlike SEM, which provides surface morphology, TEM allows the visualization of internal structures, crystallinity, defects, and phase distribution within a material. Due to its ability to achieve resolutions down to the atomic scale, TEM plays a crucial role in materials science, nanotechnology, and semiconductor research. Advanced modes such as HRTEM and Selected Area Electron Diffraction

(SAED) further enhance its analytical capabilities, making it an indispensable tool for structural and crystallographic investigations.

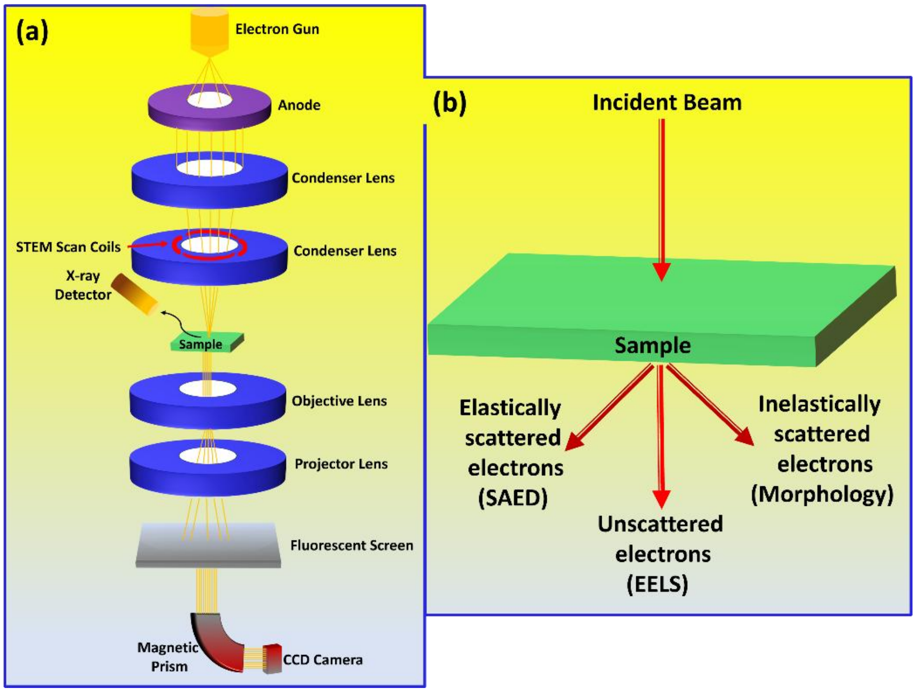

Figure 2.8. Schematic illustration of (a) TEM working principle and (b) electron scattering through a thin specimen.

A TEM setup, Figure 2.8(a), consists of several key components, including the **electron source**, which is typically a thermionic or field-emission gun that generates a highly focused electron beam. The **electron column** houses electromagnetic condenser lenses that focus the beam before it interacts with the sample. The specimen, prepared as an ultra-thin film (~100 nm or less), is held on a **TEM grid** and positioned in the path of the electron beam. Upon interaction, transmitted electrons pass through a series of **objective and projector lenses**, which magnify and resolve the structural details of the sample before the final image is formed on a **fluorescent screen, CCD camera, or a direct electron detector**. A vacuum system is essential in TEM to prevent electron scattering and maintain beam coherence.

TEM operates on the fundamental principle of electron transmission through a thin sample, Figure 2.8(b). When a high-energy electron beam (typically 100–300 keV) interacts with the specimen, some electrons are transmitted without significant deviation, while others undergo diffraction, scattering, or absorption based on the material's density, thickness, and atomic structure. The transmitted electrons are then magnified through a series of electromagnetic lenses to form an image with nanometer or even atomic-scale resolution. Contrast in TEM images arises due to variations in mass-thickness, diffraction, and phase differences, providing critical insights into the material's internal microstructure.

Essential mode is **HRTEM**, which utilizes phase contrast to visualize atomic-scale lattice fringes, enabling direct observation of crystal defects, grain boundaries, and atomic arrangements. HRTEM is particularly useful for structural analysis of nanomaterials, as it provides insights into interplanar spacing and crystallographic orientations. In addition to imaging, TEM is equipped with **SAED** capability, which allows the crystallographic structure of materials to be analyzed. By placing an aperture in the back focal plane of the objective lens, a diffraction pattern is formed, displaying bright spots corresponding to periodic atomic arrangements in the material. The SAED pattern provides information about crystal symmetry, phase identification, and lattice parameters, making it valuable for studying polycrystalline and nanostructured materials [20,21].

In this work, TEM was performed using a **JEOL JEM-2100 Field Emission Electron Microscope (HRTEM, Japan & South Korea)**, operating at **200 KeV**. This high-energy electron beam enabled the imaging of nanostructures with atomic-scale resolution, allowing for detailed analysis of morphology, lattice fringes, and crystallinity.

2.3.4 Thermogravimetric Analysis

TGA is a thermal analysis technique used to study the thermal stability, composition, and decomposition behavior of materials by monitoring their weight change as a function of temperature or time. This technique is widely applied in material science, including gas sensors, catalysts, polymers, and nanomaterials, to evaluate properties such as thermal degradation, moisture content, and phase transitions.

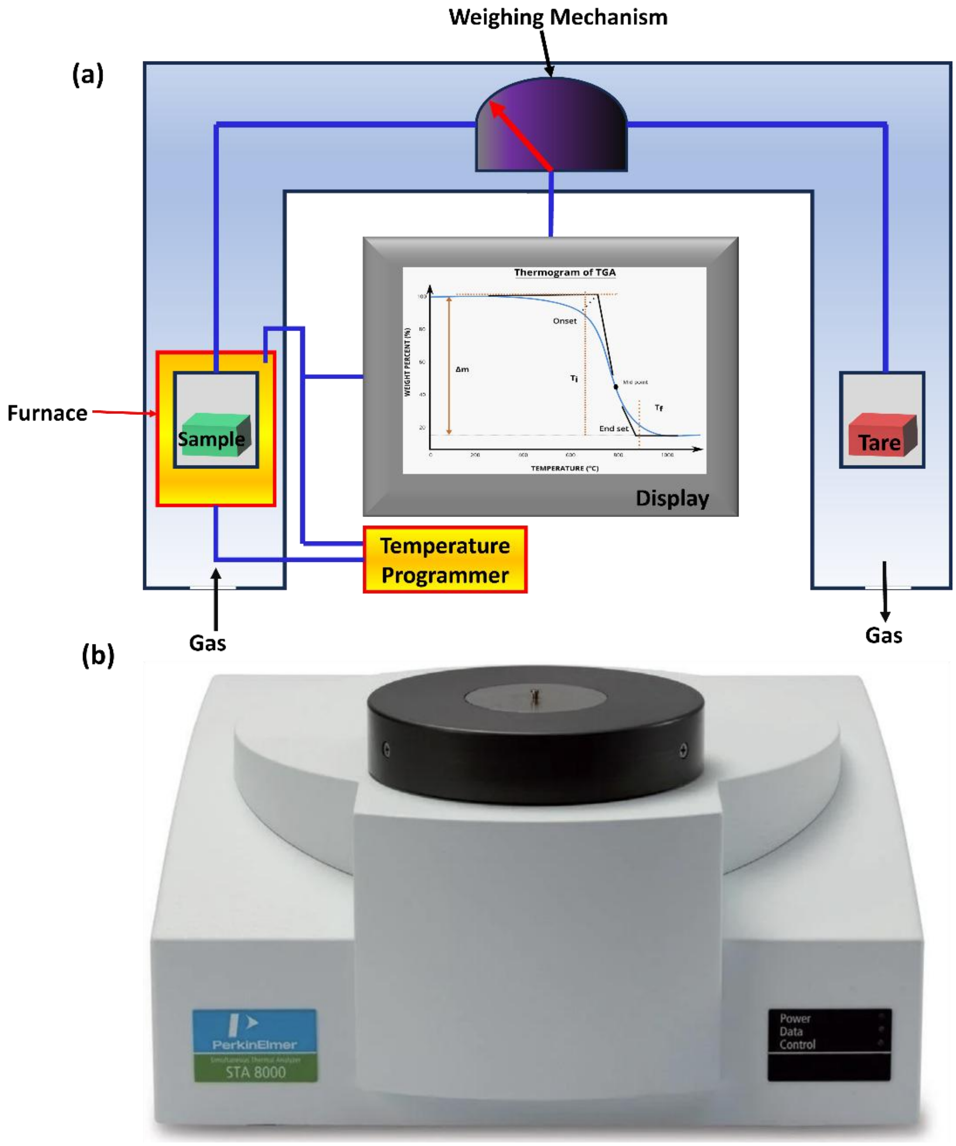

Figure 2.9. (a) Schematic of basic working principle of TGA, and (b) real image of TGA-DTA PerkinElmer, STA8000 used in this work.

A typical TGA system (Figure 2.9 (a)) consists of a high-precision balance, furnace, temperature controller, and gas flow system. The sample is placed in a platinum or alumina crucible and heated in a controlled atmosphere—inert (N_2, Ar) or oxidative (O_2, air)—at a predetermined heating rate (*e.g.*, 5–20°C/min) up to high temperatures (typically 1000°C). The weight change is continuously recorded, and the resulting thermogram provides critical information about decomposition stages and thermal stability. TGA operates based on the principle that as the material is heated, it undergoes physical and chemical changes such as evaporation, decomposition, oxidation, and phase transitions, leading to mass loss. The rate and magnitude of weight loss provide insights into the composition of the material, such as the presence of volatile components, bound water, organic content, or thermal degradation of phases [22,23].

A TGA curve typically consists of distinct weight-loss regions corresponding to different thermal events:

1. **Initial weight loss (50–200°C):** Evaporation of adsorbed water or volatile species.
2. **Intermediate weight loss (200–600°C):** Decomposition of organic components or structural changes.
3. **Final weight loss (>600°C):** Decomposition of inorganic phases or oxidation of remaining residues.

The **derivative thermogravimetric (DTG) curve**, which represents the rate of weight change, helps in identifying transition temperatures and reaction kinetics.

In this study, TGA analysis was performed to evaluate the thermal stability and phase transitions of synthesized nanomaterials. In this work, thermogravimetric and differential thermogravimetric analysis of the as prepared powder samples were investigated using **TGA-DSC (PerkinElmer, STA8000),** Figure 2.9(b), at a heating rate of 5 °C min^{-1} up to 1000 °C in an N_2 atmosphere.

2.3.5 X-Ray Photoelectron Spectroscopy

XPS is a powerful surface-sensitive analytical technique used to determine the elemental composition, chemical states, and electronic structure of materials. It is widely applied in gas sensors to analyze the oxidation states and surface chemistry of synthesized nanomaterials. The technique is based on the photoelectric effect, where X-rays incident on a material eject core-level electrons, and their kinetic energy is measured to determine binding energies characteristic of specific elements and their chemical states.

A typical XPS system (Figure 2.10) consists of an X-ray source, a sample chamber, an electron energy analyzer, and a detector. The monochromatic X-ray source, often Al Kα (1486.6 eV) or Mg Kα (1253.6 eV), irradiates the sample surface, leading to the ejection of core electrons. The emitted electrons pass through an electron energy analyzer, which measures their kinetic energy. The binding energy (BE) of these electrons is calculated using the equation:

$$BE = hv - KE - \Phi \tag{2.2}$$

where hv is the photon energy, KE is the measured kinetic energy, and Φ is the work function of the spectrometer. Since each element has characteristic binding energies, the obtained spectra provide quantitative and qualitative identification of elements present on the surface.

XPS analysis consists of **survey spectra** and **high-resolution spectra**. The survey spectrum identifies all the elements present on the material’s surface (except H and He), whereas high-resolution scans focus on specific elements, revealing their oxidation states. **Chemical shifts** in binding energy occur due to variations in electron density and bonding environment, enabling differentiation between oxidation states (e.g., W^{6+} and W^{4+} in tungsten oxides) [24].

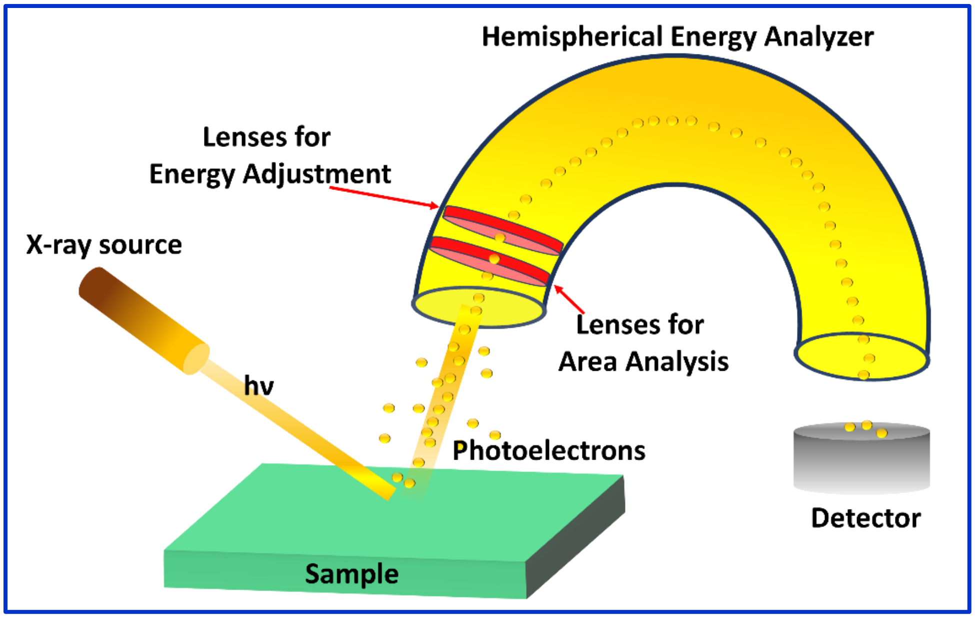

Figure 2.10. Schematic illustration for working principle of XPS.

XPS is particularly useful for studying surface chemistry in gas-sensing materials, catalysts, and metal oxides. Peak deconvolution using software like **XPSPEAK41** helps identify mixed oxidation states, defects, and interactions with adsorbed species. In this work, XPS was conducted on a **Kratos AXIS spectrometer** (**South Korea**) with an Al K*α* source (*hν* = 1486.6 eV) to confirm the oxidation states of elements in synthesized nanomaterials, ensuring phase purity and understanding surface chemical composition.

2.3.6 N_2 adsorption/desorption Analysis

N_2 adsorption/desorption analysis, commonly performed using the **BET method**, is a crucial technique for determining the **specific surface area, pore size distribution, and porosity** of nanomaterials. This technique plays a significant role in gas sensing, catalysis, and energy storage applications, where high surface area and controlled porosity enhance material performance. The method is based on the physical adsorption of nitrogen gas onto the material's surface at cryogenic temperatures (typically **−196°C or 77 K**) and measuring the amount adsorbed at different relative pressures.

A typical BET analyzer consists of a gas dosing system, vacuum chamber, adsorption/desorption unit, and thermal conductivity detector (TCD). Before measurement, the sample undergoes degassing at elevated temperatures (e.g., 200–300°C) under vacuum to remove any surface contaminants or adsorbed moisture. During analysis, nitrogen gas is introduced in controlled amounts, and the adsorption isotherm is recorded by measuring the amount of gas adsorbed as a function of relative pressure (P/P_0).

The BET equation, based on multilayer adsorption theory, is used to calculate the specific surface area (m^2/g):

$$\frac{1}{V[(P_0/P)-1]} = \frac{C-1}{V_m C}\frac{P}{P_0} + \frac{1}{V_m C} \qquad (2.3)$$

where V is the volume of adsorbed gas, V_m is the monolayer volume, P/P_0 is the relative pressure, and C is the BET constant related to adsorption energy.

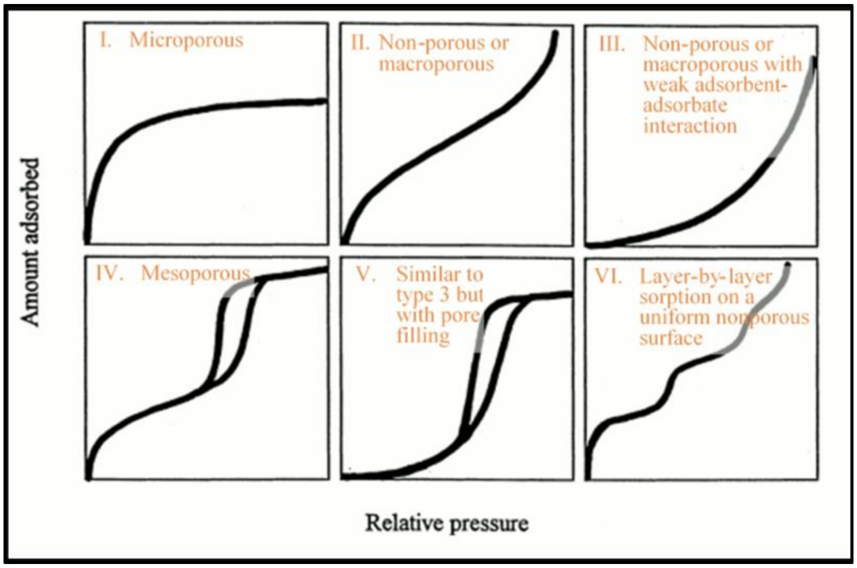

Figure 2.11. Categorization of adsorption isotherms into six different types.

The adsorption-desorption isotherm provides insights into material porosity. Different **isotherm types (I–VI)**, Figure 2.11, classify materials as microporous (<2 nm), mesoporous (2–50 nm), or macroporous (>50 nm). The Barrett-Joyner-Halenda (BJH) method is commonly used to determine pore size distribution from desorption data [25–27].

In this thesis work, N_2 adsorption/desorption analysis was conducted by **Autosob iQ2 system**, Figure 2.12, is used to measure the BET surface area of the grown materialsto determine the specific surface area and pore size distribution of synthesized nanomaterials, which are critical factors influencing gas sensing performance. The obtained adsorption-desorption isotherms were analyzed using the **Quantachrome AsiQwin analyzer** software, which facilitated precise calculation of BET surface area, pore volume, and pore size distribution.

Figure 2.12. Image of the Autosorb iQ2, used in the present thesis work for BET surface area analysis.

2.4 Gas and Humidity Sensing Measurement System

Gas and humidity sensing measurement systems are essential for evaluating the performance of nanomaterials used in sensor applications.

These systems help determine key sensing parameters such as sensitivity, selectivity, operating temperature, response/recovery time, limit of detection, and stability by exposing the material to target gases or humidity levels under controlled conditions. To evaluate the sensing performance of nanomaterials, a **dynamic flow-through gas sensing system** was used instead of a static flow method. In a static system, the gas is introduced into a closed chamber without continuous flow, leading to uneven gas distribution and difficulty in controlling concentration levels. In contrast, a dynamic flow system allows precise control over gas concentration using mass flow controllers (MFCs), ensuring uniform exposure of the sensing material to the target gas. This method also enables real-time analysis of sensor response and recovery, making it more reliable for practical applications [28,29].

2.4.1 Gas Sensing Measurement System

An indigenous instrumental set up for gas sensing experiments was fabricated in the lab. The gas sensing setup consists of a gas chamber, flow controllers, heating unit, electrical measurement setup, and data acquisition system as. The schematic is shown in Figure 2.13. The sensing material, coated onto a substrate with IDE, is placed inside the chamber and exposed to controlled concentrations of gases such as NO_2, CO, NH_3, ethanol, H_2S, SO_2, and CO_2. All the test gases were procured from Ultra-Pure Gases Pvt. Ltd., Gujarat, India (99.9 % purity). Precision MFCs regulate gas flow, ensuring accurate concentration delivery while maintaining a constant total flow rate with dry air as the carrier gas. To achieve different concentrations of the target gas, a controlled mixture of pure gas and dry air is used. The concentration (**C**) of the target gas in parts per million (ppm) can be determined using the equation:

$$C = \frac{F_{gas}}{F_{total}} \, x \, C_{Source} \tag{2.4}$$

where, F_{gas} = Flow rate of the target gas (sccm); F_{total} = Total flow rate (target gas + dry air) (sccm); C_{Source} = Source concentration of the pure gas (usually in ppm)

By adjusting F_{gas} and F_{total}, the desired gas concentration can be obtained. For instance, if 500 ppm NO_2 is available as the source gas and we mix 100 sccm NO_2 with 900 sccm dry air, the final concentration will be:

$$\boldsymbol{C = (100/(100+900)) \times 500 = 50 \text{ ppm}}$$

This method ensures precise control over gas concentration, allowing sensitivity and selectivity analysis at different levels.

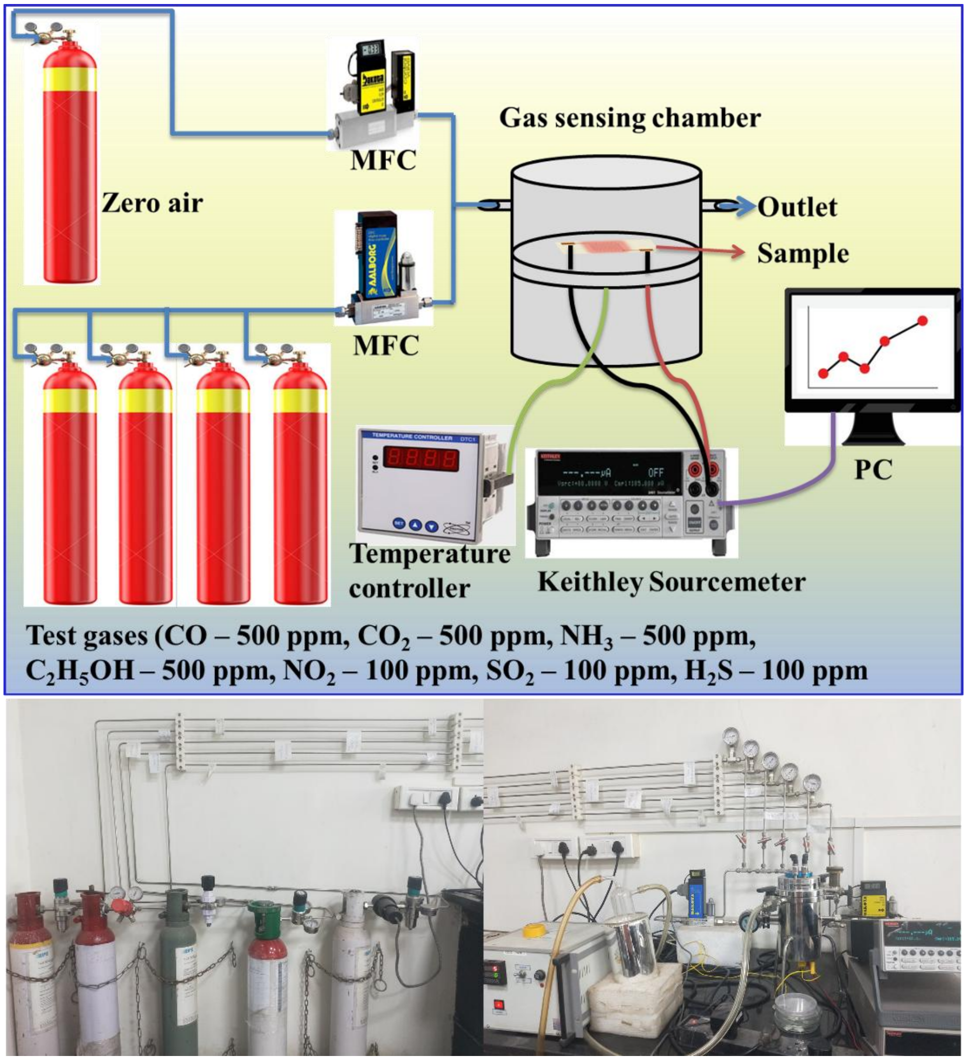

Figure 2.13. Schematic illustration and real image of the Gas-sensing setup.

2.4.2 Humidity Sensing Measurement System

The humidity sensing setup follows a similar design but focuses on controlling relative humidity (RH%) instead of gas concentration. Humidity levels are regulated using a humidifier and dry air gas system, which adjusts the water vapor concentration in the chamber. The sensor's response to humidity is recorded based on changes in resistance.

In this thesis work, to generate different relative humidity levels (**20%, 30%, 40%, 47%, 50%, 60%, 70%, 75%, 80%, 87%, 90%, 97%**), a **saturated salt solution method** is employed inside the chamber, for which one conical flask/bubbler is placed in series with the air flow MFC, which contains an appropriate saturated aqueous solution of different salts. Different salts maintain specific RH values when they reach equilibrium with water vapor. The commonly used salts and their corresponding RH values are:

Table 2.1. Commonly used salts and their corresponding RH values.

Salt Solution	Relative Humidity (%)
Potassium acetate (CH_3COOK)	20-25%
Magnesium chloride ($MgCl_2$)	30-33%
Potassium carbonate (K_2CO_3)	40-47%
Magnesium nitrate ($Mg(NO_3)_2$)	50-53%
Sodium nitrate ($NaNO_3$)	60-63%
Sodium chloride (NaCl)	70-75%
Potassium chloride (KCl)	80-86%
Potassium nitrate (KNO_3)	90-93%
Potassium sulphate (K_2SO_4)	97%

References

[1] A. Saremi, S.M. Mirkazemi, A. Sazvar, H. Rezaie, Controlling magnetic and surface properties of cobalt ferrite nanoparticles: A comparison of co-precipitation and solvothermal synthesis methods, Solid State Sci. 148 (2024) 107432. https://doi.org/10.1016/j.solidstatesciences.2023.107432.

[2] N. PATIL, R. BHASKAR, V. VYAVHARE, R. DHADGE, V. KHAIRE, Y. PATIL, Overview on Methods of Synthesis of Nanoparticles, Int. J. Curr. Pharm. Res. 13 (2021) 11–16. https://doi.org/10.22159/ijcpr.2021v13i2.41556.

[3] A. De, M.S. Kim, A. Adhikari, R. Patel, S. Kundu, Sol-gel-derived nanostructured electrocatalysts for oxygen evolution reaction: a review, J. Mater. Chem. A 12 (2024) 19720–19756. https://doi.org/10.1039/d4ta01442a.

[4] A.E. Danks, S.R. Hall, Z. Schnepp, The evolution of “sol-gel” chemistry as a technique for materials synthesis, Mater. Horizons 3 (2016) 91–112. https://doi.org/10.1039/c5mh00260e.

[5] W. Shi, S. Song, H. Zhang, Hydrothermal synthetic strategies of inorganic semiconducting nanostructures, Chem. Soc. Rev. 42 (2013) 5714–5743. https://doi.org/10.1039/c3cs60012b.

[6] S.H. Feng, G.H. Li, Hydrothermal and Solvothermal Syntheses, 2017. https://doi.org/10.1016/B978-0-444-63591-4.00004-5.

[7] D.R. Modeshia, R.I. Walton, Solvothermal synthesis of perovskites and pyrochlores: Crystallisation of functional oxides under mild conditions, Chem. Soc. Rev. 39 (2010) 4303–4325. https://doi.org/10.1039/b904702f.

[8] A.H. Mamaghani, F. Haghighat, C.S. Lee, Hydrothermal/solvothermal synthesis and treatment of TiO_2 for photocatalytic degradation of air pollutants: Preparation, characterization, properties, and performance, Chemosphere 219 (2019) 804–825. https://doi.org/10.1016/j.chemosphere.2018.12.029.

[9] R. Adel, G. Morse, F. Silvestri, E. Barrena, E. Martinez-Ferrero, M. Campoy-Quiles, P. Tiwana, M. Stella, Understanding the blade

coated to roll-to-roll coated performance gap in organic photovoltaics, Sol. Energy Mater. Sol. Cells 245 (2022) 111852. https://doi.org/10.1016/j.solmat.2022.111852.

[10] Y.Y. Shi, X.F. Wu, H. Zhao, X.Y. Zhang, H.K. Peng, J.H. Lin, Enhancing Performance of Perovskite Solar Cells: A Study on Passivating the Electron Transport Layer via Doctor-Blade Coating in Environmental Conditions, Energy and Fuels (2024). https://doi.org/10.1021/acs.energyfuels.4c04920.

[11] F. Wang, H. Zhao, J. Liang, T. Li, Y. Luo, S. Lu, X. Shi, B. Zheng, J. Du, X. Sun, Magnetron sputtering enabled synthesis of nanostructured materials for electrochemical energy storage, J. Mater. Chem. A 8 (2020) 20260–20285. https://doi.org/10.1039/d0ta07644a.

[12] J. Liang, Q. Liu, T. Li, Y. Luo, S. Lu, X. Shi, F. Zhang, A.M. Asiri, X. Sun, Magnetron sputtering enabled sustainable synthesis of nanomaterials for energy electrocatalysis, Green Chem. 23 (2021) 2834–2867. https://doi.org/10.1039/d0gc03994b.

[13] R. Garg, S. Gonuguntla, S. Sk, M.S. Iqbal, A.O. Dada, U. Pal, M. Ahmadipour, Sputtering thin films: Materials, applications, challenges and future directions, Adv. Colloid Interface Sci. 330 (2024) 103203. https://doi.org/10.1016/j.cis.2024.103203.

[14] A.A. Bunaciu, E. gabriela Udriştioiu, H.Y. Aboul-Enein, X-Ray Diffraction: Instrumentation and Applications, Crit. Rev. Anal. Chem. 45 (2015) 289–299. https://doi.org/10.1080/10408347.2014.949616.

[15] M. Borcha, I. Fodchuk, I. Krytsun, Lattice parameter determination by coincidental multi-beam X-ray diffraction, Phys. Status Solidi Appl. Mater. Sci. 206 (2009) 1699–1703. https://doi.org/10.1002/pssa.200881617.

[16] R. Das, M.E. Ali, S.B.A. Hamid, Current applications of x-ray powder diffraction - A review, Rev. Adv. Mater. Sci. 38 (2014) 95–109.

[17] R. Senthil Prabhu, R. Priyanka, M. Vijay, G.R. Kaviya Vikashini, Field Emission Scanning Electron Microscopy (Fesem) with A Very Big Future in Pharmaceutical Research, Res. Artic. | Pharm. Sci. |

OA J. | MCI Approv. | Index Copernicus 11 (2021) 2321–3272. www.ijpbs.comorwww.ijpbsonline.com.

[18] Microscopy : an introduction, 13 (2000) 40–44.

[19] B. Kämpfe, F. Luczak, B. Michel, Energy dispersive X-ray diffraction, Part. Part. Syst. Charact. 22 (2006) 391–396. https://doi.org/10.1002/ppsc.200501007.

[20] A. Mayeen, L.K. Shaji, A.K. Nair, N. Kalarikkal, Morphological characterization of nanomaterials, Elsevier Ltd., 2018. https://doi.org/10.1016/B978-0-08-101973-3.00012-2.

[21] Z.L. Wang, J.L. Lee, Electron Microscopy Techniques for Imaging and Analysis of Nanoparticles, 2nd ed., Elsevier Inc., 2008. https://doi.org/10.1016/B978-0-323-29960-2.00009-5.

[22] M.C. Tanzi, S. Farè, G. Candiani, Techniques of Analysis, 2019. https://doi.org/10.1016/b978-0-08-101034-1.00007-4.

[23] W. Pan, W. Xu, S. Li, Fundamentals of TGA and SDT, Therm. Anal. Fundam. … (2005) 1–7. http://dialnet.unirioja.es/servlet/articulo?codigo=1986690.

[24] A. V. Boryakov, S.I. Surodin, R.N. Kryukov, D.E. Nikolichev, S.Y. Zubkov, Spectral fit refinement in XPS analysis technique and its practical applications, J. Electron Spectros. Relat. Phenomena 229 (2018) 132–140. https://doi.org/10.1016/j.elspec.2017.11.004.

[25] J.C. Groen, L.A.A. Peffer, J. Pérez-Ramírez, Pore size determination in modified micro- and mesoporous materials. Pitfalls and limitations in gas adsorption data analysis, Microporous Mesoporous Mater. 60 (2003) 1–17. https://doi.org/10.1016/S1387-1811(03)00339-1.

[26] K. Sing, The use of nitrogen adsorption for the characterisation of porous materials, Colloids Surfaces A Physicochem. Eng. Asp. 187–188 (2001) 3–9. https://doi.org/10.1016/S0927-7757(01)00612-4.

[27] K. Kinashi, Y. Kambe, M. Misaki, Y. Koshiba, K. Ishida, Y. Ueda, Synthesis, characterization, photo-induced alignment, and surface orientation of poly(9,9-dioctylfluorene-alt-azobenzene)s, J. Polym. Sci. Part A Polym. Chem. 50 (2012) 5107–5114. https://doi.org/10.1002/pola.26338.

[28] Y.S. Kim, S.C. Ha, H. Yang, Y.T. Kim, Gas sensor measurement

system capable of sampling volatile organic compounds (VOCs) in wide concentration range, Sensors Actuators, B Chem. 122 (2007) 211–218. https://doi.org/10.1016/j.snb.2006.05.023.

[29] Z. Chen, C. Lu, Humidity sensors: A review of materials and mechanisms, Sens. Lett. 3 (2005) 274–295. https://doi.org/10.1166/sl.2005.045.

Chapter 3

Mn-doped $ZnSnO_3$ for Enhanced CO Sensing Performance

This chapter presents the synthesis of Mn-doped $ZnSnO_3$ *microspheres* ($Zn_{1-x}Mn_xSnO_3$) *using a simple co-precipitation method with (x = 0 to 0.15) and characterized for structural, morphological, surface area, and sensing properties. Indeed, a significant increase (≈ 311.37%) in CO gas sensing response is observed in the x = 0.10 sample compared to pure* $ZnSnO_3$ *with a simultaneous reduction in operating temperature from 250 to 200 ºC. Moreover, remarkable enhancements in response/recovery time (≈ 6.6/34.1 s) were obtained in x = 0.10 sample. The Mn-doped* $ZnSnO_3$ *could be a promising candidate for the CO gas sensing devices used for maintaining air quality.*

3.1 Introduction

As discussed in Chapter 1, rapid industrialization and urbanization have led to severe environmental and health hazards, including air pollution and toxic gas emissions. Among these, CO is highly dangerous due to its colorless and odorless nature, making detection challenging. It forms carboxyhemoglobin when inhaled, reducing oxygen transport and posing fatal risks. Since its exposure limit is 50 ppm, continuous and accurate monitoring is essential to prevent harmful effects [1-4].

Chemi-resistive gas sensors based on MOS are widely studied for detecting harmful gases due to their high sensitivity, fast response, cost-effectiveness, and suitability for portable devices [5]. However, their high operating temperature and limited selectivity pose challenges for practical applications. In this regard, ternary ABO_3 perovskite [6,7] structured MOS sensors have attracted the scientific community over the binary MOS sensors due to the presence of multiple cation sites for doping materials exhibit more potential for enhance the device performance in gas sensing applications. Out of various choices, the Zinc stannate ($ZnSnO_3$) ternary compound (*n*-type MOS) is the potential candidate due to its high electron mobility, conductivity, good stability, and attractive physical and chemical property [8] compared to binary counterparts ZnO and SnO_2. These properties enable this material to be employed in various applications such as Li-ion batteries [9], solar cells [10], photocatalysts [11], gas sensing, *etc*. [12].

Numerous studies have explored the gas sensing capabilities of porous $ZnSnO_3$ material, particularly for detecting VOCs like acetone [13], ethanol [14], butanol [15], propanols [16], formaldehyde [17], and triethylamine [18]. However, very few studies are available on the detection of gases except H_2S [12], H_2 [19], Pure $ZnSnO_3$ material usually suffers a requirement barrier due to low sensitivity, poor selectivity, and high operating temperature for the detection of gases other than VOCs. It is known that doping ternary MOS materials with transition metals can significantly enhance the gas sensing performance as it can change the interaction between the gases, oxygen molecules, and the surface electron due to an increase in porosity and large specific surface areas. Despite this, the available studies to improve the gas sensing properties on $ZnSnO_3$ doped with transition metal are significantly less, for instance, Fe [20], Al [21], Mg [22], and Pd [23] have been doped in $ZnSnO_3$ for performance improvement.

I. Karaduman *et al.* [24] and E. Della Gaspera *et al.* [25] have reported the doping of transition metal Mn to ZnO compounds where improvement of CO sensing was ascribed to the multiple oxidation states of Mn, preferred adsorption of CO molecules at the transition metal dopant sites and then their migration from Mn or Cu sites to Zn sites, and large specific surface area with increased oxygen adsorption and its reactivity with CO molecules.

In line with the aforementioned discussion, this work aimed to investigate the gas sensing performance of $ZnSnO_3$ material doped with varying concentrations of Mn. This chapter presents a simple and economical technique for synthesis of $ZnSnO_3$ with different loading of Mn ($Zn_{1-x}Mn_xSnO_3$, $x = 0$ to 0.15) using co-precipitation method and systematically investigated for structural and morphological properties. Being highly sensitive to CO among interferring gases, sensing measurements of Mn-doped $ZnSnO_3$ samples were achieved for different concentration of CO. The best performing device was undergone long-term stability and reproducibility test for repeated cycles. Finally, the plausible gas-sensing mechanism has been discussed to postulate the influence of Mn doping in the $ZnSnO_3$ perovskite microstructure.

3.2 Experimental Section

3.2.1 Materials

Materials required such as Zinc sulfate heptahydrate ($ZnSO_4.7H_2O$, >99.5%), Sodium stannate trihydrate ($Na_2SnO_3.3H_2O$, >99%), Manganese sulfate monohydrate ($MnSO_4.H_2O$, >99%), and Ammonia solution (NH_3,

~25%) were of analytical grade and purchased from Sigma-Aldrich Co. Ltd. All the reagents were used without any further purification.

3.2.2 Synthesis of pure and Mn-doped $ZnSnO_3$ microspheres

Pure and Mn-doped $ZnSnO_3$ microspheres were synthesized by a simple co-precipitation method. The Mn-doped $ZnSnO_3$ microspheres were synthesized using a co-precipitation method, as described in **Chapter 2** (**2.2.1 Synthesis of Mn-doped $ZnSnO_3$ Nanostructures by Co-precipitation)**. Aqueous solutions of $ZnSO_4$, Na_2SnO_3, and $MnSO_4$ were mixed under controlled pH conditions, followed by stirring at 60 ºC. The resulting precipitate was collected, washed, dried, and calcined at 500 ºC for 4 hours to obtain the final $ZnSnO_3$ and Mn-doped $ZnSnO_3$ samples. The final products with calculated Mn content of 0, 2.5, 5, 7.5, 10 and 15 atomic (*at*) % were named as ZSO, $Z_{0.975}Mn_{0.025}SO$, $Z_{0.95}Mn_{0.05}SO$, $Z_{0.925}Mn_{0.075}SO$, $Z_{0.9}Mn_{0.1}SO$ and $Z_{0.85}Mn_{0.15}SO$, respectively.

3.2.3 Device Fabrication

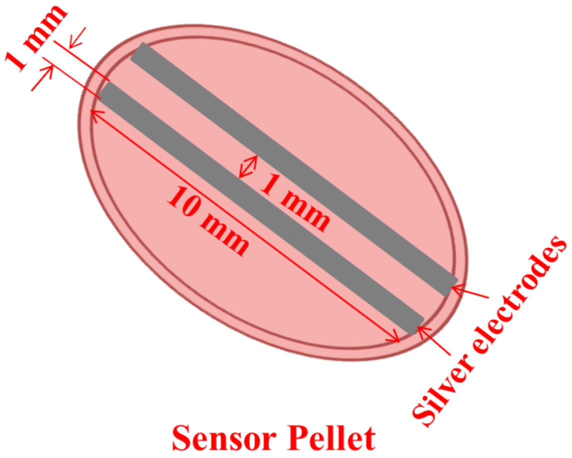

Figure 3.1. Schematic illustration of the gas sensor fabricated using pellet consisting of Mn-doped $ZnSnO_3$.

The pure ZSO and Mn-doped ZSO samples in the powder forms were pressed into pellets of 10 mm diameter, Figure 3.1, by using the hand operated hydraulic press machine under a constant load of 14 ton and then the pellet was used for the CO sensing. The ohmic contacts were designed on the pellet to fabricate the sensing element equipping it with two thin parallel silver electrodes maintaining a gap of 1 mm.

3.3 Results and Discussion

3.3.1 Structural characterization

The effect of the concentration of Mn doping on the crystal structure of the ZSO spherical particles was analyzed by the XRD characterization. The XRD patterns of pure and Mn-doped $ZnSn(OH)_6$ precursor are depicted in Figure 3.2(*a*) which are in good agreement with the JCPDS card No. 20-1455. The diffraction peaks in the pattern can be indexed to a pure *fcc*-phase $ZnSn(OH)_6$ (space group: *Pn*-3) which is in good agreement with the Reitveld refinement, as shown in Figure 3.2(*b*). The crystallites are preferentially oriented along the *x*-axis, [200] direction. Lattice parameters of the pure and Mn-doped precursors were calculated by the Rietveld refinement using the Full Prof software. The obtained lattice parameters are shown in Table 3.1 which depicts the minor increase in lattice parameters with the increase in Mn-doping concentration. The characteristic peaks of any other phases such as ZnO, SnO_2 and other phases of $ZnSnO_3$ or $ZnSn(OH)_6$ were not observed which indicates the facile substitution of Mn in $ZnSn(OH)_6$, probably due to akin ionic radius of Mn^{2+} ion (0.67 Å) with Zn^{2+} (0.74 Å).

Figure 3.2 (*c*) presented the XRD characterization patterns of single phase $Zn_{1-x}Mn_xSnO_3$ samples after annealing at 500 ºC. Only one broad peak was observed in all diffraction peaks related to the amorphous $ZnSnO_3$ (JCPDS *no.*- 28-1486). This indicates that all the pure and Mn-doped $ZnSn(OH)_6$ precursors were converted into the final product of the pure and Mn-doped $ZnSnO_3$ phase.

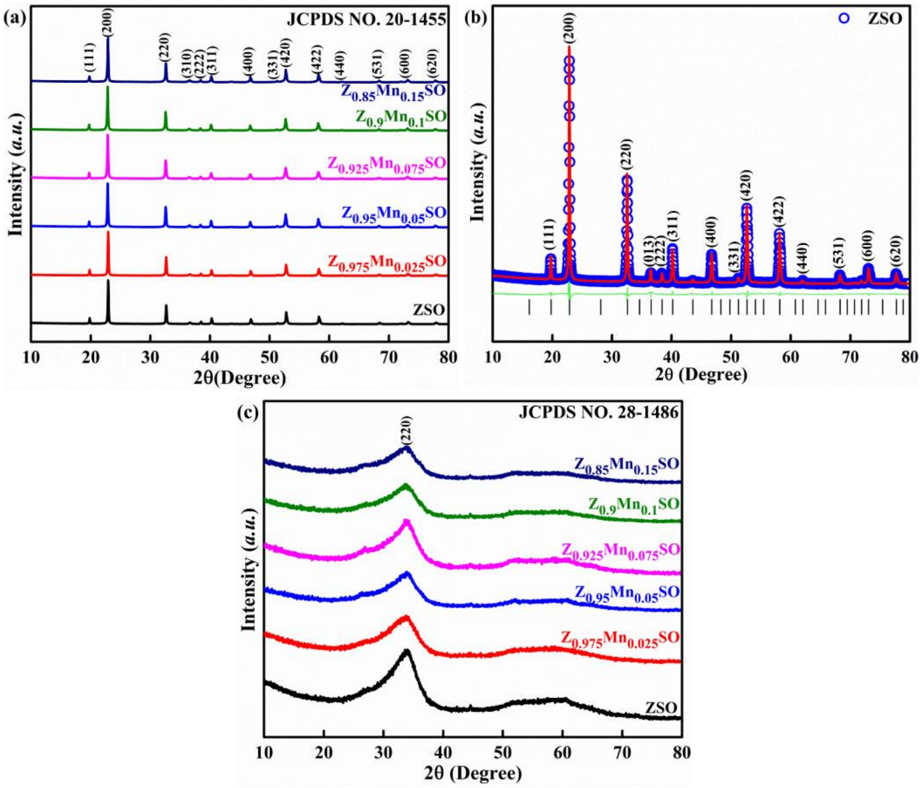

Figure 3.2. (a) XRD patterns of as-synthesized $Zn_{1-x}Mn_xSn(OH)_6$ samples (b) Reitveld refinement of the as-synthesized $ZnSn(OH)_6$ sample. (c) XRD patterns of $Zn_{1-x}Mn_xSnO_3$ samples after annealing at 500 ºC.

Table 3.1 Lattice parameters of the samples calculated by the Rietveld refinement.

$Zn_{1-x}Mn_xSn(OH)_6$	**Lattice constant (Å)** ***a*=*b*=*c***
$x = 0$	7.751±0.004
$x = 0.025$	7.754±0.002
$x = 0.05$	7.755±0.001
$x = 0.075$	7.755±0.006
$x = 0.1$	7.757±0.003
$x = 0.15$	7.761±0.003

3.3.2 Thermal analysis (TGA-DTG)

The TGA was accomplished to investigate the thermal stability of as-prepared pure and Mn-doped $ZnSn(OH)_6$ samples obtained before heat treatment, and DTG curves were used to examine the thermal decomposition of the samples. As shown in Figure 3.3, there is a noticeable weight loss of 17.94 % up to 260 ºC (2.7% from 25 ºC to 130 ºC and 15.24 % from 130 ºC to 260 ºC) and only about 3% weight loss is observed from 260 ºC to 1000 ºC. Thus, the weight loss of almost 18% up to 260 ºC from the precursor samples revealed the dehydration of adsorbed water from pure and Mn-doped $ZnSn(OH)_6$ samples and hence justifying the removal of hydroxyl (-OH) group to generate $ZnSnO_3$ and water. Further, the weight loss of almost 3% from 260 ºC to 1000 ºC is accredited to the dehydration of water molecules which were trapped within the crystals and thus required more thermal energy than the adsorbed water molecules [26].

The DTG curves exhibit the endothermic peaks at 201.19 ºC, 197.76 ºC, 199.93 ºC, 197.13 ºC, 204.90 ºC, and 197.76 ºC, for ZSO, $Z_{0.975}Mn_{0.025}SO$, $Z_{0.95}Mn_{0.05}SO$, $Z_{0.925}Mn_{0.075}SO$, $Z_{0.9}Mn_{0.1}SO$ and $Z_{0.85}Mn_{0.15}SO$, respectively, that could be attributed to the evaporation of residual moisture. The overall weight loss is about 21% in the whole process which is almost very close to the earlier reported value (21%) [27]. The rapid weight loss between 130 ºC and 260 ºC is expressed as the following chemical reaction:

$$ZnSn(OH)_6 \xrightarrow{\geq 130\ ℃} ZnSnO_3 + H_2O \qquad (3.1)$$

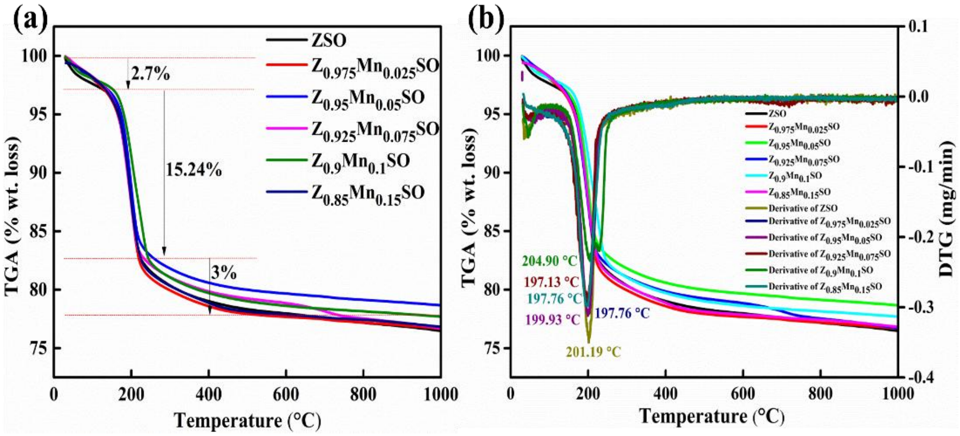

Figure 3.3. (a) TGA plot, and (b) TG-DTG plot of the as-prepared samples of the $Zn_{1-x}Mn_xSnO_3$, $x = 0, 0.025, 0.05, 0.075, 0.1, 0.15$.

3.3.3 Fourier Transform Infrared (FTIR) Spectrum Analysis

The XRD results are also consistent with those of FTIR analysis of both the as-prepared and annealed samples, Figure 3.4, revealing relevant spectral changes in both the cases. Figure 3.4(*a*) illustrates the FTIR spectra of as-prepared pure and Mn-doped $ZnSn(OH)_6$ precursors. The broad band at ~3186 cm^{-1} is ascribed to the stretching vibration modes of –OH group in water molecules. The other three peaks at 1169, 766 and 522 cm^{-1} are assigned to the bending and stretching vibration of M-OH or M-OH-M groups. Thus, the existence of these surface -OH groups characterize the as-prepared samples as $ZnSn(OH)_6$. However, Figure 3.4(*b*) shows the FTIR spectra of the $Zn_{1-x}Mn_xSnO_3$ samples after annealing at 500 ºC where all the peaks related to -OH bonds vibration were disappeared indicating the dehydration of water molecules after annealing. The strong broad absorption peak at ~457 cm^{-1} could be attributed to the metal oxide (M-O) bond of Zn-O and Sn-O and the small weak band observed at 1219 to 1731 cm^{-1} ascribed to the stretching vibration of M-O-M bonds [28,29] in the $ZnSnO_3$. Hence, the disappearance of –OH groups during annealing and the formation of $ZnSnO_3$ structure is clearly confirmed by the FTIR analysis.

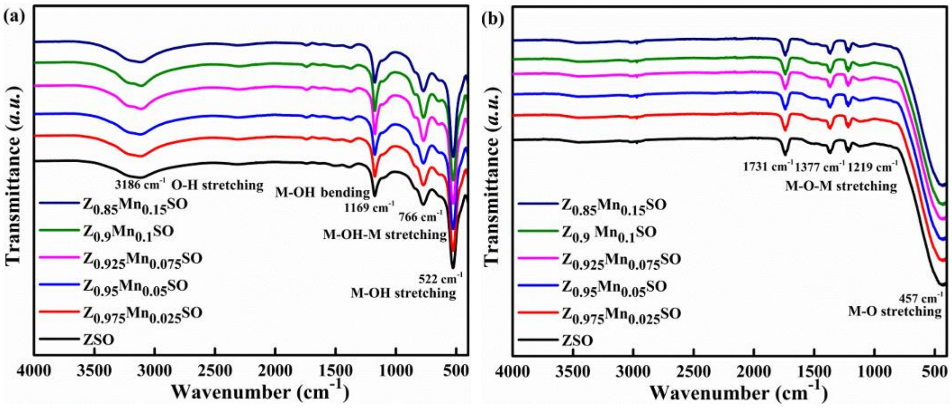

Figure 3.4. FT-IR spectra of (a) as-synthesized $Zn_{1-x}Mn_xSn(OH)_6$ samples, and (b) $Zn_{1-x}Mn_xSnO_3$ samples annealed at 500 ºC.

3.3.4 Morphological Characterization

The morphology of the pure ZSO samples and with different concentrations of Mn ($Zn_{1-x}Mn_xSnO_3$, x = 0, 0.025, 0.05, 0.075, 0.1 and 0.15) after annealed at 500 ºC were characterized by FE-SEM, as shown in Figure 3.5. From Figure 3.5 (*a-f*), it can be seen that all samples exhibit the similar spherical surface morphology. It is also noted that numerous nanoparticles are stacked together to frame porous microsphere structure. Agglomerations of the particles were seen due to the high surface energy [30] of the synthesized particles. The average outer diameter of spherical particles was also calculated and found to be decreasing from 900 nm to 500 nm with increase in concentration of Mn. Thus, Mn doping causes increase in surface area and creates pores in microspheres. This is conducive to the quick adsorption of target gas and reaction with the materials to give the better gas sensing property.

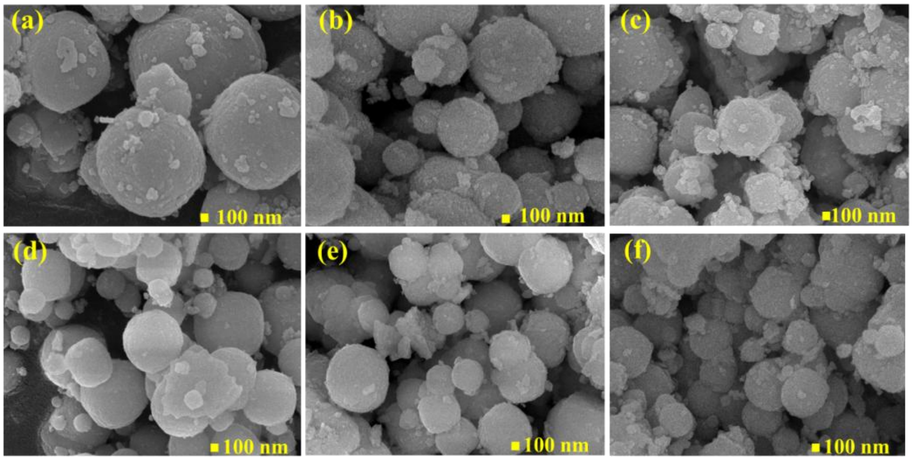

Figure 3.5. FESEM images of Zn$_{1-x}$Mn$_x$SnO$_3$ spherical particles, x = (a) 0, (b) 0.025, (c) 0.05, (d) 0.075, (e) 0.1, (f) 0.15.

EDS and SEM elemental mapping were conducted to resolve the atomic ratio and specific distribution of Zn, Sn, O and Mn elements (Z$_{0.9}$Mn$_{0.1}$SO). As shown in Figure 3.6(c-f), uniform distribution of Zn, Sn, O and Mn in the selected microsphere was clearly verified. Also, according to the EDS spectrum, Figure 3.6(b) depicted the quantitative presence of Zn, Sn, O, and Mn elements, in addition to Au element which is due to the Au coating used in the analysis.

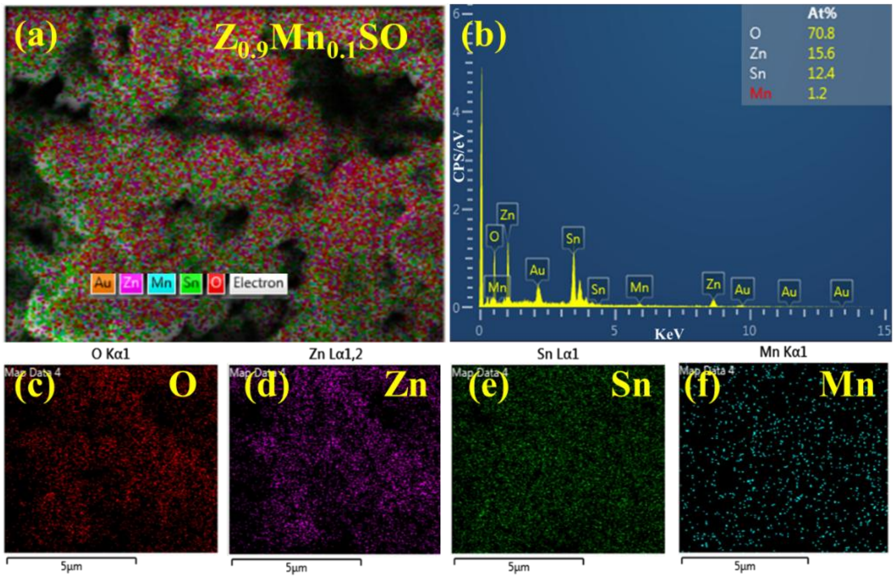

Figure 3.6. (a-f) EDS spectrum and Elemental mapping of $Zn_{1-x}Mn_xSnO_3$ samples, $x = 0.1$.

3.3.5 N_2 adsorption-desorption isotherm

N_2 adsorption-desorption isotherm analysis is another essential technique to elucidate the properties of gas-sensing materials in terms of parameters such as specific surface area of materials, pore- size distribution and specific pore volume. It is well affirmed that the higher gas-sensing performance are achieved for the materials having higher specific surface area thereby more active sites contribute to the redox reaction [31].

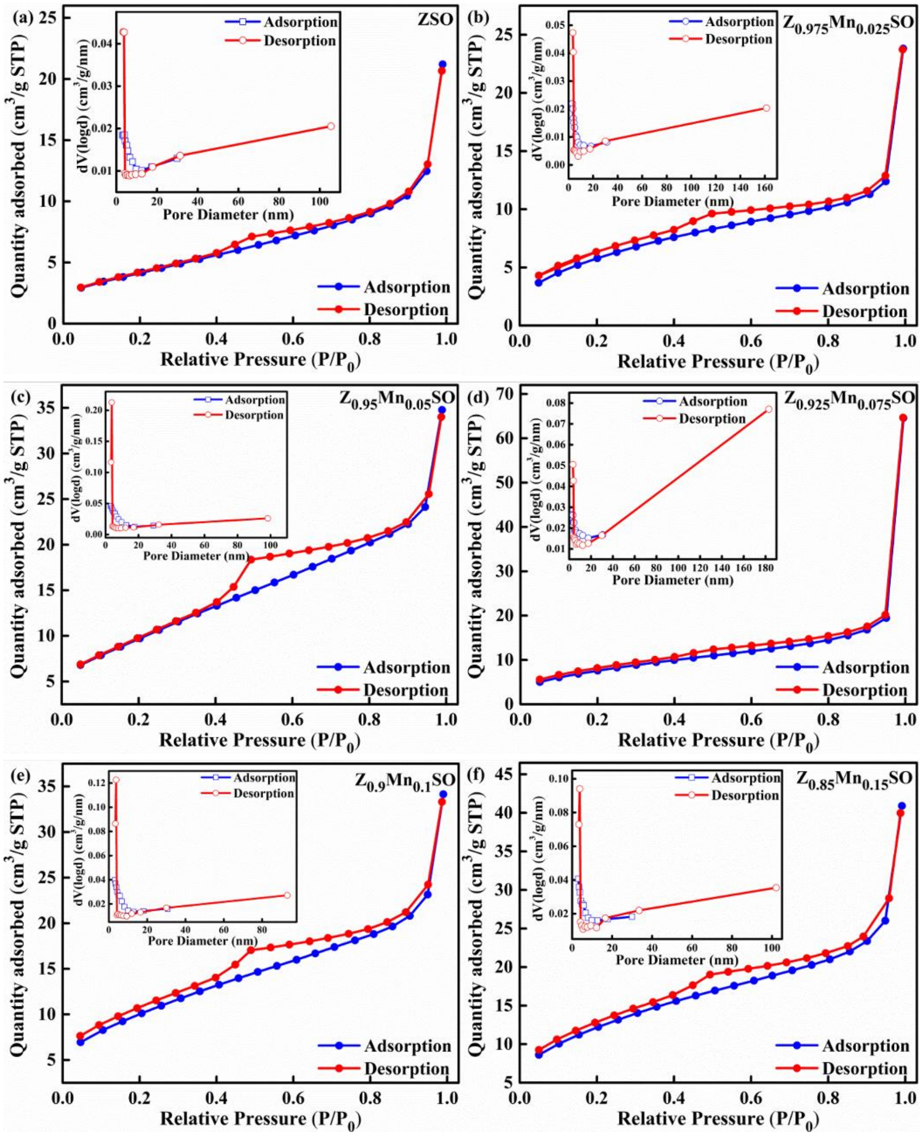

Figure 3.7. N_2 adsorption-desorption isotherm and the corresponding BJH pore size distribution of $Zn_{1-x}Mn_xSnO_3$, x = (a) 0, (b) 0.025, (c) 0.05, (d) 0.075, (e) 0.1, (f) 0.15.

Figure 3.7(a-f) represents the typical N_2 adsorption-desorption isotherm for the $Zn_{1-x}Mn_xSnO_3$ microspheres. Based on IUPAC classification, the resulting isotherms of these six materials can be classified as type-IV isotherms along with a defined hysteresis loop. The inset of Figure 3.7 (a-f) represents the BJH pore size distribution of all these respective six materials revealing the existence of mesoporous structure. The BET surface areas and BJH pore size diameter of all these six materials are represented in Table 3.2. It was observed that Mn-doped ZSO materials have higher surface area in compared to that of pure ZSO material and the increasing trend in surface area was obtained with the increase in Mn-doping concentration. Additionally, for all these six materials, bulk of the pores lies in the region of 3-18 nm (inset of Figure 3.7 (*a-f*)) and very few pores lies beyond 18 nm. The average pore diameters are 3.097, 3.088, 3.075, 3.060, 3.099 and 3.091 nm, respectively for the ZSO, $Z_{0.975}Mn_{0.025}SO$, $Z_{0.95}Mn_{0.05}SO$, $Z_{0.925}Mn_{0.075}SO$, $Z_{0.9}Mn_{0.1}SO$ and $Z_{0.85}Mn_{0.15}SO$. This increased surface area with the suitable mesoporous structure is advantageous to fast adsorption of gas promoting surface reaction thereby remarkably enhancing gas sensing properties of Mn-doped ZSO materials.

Table 3.2 Surface area, pore size and pore volume of the $Zn_{1-x}Mn_xSnO_3$ samples.

Sample	**BET (m^2/g)**	**Pore Size (nm)**	**Pore Volume (cm^3/g)**
ZSO	15.229	3.097	0.03279
$Z_{0.975}Mn_{0.025}SO$	21.340	3.088	0.03692
$Z_{0.95}Mn_{0.05}SO$	27.878	3.075	0.05281
$Z_{0.925}Mn_{0.075}SO$	30.261	3.060	0.05379

$Z_{0.9}Mn_{0.1}SO$	36.294	3.099	0.09990
$Z_{0.85}Mn_{0.15}SO$	42.999	3.091	0.06328

3.3.6 X-ray Photoelectron Spectroscopy (XPS)

Gas sensing is a surface-dominant process depending on the surface state of gas sensing materials. XPS was used to further investigate the sensing materials for the surface elemental composition and their corresponding valence state. Figure 3.8(*a*) illustrates the survey spectra of the $ZnSnO_3$ (ZSO) and $Z_{0.9}Mn_{0.1}SO$ samples. It indicates the existence of Zn, Sn, and O elements on the surface of ZSO samples, whereas presence of Zn, Sn, O, and Mn elements on the surface of $Z_{0.9}Mn_{0.1}SO$ samples which are in consistent with the EDS observations. Figure 3.8 (*b*) presents the high-resolution spectra of Zn 2*p*, two distinctive peaks of Zn 2p in ZSO at binding energies of 1021.30 eV and 1044.24 eV are signifying to Zn $2p_{3/2}$ and Zn $2p_{1/2}$, respectively. However, two distinctive peaks of Zn 2*p* in $Z_{0.9}Mn_{0.1}SO$ have an apparent shift to 1021.01 eV (Zn $2p_{3/2}$) and 1044.09 eV (Zn $2p_{1/2}$), respectively. Figure 3.8 (*c*) shows the high-resolution spectra of Sn 3*d* in ZSO and $Z_{0.9}Mn_{0.1}SO$. Two distinctive peaks of Sn 3*d* in ZSO are located at binding energies of 486.30 eV (Sn $3d_{5/2}$) and 494.71 eV (Sn $3d_{3/2}$), whereas the two distinctive peaks of Sn 3*d* in $Z_{0.9}Mn_{0.1}SO$ are shifted to 485.84 eV (Sn $3d_{5/2}$) and 494.26 eV (Sn $3d_{3/2}$), respectively. The corresponding peaks of Zn 2*p* and Sn 3*d* demonstrates the existence of Zn^{2+} and Sn^{4+} in the samples. Deconvolution of the Mn 2*p* spectrum in Figure 3.8(*d*) shows two distinctive peaks at binding energies of 640.77 eV (Mn $2p_{3/2}$) and 654.30 eV (Mn $2p_{1/2}$) having orbital splitting energy of 13.5 eV, signify presence of Mn^{2+} in $Z_{0.9}Mn_{0.1}SO$ samples. The apparent shift of the Zn 2*p* and Sn 3*d* characteristics peaks indicates the electronic interaction between the Mn^{2+} (dopant), Zn^{2+} and Sn^{4+} sites. Mn-doping makes the sample electron rich due to the generation of vacancy defects. To analyze the impact of oxygen vacancy defects, O 1*s* peaks of ZSO and $Z_{0.9}Mn_{0.1}SO$ have been analyzed as shown in Figure 3.8(*e*-*f*). The O 1*s* spectra are deconvoluted into three peaks: O_L corresponding to lattice oxygen, O_V cause by oxygen vacancy defect and O_C corresponding to chemisorbed oxygen. For ZSO sample, the three peaks centered at 529.78 eV, 531.2 eV and 532.79 eV are assigned to O_L, O_V and O_C, respectively. Similarly, the three distinctive peaks of O 1*s* in $Z_{0.9}Mn_{0.1}SO$ sample are centered at 529.05 eV, 530.11 eV and 531.46 eV, respectively. The relative percentage of each oxygen species are depicted in Figure 3.8(*e*) and Figure 3.8(*f*), respectively. Compared with pure ZSO, there is a significant reduction in O_L concentration for $Z_{0.9}Mn_{0.1}SO$ (from 40.59% to 26.70%), whereas a surge in O_V (from 38.52% to 45.25%) and O_C (from 20.88% to 28.05%) concentrations, suggesting the beneficial use of Mn-doping for enhancing the gas-sensing performance of $ZnSnO_3$.

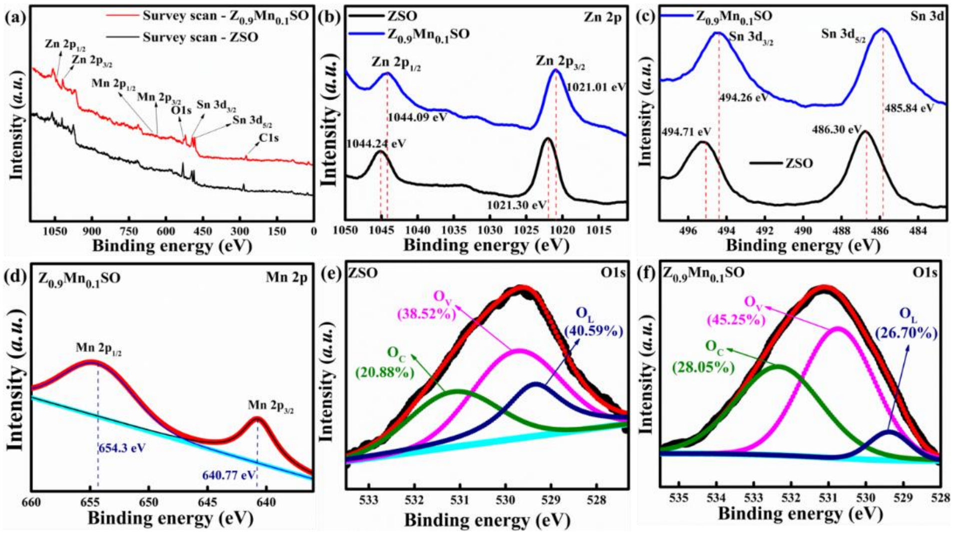

Figure 3.8. The XPS spectra of ZSO and $Z_{0.9}Mn_{0.1}SO$ samples: (a) Survey scan XPS spectra, (b) Zn 2*p* XPS spectra, (c) Sn 3*d* XPS spectra, (d) Mn 2*p* XPS spectra of $Z_{0.9}Mn_{0.1}SO$, (e) O 1*s* XPS spectra of ZSO, and (f) O 1*s* XPS spectra of $Z_{0.9}Mn_{0.1}SO$.

3.3.7 Gas Sensing Properties

The operating temperature plays an essential role in investigating the dynamic gas response of the sensor material. It significantly affects the adsorption-desorption phenomenon and reaction kinetics of the target gas with oxygen molecules on the sensor surface by improvising the activation energy in the sensing material [32]. Therefore, investigations were done to test the sensing performance of $Zn_{1-x}Mn_xSnO_3$ samples exposing it to 500 ppm CO gas at various altered operating temperatures of 50-300 ºC. Figure 3.9(*a*-*f*) depicted the *n*-type semiconducting behavior of all these six materials because of the decrease in resistance with the increase in operating temperature. Initially, sensors were stabilized for a constant resistance value under the exposure of fresh dry air at a particular operating temperature. When the sensors were exposed to CO (reducing gas), a decrease in electrical resistance value was observed, gets stabilized for a while and returns to the initial value after the CO supply was cut-off and re-exposed to the fresh dry air. It is obvious from the Figure 3.9 that Mn-doped ZSO sensors exhibit more decline in resistance value than that of pure ZSO sensors and thus exhibit higher response.

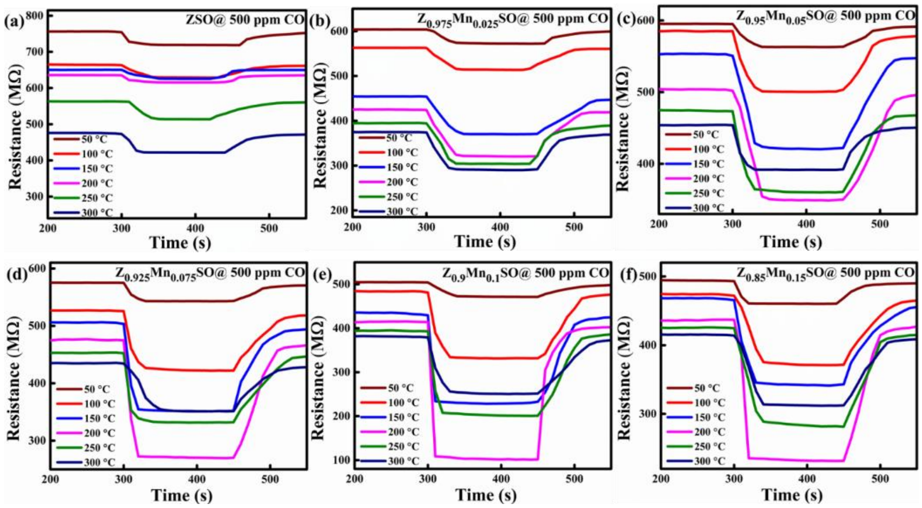

Figure 3.9. Dynamic response-recovery curves of the gas sensor based on $Zn_{1-x}Mn_xSnO_3$, x = (a) 0, (b) 0.025, (c) 0.05, (d) 0.075, (e) 0.1, and (f) 0.15.

As shown in Figure 3.10(a-b), the maximum percentage change in resistance of sensors at different operating temperature from 50 ºC to 300 ºC towards 500 ppm CO was calculated and represented in terms of response. The sensing response of all the sensors was seen to follow "increase-maximum-decrease" tendency [15]. Figure 3.10 shows that for the pure ZSO sensor, there is a small change in response and the maximum response is 5.79% at the operating temperature of 250 ºC. However, for the entire Mn-doped ZSO sensor, the operating temperature significantly drops down to 200 ºC with the remarkable enhancement in respective responses. As shown in Figure 3.10(*a*), ZSO sample doped with 10 *at* % Mn achieved the best response of~311.37% at the 200 ºC operating temperature. Because $Z_{0.9}Mn_{0.1}SO$ sample displays best gas response to CO, the optimized value of Mn-doping is 0.1 (10 *at* %). As a result, $Z_{0.9}Mn_{0.1}SO$ sample was chosen as a propitious candidate for further study in this work.

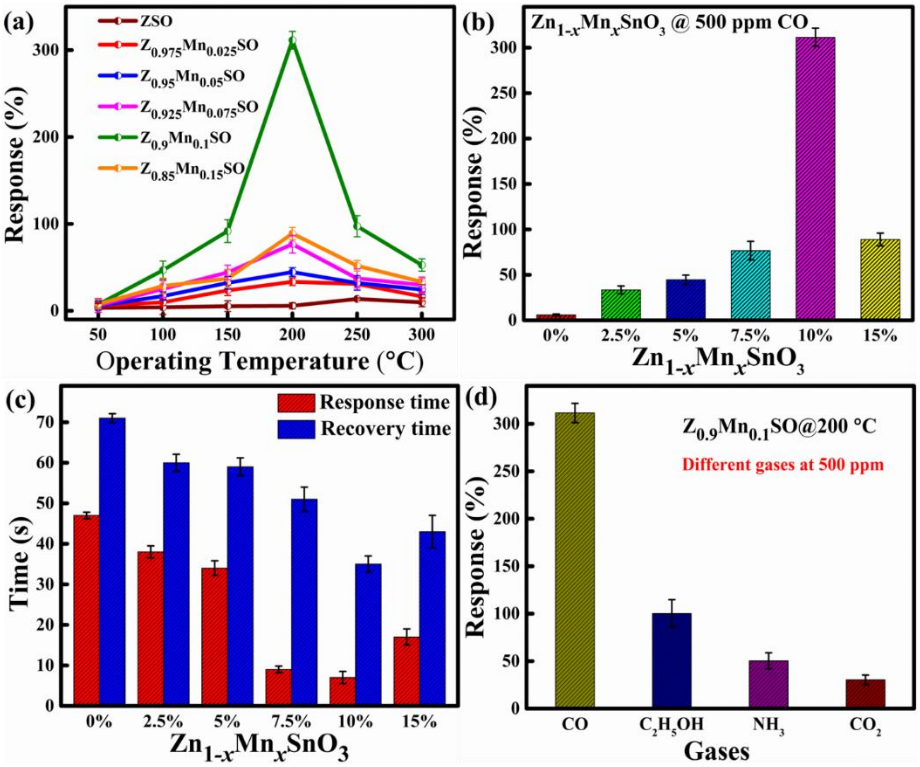

Figure 3.10. (a-b) Relationship between the responses of gas sensor exposed to 500 ppm CO gas and operating temperature. (c) Comparison of the response and recovery times of the $Zn_{1-x}Mn_xSnO_3$ sensors upon exposure to 500 ppm CO at the operating temperature of 200 ºC. (d) Selectivity study by the comparison of $Z_{0.9}Mn_{0.1}SO$ sensor responses to different gases at the operating temperature of 200 ºC.

The response time and recovery time is another essential parameter to judge the new generation gas sensor for fast detection of particular gases and speedy recovery to its ambient conditions in real application field. The response and recovery time of the 0%, 2.5%, 5%, 7.5%, 10% and 15% Mn-doped ZSO sensors towards 500 ppm CO at 200 ºC were measured (shown in Figure 3.11) for the 90% of resistance changes and the compared results are as shown in Figure 3.10(*c*). Here, it is clearly observed that $Z_{0.9}Mn_{0.1}SO$ sensor exhibit shortest response time of 6.6 s among all the six samples and also the accelerated desorption rate of CO on $Z_{0.9}Mn_{0.1}SO$ due to presence of Mn with the recovery time of 34.1 s.

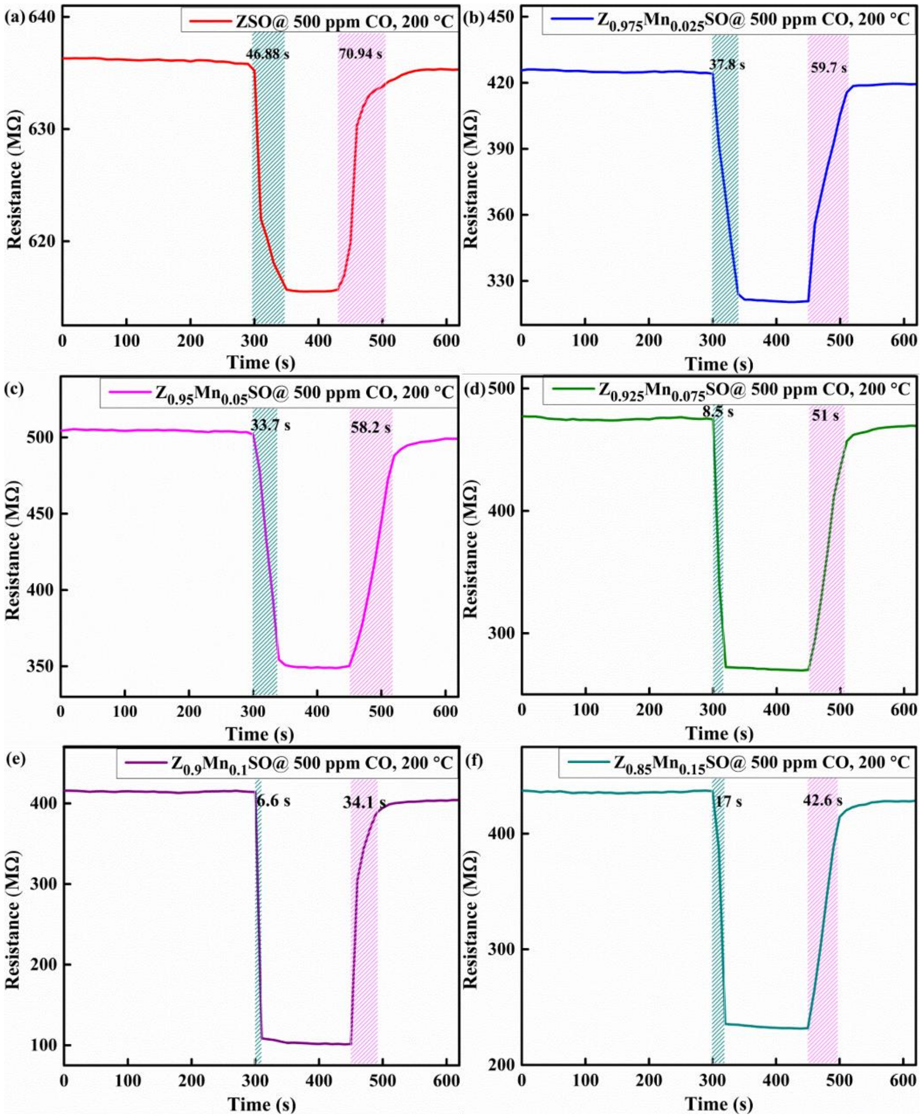

Figure 3.11. Response and recovery time curves of the $Zn_{1-x}Mn_xSnO_3$ upon exposure to 500 ppm CO at the operating temperature of 200 ºC, x = (a) 0, (b) 0.025, (c) 0.05, (d) 0.075, (e) 0.1, and (f) 0.15.

Selectivity is another critical parameter to define the gas sensor's ability to differentiate a specific target gas among other interfering gases. The responses (%) of the $Z_{0.9}Mn_{0.1}SO$ sample towards exposure to four different gases, CO, NH_3, ethanol (C_2H_5OH) and CO_2 were calculated at the operating temperature of 200 ºC. As demonstrated in Figure 3.10(*d*), the $Z_{0.9}Mn_{0.1}SO$ sensor gives excellent responses to CO, whereas low responses to other interfering gases. Thus, the result from Figure 3.10(*d*) inferred that the present $Z_{0.9}Mn_{0.1}SO$ sensor has excellent selectivity towards CO.

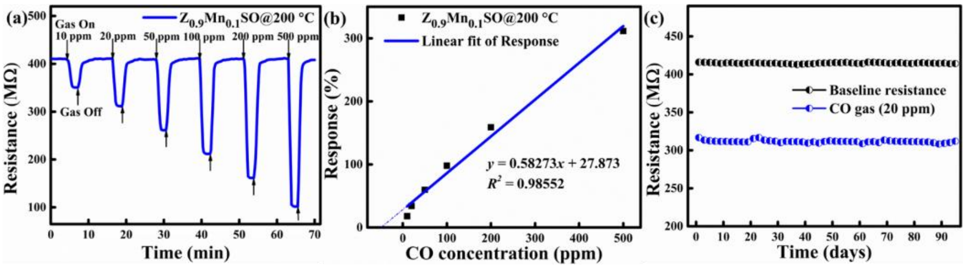

Figure 3.12. (a) Dynamic response-recovery curves towards different varying CO gas concentrations; (b) Calibration curve at 200 ºC related to $Z_{0.9}Mn_{0.1}SO$ sensor. (c) Long-term stability test for the $Z_{0.9}Mn_{0.1}SO$ sensor responding to 20 ppm CO gas.

Figure 3.12(*a*) presents the changes observed in resistance value of the $Z_{0.9}Mn_{0.1}SO$ sensor under the exposure of CO gas at varying concentrations in the range of 10 to 500 ppm. It clearly represents the increase in resistance value with respect to increase in CO concentration. Moreover, the rapid response as CO gas was injected, stable value in the presence of CO environment and then sharp recovery to the initial value when the CO gas was removed at all concentrations of CO gas. The percentage change in resistance was used to compute the response (%) and Figure 3.12(*b*) depicts the increased sensor response with CO concentration.

An approximate good linear correlation was observed with the CO concentration, where linear correlation value was found to be 0.98552. The good linear response to CO allows to reach a lower detection limit in sub-ppm level, less than 1 ppm.

Long-term stability test of the $Z_{0.9}Mn_{0.1}SO$ sensor was also conducted over the period of 95 days at fixed 20 ppm CO and at the operating temperature of 200 ℃ as illustrated in Figure 3.12(*c*). It is clearly observed that the sensor shows no significant deviation in response, confirming excellent long-term stability of the $Z_{0.9}Mn_{0.1}SO$ sensor.

Table 3.3 Comparison of recent metal-oxide based gas sensors for CO detection.

Sensing material	**Operating temperatur (°C)**	**CO (ppm)**	**Sensitivity (R_a/R_g) Or Response (%)**	**Response/recovery times (s)**	**Ref.**
$ZnSnO_3$	**250**	**500**	**5.79%**	**30/41**	**This work**
$Zn_{0.9}Mn_{0.1}SnO_3$	**200**	**500**	**311.37%**	**6.6/34.1**	**This work**
SnO_2	310	200	7.29	16/28	[33]
SnO_2	200	91	84.3%	48/51	[34]
Ni^{2+}-doped SnO_2	350	1000	6.1	-	[35]
$TiO_{1.5}/ZnO$	300	48	1.365	166/343	[36]
$CuO-SnO_2$	200	100	3.52%	-	[37]
ZnO	250	100	3.7	-	[38]
$ZnO/ZnCo_2O_4$	300	10	17.3	60/50	[39]
Mn-ZnO	300	300	2.5	40/300	[30]

Table 3.3 illustrates the comparison of present work with the sensing performance of other MOS based CO sensors, basically based on binary

type ZnO or SnO_2 or its ternary type compounds. It is worth noted that our sensor exhibited a comparably high CO sensing performance, especially high response, low operating temperature, fast response and recovery times.

3.3.8 Gas sensing mechanism

$ZnSnO_3$ belongs to the family of *n*-type metal oxide semiconductor whose gas sensing mechanism is exclusively based on the alteration in the electric resistance when exposed to the gas and explained by the most accepted oxygen adsorption-desorption theory on the material surface [40]. When $ZnSnO_3$ or $Zn_{1-x}Mn_xSnO_3$-based sensors are exposed to clean air, as shown in Figure 3.13(*a,c*), oxygen molecules present in the clean air will be adsorbed on the surface of sensing material and captivate free electrons from the surface conduction band of sensing layer. Depending on the operating temperature, adsorbed oxygen species on reacting with free electrons transforms into oxygen species of ionized form, such as O_2^-, O^-, O^{2-} [41]. As a consequence, a thick electron depletion layer (EDL) will form causing increase in electric resistance of sensor resulting less flow of electrons inside sensing material. Thus, the sensor material initially exhibits high resistance in the presence of clean air.

$$O_{2\,(gas)} \rightarrow O_{2(adsorbed)} \qquad (3.2)$$

$$O_{2(adsorbed)} + e^-_{(surface)} \rightarrow O^-_{2\,(adsorbed)} \qquad (<100\ ^{\circ}C) \qquad (3.3)$$

$$O^-_{2\,(adsorbed)} + 2e^-_{(surface)} \rightarrow 2O^-_{(adsorbed)} \qquad (100\text{-}300\ ^{\circ}C) \qquad (3.4)$$

$$O^-_{(adsorbed)} + e^-_{(surface)} \rightarrow O^{2-}_{(adsorbed)} \qquad (>300\ ^{\circ}C) \qquad (3.5)$$

As shown in Figure 3.13(*b,d*), when the $ZnSnO_3$ sensor material is exposed to reducing gas such as CO, the interaction between the CO gas and the predominant chemisorbed ionized oxygen species, O^-, can take place and the electrons captivated by the chemisorbed O^- are released back into the conduction band of sensing material, as per eqn (3.6), and produce CO_2. As a result, the thickness of the EDL layer is lessened and thus decreases the electric resistance of the sensing material and the key redox reaction involved in process of reaction with CO gas is as per following equation:

$$CO_{(gas)} + O^{-}_{(adsorbed)} \leftrightarrow CO_{2(gas)} + e^{-} \tag{3.6}$$

$$CO_{(gas)} + O_2^{-}{}_{(adsorbed)} \leftrightarrow 2CO_{2\ (gas)} + e^{-} \tag{3.7}$$

Furthermore, as the gas sensing device is re-exposed to the clean air, oxygen molecules again react with the electrons captivated from the surface conduction band of sensing material, which again forms the thick electron depletion layer and thus electric resistance recover to the initial baseline.

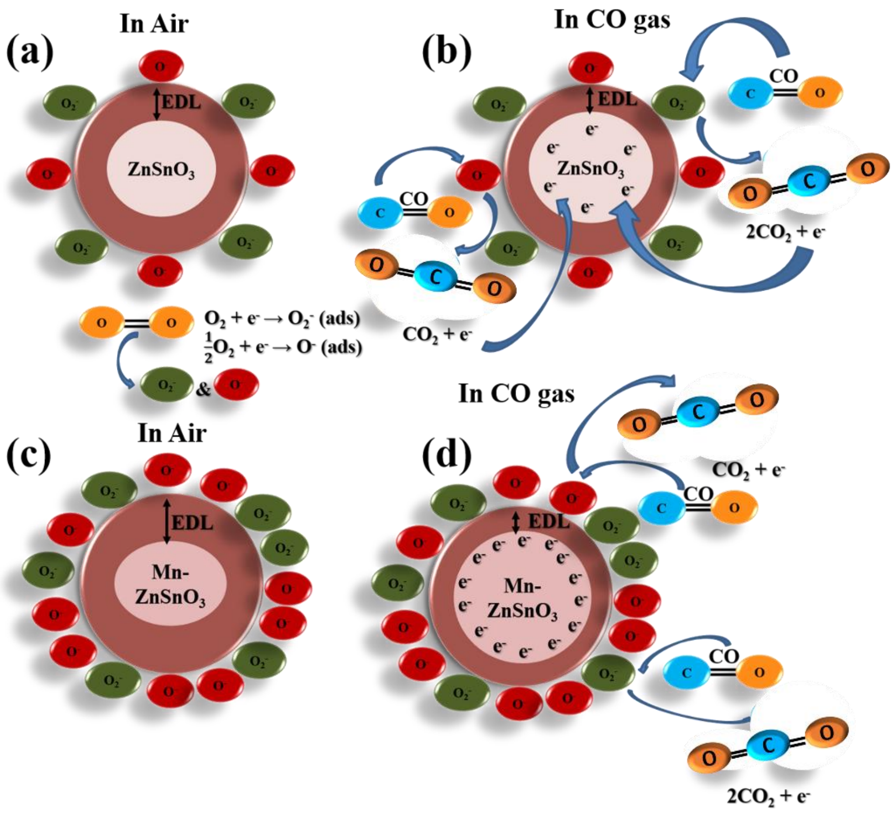

Figure 3.13. The schematic diagrams for CO gas sensing mechanism of pure and Mn-doped ZnSnO$_3$ sensors in presence of air (a) & (c) and in CO gas (b) & (d), respectively.

In addition, the gas sensing performance of $ZnSnO_3$ is greatly related to the particle size, surface area, and metal oxidation states, which can be largely influenced by the doping of transition metal elements. Transition metals are most commonly used as the sensitizers to enhance the gas sensing performance of any sensing materials. The doping of $ZnSnO_3$ by Mn element changes the particle size and increases the surface area, which results alterations in the amount of adsorbed oxygen. It is well known that with the increase in doping amount of Mn, the amount of oxygen molecules adsorbed increases for up to certain concentration of Mn and then decreases [42,43]. For up to 10 *at*% Mn, maximum number of oxygen molecules transforms into ionized O^- species and thus more number of CO molecules are involved in the reaction process. Moreover, extra thick electron depletion layer may get form at the interface with the increase in Mn concentration. Thus, when the Mn-doped $ZnSnO_3$ sensors are exposed to the CO environment, large number of electrons are freed and released back into the conduction band of sensing material $ZnSnO_3$ microspheres more conveniently. Also evidenced from the XPS spectra, doping with Mn generates a greater number of oxygen vacancies in the ZSO lattice and hence a greater number of free electrons, improving the gas sensing. Simultaneously, Mn site in $ZnSnO_3$ plays a critical role to adsorb CO molecules at all temperatures. CO molecules are preferably adsorbed on the Mn sites to form bonds between Mn and CO. The interaction results in donation of 5σ electrons of CO to the metal and π electrons back bonding from *d*-orbitals of Mn to CO. First, the CO molecules adsorbed at the Mn sites and then migrate from Mn sites to Zn sites, through which Mn sites improve the CO adsorption and their interaction with oxygen species. Therefore, the doping of transition metal Mn effectively helps in intensifying the gas sensing performance of $ZnSnO_3$ microspheres towards CO gas.

3.4 Conclusions

In summary, porous Mn-doped $ZnSnO_3$ microspheres were synthesized by a simple co-precipitation method. The characterization results revealed that the Mn-doped $ZnSnO_3$ maintain the face-centered cubic structure of pure $ZnSnO_3$ and exhibit the micro spherical morphology in the increasing order of surface area with the Mn concentration. The Mn-doping was confirmed by XPS. The BET measurements revealed the increase in the surface area with increase in Mn doping. The gas sensing performance analysis of the $Zn_{1-x}Mn_xSnO_3$ chemi-resistive sensors with different Mn concentration towards CO gas displayed enhanced sensing characteristics with respect to pure $ZnSnO_3$ sensor. To be specific, the MOS sensor based on 10 *at*% Mn-doped $ZnSnO_3$ exhibited remarkable high response to CO gas at the reduced operating temperature of 200 ºC. Moreover, the $Z_{0.9}Mn_{0.1}SO$ sensor exhibit fast response and recovery time of 6.6 s and 34.1 s, respectively, with the good stability and reproducibility. The enhanced gas sensing properties to CO can be ascribed to the sensitization effects of Mn and porous structure. On the basis of this study, these Mn-doped porous $ZnSnO_3$ microspheres are propitious to be applied for practical applications for monitoring CO gas in air.

References

[1] C. Patel, B. Mandal, R.G. Jadhav, T. Ghosh, M. Dubey, A.K. Das, M.T. Htay, V. V. Atuchin, S. Mukherjee, S, N Co-Doped Carbon Dot-Functionalized WO_3 Nanostructures for NO_2 and H_2S Detection, ACS Appl. Nano Mater. 5 (2022) 2492–2500. https://doi.org/10.1021/acsanm.1c04174.

[2] P.M. Shirage, A.K. Rana, Y. Kumar, S. Sen, S.G. Leonardi, G. Neri, Sr- and Ni-doping in ZnO nanorods synthesized by a simple wet chemical method as excellent materials for CO and CO_2 gas sensing, RSC Adv. 6 (2016) 82733–82742. https://doi.org/10.1039/c6ra15891a.

[3] W. Zhang, F. Yang, J. Xu, C. Gu, K. Zhou, Sensitive carbon

monoxide gas sensor based on chemiluminescence on Nano-Au/Nd_2O_3-$Ca_3Nd_2O_6$: Working condition optimization by response surface methodology, ACS Omega 5 (2020) 20034–20041. https://doi.org/10.1021/acsomega.0c01481.

[4] G. Shi, T. Yoon, S. Cha, S. Kim, M. Yousuf, N. Ahmed, D. Kim, H.W. Kang, K.S. Kim, Turn-on and turn-off fluorescent probes for carbon monoxide detection and blood carboxyhemoglobin determination, ACS Sensors 3 (2018) 1102–1108. https://doi.org/10.1021/acssensors.8b00083.

[5] A. Dey, Semiconductor metal oxide gas sensors: A review, Mater. Sci. Eng. B Solid-State Mater. Adv. Technol. 229 (2018) 206–217. https://doi.org/10.1016/j.mseb.2017.12.036.

[6] A.K. Yadav, P. Rajput, O. Alshammari, M. Khan, Anita, G. Kumar, S. Kumar, P.M. Shirage, S. Biring, S. Sen, Structural distortion, ferroelectricity and ferromagnetism in $Pb(Ti_{1-x}Fe_x)O_3$, J. Alloys Compd. 701 (2017) 619–625. https://doi.org/10.1016/j.jallcom.2017.01.127.

[7] S. Chand Yadav, A. Srivastava, V. Manjunath, A. Kanwade, R.S. Devan, P.M. Shirage, Properties, performance and multidimensional applications of stable lead-free $Cs_2AgBiBr_6$ double perovskite, Mater. Today Phys. 26 (2022) 100731. https://doi.org/10.1016/j.mtphys.2022.100731.

[8] S.S. Nalimova, A.I. Maksimov, L.B. Matyushkin, V.A. Moshnikov, Current State of Studies on Synthesis and Application of Zinc Stannate (Review), Glas. Phys. Chem. 45 (2019) 251–260. https://doi.org/10.1134/S1087659619040096.

[9] Q. Xie, Y. Ma, X. Zhang, H. Guo, A. Lu, L. Wang, G. Yue, D.L. Peng, Synthesis of amorphous ZnSnO3-C hollow microcubes as advanced anode materials for lithium ion batteries, Electrochim. Acta 141 (2014) 374–383. https://doi.org/10.1016/j.electacta.2014.07.095.

[10] S.C. Yadav, A. Sharma, R.S. Devan, P.M. Shirage, Role of different counter electrodes on performance of TiO_2 based dye-sensitized solar cell (DSSC) fabricated with dye extracted from Hibiscus Sabdariffa as sensitizer, Opt. Mater. (Amst). 124 (2022) 112066.

https://doi.org/10.1016/j.optmat.2022.112066.

[11] C. Fang, B. Geng, J. Liu, F. Zhan, D-fructose molecule template route to ultra-thin ZnSnO3 nanowire architectures and their application as efficient photocatalyst, Chem. Commun. (2009) 2350–2352. https://doi.org/10.1039/b821459j.

[12] J. Xu, X. Jia, X. Lou, J. Shen, One-step hydrothermal synthesis and gas sensing property of $ZnSnO_3$ microparticles, Solid. State. Electron. 50 (2006) 504–507. https://doi.org/10.1016/j.sse.2006.02.001.

[13] Y. Yin, F. Li, N. Zhang, S. Ruan, H. Zhang, Y. Chen, Improved gas sensing properties of silver-functionalized $ZnSnO_3$ hollow nanocubes, Inorg. Chem. Front. 5 (2018) 2123–2131. https://doi.org/10.1039/c8qi00470f.

[14] H. Men, P. Gao, B. Zhou, Y. Chen, C. Zhu, G. Xiao, L. Wang, M. Zhang, Fast synthesis of ultra-thin $ZnSnO_3$ nanorods with high ethanol sensing properties, Chem. Commun. 46 (2010) 7581–7583. https://doi.org/10.1039/c0cc02222e.

[15] G. Feng, Y. Che, C. Song, J. Xiao, X. Fan, S. Sun, G. Huang, Y. Ma, Morphology-controlled synthesis of $ZnSnO_3$ hollow spheres and their n-butanol gas-sensing performance, Ceram. Int. 47 (2021) 2471–2482. https://doi.org/10.1016/j.ceramint.2020.09.090.

[16] L. Du, D. Wang, K. Gu, M. Zhang, Construction of PdO-decorated double-shell $ZnSnO_3$ hollow microspheres for: n-propanol detection at low temperature, Inorg. Chem. Front. 8 (2021) 787–795. https://doi.org/10.1039/d0qi01292k.

[17] J. Zheng, H. Hou, H. Fu, L. Gao, H. Liu, Size-controlled synthesis of porous $ZnSnO_3$ nanocubes for improving formaldehyde gas sensitivity, RSC Adv. 11 (2021) 20268–20277. https://doi.org/10.1039/d1ra01852c.

[18] B.S. Sá, C.A. Zito, T.M. Perfecto, D.P. Volanti, Porous $ZnSnO_3$ nanocubes as a triethylamine sensor, Sensors Actuators, B Chem. 338 (2021). https://doi.org/10.1016/j.snb.2021.129869.

[19] P. Wadkar, D. Bauskar, P. Patil, High performance H_2 sensor based on $ZnSnO_3$ cubic crystallites synthesized by a hydrothermal method,

Talanta 105 (2013) 327–332. https://doi.org/10.1016/j.talanta.2012.10.051.

[20] X. Wang, J. Ma, Q. Ren, M. Wang, Z. Yang, J. Xin, Effects of Fe^{3+}-doping and nano-TiO_2/WO_3 decoration on the ultraviolet absorption and gas-sensing properties of $ZnSnO_3$ solid particles, Sensors Actuators, B Chem. 344 (2021) 130223. https://doi.org/10.1016/j.snb.2021.130223.

[21] X. Wang, T. Tao, Z. Qi, B. Leng, W. Xu, J. Ma, M. Wang, Broad-spectrum UV absorption and gas-sensing improvement of $ZnSnO_3$ cubic particles based on Al-doping and nano-TiO_2 decoration, Sensors Actuators, B Chem. 326 (2021) 129013. https://doi.org/10.1016/j.snb.2020.129013.

[22] X. Wang, H. Li, X. Zhu, M. Xia, T. Tao, B. Leng, W. Xu, Improving ethanol sensitivity of $ZnSnO_3$ sensor at low temperature with multi-measures: Mg doping, nano-TiO_2 decoration and UV radiation, Sensors Actuators, B Chem. 297 (2019) 126745. https://doi.org/10.1016/j.snb.2019.126745.

[23] S. Bai, W. Tong, Y. Tian, H. Fu, Y. Zhao, X. Shu, R. Luo, D. Li, A. Chen, Facile synthesis of Pd-doped $ZnSnO_3$ hierarchical microspheres for enhancing sensing properties of formaldehyde, J. Mater. Sci. 54 (2019) 2025–2036. https://doi.org/10.1007/s10853-017-1588-2.

[24] I. Karaduman, M.A. Yıldırım, S.T. Yıldırım, A. Ateş, Y.A. Özdemir, S. Acar, The effect of different doping elements on the CO gas sensing properties of ZnO nanostructures, J. Mater. Sci. Mater. Electron. 28 (2017) 18154–18163. https://doi.org/10.1007/s10854-017-7761-1.

[25] E. Della Gaspera, M. Guglielmi, G. Perotto, S. Agnoli, G. Granozzi, M.L. Post, A. Martucci, CO optical sensing properties of nanocrystalline ZnO-Au films: Effect of doping with transition metal ions, Sensors Actuators, B Chem. 161 (2012) 675–683. https://doi.org/10.1016/j.snb.2011.11.011.

[26] A. Sharma, Y. Kumar, P.M. Shirage, Structural, optical and excellent humidity sensing behaviour of $ZnSnO_3$ nanoparticles: effect of annealing, J. Mater. Sci. Mater. Electron. 29 (2018) 10769–10783.

https://doi.org/10.1007/s10854-018-9143-8.

[27] R. Guo, Y. Guo, H. Duan, H. Li, H. Liu, Synthesis of Orthorhombic Perovskite-Type $ZnSnO_3$ Single-Crystal Nanoplates and Their Application in Energy Harvesting, ACS Appl. Mater. Interfaces 9 (2017) 8271–8279. https://doi.org/10.1021/acsami.6b16629.

[28] Y. Chen, B. Qu, L. Mei, D. Lei, L. Chen, Q. Li, T. Wang, Synthesis of ZnSnO3 mesocrystals from regular cube-like to sheet-like structures and their comparative electrochemical properties in Li-ion batteries, J. Mater. Chem. 22 (2012) 25373–25379. https://doi.org/10.1039/c2jm33123c.

[29] S. Paul, S. Basak, W. Ali, Zinc Stannate Nanostructure: Is It a New Class of Material for Multifunctional Cotton Textiles?, ACS Omega 4 (2019) 21827–21838. https://doi.org/10.1021/acsomega.9b02719.

[30] M.H. Darvishnejad, A. Anaraki Firooz, J. Beheshtian, A.A. Khodadadi, Highly sensitive and selective ethanol and acetone gas sensors by adding some dopants (Mn, Fe, Co, Ni) onto hexagonal ZnO plates, RSC Adv. 6 (2016) 7838–7845. https://doi.org/10.1039/c5ra24169c.

[31] H. Bai, H. Guo, C. Feng, J. Wang, B. Liu, Z. Xie, F. Guo, D. Chen, R. Zhang, Y. Zheng, Highly responsive and selective ppb-level NO 2 gas sensor based on porous Pd-functionalized CuO/rGO at room temperature , J. Mater. Chem. C 10 (2022) 3756–3769. https://doi.org/10.1039/d1tc05231d.

[32] Y. Fan, K. Li, X. Ren, W. Yan, C. Zhu, Y. Zhao, W. Zeng, Z. Chen, S. Wang, A highly selective gas sensor based on the WO_3/WS_2 van der Waals heterojunction for the 2-chloroethyl ethyl sulfide (2-CEES) sensing application, J. Mater. Chem. C 9 (2021) 17496–17503. https://doi.org/10.1039/d1tc04678k.

[33] Q. Zhou, W. Chen, L. Xu, R. Kumar, Y. Gui, Z. Zhao, C. Tang, S. Zhu, Highly sensitive carbon monoxide (CO) gas sensors based on Ni and Zn doped SnO_2 nanomaterials, Ceram. Int. 44 (2018) 4392–4399. https://doi.org/10.1016/j.ceramint.2017.12.038.

[34] A.K. Gangwar, S. Srivastava, R. Godiwal, J. Jaiswal, P. Vashishtha, S. Pal, P. Pal, G. Gupta, P. Singh, Room temperature sputtered

nanocrystalline SnO_2 thin films sensitized with Pd nanoparticles for high performance CO gas sensing application, Opt. Mater. (Amst). 128 (2022) 112362. https://doi.org/10.1016/j.optmat.2022.112362.

[35] L.S. Zhang, X.M. Guo, Investigation on gas sensing and temperature modulation properties of Ni^{2+} doped SnO_2 materials to CO and H_2, Mater. Sci. Semicond. Process. 142 (2022) 106516. https://doi.org/10.1016/j.mssp.2022.106516.

[36] L. Vatandoust, A. Habibi, H. Naghshara, S. Mohammadi, Fabrication and investigation of $TiO_{1.5}$/ZnO nanocomposite nanosensor for detection of CO and CH_4 gases, Surfaces and Interfaces 31 (2022) 102001. https://doi.org/10.1016/j.surfin.2022.102001.

[37] S.B. Dhage, V.L. Patil, P.S. Patil, J. Ryu, D.R. Patil, Y.S. Malghe, Synthesis and characterization of CuO-SnO_2 nanocomposite for CO gas sensing application, Mater. Lett. 305 (2021) 130831. https://doi.org/10.1016/j.matlet.2021.130831.

[38] A.S. Mokrushin, Y.M. Gorban', N.P. Simonenko, E.P. Simonenko, V.G. Sevast'yanov, N.T. Kuznetsov, Nanostructured ZnO Films with Enhanced Sensitivity to CO Synthesized by AACVD, Russ. J. Inorg. Chem. 66 (2021) 1447–1454. https://doi.org/10.1134/S0036023621090072.

[39] Y.V. Kaneti, N.L. Wulan Septiani, I. Saptiama, X. Jiang, B. Yuliarto, M.J.A. Shiddiky, N. Fukumitsu, Y.M. Kang, D. Golberg, Y. Yamauchi, Self-sacrificial templated synthesis of a three-dimensional hierarchical macroporous honeycomb-like ZnO/$ZnCo_2O_4$ hybrid for carbon monoxide sensing, J. Mater. Chem. A 7 (2019) 3415–3425. https://doi.org/10.1039/c8ta11380g.

[40] T. Zhou, T. Zhang, R. Zhang, Z. Lou, J. Deng, L. Wang, Hollow ZnSnO3 Cubes with Controllable Shells Enabling Highly Efficient Chemical Sensing Detection of Formaldehyde Vapors, ACS Appl. Mater. Interfaces 9 (2017) 14525–14533. https://doi.org/10.1021/acsami.7b03112.

[41] X. Ma, S. Guo, J. Shen, Y. Chen, C. Chen, L. Sun, X. Zhang, S. Ruan, Synthesis and enhanced gas sensing properties of Au-nanoparticle decorated CdS nanowires, RSC Adv. 6 (2016) 70907–70912. https://doi.org/10.1039/c6ra10963b.

[42] A. Xukeer, Z. Wu, Q. Sun, F. Zhong, M. Zhang, M. Long, H. Duan, Enhanced gas sensing performance of perovskite $YFe_{1-x}Mn_xO_3$ by doping manganese ions, RSC Adv. 10 (2020) 30428–30438. https://doi.org/10.1039/d0ra01375g.

[43] Y. Bai, Y. Qin, P. Qiu, Boosting the acetone sensing of SnS nanoflakes by spin Mn substitution: a novel adsorption-desorption perspective, Environ. Sci. Nano 8 (2021) 1096–1108. https://doi.org/10.1039/d0en01251c.

Chapter 4

NASICON-type $Na_3Fe_2(PO_4)_3$ for an Excellent Room-Temperature CO Sensing

This chapter presents an ultra-sensitive room temperature CO gas sensor based on $Na_3Fe_2(PO_4)_3$ *(NFP, NASICON-type material) synthesized via a simple sol-gel method. The plate-like NFP powder was coated on Cu interdigitated electrodes to fabricate the sensor. The device exhibited excellent selectivity and an ultra-fast response (~417.58 in 14 s) to 500 ppm CO, recovering in just 3 s. The response was 100 times higher than the blank signal and 5-500 times superior to conventional sensors. With excellent stability and reproducibility, NFP proves to be a promising, cost-effective CO sensing material for next-generation applications.*

4.1 Introduction

In chapter 3, the gas-sensing application of Mn-doped $ZnSnO_3$ towards CO gas sensing was studied. The highlights of the earlier work are the importance of doping and optimizing dopant concentration in enhancing the sensitivity of $ZnSnO_3$ towards CO. The drawback of Mn-$ZnSnO_3$ is that operating temperature is still significantly high from room temperature. Now our attention has been shifted towards selecting functional materials exhibiting room temperature sensing to CO gas.

As already discussed in previous chapter, CO is a highly toxic air pollutant that poses serious risks to both the environment and human health, which originates from incomplete combustion in vehicles, industries, and fossil fuels [1-4]. Being colorless and odorless, CO is undetectable by human senses [5] and is often termed the "silent killer" due to its ability to disrupt oxygen supply in the bloodstream [6]. According to WHO guidelines (2021) for indoor air quality, the recommended short-term 24-hour exposure to CO indoor air quality guideline (AQG) level is 3.5 ppm, AQG level for 8-hour is 8.58 ppm, AQG level for 1 hour is 30 ppm and AQG level for 15-min is 85.8 ppm [7-10]. Thus, it is extremely important to consistantly find new cost-effective and high performance sensors for the detection of CO at room temperature [11-13]. The high working temperature of MOS-based sensors (>150 ℃) would increase energy usage and significantly shorten the device's lifespan. Designing excellent performing sensing materials that can track low concentration CO gas at ambient temperature is crucial in this regard [14-16].

NASICON [17-19] materials are widely explored for sodium-ion battery [20-24] as the solid electrolyte, cathode material [25], sodium removal from water, catalysis *etc*. Good electrical conductivity characteristics of some NASICON such as $LiZr_2(PO_4)_3$, NFP, *etc*. [26-28] make them sensitive to molecules present in atmosphere and thus beneficial for detecting many gases or pollutants present in the ambient atmosphere [29,30]. Over the past decade, several NASICON-type materials utilized for gas sensing are based on electrochemical-type or potentiometric-type or optical waveguide type gas sensors. In electrochemical-type gas sensors, NASICON based materials are generally utilized as a solid electrolyte instead directly as sensing materials for example, $Na_3Zr_2Si_2PO_{12}$ for CO gas detection, $Na_{2,8}Zr_2Si_{1,8}P_{1,2}O_{12}$, *etc.* N. Patima *et. al.* reported the gas sensing application of lithium iron phosphate with different element doping for different gas detection. For example, Ni-doped lithium iron phosphate ($LiFe_{0.995}Ni_{0.005}PO_4$) [31] nanoparticle was developed as a optical-electrochemical type gas sensor for the detection of 100 ppm xylene gas and silver-and-yttrium-co doped lithium iron phosphate ($LiFe_{1-0.01x}Y_{0.005x}Ag_{0.005x}PO_4$) was fabricated as a optical waveguide type formaldehyde gas sensors [28]. G. Jasinski *et. al.* compares the lithium-based (LISICON) and sodium-based (NASICON) sensors. It seems that NASICON-based electrocatalytic gas sensors showed promising sensing performance over LISICON based sensors at all temperature of operation. Moreover, NASICON-based sensors exhibit potential for multi-gas detection when altered operating temperature during detection [32,33].

In this chapter, the gas sensing ability of NASICON-type $Na_3Fe_2(PO_4)_3$ material with microstructure synthesized by very cost-effective and simple sol-gel technique has been demonstrated. Gas sensing device was developed based on the resistive gas sensor module. Exposure of this material to several interferring gases such as CO, NH_3, CO_2, C_2H_5OH, H_2S, SO_2 and NO_2 is then carried out at room temperature to several high temperatures. Being an exceptionally highly sensitive to CO gas at room temperature, measurements for varying CO gas concentrations were achieved. Sensor showed rapid response of ~14 s upon exposed to 500 ppm CO gas and recovered to the baseline in ~3 s after the removal of CO gas. The stability and reproducibility were tested several times to confirm the CO detection by $Na_3Fe_2(PO_4)_3$. It is expected that our results will pave the way for the use of this new NASICON-type battery material for development of next generation gas sensing devices.

4.2 Experimental

4.2.1 Materials

Sodium nitrate ($NaNO_3$) (Merk; 99%), Iron nitrate nonahydrate ($Fe(NO_3)_3.9H_2O$) (Alfa Aesar; 98%-101%), Ammonium dihydrogen phosphate ($NH_4H_2PO_4$) (Alfa Aesar; 98%), and Citric acid monohydrate ($C_6H_8O_7.H_2O$) (Alfa Aesar; 99%) were purchased of analytical grade. All the chemicals were directly used without any further purification.

4.2.2 Synthesis of $Na_3Fe_2(PO_4)_3$

The NFP material was synthesized *via* the sol-gel method, as detailed in **Chapter 2 (2.2.2 Synthesis of Sensing Material by Sol-gel method)**. A stoichiometric mixture of $NaNO_3$, $Fe(NO_3)_3.9H_2O$, $NH_4H_2PO_4$, and $C_6H_8O_7.H_2O$ (chelating agent) was dissolved in DI water and stirred at 80 °C. After 9 hours, the solution formed a gel precursor, which was dried at 100 °C. The resulting black powder was finely ground and annealed at 700 °C for 10 hours to obtain the final porous NFP material.

4.2.3 Sensor Fabrication

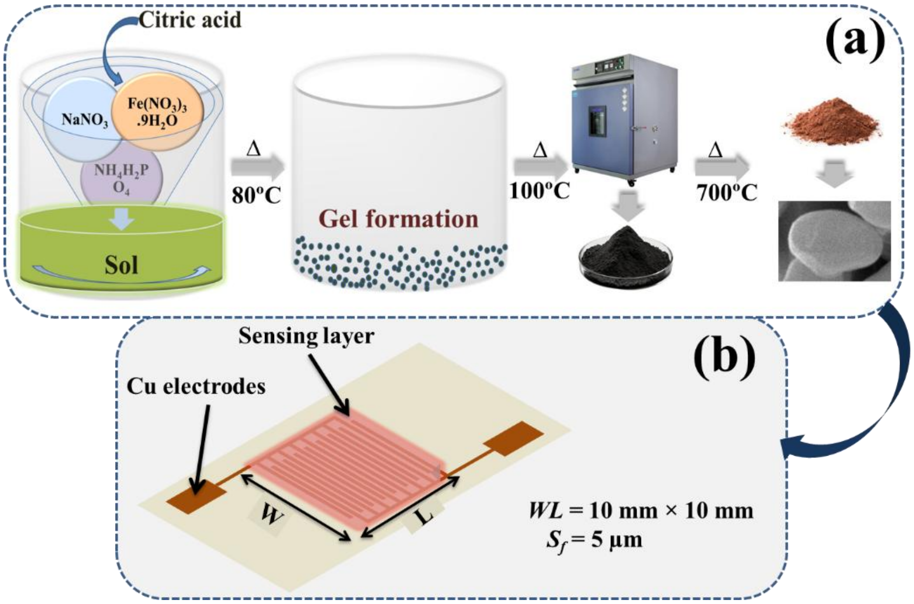

Figure 4.1. Schematic illustartion of the process for fabricating NFP gas sensor.

The gas sensors were fabricated as per the following route as represented in Figure 4.1. The finally obtained annealed sensing materials based on NFP powders were mixed with drops of DI water in an agate mortar to form a homogeneous paste and uniformly coated on the IDE based on Cu metal material on the printed circuit board (PCB). The Cu metal PCB was cut with electric discharge machining to form the IDE pattern shown in Figure 4.1(*b*), where the spacing between the electrode fingers (S_f) is kept 5 µm and the overall width (*W*) and length (*L*) of sensor are fixed at 10 mm, respectively.

4.3 Results and Discussion

4.3.1 Thermogravimetric Analysis

Thermal analysis of the precursor sample is shown with the help of TGA and DTG curves in Figure 4.2.

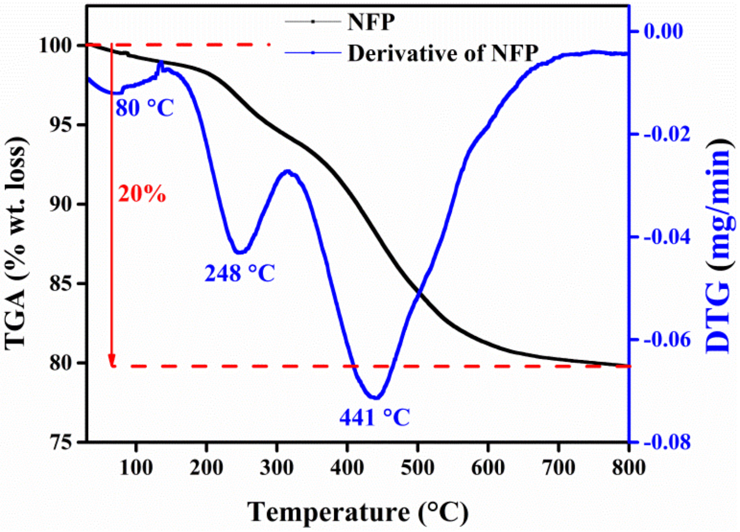

Figure 4.2. TGA-DTG curves of NFP precursor sample.

It can be observed from the curves that the global weight loss of about 20% is in three multistage process starting with losing absorbed water (about 1.5%) below 155℃. Two endothermic peaks at 80 ℃ and 248 ℃ corresponds to the free and structural water losses. Following an exothermic peak at ~441 ℃ that corresponds to the thermal decompostion of citric acid and ammonium dihydrogen phosphate complexes to start the formation of NFP [34-36]. The weight remains stable after 700 ℃. Thus, the annealed tempearture was set to optimized at 700 ℃ to achieve the particular morphology of the NFP particles.

4.3.2 Morphological Characterization

Figure 4.3(*a*) and (*b*) illustrates the low and high magnication (x 5,000 and x 20,000, respectively) surface morphology of the NFP powder sample characterized by FESEM, which exhibits plate-like morphology with a average size of 736.63 nm and are interconnected with each other to pattern a 3D framework in NFP. Figure 4.3(*c*) and Figure 4.3(*d*-*g*) demonstrates the EDS and elemental mapping, respectively, results which confirms the presence of Na, Fe, P and O atoms in stoichiometric atomic ratio and their homogeneous distribution in NFP particles, which manifests high purity of this material.

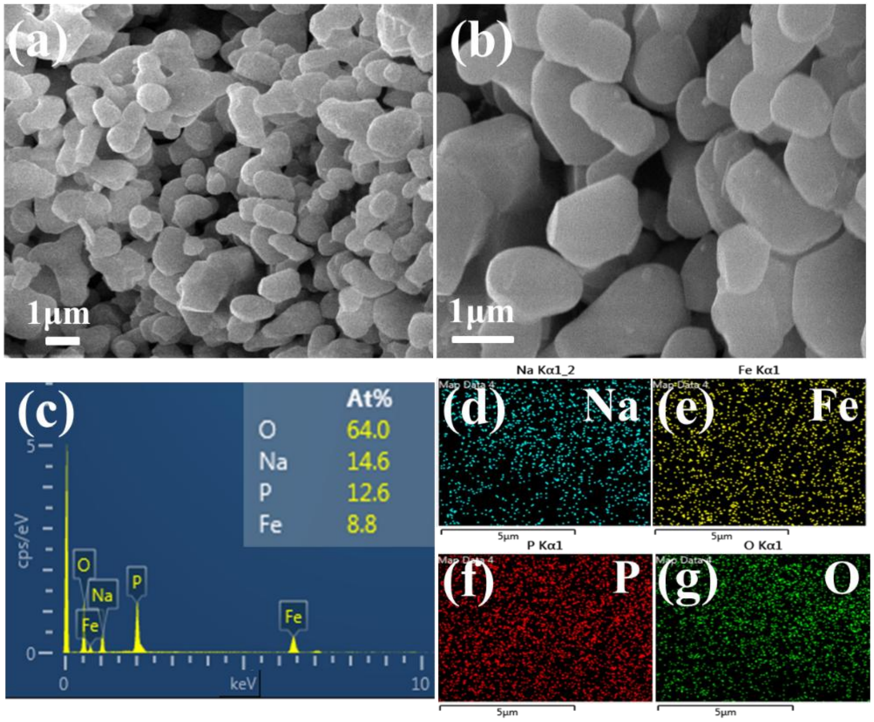

Figure 4.3. (*a*) Low and (*b*) high magnification top-view FESEM image of the NFP plate-like morphology; (*c*) EDS analysis and (*d*-*g*) elemental mapping images of Na, Fe, P and O, respectively.

4.3.3 Structural Characterization

To confirm the crystal structure and phase purity of the NFP sample, XRD pattern is shown in Figure 4.4(*a*). All of the diffraction peaks in XRD pattern can only be indexed to pure NFP and no diffraction paeks are related to impurities. The Rietveld refinement was carried out using the Full Prof software used the monoclinic structured unit cell in the space group *C*2/*c*, *a* = 15.07(7) Å, *b* = 8.740(5) Å, *c* = 8.724(9) Å, α = γ = 90º, and β = 125.1(1)º, and the results obtained are shown in Table 4.1 confirms the monoclinic structure of NFP in the space group *C*2/*c*. Figure 4.4(*b*) illustrates the monoclinic crystal structure of NFP. Na^+ ions possess two crystallographic sites, thus it is a typical NASICON-type structure where PO_4 tetrahedra and FeO_6 octahedra are alternatively connected to form lantern units of $[Fe_2(PO_4)_3]$ [37].

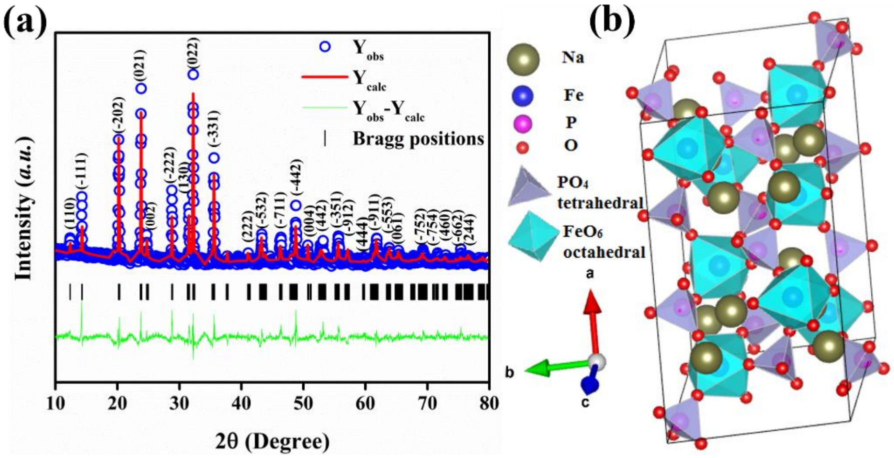

Figure 4.4. (*a*) XRD pattern and (*b*) Crystal structure of NFP.

Table 4.1 Refined lattice parameters of NFP

Sample	Crystal structure	Space group	*a* (Å)	*b (Å)*	*c* (Å)	α = γ (deg)	β (deg)
NFP	Monoclinic	*C*2/*c*	15.150(4)	8.782(3)	8.722(3)	90	125.08(4)

4.3.4 X-ray Photoelectron Spectroscopy

Gas detection is a surface-dominant phenomena which greatly depends on the surface state of the sensing materials. XPS was performed to study the NFP sensing material for the defect, surface elemental distribution, and the corresponding valence state. Figure 4.5(*a*) presents the survey scan of NFP, which clearly indicates that the NFP sample consisted of sodium (Na), iron (Fe), phosphorus (P) and oxygen (O). Figure 4.5(*b*) shows the Na 1*s* spectra of NFP located at 1071.89 eV, ascribed to the NaO group of NFP. Figure 4.5(*c*) shows the deconvoluted high resolution narrow spectra of Fe 2*p*. The two distinctive peaks of Fe 2*p* centered at binding energy of 729.32 eV and 715.08 eV represents the existence of two Fe 2*p* spin orbit coupling (Fe2*p*3/2 and Fe2*p*1/2) that are attributed to the Fe^{3+} ions binding energy, also the peaks located at binding energies of 726.15 eV and 711.87 eV are in consistent with Fe^{2+} ions binding energy. As shown in Figure 4.5(*d*), the presence of only one P 2*p* peak at 133.82 eV binding energy corresponds to the one environment of P in the form $(PO_4)^{3-}$ group of the NFP compound. The O 1*s* spectrum as shown in Figure 4.5(*e*), are deconvoluted into three peaks to investigate the contribution of oxygen vacancy defects: O_L corresponds to lattice oxygen, whereas O_V corresponds to the signal arising from oxygen atoms that are bound to an atom with an oxygen deficiency and O_C represents the percentage of chemisorbed oxygen [38]. The three deconvoluted peculiar peaks of O 1*s* in NFP centered at binding energies 529.97 eV, 531.77 eV, and 534.44 eV are corresponds to O_L, O_V and O_C, respectively. In the case oxide materials, oxygen vacancies have found to play a significant role in enhancing gas sensing performance. The presence of O_V can act as more active sites for gas molecules to adsorb onto the surface of the sensing material. This can result in a higher sensitivity towards gas molecules and a lower detection limit. As seen in Figure 4.5(*e*), the higher relative area of O_V and O_C in compare to O_L suggesting the NFP as propitious material for gas sensing application.

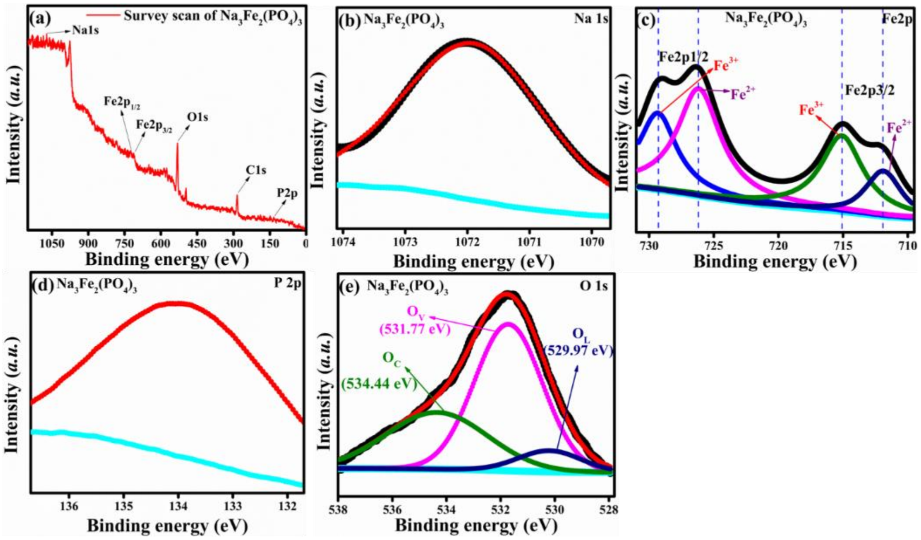

Figure 4.5. (*a*) Survey scan XPS spectra of NFP, (*b*) Na 1*s* XPS spectra, (*c*) Fe 2*p* XPS spectra, (*d*) P 2*p* XPS spectra, and (*e*) O1*s* XPS spectra of NFP.

4.3.5 Gas sensing studies

Before starting the gas sensing, the current – voltage (*I*-*V)* characteristics of the NFP sensing material was measured under a constant sweeping voltage between the -5 V to +5 V with step 0.05 V at room temperature. Figure 4.6(*a*) illustrates the *I*-*V* curve of the NFP sensor tested by Keithley-2401 sourcemeter, and exhibited the nearly linear *I*-*V* relationship. The linear *I*-*V* curve indicated that the current conduction is mainly enforced by the bulk sensing material instead of Schottky contacts [39,40]. Different gases have different response characteristics towards particular material. First, we observed the influence of various gases (CO, C_2H_5OH, SO_2, NO_2, H_2S, NH_3 and CO_2) on the gas sensing performance of NFP sensor in prospect of variation in electrical resistance at the room temperature (27 ℃). From Figure 4.6(*b*-*h*), it can be observed that the resistance of NFP sensing material increased drastically high in the presence of CO gas, bringing a relatively highest response value (Figure 4.6(*i*)) for NFP material towards CO gas (R = 460.74) compared to other interferring gases (C_2H_5OH, R = 53.23; NH_3, R = 78.37; CO_2, R = 84.36; SO_2, R = 45; H_2S, R = 49.98; NO_2, R = 58.56). Thus, it becomes obvious that NFP sensing material provided a better opportunity for selectively distinguishing CO gas at the room temperature condition.

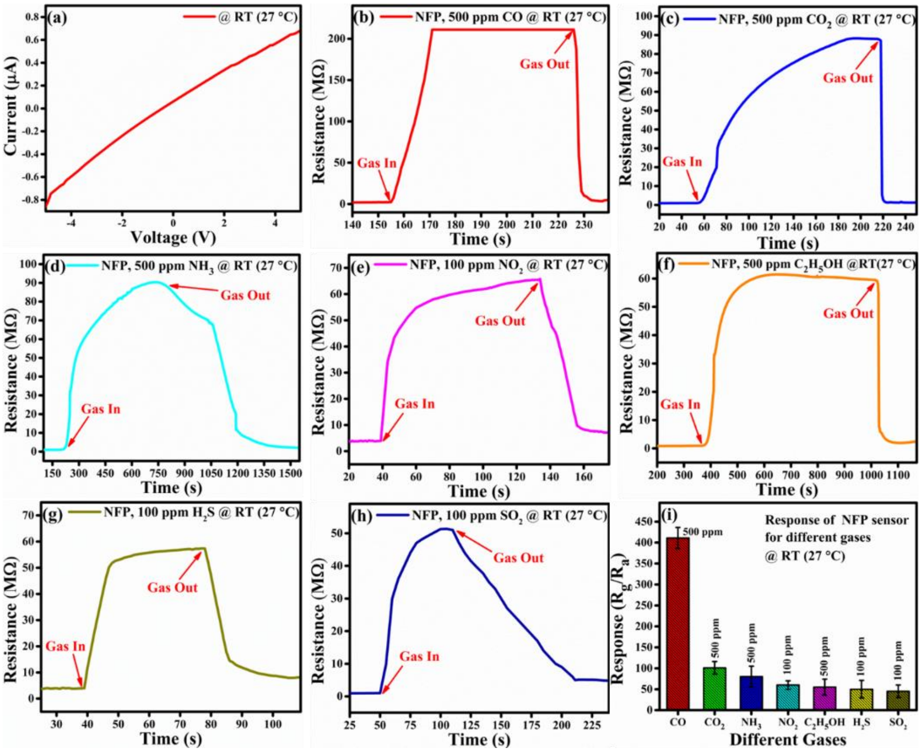

Figure 4.6. (*a*) The current-voltage (*I*-*V*) curve of the NFP sensor measured at room temperature; (*b*-*h*) Resistance measurement of NFP sensor when exposed to different gases, (*i*) Selectivity study with response value.

Figure 4.7(*a*-*c*) shows the electrical resistance variation of the NFP sensing material when exposed to CO gas at different temperatures above room temperature. It was observed that the change in resistance was reduced significantly as NFP material was exposed to gas at higher temperatures, shown in Table 4.2, with a simultaneous drastic increase in response and recovery time. As presented in Figure 4.7(*d*), sensing of 500 ppm CO gas by the NFP sensor for the 90% change in response at room temperature was achieved in just remarkable 14 s response time and 3 s recovery time (for the 20 ppm CO gas, ζ_{Res} = 22 S and ζ_{Rec} = 4 s, Figure 4.7(*f*)), which was increased to 109 s and 40 s at 150 ℃, respectively. Because the NFP is polyanionic material, the spin-polarised effect takes place resulting the higher baseline resistance at higher temperature. At higher temperature, there will be a steady state between gas adsoption and desorption, and because desorption is quite favorable at high temperatures, response will be reduced [41,42]. This concludes that NFP sensor exhibits superior response to CO gas at room temperature (27 ℃) to 50 ℃ and weak response at higher temperature.

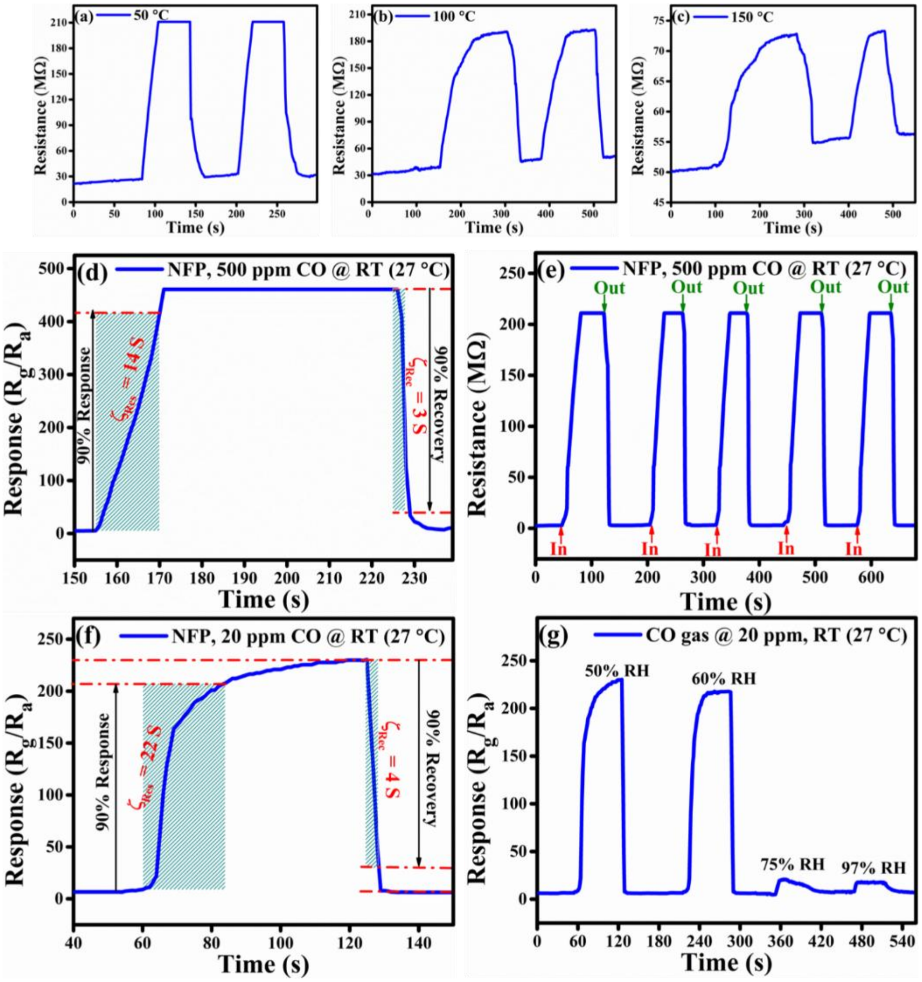

Figure 4.7. (*a-c*) Resistance measurement of NFP sensor exposed to CO gas at different temperatures, (*d*) Response and recovery time characteristics of NFP sensor exposed to 500 ppm CO gas, (*e*) Repeatability test for multiple consecutive cycles, (*f*) Response and recovery time characteristics of NFP sensor when exposed to 20 ppm CO gas, and (*g*) Response of the NFP sensor towards 20 ppm CO under different relative humidity at room temperature.

Thus, NFP material can be one of the best suited sensing material for normal room temperature (27 ℃) to high summer environment condition (50-60 ℃). We also examined the repeatability test to this NFP sensor for up to 5 consecutive cycles, as shown in Figure 4.7(*e*). The sensor maintained its superior sensing characteristics to CO gas for multiple cycles. For practically realizing the operation of the gas sensor in real time ambient conditions, the investigation of RH becomes vital. Humidity is the major concern in the operation of gas sensors under ambient conditions. Figure 4.7(*g*) presents the response of the NFP sensor measured under different RH conditions varying from 50 to 97% for 20 ppm CO exposure. The response decreases significantly from ~ 220 to ~ 20 as the RH increases from 50% to 97%. Though the response is reduced to ~ 20 at 97% RH, it is quite significant response of the NFP sensor which demonstrated the reliability of NFP sensor for CO sensing even under harsh humid conditions. In harsh humid conditions, the adsorption of water molecules at the surface of the NFP sensing material results in the minimal active sites available to adsorb CO molecules. Since both the response and available active sites are directly proportional to each other, both are reduced simultaneously in a harsh humid condition.

Table 4.2 CO sensing performance of NFP sensor at different temperatures.

	RT(27 °C)	**50 °C**	**100 °C**	**150 °C**
Response time	14 s	20 s	62 s	109 s
Recovery time	3 s	11 s	28 s	40 s
Δ*R* (Change in resistance)	208.5 MΩ	186 MΩ	151 MΩ	22 MΩ

Figure 4.8(*a*) illustrates the gas sensing studies of NFP sensor by recording the resistance variation when sensors were exposed to different CO gas concentrations ranging from 2.5 to 500 ppm at the room temperature. According to the International Union of Pure and Applied

Chemistry (IUPAC) defination, the limit of detection (LoD) should be calculated based on the response signal if the ratio of response signal-to-noise is greater than 3 [43]. We took 10 data points at baseline resistance (as shown in Figure 4.8(c)) before CO gas exposure to obtain the root-mean-square (rms_{noise}). V_x^2 was derived using the fifth-order polynomial fit as per following equation.

$$V_x^2 = \sum_{i=1}^{n} (y_i - y)^2 \tag{4.1}$$

Where y_i represents measured data points and y is the corresponding data points from the curve-fitting. Above obtained V_x^2 was used to calculate the rms_{noise} as per following equation:

$$rms_{noise} = \sqrt{\frac{V_x^2}{N}} \tag{4.2}$$

where N is the number of data points taken in the fifth-order polynomial curve fitting. Based on the obtained V_x^2 value in Figure 4.8(c), rms_{noise} was calculated to be $8.732\ X\ 10^{-4}$. The LOD of the fabricated sensing device can be calculated using the following equation [44,45]:

$$LoD = 3 * {}^{rms_{noise}}/_{slope} \tag{4.3}$$

where slope was obtained by applying linear regression fit to the relation between logarithm of gas response and logarithm of gas concentration (slope = 0.29442, Figure 4.8(b)). Based on the above data and equations, the LoD was calculated to be 8.897 ppb. The Langmuir adsorption isotherm model was applied to analyze the adsorption-desorption kinetics of NFP sensor exposed to CO gas. The response percentage (sensitivity) of the sensor with respect to CO concentrations follows the Langmuir adsorption isotherm which is governed by following equation:

$$S = \frac{S_{max} * K * C}{(1 + KC)} \tag{4.4}$$

Where S is sensing response, S_{max} is the maximum/saturated sensing response, K is the equilibrium gas adsorption constant and C is the concentration of gas adsorbed. The langmuir curve is the representation of the quantitative relationship between gas sensitivity and concentration explicitly [46,47]. As shown in Figure 4.8(*d*), most of the data fall well on the Langmuir adsorption isotherm curve, implying that gas responsivity of the NFP sensor is dominated by the concentration of CO gas adsorption at the surface of NFP. The high gas sensitivity at low concentrations would be beneficial for early CO gas detection. In addition, well agreement of data points with Langmuir adsorption isotherm demonstrates that the mechanism of CO gas sensing in NFP sensing device is charge transfer.

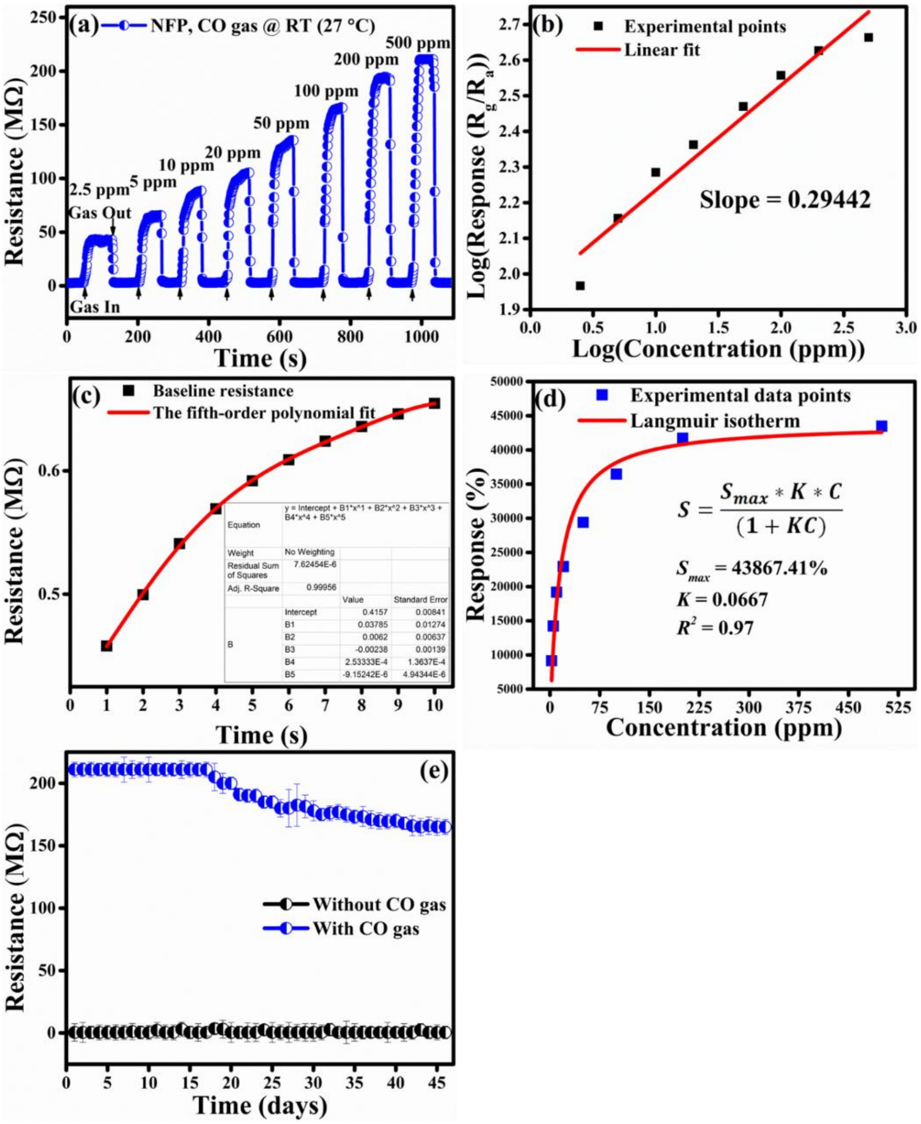

Figure 4.8. (*a*) Resistance versus time for CO concentrations ranging from 2.5 to 500 ppm for the NFP sensor. (*b*) Sensor response as a function of CO gas concentration. Inset is a corresponding linear fit of the response and CO

concentration. (*c*) Calculation of the rms_{noise} using fifth-order polynomial of 10 baseline resistance points. (*d*) Langmuir adsorption isotherm fit of the responses with respect to CO concentration at room temperature. (*e*) Stability test of the NFP sensor responding to CO gas for 45 days.

The stability is also a crucial property of the gas sensor. Stability of the NFP sensor was observed for the time cycle of 45 days at fixed concentration of CO gas keeping at the room temperature 27 ℃ as shown in Figure 4.8(*e*). The sensor shows maximum gas response of 460.74 consistantly for 17 days and it was dropped to ~350 *i.e.* stability of ~75% after 45 days. Indeed, this decreased CO response is still higher than the response towards other interferring gases at the same operating condition. This decrease in response and stability of the NFP sensor can be referred to the humidity effect on the NFP film. The material's sensitivity, selectivity and stability towards CO gas can be improved by optimizing its crystal structure, doping it with other elements, and controlling its operating conditions such as tempearture and humidity. Thus, it can be inferred that NFP sensor can stand as a reliable sensor for practical applications of CO monitoring.

Table 4.3 summerized the gas sensing properties of the NFP sensor and those recently reported new solution or composite based sensor towards CO detection. As compared with recently reported perovskites, binary/ternary oxides, as well as the reported nanocompsites, the NFP sensor can operate at RT. Moreover, NFP sensor shows the better response to CO gas with fast response and recovery times than any other compounds at RT, indicating excellent potential in the field of sensing harmful CO gas.

Table 4.3 Comparison of CO sensing performance of NFP sensor with recently reported CO sensors.

Sensing material	Transducer	Operating temperature	Concentration (ppm)	Response	Response/Recovery time	Ref.
$Na_3Fe_2(PO_4)_3$	**Resistive**	**RT**	**500**	**417.58 (>5000%)**	**14/3 s**	**This work**
		RT	**20**	**230**	**22/4 s**	**This work**
$Zn_{0.9}Mn_{0.1}SnO_3$	Resistive	200	500	4.088	6.6/34 s	48
WO_3	FET sensor	392	100	80.5	-	49
Pt NP-CuO NW EMSI	Resistor	200	45	25	-	50
PEDOT:PSS/PPA nanocomposite	Resistive	RT	100	18.5%	58/61 s	40
MWCNT@Pd NS	Resistive	RT	10	3.6%	74/25 s	51
Au-SnO_2-co-decorated WS_2 NS	Resistive (Self heating mode)	RT (4.7 V)	50	3.687	200/325 s	38
Ag-ZnO/MoS_2 nanocomposite	Resistive	RT	100	5.08%	50/40 s	52
SnO_2/$MoSe_2$	Resistive	RT	100	9.2%	20/16 s	10
SnO_2-NaOH	Resistive	75	60	32	42/120 s	53

4.3.6 Plausible Sensing Mechanism

Figure 4.9 illustrates the schematic diagram of the proposed gas sensing mechanism of NFP which is based on the resistance change model attributable to electron transfer [54,55] during the reversible gas adsorption and desorption process on the NFP surface. When NFP plate-like based gas sensor is exposed to ambient environment at room temperature, the oxygen molecules were adsorbed onto the NFP surface and becomes ionozed to form chemisorbed oxygen species O_2^- at room temperature. As it seizes the electrons from the surface, it leads to the formation of hole accumulation layer (HAL) near the surface resulting increase in hole concentration and a decline in resistance The following reaction can take place upon exposure of the sensing material to the ambient environment and CO gas:

$O_2\,(\text{gas}) \rightarrow O_2(\text{adsorbed})$ (4.5)

$O_2(\text{adsorbed}) \rightarrow O_2^-\,(\text{adsorbed}) + h^+$ $(T < 100\ ^{\circ}\text{C})$ (4.6)

$O_2^-(\text{adsorbed}) \rightarrow 2O^-(\text{adsorbed}) + h^+\ (100\ ^{\circ}\text{C} < T < 300\ ^{\circ}\text{C})$ (4.7)

$2CO\,(\text{gas}) + O_2^-\,(\text{adsorbed}) \rightarrow 2CO_2 + e^-$ (4.8)

$e^- + h^+ \rightarrow Null$ (4.9)

Under the environment of CO gas, the CO gas molecules reacts with chemisorbed oxygen species O_2^- and oxidized to form CO_2. The generation of free electrons is due to the reduction of the surface oxygen ions (O_2^-) to form oxygen vacancies, which can capture the free electrons. The oxygen vacancies act as electron acceptors, and their concentration increases when CO gas is present. Moreover, the free electrons generated by the reaction are captured by Fe^{2+} ions in the NFP material, causing a change in the electrical conductivity of the material that can be measured and used to detect the presence of CO gas (eq 4.11). In this process, the electrons are released back to the sensor surface. Thereby, the combination of these large numbers of electrons with existing holes reduces the thickness of HAL prompted to an increase in electrical resistance of NFP. Reversibly, the electrons are transferred to the oxygen species under the exposure of ambient environment causing the formation/increase of the thickness of HAL near the surface, thereby recovers the sensor resistance back to the baseline resistance. The enhanced sensitivity of NFP to CO gas is mainly the consequence of the defects and functional groups. As shown in crystal structure and XPS spectra of NFP, large number of defects and functional groups are present on surface of NFP. When NFP is exposed to CO atmosphere, CO gas molecules can combine with these surface groups of NFP, such as–O, NaO, FeO_6 octahedra, and PO_4 tetrahedra [8]. For example, the effect of NaO group of NFP can be explained by eq 4.10 followed by eqs 4.5 to 4.9:

$$2NaO \rightarrow 2Na^{+} + O_2 + 2\,e^{-} \qquad (4.10)$$

The effect of presence of FeO_6 octahedra is given by eq 4.11:

$$Fe^{2+} + CO + \frac{1}{2}O_2^{-} \rightarrow Fe^{3+} + CO_2 + 2e^{-} \qquad (4.11)$$

O_2 and CO molecules will react with Na^{+} ions at the surface. FeO_6 is a coordination complex that contains Fe and O atoms. Fe is a transition metal that can exist in different oxidation states, and in this material, it exists in the 3+ state. The FeO_6 units in NFP are arranged in a three-dimensional network, which provides numerous sites for CO gas molecules to adsorb onto. This enhances the interaction between the material and the CO gas, which leads to a higher sensing performance. FeO_6 octahedral units are responsible for the redox activity of the material. They provide sites for the oxidation and reduction reactions that occur during CO sensing. The Fe atoms in the octahedral units can easily loss or gain electrons, depending on the presence of CO. This property allows NFP to detect low concentrations of CO with high sensitivity. Any distortion in FeO_6 octahedra and PO_4 tetrahedra results in an increase in bulk oxygen mobility which can be reasonable for enhanced CO selectivity. Furthermore, as confirmed by XPS characterization (Figure 4.5(*e*)), high concentration of oxygen vacancies (O_V) and surface chemisorbed oxygen are obtained on NFP due to FeO_6 and PO_4 distortion, which is crucial to promote the surface reactivity and enhance the CO selectivity. The presence of sodium, iron and phosphate ions in the material leads to more number of oxygen species available and thus, more number of active sites to form the chemisorbed oxygen species that react with CO gas molecules. Consequently, NFP sensor exhibits remarkably high response to CO gas.

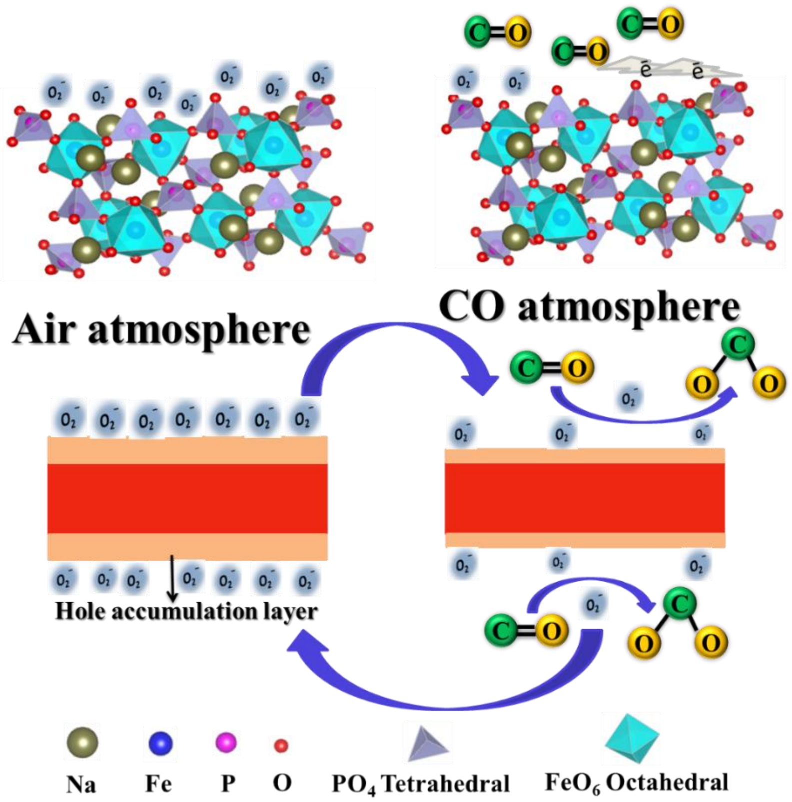

Figure 4.9. Schematic diagram of the possible gas-sensing mechanism of NASICON-type NFP sensors to CO gas.

4.4 Conclusions

In this study, we successfully demonstrated the NASICON-type NFP battery material as a cost-effective and sustainable new gas sensing material.. The NFP material fabricated with simple and economical sol-gel technique and the physico-chemical properties were investigated. The synthsized material exhibits monoclinic structure in the space group of C2/c with plate-like morphology. The thick-film NFP sensor was investigated for sensing characteristics towards different gas environment such as CO, NH_3, CO_2, C_2H_5OH, NO_2, SO_2, and H_2S. In particular, the NFP sensor exhibited superior selective gas sensing characteristics towards CO gas at the room temperature with very high response value, good stability cycle, fast response-recovery time and limit of detection to sub-ppb level, which can be ascribed to the chemical properties of sodium, FeO_6 octahedra, PO_4

tetrahedra and presence of more number of oxygen in surface reactivity. This study highlights the NASICON-type NFP as a next generation gas sensing materials that only employ cost-effective and earth-abundant elements.

References

[1] D. Wang, D. Zhang, Q. Pan, T. Wang, F. Chen, Gas sensing performance of carbon monoxide sensor based on rod-shaped tin diselenide/MOFs derived zinc oxide polyhedron at room temperature, Sensors Actuators B Chem. 371 (2022) 132481. doi:10.1016/j.snb.2022.132481.

[2] S.C. Yadav, A. Sharma, R.S. Devan, P.M. Shirage, Role of different counter electrodes on performance of TiO_2 based dye-sensitized solar cell (DSSC) fabricated with dye extracted from Hibiscus Sabdariffa as sensitizer, Opt. Mater. (Amst). 124 (2022) 112066. doi:10.1016/j.optmat.2022.112066.

[3] P.M. Shirage, A.K. Rana, Y. Kumar, S. Sen, S.G. Leonardi, G. Neri, Sr- and Ni-doping in ZnO nanorods synthesized by a simple wet chemical method as excellent materials for CO and CO_2 gas sensing, RSC Adv. 6 (2016) 82733–82742. doi:10.1039/c6ra15891a.

[4] A.K. Rana, R. Das, Y. Kumar, S. Sen, P.M. Shirage, Growth of transparent $Zn_{1-x}Sr_xO$ ($0.0 \leq x \leq 0.08$) films by facile wet chemical method: Effect of Sr doping on the structural, optical and sensing properties, Appl. Surf. Sci. 379 (2016) 23–32. doi:10.1016/j.apsusc.2016.04.066.

[5] J.-H. Kim, I. Sakaguchi, S. Hishita, T. Ohsawa, T.T. Suzuki, N. Saito, Ru-Implanted WS_2 Nanosheet Gas Sensors to Enhance Sensing Performance Towards CO Gas in Self-Heating Mode, SSRN Electron. J. 370 (2022) 132454. doi:10.2139/ssrn.4139408.

[6] L. Li, Y. Yang, D. Deng, H. Song, Y. Lv, Photocatalysis enhanced cataluminescence gas sensor for carbon monoxide based on perylenetetracarboxylic diimide, Sensors Actuators, B Chem. 315 (2020). doi:10.1016/j.snb.2020.128080.

[7] D. Wang, D. Zhang, M. Tang, H. Zhang, T. Sun, C. Yang, R. Mao,

K. Li, J. Wang, Ethylene chlorotrifluoroethylene/hydrogel-based liquid-solid triboelectric nanogenerator driven self-powered MXene-based sensor system for marine environmental monitoring, Nano Energy. 100 (2022) 107509. doi: https://doi.org/10.1016/j.nanoen.2022.107509.

[8] D. Zhang, L. Yu, D. Wang, Y. Yang, Q. Mi, J. Zhang, Multifunctional latex/ polytetrafluoroethylene-based triboelectric nanogenerator for self-powered organ-like mxene/metal-organic framework-derived cuo nanohybrid ammonia sensor, ACS Nano. 15 (2021) 2911–2919. doi:10.1021/acsnano.0c09015.

[9] D. Wang, D. Zhang, J. Guo, Y. Hu, Y. Yang, T. Sun, H. Zhang, X. Liu, Multifunctional poly(vinyl alcohol)/Ag nanofibers-based triboelectric nanogenerator for self-powered MXene/tungsten oxide nanohybrid NO_2 gas sensor, Nano Energy. 89 (2021) 106410. doi:10.1016/j.nanoen.2021.106410.

[10] Z. Yang, D. Zhang, D. Wang, Carbon monoxide gas sensing properties of metal-organic frameworks-derived tin dioxide nanoparticles/molybdenum diselenide nanoflowers, Sensors Actuators, B Chem. 304 (2020) 127369. doi:10.1016/j.snb.2019.127369.

[11] S. Chand Yadav, A. Srivastava, V. Manjunath, A. Kanwade, R.S. Devan, P.M. Shirage, Properties, performance and multidimensional applications of stable lead-free $Cs_2AgBiBr_6$ double perovskite, Mater. Today Phys. 26 (2022) 100731. doi:10.1016/j.mtphys.2022.100731.

[12] A. Srivastava, B. Singh Chauhan, S. Chand Yadav, M. Kumar Tiwari, J. Akash Kumar Satrughna, A. Kanwade, K. Bala, P.M. Shirage, Performance of dye-sensitized solar cells by utilizing Codiaeum Variegatum Leaf and Delonix Regia Flower as natural sensitizers, Chem. Phys. Lett. 807 (2022) 140087. doi:10.1016/j.cplett.2022.140087.

[13] S.C. Yadav, V. Manjunath, A. Srivastava, R.S. Devan, P.M. Shirage, Stable lead-free $Cs_4CuSb_2Cl_{12}$ layered double perovskite solar cells yielding theoretical efficiency close to 30%, Opt. Mater. (Amst). 132 (2022) 112676. doi:10.1016/j.optmat.2022.112676.

[14] B. Ouyang, J. Wang, T. He, C.J. Bartel, H. Huo, Y. Wang, V.

Lacivita, H. Kim, G. Ceder, Synthetic accessibility and stability rules of NASICONs, Nat. Commun. 12 (2021) 1–11. doi:10.1038/s41467-021-26006-3.

[15] H. Park, K. Jung, M. Nezafati, C.S. Kim, B. Kang, Sodium Ion Diffusion in Nasicon ($Na_3Zr_2Si_2PO_{12}$) Solid Electrolytes: Effects of Excess Sodium, ACS Appl. Mater. Interfaces. 8 (2016) 27814–27824. doi:10.1021/acsami.6b09992.

[16] S. Wang, J. Zheng, L. He, L. Zhang, X. Ge, S. Li, X. Wang, Z. Zhang, Carbon-Modified NASICON $Na_4FeV(PO_4)_3$ Cathode with Enhanced Kinetics for High-Performance Sodium-Ion Batteries, ACS Appl. Energy Mater. (2022). doi:10.1021/acsaem.2c01278.

[17] V.R.R. Boddu, D. Puthusseri, P.M. Shirage, P. Mathur, V.G. Pol, Layered Na_xCoO_2-based cathodes for advanced Na-ion batteries: review on challenges and advancements, Ionics (Kiel). 27 (2021) 4549–4572. doi:10.1007/s11581-021-04265-w.

[18] V.R. Reddy Boddu, M. Palanisamy, L. Sinha, S.C. Yadav, V.G. Pol, P.M. Shirage, Hysteresis abated P2-type $NaCoO_2$ cathode reveals highly reversible multiple phase transitions for high-rate sodium-ion batteries, Sustain. Energy Fuels. 5 (2021) 3219–3228. doi:10.1039/d1se00490e.

[19] M. Palanisamy, V.R. Reddy Boddu, P.M. Shirage, V.G. Pol, Discharge State of Layered P2-Type Cathode Reveals Unsafe than Charge Condition in Thermal Runaway Event for Sodium-Ion Batteries, ACS Appl. Mater. Interfaces. 13 (2021) 31594–31604. doi:10.1021/acsami.1c04482.

[20] Lichchhavi, H. Lee, Y. Ohshita, A.K. Singh, P.M. Shirage, Transformation of Battery to High Performance Pseudocapacitor by the Hybridization of $W_{18}O_{49}$ with RuO_2 Nanostructures, Langmuir. 37 (2021) 1141–1151. doi:10.1021/acs.langmuir.0c03056.

[21] A. Kanwade, S. Gupta, A. Kankane, M.K. Tiwari, A. Srivastava, J.A. Kumar Satrughna, S. Chand Yadav, P.M. Shirage, Correction: Transition metal oxides as a cathode for indispensable Na-ion batteries, RSC Adv. 12 (2022) 24478–24479. doi:10.1039/D2RA90080G.

[22] A. Kanwade, S. Gupta, A. Kankane, A. Srivastava, S.C. Yadav, P.M.

Shirage, Phosphate-based cathode materials to boost the electrochemical performance of sodium-ion batteries, Sustain. Energy Fuels. 6 (2022) 3114–3147. doi:10.1039/D2SE00475E.

[23] H. Xu, S. Wang, H. Wilson, F. Zhao, A. Manthiram, Y-Doped NASICON-type $LiZr_2(PO_4)_3$ Solid Electrolytes for Lithium-Metal Batteries, Chem. Mater. 29 (2017) 7206–7212. doi:10.1021/acs.chemmater.7b01463.

[24] M. Chen, W. Hua, J. Xiao, D. Cortie, W. Chen, E. Wang, Z. Hu, Q. Gu, X. Wang, S. Indris, S.L. Chou, S.X. Dou, NASICON-type air-stable and all-climate cathode for sodium-ion batteries with low cost and high-power density, Nat. Commun. 10 (2019) 1–11. doi:10.1038/s41467-019-09170-5.

[25] P. Nizamidin, A. Yimit, A. Abdurrahmana, K. Itohb, Formaldehyde gas sensor based on silver-and-yttrium-co doped-lithium iron phosphate thin film optical waveguide, Sensors Actuators, B Chem. 176 (2013) 460–466. doi:10.1016/j.snb.2012.10.037.

[26] H. Bin Sun, J.Z. Guo, Y. Zhang, T. Wei, Y.X. Zhou, L.L. Zhang, X.L. Wu, Y. Huang, W. Luo, High-Voltage All-Solid-State Na-Ion-Based Full Cells Enabled by All NASICON-Structured Materials, ACS Appl. Mater. Interfaces. 11 (2019) 24192–24197. doi:10.1021/acsami.9b07647.

[27] S.H. Santagneli, H.V.A. Baldacim, S.J.L. Ribeiro, S. Kundu, A.C.M. Rodrigues, C. Doerenkamp, H. Eckert, Preparation, structural characterization, and electrical conductivity of highly ion-conducting glasses and glass ceramics in the system $Li_{1+x}Al_xSn_yGe_{2-(x+y)}(PO_4)_3$, J. Phys. Chem. C. 120 (2016) 14556–14567. doi:10.1021/acs.jpcc.6b04839.

[28] N. Patima, Y. Abliz, I. Kiminori, Synthesis and optical-electrochemical gas sensing applications of Ni-doped $LiFePO_4$ nano-particles, New J. Chem. 40 (2016) 295–301. doi:10.1039/c5nj02018b.

[29] V.M. Pratiwi, A.A. Wibowo, Widyastuti, H. Purwaningsih, F.A. Maulana, Characterization of nasicon structure prepared with titanium dioxide doping for NO_x gas sensor application, Mater. Sci. Forum. 964 MSF (2019) 168–173. doi:10.4028/www.scientific.net/MSF.964.168.

[30] G. Jasinski, P. Jasinski, B. Chachulski, A. Nowakowski, Electrocatalytic gas sensors based on Nasicon and Lisicon, Mater. Sci. Pol. 24 (2006) 261–268.

[31] S. Wang, N. Gao, G. Wang, C. He, S. Lv, J. Qiu, Three-dimensional hierarchical $Na_3Fe_2(PO_4)_3$/C with superior and fast sodium uptake for efficient hybrid capacitive deionization, Desalination. 520 (2021) 115341. doi:10.1016/j.desal.2021.115341.

[32] Y. Cao, Y. Liu, T. Chen, X. Xia, L.C. Zhang, J. Zhang, Y. Xia, Sol-gel synthesis of porous $Na_3Fe_2(PO_4)_3$ with enhanced sodium-ion storage capability, Ionics (Kiel). 25 (2019) 1083–1090. doi:10.1007/s11581-018-2804-z.

[33] E. Palacios, P. Leret, J.F. Fernández, A.H. De Aza, M.A. Rodríguez, Synthesis of amorphous acid iron phosphate nanoparticles, J. Nanoparticle Res. 14 (2012). doi:10.1007/s11051-012-1131-y.

[34] S. Qiu, X. Wu, M. Wang, M. Lucero, Y. Wang, J. Wang, Z. Yang, W. Xu, Q. Wang, M. Gu, J. Wen, Y. Huang, Z.J. Xu, Z. Feng, NASICON-type $Na_3Fe_2(PO_4)_3$ as a low-cost and high-rate anode material for aqueous sodium-ion batteries, Nano Energy. 64 (2019) 103941. doi:10.1016/j.nanoen.2019.103941.

[35] B. Mandal, A.K. Thakur, AC impedance spectroscopy of NASICON type $Na_3Fe_2(PO_4)_3$ ceramic, AIP Conf. Proc. 1953 (2018). doi:10.1063/1.5032673.

[36] A.A. Nogai, Z.M. Salikhodzha, A.S. Nogai, D.E. Uskenbaev, Conducting and dielectric properties of $Na_3Fe_2(PO_4)_3$ and Na_2FePO_4F, Eurasian J. Phys. Funct. Mater. 5 (2021) 222–234. doi:10.32523/EJPFM.2021050307.

[37] B. Shen, F. Li, Y. Xie, J. Luo, P. Fan, A. Zhong, High performance ammonia gas sensor based on GaN honeycomb nanonetwork, Sensors Actuators, A Phys. 312 (2020). doi:10.1016/j.sna.2020.112172.

[38] D. Han, X. Han, X. Zhang, W. Wang, D. Li, H. Li, S. Sang, Highly sensitive and rapidly responding room-temperature NH_3 gas sensor that is based on exfoliated black phosphorus, Sensors Actuators B Chem. 367 (2022) 132038. doi:10.1016/j.snb.2022.132038.

[39] J. Li, Y. Lu, Q. Ye, M. Cinke, J. Han, M. Meyyappan, Carbon

nanotube sensors for gas and organic vapor detection, Nano Lett. 3 (2003) 929–933. doi:10.1021/nl034220x.

[40] Y. Xu, X. Li, Y. Song, R. Zhang, W. Yuan, D. Xia, Q. Xue, End Group Modification for Black Phosphorus: Simultaneous Improvement of Chemical Stability and Gas Sensing Performance, ACS Appl. Mater. Interfaces. 13 (2021) 50270–50280. doi:10.1021/acsami.1c16776.

[41] R. Kumar, R.N. Jenjeti, S. Sampath, Two-Dimensional, Few-Layer $MnPS_3$ for Selective NO_2 Gas Sensing under Ambient Conditions, ACS Sensors. 5 (2020) 404–411. doi:10.1021/acssensors.9b02064.

[42] M.K. Tiwari, S.C. Yadav, A. Srivastava, A. Kanwade, J.A.K. Satrughna, S.S. Mali, J. V. Patil, C.K. Hong, P.M. Shirage, Enhancement of CO gas sensing performance by Mn-doped porous $ZnSnO_3$ microspheres , RSC Adv. 12 (2022) 32249–32261. doi:10.1039/d2ra06785d.

[43] G. Jung, S. Hong, Y. Jeong, W. Shin, J. Park, D. Kim, J.H. Lee, Highly Selective and Low-Power Carbon Monoxide Gas Sensor Based on the Chain Reaction of Oxygen and Carbon Monoxide to WO_3, ACS Appl. Mater. Interfaces. 14 (2022) 17950–17958. doi:10.1021/acsami.1c25221.

[44] Z. Ziadi, A.J. Porkovich, P. Kumar, A. Datta, E. Danielson, V. Singh, T. Sasaki, M. Sowwan, Electronic Metal-Support Interactions at the Catalytic Interfaces of CuO Nanowires Decorated with Pt Nanoparticles for Methanol Oxidation and CO Sensing, ACS Appl. Nano Mater. 3 (2020) 8257–8267. doi:10.1021/acsanm.0c01685.

[45] M.O. Farea, H.A. Alhadlaq, Z.A.M. Alaizeri, A.A.A. Ahmed, M.O. Sallam, M. Ahamed, High Performance of Carbon Monoxide Gas Sensor Based on a Novel PEDOT:PSS/PPA Nanocomposite, ACS Omega. 7 (2022) 22492–22499. doi:10.1021/acsomega.2c01664.

[46] A. Kumar, Y. Zhao, M.M. Mohammadi, J. Liu, T. Thundat, M.T. Swihart, Palladium Nanosheet-Based Dual Gas Sensors for Sensitive Room-Temperature Hydrogen and Carbon Monoxide Detection, ACS Sensors. 7 (2022) 225–234. doi:10.1021/acssensors.1c02015.

[47] J.H. Kim, J.Y. Kim, A. Mirzaei, H.W. Kim, S.S. Kim, Synergistic effects of SnO_2 and Au nanoparticles decorated on WS_2 nanosheets

for flexible, room-temperature CO gas sensing, Sensors Actuators, B Chem. 332 (2021) 129493. doi:10.1016/j.snb.2021.129493.

[48] D. Zhang, Y. Sun, C. Jiang, Y. Yao, W. Dongyue, Y. Zhang, Room-temperature highly sensitive CO gas sensor based on Ag-loaded zinc oxide/molybdenum disulfide ternary nanocomposite and its sensing properties, Sensors Actuators, B Chem. 253 (2017) 1120–1128. doi:10.1016/j.snb.2017.07.173.

[49] K. Mazumder, A. Sharma, Y. Kumar, P.M. Shirage, Effect of Cu intercalation on humidity sensing properties of Bi_2Se_3 topological insulator single crystals, Phys. Chem. Chem. Phys. 20 (2018) 28257–28266. doi:10.1039/c8cp05452e.

[50] L. Sinha, P.M. Shirage, Surface Oxygen Vacancy Formulated Energy Storage Application: Pseudocapacitor-Battery Trait of $W_{18}O_{49}$ Nanorods , J. Electrochem. Soc. 166 (2019) A3496–A3503. doi:10.1149/2.1251914jes.

[51] M. González-Garnica, A. Galdámez-Martínez, F. Malagón, C.D. Ramos, G. Santana, R. Abolhassani, P. Kumar Panda, A. Kaushik, Y.K. Mishra, T.V.K. Karthik, A. Dutt, One dimensional Au-ZnO hybrid nanostructures based CO_2 detection: Growth mechanism and role of the seed layer on sensing performance, Sensors Actuators, B Chem. 337 (2021). doi:10.1016/j.snb.2021.129765.

[52] Y.K. Mishra, G. Modi, V. Cretu, V. Postica, O. Lupan, T. Reimer, I. Paulowicz, V. Hrkac, W. Benecke, L. Kienle, R. Adelung, Direct Growth of Freestanding ZnO Tetrapod Networks for Multifunctional Applications in Photocatalysis, UV Photodetection, and Gas Sensing, ACS Appl. Mater. Interfaces. 7 (2015) 14303–14316. doi:10.1021/acsami.5b02816.

[53] R. Malik, V.K. Tomer, Y.K. Mishra, L. Lin, Functional gas sensing nanomaterials: A panoramic view, Appl. Phys. Rev. 7 (2020). doi:10.1063/1.5123479.

[54] Y. Yang, C.C. Liu, Development of a NASICON-based amperometric carbon dioxide sensor, Sensors Actuators, B Chem. 62 (2000) 30–34. doi:10.1016/S0925-4005(99)00370-6.

[55] X. Zhang, C. Pei, X. Chang, S. Chen, R. Liu, Z.J. Zhao, R. Mu, J. Gong, FeO_6 Octahedral Distortion Activates Lattice Oxygen in

Perovskite Ferrite for Methane Partial Oxidation Coupled with CO_2 Splitting, J. Am. Chem. Soc. 142 (2020) 11540–11549. doi:10.1021/jacs.0c04643.

Chapter 5

$W_{18}O_{49}$ Nanofibers Functionalized with Graphene as a Selective Sensing of NO_2 Gas at Room Temperature

This chapter presents a room-temperature NO_2 gas sensor based on $W_{18}O_{49}$ nanofibers decorated with 2D graphene, coated on Cu interdigitated electrodes via DC sputtering. The $W_{18}O_{49}$/Gr1.5% sensor exhibited a high response (~150-160 times) to NO_2, with an ultra-fast 3 s response and 6 s recovery time. It demonstrated excellent selectivity, reproducibility (3 months), and stability across 20%-97% humidity conditions, with a 0.3 ppm detection limit. While $W_{18}O_{49}$/Gr3% showed higher selectivity, $W_{18}O_{49}$/Gr1.5% provided superior sensitivity, attributed to oxygen vacancies, defects, and strong Cu contacts, making it ideal for environmental NO_2 detection.

5.1 Introduction

This chapter focuses on development of advanced nanostructures to fabricate the sensor exhibiting room temperature sensing of NO_2 gas, which stands out as one of the particularly menacing pollutants, a noxious gas and being a pervasive pollutant primarily emitted from industrial activities, fossil fuel combustion and vehicular emissions. Its toxic effects on respiratory health are well-documented, necessitating stringent air quality regulatory standards and exposure limits [1–5]. Several renowned agencies have fixed the air quality standard for NO_2. For instance, the NIOSH set the short-term 15 min NO_2 exposure limit to less than 3 ppm and long-term exposure 8-hour limit to 1 ppm [6]. Addressing these growing environmental and health concerns, there is an imminent demand for gas sensor devices with heightened sensitivity and selectively tailored for the room temperature detection of NO_2 at minimal concentrations.

In recent literatures, innovative approaches have been explored [7,8] for fabrication of gas sensors to enhance their performance such as incorporating 1D nanostructures like nanowires, nanoneedles, nanofibers, nanotubes, etc. by additional carbon-based materials like 2D nanostructured Graphene (Gr) [9] to augment their sensing capabilities. One such approach that received great attention involves the integration of 1D transition metal oxide nanowires/nanofibers/nanorods, such as tungsten oxide (WO_3 and $W_{18}O_{49}$), with Gr to create hybrid nanocomposites with synergistic properties. WO_3 being *n*-type metal oxide semiconductor with large band gap ($E_g > 2.6$) shows excellent sensitivity and selectivity to several gases such as ethanol, NO_2, H_2S, and NH_3 depending on different operating conditions. Though WO_3 is one of the effective materials, making a device with this for good sensitivity and selectivity to one particular gas at room temperature is quite challenging [10]. $W_{18}O_{49}$ ($WO_{2.7}$) is one of the most attractive non-stoichiometric forms of tungsten oxide and it has promised improved sensing results than WO_3 due to its unique physico-chemical properties, especially larger oxygen vacancies and surface area [11–13].

Moreover, the hybrid structures, *i.e.* WO_3 with Gr or $W_{18}O_{49}$ with Gr, not only provide an increased surface area facilitating for gas adsorption but also facilitate charge transfer processes, resulting to enhanced gas sensing performance. Compared to WO_3, the gas sensing applications of $W_{18}O_{49}$ hybrid with Gr layered structure are scarce in the literature.

Zhang *et al.* [14] synthesized $W_{18}O_{49}$ ultrafine nanowires of diameter 0.8 nm to exhibit ultrahigh selective sensitivity of acetone among VOCs. Qiu *et al.* [15] reported the construction of $W_{18}O_{49}$/G nanocomposites for the detection of ethanol vapors where highest sensitivity of only 16.47 was obtained at 340 °C high operating temperature. Wang *et al.* [16] (2020) proposed a strategy of self-assembly hybrid structure of WO_3 nanosheets-$W_{18}O_{49}$ nanowires composite, which achieved ultra-high sensitivity to 10 ppm NO_2 gas but at elevated temperature of 160 °C. In 2023, Manoharan *et al.* [10] fabricated oxygen-deficient $W_{18}O_{49}$ supported with WS_2 heterojunctions to obtain the room temperature sensing of NO_x and NH_3. Though, they achieved the desired room temperature sensing at low ppm (0.6 and 0.5 ppm, respectively), selectivity between NO_x and NH_3 would hindrance its practical applications.

In this work, we synthesized 1D nanostructured $W_{18}O_{49}$ nanofibers integrated with 2D Gr (carbon atom with sp2 hybridization) to fabricate $W_{18}O_{49}$/Gr hybrid heterojunction. The study emphasized on examining the alterations in wt% of Gr material to develop the adequate $W_{18}O_{49}$/Gr-based gas sensors for selective detection of NO_2 gas at room temperature and atmospheric pressure. Crumpled Gr decorated with $W_{18}O_{49}$ nanofibers were deposited on Cu sputtered IDE. $W_{18}O_{49}$ nanofibers serve as active sites for NO_2 detection while crumpled Gr offers increased surface area and roughness that promotes surface adsorption [17–20]. The developed sensor holds great promise for their applications in industrial safety, environmental monitoring, and public health, contributing to the mitigation of NO_2-related air pollution and its associated health impacts.

5.2 Experimental

5.2.1 Chemicals and Gases

All the chemicals and reagents were of analytical grade, which were used as received without any further purification. Sodium tungsten dyhydrate ($Na_2WO_4.2H_2O$) was procured from Sisco Research Laboratories Pvt. Ltd., India. Sodium sulfate (Na_2SO_4), Potassium sulfate (K_2SO_4), and Ethanol (C_2H_5OH, EMSURE, ACS, ISO, absolute for analysis) were procured from Merck KGaA, Germany. Graphene powder (1-5 layers thick x 0.5-5 microns wide, surface area 650-750 m^2/g) was purchased from Strem Chemicals, USA.

5.2.2 Synthesis of WO_3 or $W_{18}O_{49}$ nanofibers

WO_3 and $W_{18}O_{49}$ nanofiber bundles were synthesized *via* a hydrothermal method as already discussed in **Chapter 2, Section 2.2.3 Synthesis of Sensing Material by Hydrothermal method (Figure 2.3(a))**. WO_3 NFs were prepared by adjusting $Na_2WO_4 \cdot 2H_2O$ solution to pH 1.25 using HCl, followed by adding Na_2SO_4 and K_2SO_4, and hydrothermal treatment at 180°C for 16 h. $W_{18}O_{49}$ NFs were synthesized similarly, with doubled Na_2SO_4 and K_2SO_4 concentrations. The final products were washed, dried, and used for gas sensing applications.

5.2.3 Synthesis of WO_3/Gr or $W_{18}O_{49}$/Gr nanocomposite

WO_3/Gr and $W_{18}O_{49}$/Gr nanocomposites were synthesized with slight modifications to the hydrothermal process as discussed in **Chapter 2, Figure 2.3(b)**. Different graphene weight percentages (0.5%, 1.5%, and 3%) were dispersed in solution after Na_2SO_4 and K_2SO_4 addition, followed by ultrasonication and stirring for 1 h each. The mixture underwent hydrothermal treatment at 180°C for 16 h, centrifugation, and vacuum drying at 80°C for 10 h to obtain the final composites.

5.2.4 Sensor Fabrication

The Cu-based IDE were prepared by PVD technique. Kapton tape as a shadow mask affixed onto the corning glass substrate in a specific pattern as shown in Figure 5.1. Cu was DC sputtered over the glass substrates in a pattern, conducted at a power of 9 W to ensure uniform and controlled deposition of Cu atoms. The resulting IDE electrodes exhibited a thickness of approximately 375 nm, as determined through FESEM. The IDE design included electrodes with a width of 0.8 mm and a spacing between electrode fingers of 0.5 mm. Additionally, contact pads measuring 5 mm x 5 mm were incorporated to facilitate electrical connections of each Cu electrode. The sensor was fabricated by adding 10 mg synthesized materials and 4-5 drops of absolute ethanol in a mortar, followed by thorough grinding sufficiently until a uniformly blended paste was formed. The paste was then coated by 25 µm gapped doctor blade film applicator, ensuring that it covered the electrode pattern completely and uniformly.

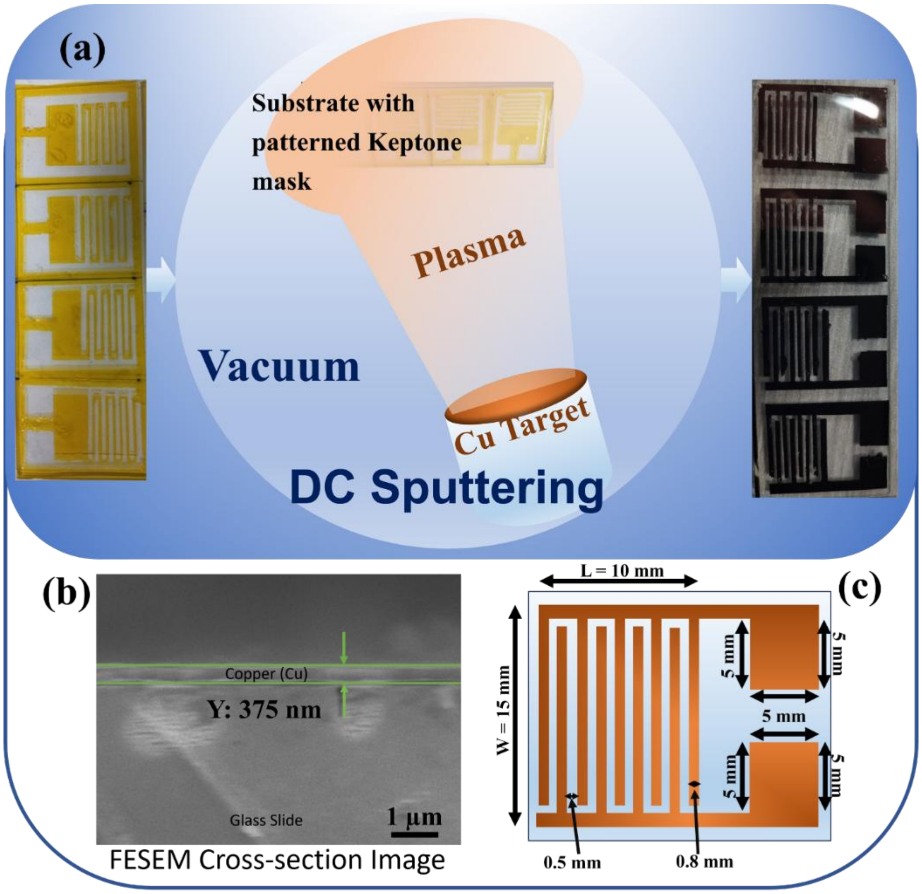

Figure 5.1. (a) Schematic illustration of the preparation of Cu-based IDE

by DC sputtering, (b) Thickness of the DC sputtered Cu on glass substrate, and (c) Designing of IDE pattern.

5.3 Results and Discussion

5.3.1 X-ray Diffraction

The XRD patterns are shown in Figure 5.2 to validate the crystalline phases of the samples. Figure 5.2(a) shows the Rietveld refined XRD pattern of WO_3 nanostructures, where all the obtained diffraction peaks could only be indexed to hexagonal phase structure of WO_3 (Ref. File no. – 96-100-4058) in a space group of *P*6/*mmm*.

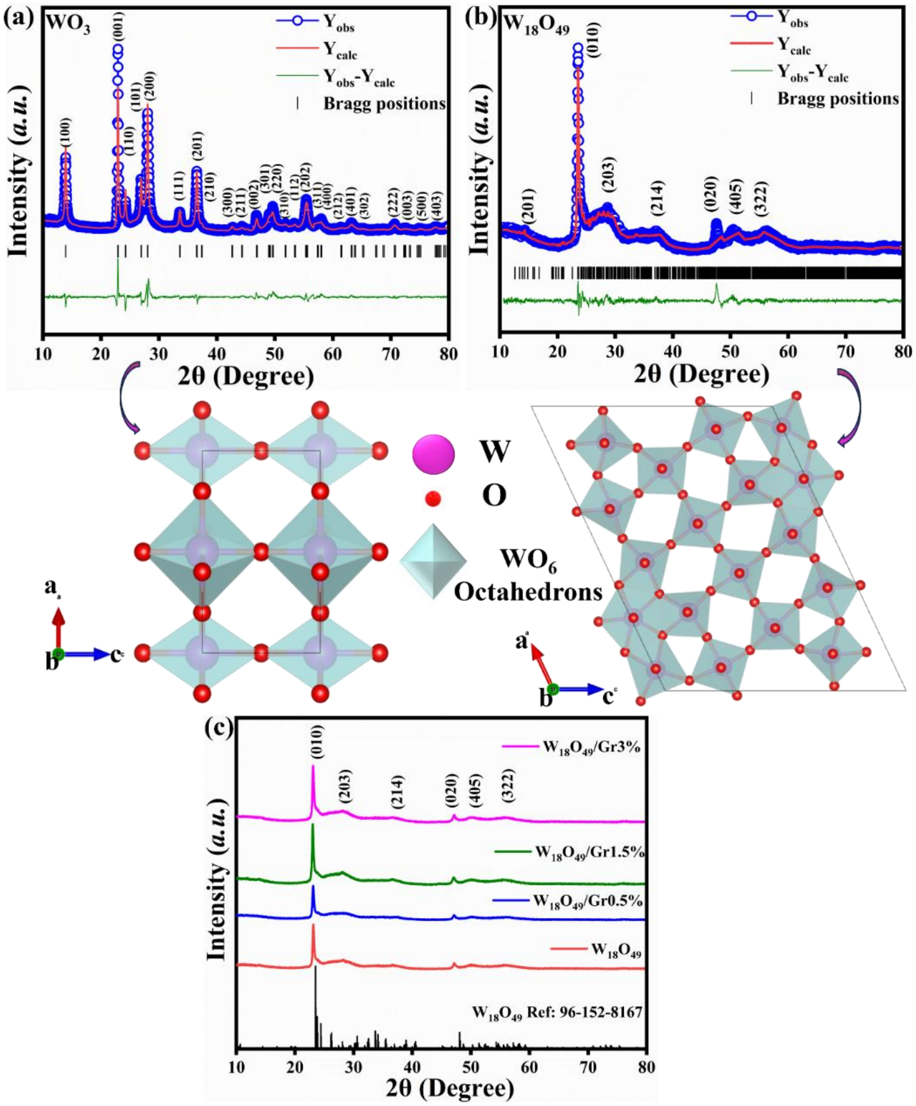

Figure 5.2. Rietveld refined XRD pattern of (a) pristine WO_3, (b) pristine $W_{18}O_{49}$ with their respective crystal structure images. (c) XRD pattern of $W_{18}O_{49}$/Gr(x%), x = 0, 0.5, 1.5, and 3.

Rietveld refinement to calculate the lattice parameters was carried out using FullProf software. No peaks are related to any other phases or impurities were identified. Likewise, Figure 5.2(b) shows the Rietveld refined XRD pattern of $W_{18}O_{49}$ nanostructures, where all the diffraction peaks can only be indexed to the monoclinic phase structure of $W_{18}O_{49}$ in a space group of *P*12/*m*1 (Ref. File. No.- 96-152-8167). The prominent peaks at $2\theta = 23.4^\circ$ assigned to the reflections from (010) plane of $W_{18}O_{49}$. Other diffraction peaks are less intense and sharp, indicating preferential growth along (010) direction. The fundamental unit of $W_{18}O_{49}$ nanostructures consists of WO_6 octahedra, which share corners and edges to form the overall nanostructure. Moreover, XRD pattern of the $W_{18}O_{49}$/Gr(*x*%) hybrid nanocomposite materials along with $W_{18}O_{49}$ were presented in Figure 5.2(c). Interestingly, no diffraction peaks of graphene were observed due to the mixing of graphene into the $W_{18}O_{49}$ matrix because of the low content of graphene in the hybrid. The phenomenon is in good agreement with the prior study [21,22].

Table 5.1 Refined lattice parameters

Sample	Crystal structure	Space group	*a* (Å)	*b* (Å)	*c* (Å)	α (deg)	B (deg)	γ (deg)
WO_3	Hexagonal	P6/mmm	7.344(1)	7.344(1)	3.875(3)	90	90	120
$W_{18}O_{49}$	Monoclinic	P12/m1	18.626(8)	3.780(2)	14.058(7)	90	114.950(5)	90
$W_{18}O_{49}$/Gr1.5%	Monoclinic	P12/m1	18.635(6)	3.782(4)	14.028(6)	90	115	90

5.3.2 Field Emission-Scanning Electron Microscopy (FESEM) of Pristine samples

Low and high magnification surface morphology of the pristine WO_3 and $W_{18}O_{49}$ gas sensing materials are illustrated in Figure 5.3. Pristine WO_3, Figure 5.3(a, b, c), were composed of thin interlaced nanowires and Pristine

$W_{18}O_{49}$, Figure 5.3(d, e, f), were composed of thin interlaced porous nanofibers with diameters ranged from ~10 to ~60 nm. These nanowires and nanofibers are interlaced among them to form large woven like cluster.

5.3.3 FESEM and High-Resolution Transmission Electron Microscopy (HRTEM) of Composites

Figure 5.4 shows the FESEM and HRTEM analysis of the best optimized gas sensing material, $W_{18}O_{49}$/Gr1.5% nanocomposite. Figure 5.4(a-d) evidenced the nucleation and growth of $W_{18}O_{49}$ nanofibers on graphene support. 1D $W_{18}O_{49}$ nanofibers decorated graphene sheets are advantageous for enhanced gas sensing characteristics, including a high surface area, high surface-to-volume ratio, porosity, and surface roughness to enhance the active sites for fast adsorption of gas molecules. The cross-section SEM images of a typical fabricated gas sensor were also presented in Figure 5.5.

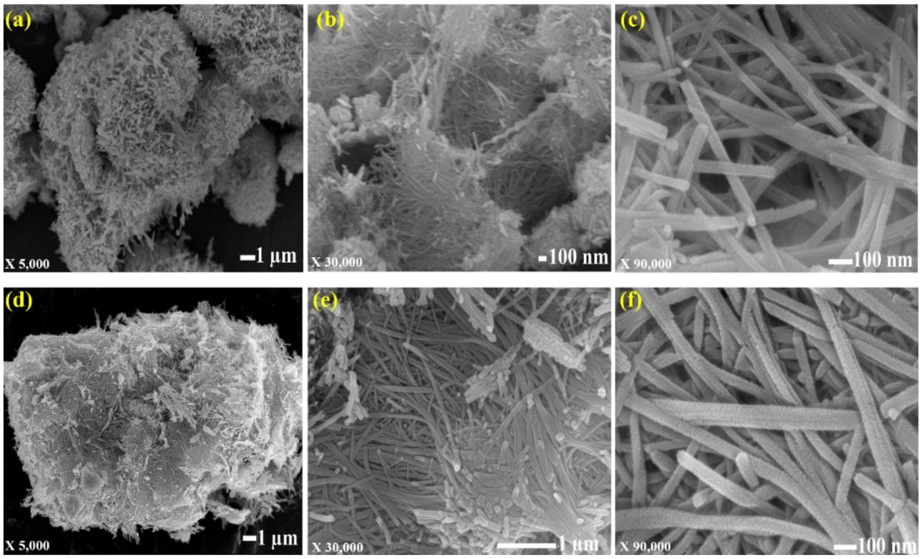

Figure 5.3. Low and High magnification FE-SEM images of (a), (b) and (c) pristine WO_3; and (d), (e) and (f) pristine $W_{18}O_{49}$ gas sensing materials.

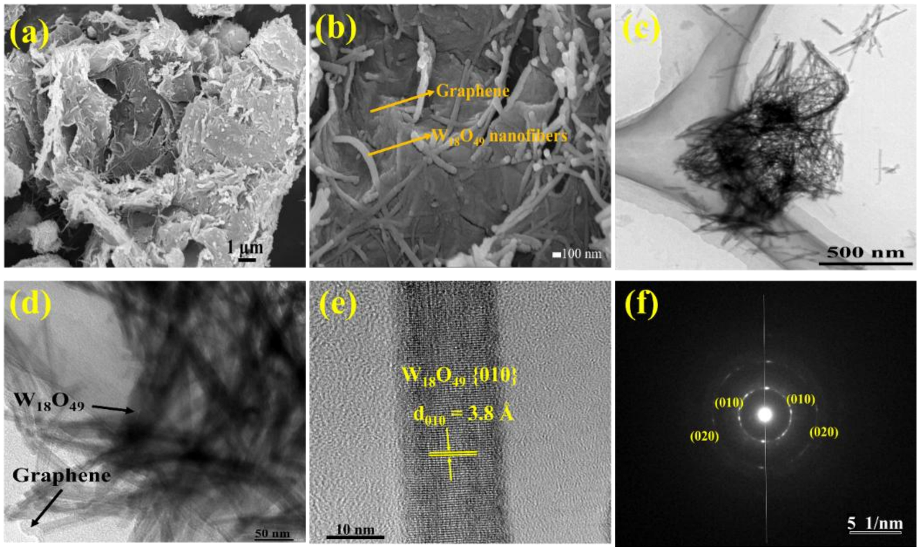

Figure 5.4. (a) Low and (b) High magnification FE-SEM image, (c) and (d) TEM images, (e) HR-TEM image, and (f) selected area electron diffraction (SAED) pattern of the HRTEM image of the optimized $W_{18}O_{49}$/Gr1.5% gas sensing material.

TEM images (Figure 5.4(c-d)) agreed well with the FE-SEM analysis. The HR-TEM image as presented in Figure 5.4(e) demonstrates the crystalline nature of the $W_{18}O_{49}$/Gr1.5% hybrid nanocomposites. The lattice-fringe spacing of the single nanofibers give a *d*-spacing of approximately 3.8 Å corresponding to the (010) plane of monoclinic $W_{18}O_{49}$. Figure 5.4(f) presents the obtained SAED pattern that reveals the polycrystalline nature of the hybrid nanostructures owing to the arrangement of both diffraction spots and ring pattern. The diffraction spots indexed to the (010) and (020) planes of $W_{18}O_{49}$, also corroborated by the XRD image. Additionally, an intriguing feature deduced from the SAED pattern is the presence of diffraction spots displaying a streaking pattern, indicative of unequally spaced planar defects aligned with the nanofiber's growth axis. Such a phenomenon is intrinsic to $W_{18}O_{49}$ due to its oxygen sub stoichiometry, which contributes to the formation of extended planar defects [23,24].

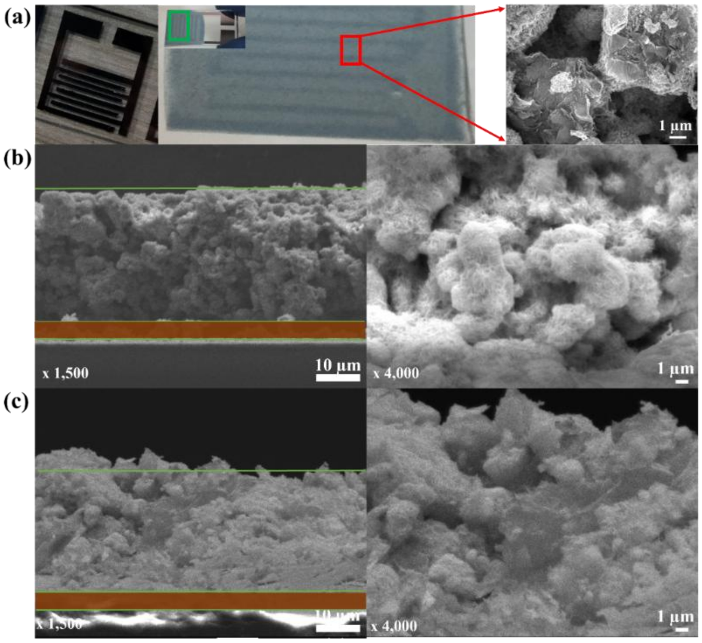

Figure 5.5. (a) Front-view of fabricated gas sensor on IDE & SEM image of a typical fabricated $W_{18}O_{49}$-garphene composite-based gas sensor, Cross-section SEM image of (b) pristine $W_{18}O_{49}$-based sensor on IDE, and (c) $W_{18}O_{49}$/Gr1.5% -based sensor on IDE.

5.3.4 X-ray Photoelectron Spectroscopy

The efficacy of gas sensitivity relies heavily on the surface condition of the gas-sensing materials, as gas sensing is primarily influenced by surface characteristics. XPS analysis was employed to probe the gas sensing materials for the electronic structures of surface ions, and defects. Figure 5.6 shows the survey scan of pristine WO_3, pristine $W_{18}O_{49}$, and $W_{18}O_{49}$ nanofibers hybrid composite with 0.5 wt%, 1.5 wt% and 3 wt% graphene sheets. It confirms the presence of elements W and O in all the samples, and intense C peak due to presence of graphene in hybrid nanocomposite materials as shown in Figure 5.6(c-e).

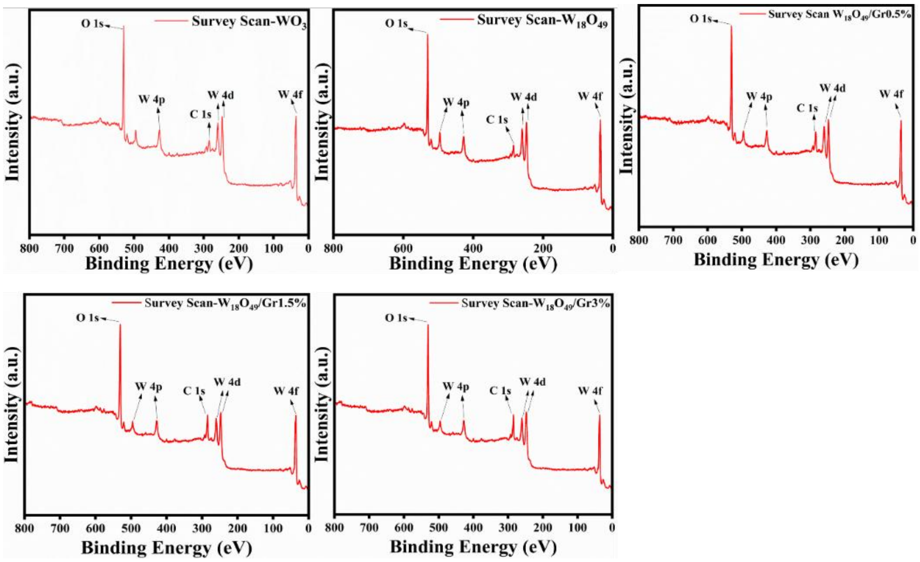

Figure 5.6. Survey XPS spectrum of pristine and nanocomposite gas-sensing materials.

The high-resolution XPS spectra of W 4f were revealed in Figure 5.7(a). All W elements in pristine WO_3 was observed in hexavalent state, which aligns with findings reported in prior studies [25]. The W 4f spectra of pristine $W_{18}O_{49}$ and hybrid nanocomposites was deconvoluted into two doublets, which represents different oxidation states of W atoms. The well-resolved high intense doublet peaks located at 35.49-35.98 and 37.60-38.09 eV corresponds to W^{6+} oxidation state, whereas the low intense doublet peaks centered at 34.2-34.3 and 36.19-31 eV agreed with the W^{5+} oxidation state [26,27]. It confirmed the non-stoichiometric synthesis of $W_{18}O_{49}$ (oxygen deficient). The O1s spectra were deconvoluted into three doublet peaks, Figure 5.7(b), with binding energy centered at 529.52-529.83, 530.41-530.72, and 531.6-532.03 eV, which are determined to lattice oxygen (O_L), surface chemisorbed oxygen (O_C), and oxygen vacancies (O_V), respectively [28,29]. $W_{18}O_{49}$/Gr1.5% hybrid nanocomposite has a lowest O_L content and a high (O_V+O_C) content, which makes this respective composition as a propitious material for enhanced gas sensing performance characteristics.

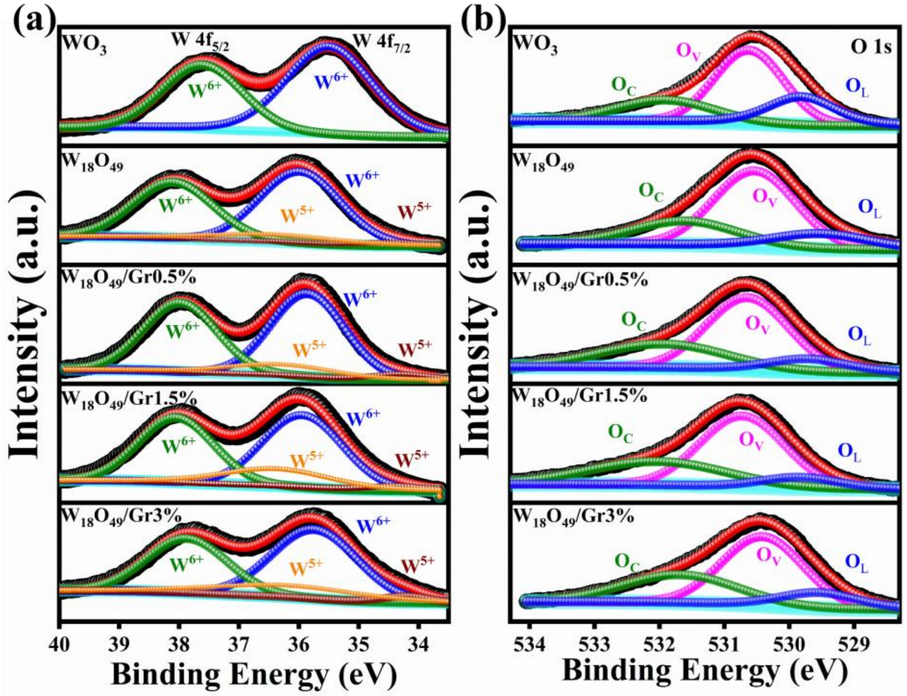

Figure 5.7. High-resolution XPS spectra of (a) W 4f, and (b) O 1s orbitals of pristine and nanocomposite gas-sensing materials.

5.3.5 BET Analysis

Figure 5.8 and Figure 5.9 illustrates the nitrogen adsorption-desorption isotherm profiles for $W_{18}O_{49}$, $W_{18}O_{49}$/Gr1.5% and WO_3, WO_3/Gr0.5%, WO_3/Gr1.5%, $W_{18}O_{49}$/Gr0.5%, $W_{18}O_{49}$/Gr3%, respectively. The corresponding evaluation of the BET surface area (m^2/g), average pore size (nm) and pore volume (cm^3/g) are depicted in the Table 5.2. The analysis was repeated three times (N = 3) to calculate the standard deviation.

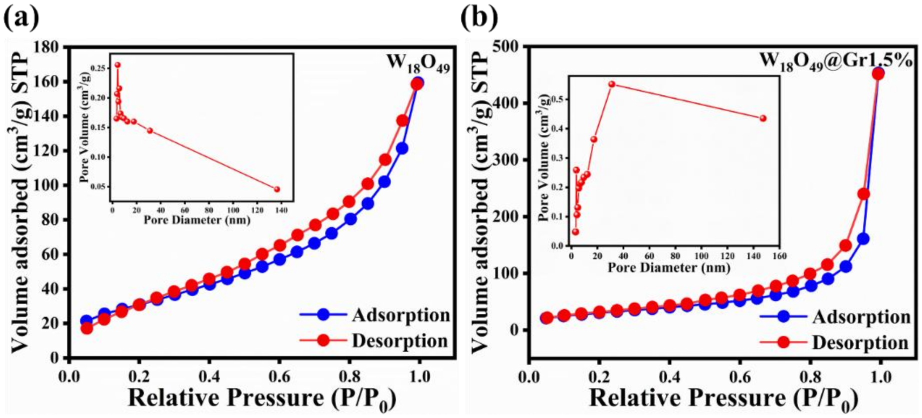

Figure 5.8. Nitrogen adsorption-desorption isotherms profile of the (a) pristine $W_{18}O_{49}$ and (b) $W_{18}O_{49}$/Gr1.5% samples.

In consonance with IUPAC classification, mesoporous features were evident in the BET-BJH plots of the WO_3 or $W_{18}O_{49}$ nanofibers-Gr hybrid scaffold that shows typical type-IV isotherm with H_3 hysteresis loops. The results revealed a notable trend wherein $W_{18}O_{49}$ exhibits higher surface area than WO_3 and the surface area initially increased with the incorporation of graphene, peaking at 1.5 wt% Gr content scaffold with $W_{18}O_{49}$ nanofibers.

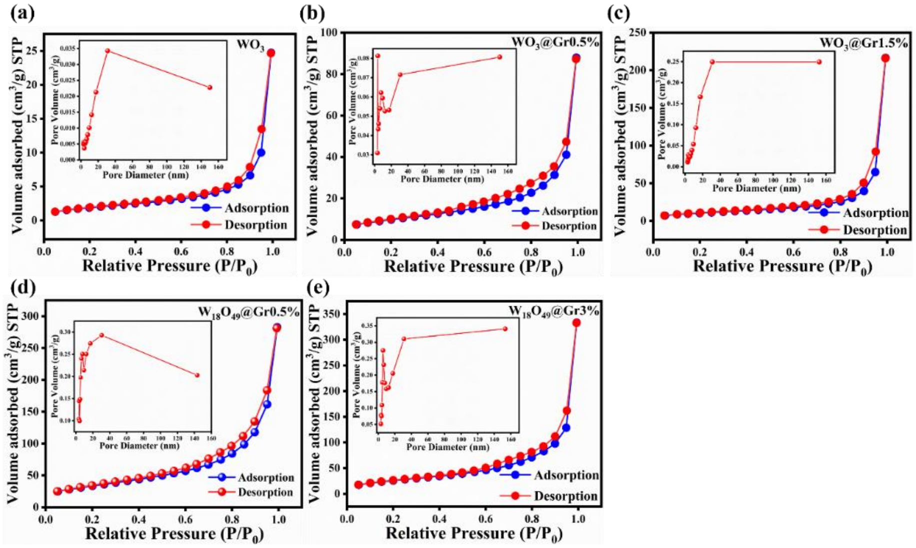

Figure 5.9. Nitrogen adsorption-desorption isotherms profile of the (a) pristine WO_3, (b) WO_3/Gr0.5%, (c) WO_3/Gr1.5%, (d) $W_{18}O_{49}$/Gr0.5%, and (e) $W_{18}O_{49}$/Gr3% samples.

Table 5.2 Surface area calculation for pristine and different mol% Gr-loaded WO_3 and $W_{18}O_{49}$.

Samples	**Surface Area (m^2/g)**	**Average Pore Size (nm)**	**Pore Volume (cm^3/g)**
WO_3	6.818±0.004	3.406±0.001	0.034±0.002
WO_3/Gr0.5%	34.275±0.006	3.826±0.007	0.081±0.005
WO_3/Gr1.5%	37.724±0.003	17.392±0.003	0.25±0.002

$W_{18}O_{49}$	94.392±0.002	4.324±0.003	0.25±0.002
$W_{18}O_{49}$/Gr0.5%	115.347±0.008	3.832±0.002	0.29±0.003
$W_{18}O_{49}$/Gr1.5%	**119.233±0.007**	3.830±0.001	**0.55±0.003**
$W_{18}O_{49}$/Gr3%	110.091±0.006	5.627±0.003	0.34±0.001

Subsequently, a decline in surface area was observed upon further augmentation of graphene concentration (>1.5%) which will affect the gas sensitivity of the corresponding sensing materials. It can be inferred that the nanocomposite comprising 1.5 wt% Gr hybridized with $W_{18}O_{49}$ nanofibers, that exhibits highest surface area of 119.233 m^2/g with mesoporosity, is poised to exhibit the highest sensitivity to NO_2 gas, owing to its more active reaction sites and channels for fast gas adsorption and desorption activity.

5.3.6 Gas Sensing Measurements

The *I-V* measurements of both pristine and hybrid nanocomposites on Cu IDE electrodes were carried out, using a Keithley-2401 Sourcemeter, with the constant sweeping voltage from -5 V to +5 V with a step of 0.05 V at room temperature, as shown in Figure 5.10. The linear behavior observed in the *I-V* plot suggests that there is a good ohmic contact between the deposited gas sensing materials with Cu contacts. Also, as seen in Figure 5.10, the increase in the current value of graphene decorated nanofibers compared to pristine WO_3 and $W_{18}O_{49}$ is obvious because of increase in Gr content.

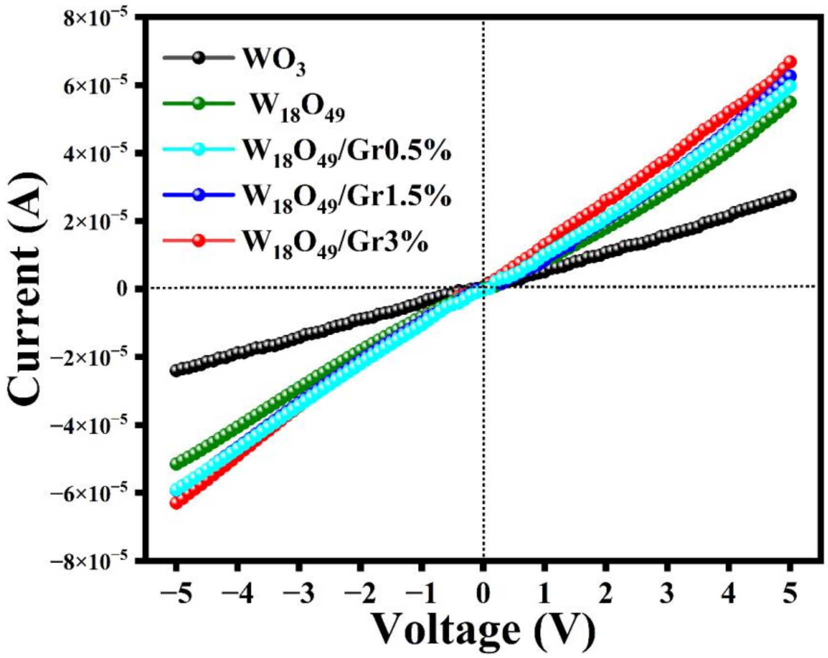

Figure 5.10. I-V measurements of pristine WO_3 and $W_{18}O_{49}$, and hybrid nanocomposites of $W_{18}O_{49}$ with graphene on the Cu IDE contacts measured at room temperature.

The gas-sensing measurements were initiated with the study of pristine WO_3 and $W_{18}O_{49}$ self-assembled nanofibers-based sensors by exposing the respective sensors to several gases NH_3, Ethanol, NO_2, H_2S, SO_2, and CO at room temperature and recording the corresponding change in signals (resistance), as shown in Figure 5.11. The gas-sensing measurements were repeated four times (N = 4) for each of the samples. The observed increase in resistance when exposed to these gases reaffirmed the *n*-type behavior of both the sensors. Sensor recovery was achieved by using a rotary pump to purge the system, followed by exposure to ambient conditions. It is clearly visible from Figure 5.11(a) that the pristine WO_3-based sensors exhibit non-selective responses to all gases. On the contrary, Figure 5.11(b), the pristine $W_{18}O_{49}$-based sensors own higher resistance towards NO_2 gas, but not less towards other gases. Thus, the comparative study, as seen in Figure 5.11(c), clearly distinguished the $W_{18}O_{49}$ nanofibers over WO_3 nanostructure and has been thus selected for further investigation of the sensing performances of its hybrid nanocomposite with different wt% of graphene.

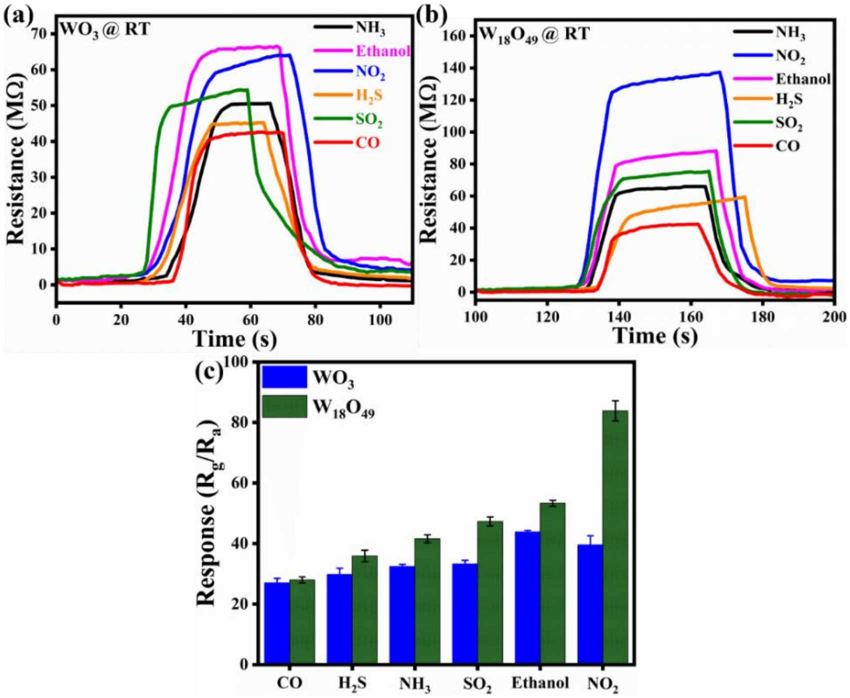

Figure 5.11. Dynamic resistances of pristine (a) WO_3 and (b) $W_{18}O_{49}$-based sensors, and (c) comparative gas responses under 100 ppm of several gases at room temperature.

The influence of different weight ratios of graphene in $W_{18}O_{49}$/Gr nanocomposites for gas sensing performances are presented in Figure 5.12. Figure 5.12(a-f) reflect the dynamic response-recovery characteristics of the $W_{18}O_{49}$/Gr(x)% (x = 0.5, 1.5 & 3 %) sensor devices, when exposed to 100 ppm of the mentioned gases at room temperature. The effect of increased graphene content is also evident in Figure 5.12(a, c, & e), where the R_a value decreased from 1.5 MΩ for pristine $W_{18}O_{49}$ to 1.2 MΩ for $W_{18}O_{49}$/Gr0.5%, Figure 5.12(a), and further to 97 KΩ for $W_{18}O_{49}$/Gr3%, Figure 5.12(e), samples. Moreover, the response to different gases is also affected by the amounts of Gr loading as well as their specific surface area and (O_L, O_V, O_C) contents. The response by pristine $W_{18}O_{49}$-based sensors was ~83.85 under the exposure of NO_2 gas, which was increased to 94.17 for $W_{18}O_{49}$/Gr0.5% sensors (Figure 5.12(b). Meanwhile, the response gets significantly reduced under the exposure of all other gases except NO_2 with the increase in Gr content, enhancing the selectivity of the sensors towards NO_2. The $W_{18}O_{49}$/Gr1.5%-based sensors attained a maximum response value of ~158 when 100 ppm NO_2 gas was injected at room temperature, which was (~6 to ~30) times higher than that of $W_{18}O_{49}$/Gr1.5% exposed under other gases and (~2 to ~4) times higher than that of $W_{18}O_{49}$, $W_{18}O_{49}$/Gr0.5%, & $W_{18}O_{49}$/Gr3% exposed under similar NO_2 gas environment.

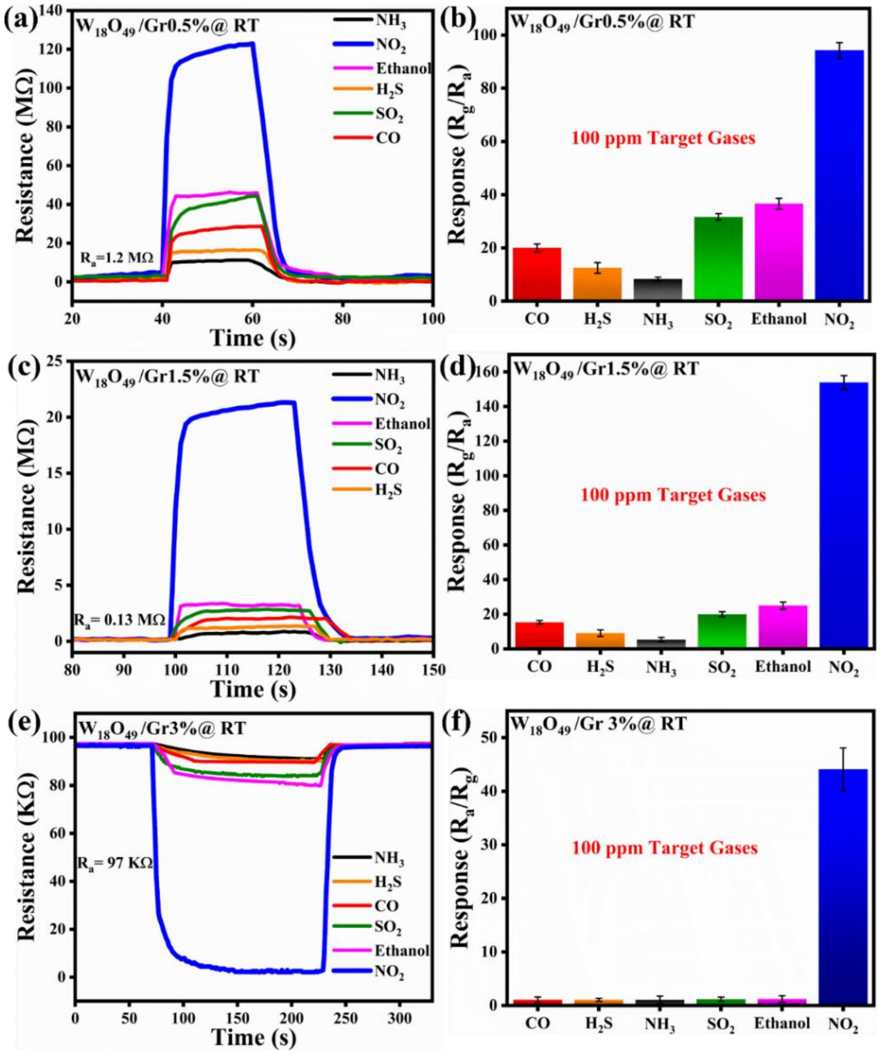

Figure 5.12. Dynamic response-recovery characteristics of (a) & (b) $W_{18}O_{49}$/Gr0.5%, (c) & (d) $W_{18}O_{49}$/Gr1.5%, and (e) & (f) $W_{18}O_{49}$/Gr3%-based sensor devices.

It is noted through Figure 5.12(e) that $W_{18}O_{49}$/Gr3% sensor revealed behavioral change from *n*-type to *p*-type nature due to high graphene content. Although the selectivity of the $W_{18}O_{49}$/Gr sensor ($W_{18}O_{49}$/Gr3%) enhanced dramatically, the gas response value began to reduce instead. This behavior is attributed to the enhanced conductivity of $W_{18}O_{49}$/Gr nanocomposites sensor imparted by the increased Gr content, which effectively suppresses the resistance variation in the $W_{18}O_{49}$/Gr3% embedded structure-based sensor [30,31]. Though the $W_{18}O_{49}$/Gr3% nanocomposite sensor accomplished best selectivity characteristics, the $W_{18}O_{49}$/Gr1.5% nanocomposite sensor reveals the good selectivity with high response value. The high response of $W_{18}O_{49}$/Gr1.5% sensor is also in well agreement with the XPS and BET analysis, least O_L (higher $O_V + O_C$) and highest specific surface area, respectively. Thus, $W_{18}O_{49}$/Gr1.5% nanocomposite sensor has been selected for further investigation of the gas sensing characteristics in this work.

Figure 5.13 demonstrated the dynamic response and recovery characteristics of $W_{18}O_{49}$/Gr1.5%-based sensor toward 100 ppm NO_2 gas and zero air to probe the response time and recovery time. Response time and recovery time are the important parameters of any gas sensing device to know how quick the respective sensor responds. Response time (T_{Res}) measured is the time required for a gas sensor to reach 90% change in resistance from original stable resistance value in the presence of target gas. And, Recovery time (T_{Rec}) is the time needed for the resistance of a gas sensor to return to 90% of its original baseline value after the removal of the target gas. As observed, the $W_{18}O_{49}$/Gr1.5%-based sensor exhibits short response time of 3 s for the 90% change in response and a rapid recovery time of 6 s in 100 ppm NO_2 at room temperature. The rapid response and recovery times inferred the rapid reaction of large number of NO_2 molecules could happen with oxygen species on $W_{18}O_{49}$/Gr1.5% nanocomposites resulting quick increase in resistance and rapid desorption of NO_2 molecules for complete removal process, respectively [32].

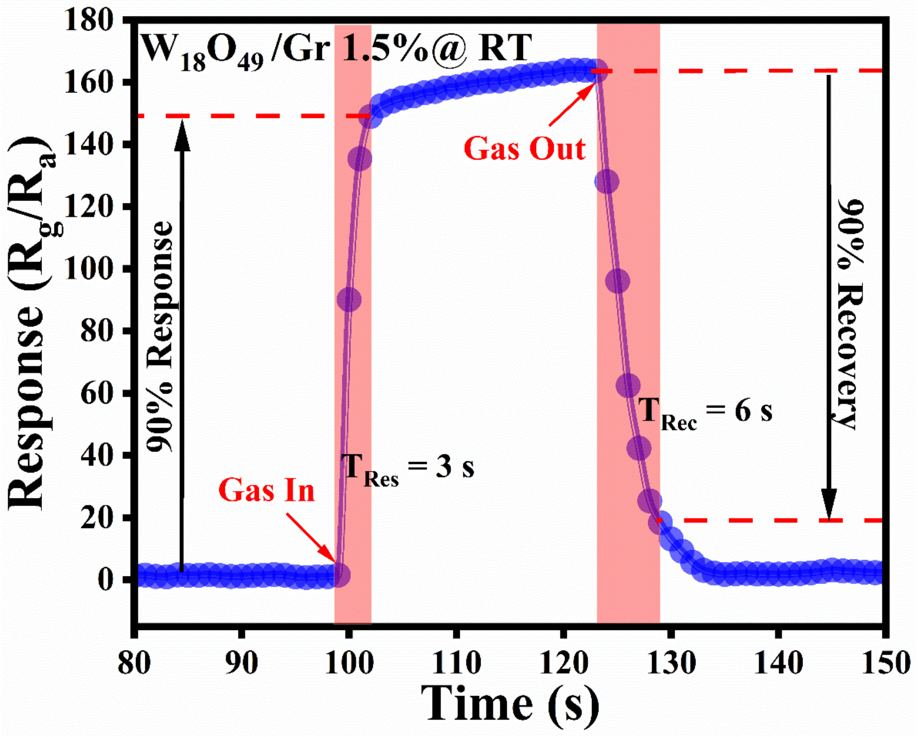

Figure 5.13. The response and recovery times of the optimized $W_{18}O_{49}$/Gr1.5%-based sensor under 100 ppm NO_2 gas concentration at room temperature.

$W_{18}O_{49}$/Gr1.5% hybrid sensors were also evaluated for the sensing performance by monitoring the alterations in resistance value with time when sensors were exposed to different low NO_2 concentrations ranging from 1 ppm to 100 ppm at room temperature. The dynamic responses and corresponding calibration curve of the $W_{18}O_{49}$/Gr1.5% hybrid sensor are illustrated in Figure 5.14(a) and Figure 5.14(b), respectively. The $W_{18}O_{49}$/Gr1.5% hybrid sensor response exhibits a strong linear relationship in the log-log plot with respect to NO_2 concentration. The responses of the $W_{18}O_{49}$/Gr1.5% hybrid sensors at varying NO_2 concentrations of 1, 2.5, 5 10, 20, 35, 50, 75, and 100 ppm are 16.78, 26.15, 36.85, 51.27, 71.01, 94.31, 113.40, 137.90, and 158.18, respectively. This favorable response enables the $W_{18}O_{49}$/Gr1.5% hybrid sensor to achieve a LoD, minimum concentration level at which the sensor response becomes distinctly discernible from the background signal [33], of ~0.3 ppm. The LoD was also calculated by the standard 3-sigma approach using following expression:

$$LoD = 3\,\sigma/m \qquad (5.1)$$

Where, σ is the standard deviation of the least concentration and m is the slope of the calibration curve.

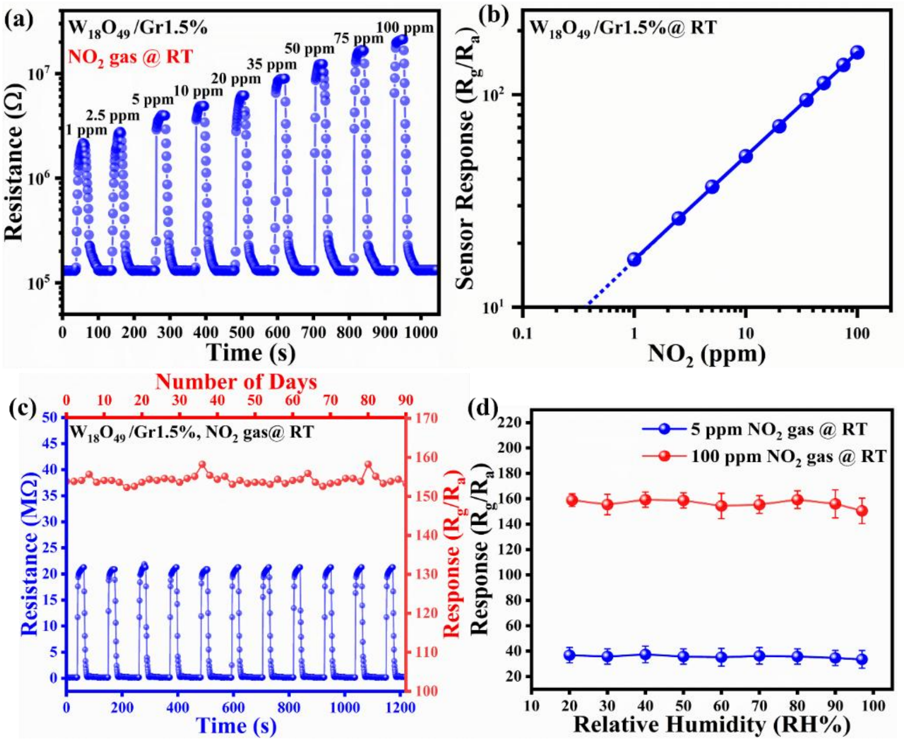

Figure 5.14. (a) Dynamic response towards varying NO_2 concentrations, (b) calibration curve at room temperature, (c) 11 repeated cycles and long-term stability, and (d) responses towards 5 ppm and 100 ppm NO_2 in different relative humidity conditions at room temperature related to optimal $W_{18}O_{49}$/Gr1.5% sensor.

In calibration curve Figure 5.15, the slope (m) of the calibrated curve, σ, and linear regression coefficient were observed as 0.314, 0.025, and 0.992, respectively. Hence, the limit of detection calculated by equation (5.1) is obtained as 0.239 ppm, which is close to the LoD ~0.3 ppm, as obtained in logarithmic calibration Figure 5.14(b).

For the practical realization of the efficacy of sensor device, repeatability, long-term stability and performance under varying humidity conditions are crucial criteria for appraising its performance. The repeatability of the optimal $W_{18}O_{49}$/Gr1.5% nanocomposite-based sensor was conducted for a 11 cycles tests towards 100 ppm NO_2 at room temperature as illustrated in Figure 5.14(c), where m and σ were calculated as 4.991 and 8.30669, respectively.

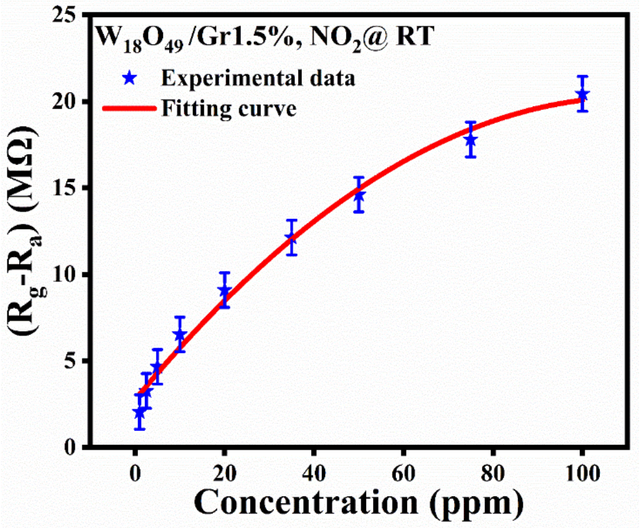

Figure 5.15. Calibration curve and response of the sensor *w.r.t.* NO_2 concentration.

Outcomes indicate that the resistance of the optimized $W_{18}O_{49}$/Gr1.5% nanocomposite-based sensor demonstrates outstanding recovery to its initial baselines (R_a = ~0.13 MΩ) throughout the 11 testing cycles, highlighting its excellent repeatability. The optimized $W_{18}O_{49}$/Gr1.5% nanocomposite-based sensor was then undergoing long-term stability test every alternate day for 3 months under the exposure of 100 ppm NO_2 at room temperature without humidity control. It was observed that the response of the $W_{18}O_{49}$/Gr1.5% nanocomposite-based sensor was not exactly constant as of the initial response value, rather fluctuates within 3% with respect to initial value (m = 154.181, σ = 1.168). Thus, $W_{18}O_{49}$/Gr1.5% nanocomposite-based sensor fabricated in this study exhibits outstanding stability. Figure 5.14(d) elucidates the relationship between response of $W_{18}O_{49}$/Gr1.5% nanocomposite-based sensor and relative humidity (RH) from 20% to 97% under 5 ppm and 100 ppm NO_2

gas environment at room temperature. Under both the low and high NO_2 concentrations, the optimal $W_{18}O_{49}$/Gr1.5% nanocomposite-based sensor maintained its initial response value with the fluctuation within 10%, which demonstrated the reliability of the fabricated sensor even under harsh humid conditions. The stability of $W_{18}O_{49}$/Gr1.5% nanocomposite-based sensor across a wide range of humidity could be attributed to the hydrophobic nature of graphene, which minimizes the impact of water molecules on the sensing surface. Additionally, $W_{18}O_{49}$ nanofibers maintain their interaction with NO_2 despite the presence of moisture, due to their intrinsic properties and the hybrid structure that allows for efficient electron transfer and adsorption. Given the outcomes, it can be thus conclusively stated that the optimized $W_{18}O_{49}$/Gr1.5% nanocomposite-based sensor holds promising potential to detect NO_2 gas at room temperature in practical applications.

Table 5.3 summarizes the gas-sensing performance of previously reported sensors based on WO_3, $W_{18}O_{49}$, and its composites towards NO_2 gas with our present work, $W_{18}O_{49}$/Gr1.5% nanocomposite-based sensor. It is obvious to note that the majority of pristine or hybrid sensors based on WO_x operated at elevated temperatures. In contrast, our proposed $W_{18}O_{49}$/Gr1.5% nanocomposite-based sensor, as tested in this present work, exhibits significantly enhanced selective sensitivity towards NO_2 gas while operating at RT, LoD of ~0.3 ppm, along with rapid response time and recovery time. Moreover, the device’s sensitivity and reliability can further be enhanced through the modification of graphene and $W_{18}O_{49}$ hybrid structure.

Table 5.3. Comparison of NO_2 gas sensors based on tungsten oxide and its composite structure from earlier publications and this work.

Sensing Materials	**Operating temperature (°C)**	**Concentration (ppm)**	**Response**	**Response/Recovery time (s)**	**Ref.**
WO_3/PS	RT	2	3.37	120/1200	[34]
SnO_2/WO_3	RT	200	1.96	110/-	[35]
WO_3 Hollow spheres	RT	0.3	15.1	670/2940	[36]
$W_{18}O_{49}$/CuO core-shell nanorods	50	1	7.4	-	[37]
Plate-like NiO/WO_3	RT	30	4.8	2.5/1.1	[38]
WS_2/ $W_{18}O_{49}$	RT	5	35	77/690	[10]
$W_{18}O_{49}$/Gr1.5%	**RT**	**100**	**~158**	**3/6**	**This work**
		5	**~36.85**	**3/9**	
		1	**~16.78**	**7/9**	

5.3.7 Plausible Gas Sensing Mechanism

The exceptional NO_2 gas-sensing performance of the $W_{18}O_{49}$/Gr1.5% nanocomposite-based sensor can be attributed to several synergistic interactions between $W_{18}O_{49}$ nanofibers and graphene sheets, facilitating efficient gas adsorption, charge transfer, and long-term signal stability even under varying humidity conditions. The high surface area and abundant active sites of $W_{18}O_{49}$ nanofibers promote effective NO_2 adsorption, while the crumpled graphene sheets enhance the dispersion of $W_{18}O_{49}$, preventing agglomeration and increasing the available surface area. Figure 5.16 demonstrates the schematic illustration of the plausible NO_2 sensing mechanism based on the resistance change model attributable to electron transfer while adsorption-desorption process. When the sensor is brought to ambient air atmosphere from vacuum, the oxygen molecules adsorbed onto the surface and ionized to form O_2^- oxygen species at RT (eq. 5.2, 5.3).

$$O_2 \text{ (gas)} \rightarrow O_2 \text{ (ads)} \tag{5.2}$$

$$O_2 \text{ (ads)} + e^- \rightarrow O_2^- \text{ (ads)} \quad (T < 100°C) \tag{5.3}$$

Upon exposure to NO_2, the gas molecules adsorb onto the surface of the $W_{18}O_{49}$ nanofibers and graphene sheets, leading to electron transfer processes that significantly impact the electrical resistance of the composite. $W_{18}O_{49}$ nanofibers, being *n*-type semiconductors, release electrons when NO_2, an oxidizing gas, adsorbs onto their surface. The interaction can be described by following reaction[39] (eq. 5.4-5.7):

$$NO_2 \text{ (gas)} + e^- \rightarrow NO_2^- \text{(ads)} \tag{5.4}$$

This adsorption process depletes electrons from the conduction band of $W_{18}O_{49}$, increasing its resistance. In the presence of graphene, which has a high electron mobility [40] and large surface area, the composite structure facilitates efficient electron transfer and enhances gas adsorption. The graphene sheets act as conductive channels, aiding in the rapid transport of electrons and amplifying the sensor's response to NO_2. Additionally, the high BET specific surface area of $W_{18}O_{49}$/Gr1.5% nanocomposite increases the number of active sites for NO_2 adsorption, while XPS analysis shows that $W_{18}O_{49}$/Gr1.5% has the low concentration of O_L and high (O_V+O_C) content. These characteristics act as additional adsorption sites, further depleting electrons and increasing resistance:

$$NO_2 \text{ (gas)} + O_{Vac} + e^- \rightarrow NO_2^- \text{(ads)} \tag{5.5}$$

$$NO_2 \text{ (gas)} + O_2^- \text{ (ads)} + 2e^- \rightarrow NO_2^- \text{(ads)} + 2O^- \text{ (ads)} \tag{5.6}$$

$$NO_2^- \text{(ads)} + O_2^- + e^- \rightarrow NO_2 \text{ (gas)} + 2O^- \text{ (ads)} \tag{5.7}$$

When the NO_2 gas is removed, *i.e.* $W_{18}O_{49}$/Gr1.5% nanocomposite-based sensor under dry synthetic air, the adsorbed NO_2^-(ads) ions release the captive electrons back to the $W_{18}O_{49}$ nanofibers, leading to a decrease in resistance and a return to the initial state *i.e.* baseline resistance level. The fast recovery is due to the effective desorption of NO_2 from the active sites, aided by high conductivity of graphene which quickly re-establishes the original electron distribution. Owing to above mentioned synergy, $W_{18}O_{49}$/Gr1.5% nanocomposite-based sensor exhibited prominent gas sensing properties.

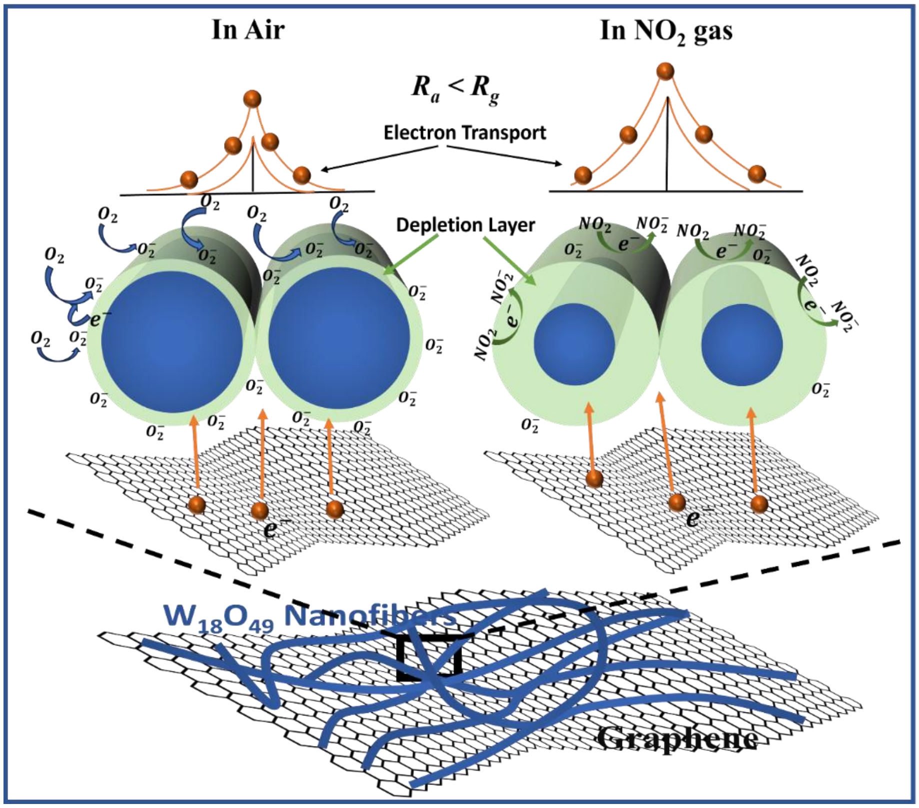

Figure 5.16. Schematic illustration of the plausible gas-sensing mechanism of the $W_{18}O_{49}$/Gr nanocomposite sensor in ambient air and NO_2 gas.

5.4 Conclusions

In summary, the pristine WO_3, $W_{18}O_{49}$ nanofibers, and the $W_{18}O_{49}$/Gr(x%) nanocomposite were successfully synthesized by simple hydrothermal method, where the pH of 1.25 was kept constant for all solution and varied the concentration of precursors. Specifically, in $W_{18}O_{49}$/Gr1.5% nanocomposite, $W_{18}O_{49}$ nanofibers grown on graphene support and formed the self-assembled hierarchical structure, consisting of interlaced nanofibers. The synthesized nanocomposites deposited onto Cu sputtered IDE presents a promising avenue for achieving selective detection of NO_2 gas at room temperature. Through systematics gas-sensing experiments, it has been demonstrated that the optimal $W_{18}O_{49}$/Gr1.5% nanocomposite-based sensor exhibited unparalleled sensitivity (under 100 ppm NO_2, R = ~158, R_a = ~0.13 MΩ, R_g = ~20.5 MΩ) across the broad range of relative humidity from 20% to 97%. The respective sensors established quick response time (3 s) and rapid recovery time (6 s), along with the possible LoD ~0.3 ppm. Moreover, the observed repeatability and stability of the $W_{18}O_{49}$/Gr1.5% nanocomposite sensor response over extended periods (3 months) underscores its viability for long-term monitoring. To encapsulate, the synergistic effects of $W_{18}O_{49}$ nanofibers and graphene, including enhanced surface area, efficient charge transfer, and reduced moisture interference, collectively make the $W_{18}O_{49}$/Gr1.5% nanocomposite a highly effective and reliable sensor for detection of NO_2 in diverse environmental conditions, demonstrating excellent potential for practical applications.

References

[1] V.S. Bhati, A. Kumar, M.O. Valappil, S. Alwarappan, M. Kumar, Phosphorene Oxide Quantum Dots Decorated ZnO Nanostructure-Based Hydrogen Gas Sensor, IEEE Sens J 21 (2021) 7283–7290. https://doi.org/10.1109/JSEN.2020.3046675.

[2] M.K. Tiwari, S.C. Yadav, A. Srivastava, A. Kanwade, J.A.K. Satrughna, S.S. Mali, J. V. Patil, C.K. Hong, P.M. Shirage, Enhancement of CO gas sensing performance by Mn-doped porous ZnSnO3 microspheres, RSC Adv 12 (2022) 32249–32261. https://doi.org/10.1039/d2ra06785d.

[3] M. Zhang, H.C. Su, Y. Rheem, C.M. Hangarter, N. V. Myung, A rapid room-temperature NO_2 sensor based on tellurium-SWNT hybrid nanostructures, Journal of Physical Chemistry C 116 (2012) 20067–20074. https://doi.org/10.1021/jp305393c.

[4] I. Tanyeli, I. Darmadi, M. Sech, C. Tiburski, J. Fritzsche, O. Andersson, C. Langhammer, Nanoplasmonic NO_2 Sensor with a Sub-10 Parts per Billion Limit of Detection in Urban Air, ACS Sens 7 (2022) 1008–1018. https://doi.org/10.1021/acssensors.1c02463.

[5] K.W. Huang, C. Sivakumar, C.H. Wu, C.W. Lee, W.E. Lee, F.Y. Tsai, M.S. Ho, Highly Efficient Room Temperature NO_2 Sensor Using Two-Phase TiO_x Heterogeneous Nanoparticles, ACS Appl Mater Interfaces 16 (2024) 10485–10495. https://doi.org/10.1021/acsami.3c15770.

[6] M.K. Tiwari, S. Chand Yadav, A. Kanwade, J.A. Kumar Satrughna, S.M. Rajore, P.M. Shirage, Advancements in lanthanide-based perovskite oxide semiconductors for gas sensing applications: a focus on doping effects and development, Analytical Methods 15 (2023) 5754–5787. https://doi.org/10.1039/d3ay01420g.

[7] S. Chand Yadav, A. Srivastava, V. Manjunath, A. Kanwade, R.S. Devan, P.M. Shirage, Properties, performance and multidimensional applications of stable lead-free $Cs_2AgBiBr_6$ double perovskite, Materials Today Physics 26 (2022) 100731. https://doi.org/10.1016/j.mtphys.2022.100731.

[8] A. Srivastava, J.A.K. Satrughna, M.K. Tiwari, A. Kanwade, S.C. Yadav, K. Bala, P.M. Shirage, Effect of $Ti_{1-x}Fe_xO_2$ photoanodes on the performance of dye-sensitized solar cells utilizing natural betalain pigments extracted from Beta vulgaris (BV), Energy Advances 2 (2022) 148–160. https://doi.org/10.1039/d2ya00197g.

[9] A.R. Kanwade, A.K.S. Jena, S.M. Rajore, S.S. Mali, J. V. Patil, C.K. Hong, P.M. Shirage, Revealing the potential of graphene-embedded $Na_3Fe_2(PO_4)_3$ for enhanced sodium-ion battery performance, J Mater Sci (2024). https://doi.org/10.1007/s10853-024-09698-y.

[10] M. Manoharan, K. Govindharaj, K. Muthumalai, R. Pandian, Y. Haldorai, R.T. Rajendra Kumar, Highly Selective Room Temperature Detection of NH_3 and NO_x Using Oxygen-Deficient $W_{18}O_{49}$-Supported WS_2 Heterojunctions, ACS Appl Mater Interfaces 15 (2023) 4703–4712. https://doi.org/10.1021/acsami.2c18732.

[11] Y.M. Shirke, S. Porel Mukherjee, Selective synthesis of WO_3 and $W_{18}O_{49}$ nanostructures: ligand-free pH-dependent morphology-controlled self-assembly of hierarchical architectures from 1D

nanostructure and sunlight-driven photocatalytic degradation, CrystEngComm 19 (2017) 2096–2105. https://doi.org/10.1039/c6ce02518h.

[12] C.T. Pan, C.Y. Su, Y.C. Luo, Study on comparing WO_3 and $W_{18}O_{49}$ gas sensing abilities under NO_2 environment, Microsystem Technologies 23 (2017) 2113–2123. https://doi.org/10.1007/s00542-016-3065-2.

[13] W. Yu, Z. Shen, F. Peng, Y. Lu, M. Ge, X. Fu, Y. Sun, X. Chen, N. Dai, Improving gas sensing performance by oxygen vacancies in sub-stoichiometric WO_{3-x}, RSC Adv 9 (2019) 7723–7728. https://doi.org/10.1039/c9ra00116f.

[14] W. Zhang, Y. Fan, T. Yuan, B. Lu, Y. Liu, Z. Li, G. Li, Z. Cheng, J. Xu, Ultrafine Tungsten Oxide Nanowires: Synthesis and Highly Selective Acetone Sensing and Mechanism Analysis, ACS Appl Mater Interfaces 12 (2020) 3755–3763. https://doi.org/10.1021/acsami.9b19706.

[15] Y. Qiu, Y. Wang, C. Song, Facile synthesis of $W_{18}O_{49}$/Graphene nanocomposites for highly sensitive ethanol gas sensors, Colloids Surf A Physicochem Eng Asp 616 (2021). https://doi.org/10.1016/j.colsurfa.2021.126300.

[16] B.R. Wang, R.Z. Wang, L.Y. Liu, C. Wang, Y.F. Zhang, J.B. Sun, WO_3Nanosheet/$W_{18}O_{49}$ Nanowire Composites for NO_2 Sensing, ACS Appl Nano Mater 3 (2020) 5473–5480. https://doi.org/10.1021/acsanm.0c00794.

[17] J. Song, Z. Yu, M.L. Gordin, D. Wang, Advanced Sulfur Cathode Enabled by Highly Crumpled Nitrogen-Doped Graphene Sheets for High-Energy-Density Lithium-Sulfur Batteries, Nano Lett 16 (2016) 864–870. https://doi.org/10.1021/acs.nanolett.5b03217.

[18] Z. Chen, J. Wang, A. Umar, Y. Wang, H. Li, G. Zhou, Three-Dimensional Crumpled Graphene-Based Nanosheets with Ultrahigh NO_2 Gas Sensibility, ACS Appl Mater Interfaces 9 (2017) 11819–11827. https://doi.org/10.1021/acsami.7b01229.

[19] A. Amiri, G. Ahmadi, M. Shanbedi, M. Savari, S.N. Kazi, B.T. Chew, Microwave-Assisted Synthesis of Highly-Crumpled, Few-Layered Graphene and Nitrogen-Doped Graphene for Use as High-

Performance Electrodes in Capacitive Deionization, Sci Rep 5 (2015). https://doi.org/10.1038/srep17503.

[20] F. Yavari, Z. Chen, A. V. Thomas, W. Ren, H.M. Cheng, N. Koratkar, High sensitivity gas detection using a macroscopic three-dimensional graphene foam network, Sci Rep 1 (2011). https://doi.org/10.1038/srep00166.

[21] G. Wang, Y. Yang, D. Han, Y. Li, Oxygen defective metal oxides for energy conversion and storage, Nano Today 13 (2017) 23–39. https://doi.org/10.1016/j.nantod.2017.02.009.

[22] K. Manthiram, A.P. Alivisatos, Tunable localized surface plasmon resonances in tungsten oxide nanocrystals, J Am Chem Soc 134 (2012) 3995–3998. https://doi.org/10.1021/ja211363w.

[23] L. Sinha, H. Lee, Y. Ohshita, P.M. Shirage, Defect Mediated W18O49 Nanorods Bundle for Nonenzymatic Amperometric Glucose Sensing Application, ACS Biomater Sci Eng 6 (2020) 1909–1919. https://doi.org/10.1021/acsbiomaterials.9b01791.

[24] A.M. Smith, M.G. Kast, B.A. Nail, S. Aloni, S.W. Boettcher, A planar-defect-driven growth mechanism of oxygen deficient tungsten oxide nanowires, J Mater Chem A Mater 2 (2014) 6121–6129. https://doi.org/10.1039/c3ta14163b.

[25] M.H. Vu, C.C. Nguyen, T.O. Do, Synergistic Effect of Fe Doping and Plasmonic Au Nanoparticles on $W_{18}O_{49}$ Nanorods for Enhancing Photoelectrochemical Nitrogen Reduction, ACS Sustain Chem Eng 8 (2020) 12321–12330. https://doi.org/10.1021/acssuschemeng.0c04662.

[26] T. Yan, S. Chen, W. Sun, Y. Liu, L. Pan, C. Shi, X. Zhang, Z.F. Huang, J.J. Zou, IrO_2 Nanoparticle-Decorated Ir-Doped $W_{18}O_{49}$ Nanowires with High Mass Specific OER Activity for Proton Exchange Membrane Electrolysis, ACS Appl Mater Interfaces 15 (2023) 6912–6922. https://doi.org/10.1021/acsami.2c20529.

[27] S. Zeb, Y. Cui, H. Zhao, Y. Sui, Z. Yang, Z.U. Khan, S.M. Ahmad, M. Ikram, Y. Gao, X. Jiang, Synergistic Effect of Au-PdO Modified Cu-Doped $K_2W_4O_{13}$ Nanowires for Dual Selectivity High Performance Gas Sensing, ACS Appl Mater Interfaces 14 (2022) 13836–13847. https://doi.org/10.1021/acsami.1c23051.

[28] W. Zhang, Y. Fan, T. Yuan, B. Lu, Y. Liu, Z. Li, G. Li, Z. Cheng, J. Xu, Ultrafine Tungsten Oxide Nanowires: Synthesis and Highly Selective Acetone Sensing and Mechanism Analysis, ACS Appl Mater Interfaces 12 (2020) 3755–3763. https://doi.org/10.1021/acsami.9b19706.

[29] L. Sinha, P.M. Shirage, Surface Oxygen Vacancy Formulated Energy Storage Application: Pseudocapacitor-Battery Trait of $W_{18}O_{49}$ Nanorods, J Electrochem Soc 166 (2019) A3496–A3503. https://doi.org/10.1149/2.1251914jes.

[30] Y. Qiu, Y. Wang, C. Song, Facile synthesis of $W_{18}O_{49}$/Graphene nanocomposites for highly sensitive ethanol gas sensors, Colloids Surf A Physicochem Eng Asp 616 (2021). https://doi.org/10.1016/j.colsurfa.2021.126300.

[31] X. Chang, Q. Zhou, S. Sun, C. Shao, Y. Lei, T. Liu, L. Dong, Y. Yin, Graphene-tungsten oxide nanocomposites with highly enhanced gas-sensing performance, J Alloys Compd 705 (2017) 659–667. https://doi.org/10.1016/j.jallcom.2017.02.197.

[32] D. Jadsadapattarakul, C. Thanachayanont, J. Nukeaw, T. Sooknoi, Improved selectivity, response time and recovery time by [0 1 0] highly preferred-orientation silicalite-1 layer coated on SnO_2 thin film sensor for selective ethylene gas detection, Sens Actuators B Chem 144 (2010) 73–80. https://doi.org/10.1016/j.snb.2009.10.035.

[33] K.W. Huang, C. Sivakumar, C.H. Wu, C.W. Lee, W.E. Lee, F.Y. Tsai, M.S. Ho, Highly Efficient Room Temperature NO_2 Sensor Using Two-Phase TiO_x Heterogeneous Nanoparticles, ACS Appl Mater Interfaces 16 (2024) 10485–10495. https://doi.org/10.1021/acsami.3c15770.

[34] W. Yan, M. Hu, P. Zeng, S. Ma, M. Li, Room temperature NO_2-sensing properties of WO_3 nanoparticles/porous silicon, Appl Surf Sci 292 (2014) 551–555. https://doi.org/10.1016/j.apsusc.2013.11.169.

[35] A.A. Najim, S.S. Shaker, M.A.H. Muhi, Room Temperature NO_2 Gas Sensor Based on SnO_2-WO_3 Thin Films, Plasmonics 12 (2017) 1051–1055. https://doi.org/10.1007/s11468-016-0358-3.

[36] J. Zhao, M. Hu, Y. Liang, Q. Li, X. Zhang, Z. Wang, A room temperature sub-ppm NO2 gas sensor based on WO_3 hollow spheres, New Journal of Chemistry 44 (2020) 5064–5070. https://doi.org/10.1039/c9nj06384f.

[37] Y. Qin, X. Zhang, Y. Liu, W. Xie, Highly aligned array of $W_{18}O_{49}$/CuO core-shell nanorods and its promising NO_2 sensing properties, J Alloys Compd 673 (2016) 364–371. https://doi.org/10.1016/j.jallcom.2016.02.242.

[38] M. Bao, Y. Chen, F. Li, J. Ma, T. Lv, Y. Tang, L. Chen, Z. Xu, T. Wang, Plate-like p-n heterogeneous NiO/WO_3 nanocomposites for high performance room temperature NO_2 sensors, Nanoscale 6 (2014) 4063–4066. https://doi.org/10.1039/c3nr05268k.

[39] S. Zhang, X. Lai, R. Xiao, L. Pang, Z. Lu, X. He, J. Gao, Size-Dependent Response of Hydrothermally Grown SnO_2 for a High-Performance NO_2 Sensor and the Impact of Oxygen, ACS Sens 9 (2024) 195–205. https://doi.org/10.1021/acssensors.3c01825.

[40] A. Kanwade, S. Gupta, A. Kankane, M.K. Tiwari, A. Srivastava, J.A. Kumar Satrughna, S. Chand Yadav, P.M. Shirage, Transition metal oxides as a cathode for indispensable Na-ion batteries, RSC Adv 12 (2022) 23284–23310. https://doi.org/10.1039/d2ra03601k.

Chapter 6

$W_{18}O_{49}$ Nanowires Interlinked Network on FTO for Selective NO_2 Gas Sensing

This chapter introduces the direct growth of WO_3 *and* $W_{18}O_{49}$ *nanowires on patterned fluorine-doped tin oxide (FTO) by a hydrothermal technique, obviating the necessity for traditional IDE designs based on Pt, Ag, Au or Cu. The resulting* $W_{18}O_{49}$ *nanowires network exhibits a distinctive interconnected morphology which facilitates the selective detection of* NO_2 *gas with significantly superior response value, in contrast to* WO_3 *nanowires. The* $W_{18}O_{49}$ *nanowires network further demonstrates quick response and recovery time compared to* WO_3 *nanowires network. In contrast to powdered forms that generate nanowires without interconnectedness, direct growth on patterned FTO results in a robustly networked nanowire structure crucial for enhanced gas sensing performance.*

6.1 Introduction

As discussed in previous chapter, NO_2 is classified among the critical air pollutant having severe hazardous effects on both environment and the human health [1-4]. Despite advancements in sensing technologies, attaining high selectivity and sensitivity for NO_2 in the presence of interfering gases remains a substantial challenge, necessitating the investigation of novel sensing materials and architectures [5–9].

As seen in chapter 5, WO_3 have become prominent contenders for NO_2 gas sensing owing to their chemical stability, elevated surface reactivity, and tunable electrical characteristics. $W_{18}O_{49}$, among its sub-stoichiometric phases [10–12], has garnered significant interest due to its elevated oxygen vacancy density, facilitating efficient adsorption and desorption of gas molecules, a vital factor in enhancing gas-sensing performance. Notwithstanding these inherent benefits, the conventional configuration of WO_3 and $W_{18}O_{49}$-based gas sensors often employ powder-based films or randomly oriented nanostructures. These approaches encountered limitations such as slower response and recovery times, limited charge transport pathways, inefficient gas adsorption because of uneven surface exposure. To overcome these limitations, the design of sophisticated structures with enhanced connectivity and morphology is essential.

Typically, the gas sensors often utilize ceramic tubes/plates or glass as substrates with Au or Pt-based two-point or four-point contacts different IDE pattern printed on it using precise lithography or printing techniques [13–15]. The gas-sensing materials are coated on these prefabricated electrodes by a doctor-blade, screen-printing or drop-coating method, and annealed at an elevated temperature to form the film for gas-sensing. While stable and durable, they come with several drawbacks such as high fabrication cost and complexity of the device [16,17]. Additionally, the deposition of active sensing materials on these IDEs often introduces significant interfacial resistance due to weak adhesion and contact with the sensing material, uneven distribution, and limited electrical conductivity, which can adversely affect sensor performance with reduced sensitivity [18–22].

This study deals with the direct growth of nanostructures on pre-patterned conductive substrates, FTO, representing a transformative approach for enhancing gas sensing performance [23–25]. Through the integration of active sensing material with pre-patterned conductive substrates, this strategy minimizes interfacial losses, promotes efficient charge transport, and enables precise control over nanostructure morphology. In this work, $W_{18}O_{49}$ nanowires grown directly on patterned FTO substrates provide a viable solution. The resulting interconnected morphology of the nanowires, characterized by thin interlinking features, resembles a highly interconnected fibrous network, providing enhanced surface area and efficient electron transport pathways. Such an approach not only enhances the interaction with gas molecules but also accelerates the charge transfer dynamics, leading to improved sensing performance. Comparative studies with powder-based $W_{18}O_{49}$ and WO_3 sensors highlight the critical role of the interconnected network and the direct substrate integration in achieving superior gas-sensing performance. The findings underscore the potential of $W_{18}O_{49}$ networked nanostructures in advancing selective and efficient NO_2 gas sensing, offering a pathway for further innovations in environmental monitoring.

6.2 Experimental

6.2.1 Materials

$Na_2WO_4.2H_2O$; 99.9%; Sisco Research Laboratories Pvt. Ltd., India. Na_2SO_4; 99.9%, K_2SO_4; 99.8%, and Absolute C_2H_5OH (EMSURE, ACS, ISO, absolute for analysis) were procured from Merck KGaA, Germany. Zinc powder (Zn) for etching, HCl (37% w/w), Fluorine-doped tin oxide (FTO; sheet resistance: ~13Ω/sq) were procured from Sigma-Aldrich.

6.2.2 Material Synthesis and Device Fabrication

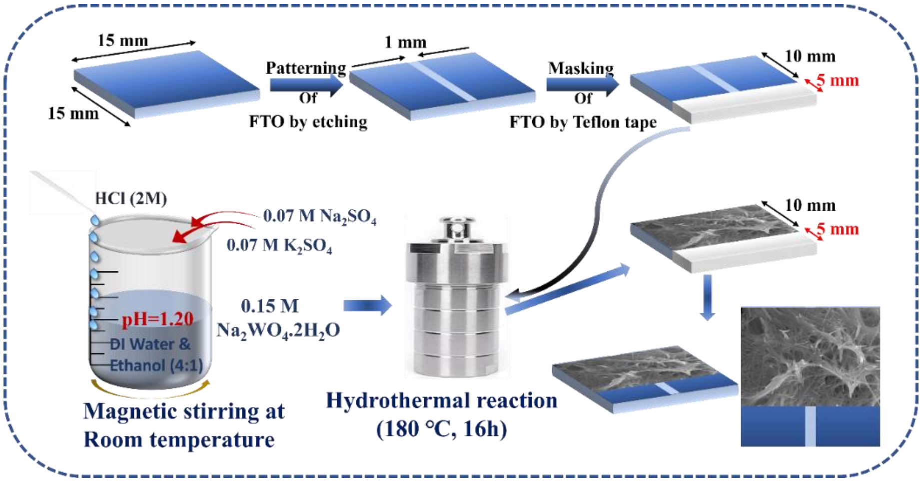

Figure 6.1. Schematic representation of pattern formation and fabrication of $W_{18}O_{49}$ nanowires network on patterned FTO.

First, the pattern for two-point electrical contacts, as shown in Figure 6.1, were formed on FTO substrates using chemical etching with concentrated HCl and Zn powder. The FTO substrates were then cleaned with DI water, ethanol and acetone by ultrasonic treatment. Meanwhile, the precursor solution for the synthesis of $W_{18}O_{49}$ was prepared by dissolving 0.15 M $Na_2WO_4.2H_2O$ into 4:1 mixture of DI water and ethanol. The pH of the solution was then adjusted to 1.20 from 8.7 by adding 2 M HCl dropwise. For $W_{18}O_{49}$, 0.07 M concentrations of both Na_2SO_4 and K_2SO_4 were added, while 0.035 M concentrations of both were added for yielding WO_3. After vigorous stirring, the resulting solution and the patterned FTO substrates were transferred to a Teflon-lined autoclave for hydrothermal treatment at 180 °C for 16 hours. Post synthesis, the substrates were washed with DI water, dried at room temperature and subsequently heat treated at 100 °C for 10 hours to remove organics.

6.3 Results and Discussion

6.3.1 X-ray diffraction Analysis

The crystalline structure and phase purity of the WO_3 and $W_{18}O_{49}$ NWs synthesized on patterned FTO substrates were identified using powder XRD analysis. All the diffraction peaks in the XRD pattern of pristine WO_3

NWs and WO_3 NWs/FTO (Figure 6.2(a)) could only be indexed to the hexagonal phase structure in a space group of *P*6/*mmm* (Ref. file no. 96-100-4058). Likewise, all the diffraction peaks in the XRD pattern of pristine $W_{18}O_{49}$ NWs and $W_{18}O_{49}$ NWs/FTO (Figure 6.2(b)) could only be indexed to the monoclinic phase structure in a space group of *P*12/*m*1 (Ref. file no. 96-152-8167).

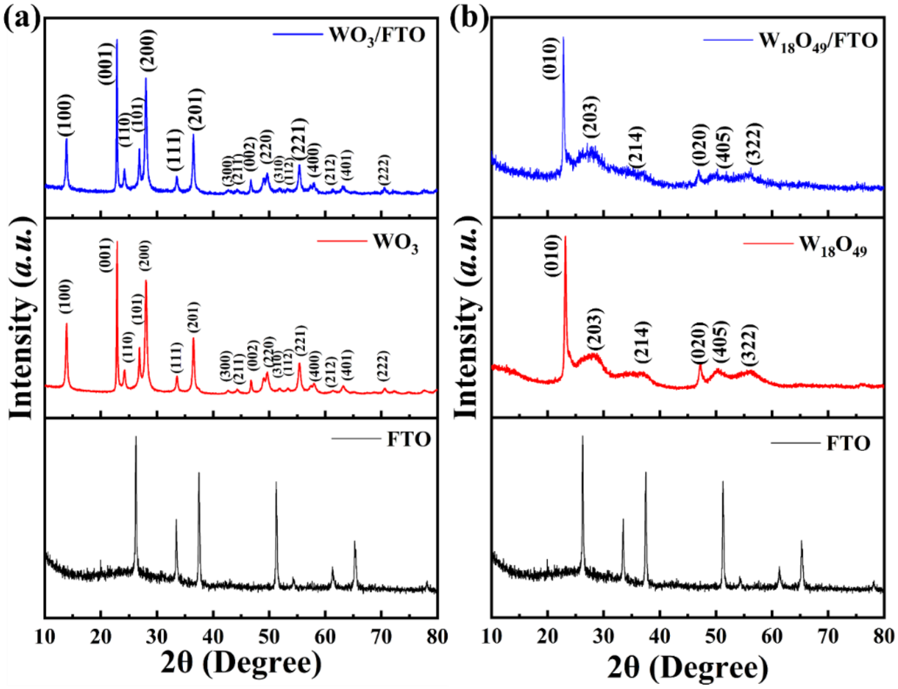

Figure 6.2. XRD patterns of (a) bare FTO, pristine WO_3 powder, and WO_3 NWs grown on FTO hydrothermally, and (b) bare FTO, pristine $W_{18}O_{49}$ powder, and $W_{18}O_{49}$ NWs grown on FTO hydrothermally.

The intensive distinct peak at $2\theta = 23.4^\circ$ correspond to the (010) planes, indicates preferential growth of $W_{18}O_{49}$ NWs along [010] direction. The Rietveld refined XRD patterns of both the WO_3 NWs/FTO and $W_{18}O_{49}$ NWs/FTO samples, calculated using FullProf software, are shown in Figure 6.3 and the obtained lattice parameters are summarized in Table 6.1. Interestingly, no diffraction peaks corresponding to the FTO were observed in the XRD patterns of both WO_3 NWs/FTO and $W_{18}O_{49}$ NWs/FTO, suggesting complete coverage of the substrate by the respective sensing material.

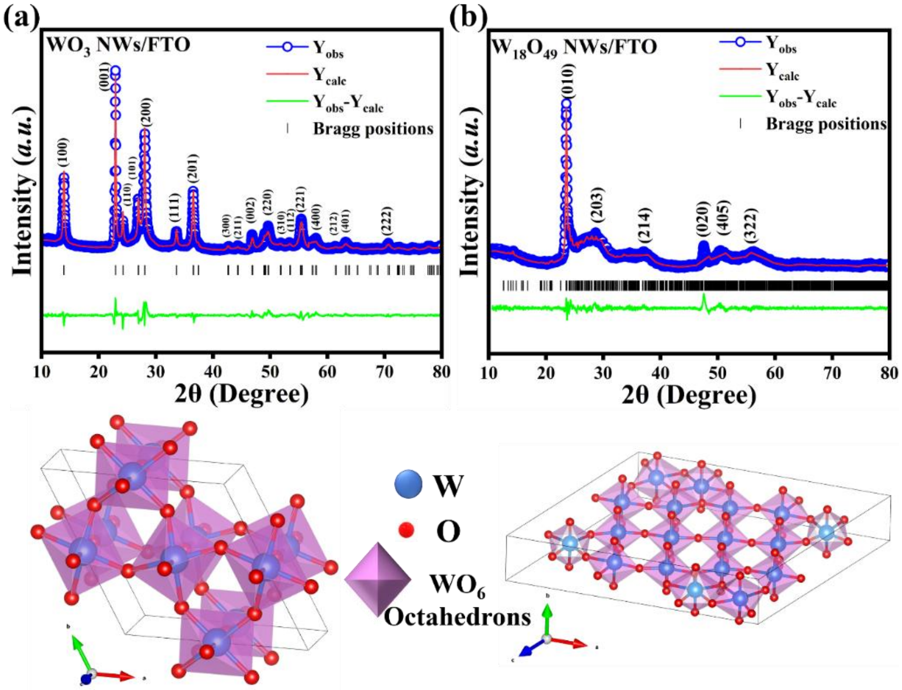

Figure 6.3. Rietveld refined XRD pattern of (a) WO_3 NWs grown on FTO hydrothermally, and (b) $W_{18}O_{49}$ NWs grown on FTO hydrothermally, with their respective crystal structure images.

Table 6.1. **Rietveld refined lattice parameters**

Sample	Crystal structure	Space group	*a* (Å)	*b (Å)*	*c* (Å)	α (deg)	Β (deg)	γ (deg)
WO_3 NWs/FTO	Hexagonal	*P*6/*mmm*	7.344(1)	7.344(1)	3.881(4)	90	90	120
$W_{18}O_{49}$ NWs/FTO	Monoclinic	*P*12/*m*1	18.668(6)	3.859(3)	14.181(8)	90	114.767(7)	90

6.3.2 FE-SEM and HR-TEM Analysis

The morphological characteristics of the WO_3 NWs/FTO and $W_{18}O_{49}$ NWs/FTO samples were investigated using FESEM. Figure 6.5(a-f) reveals the dense and highly interconnected network of WO_3 and $W_{18}O_{49}$ nanowires (Mean diameters of 68 ± 1.53 nm and 31 ± 2.95 nm, respectively) grown directly on patterned FTO substrate, while in the FESEM images of WO_3

and $W_{18}O_{49}$ synthesized without support of FTO, Figure 6.4, show random clustering of nanowires with no interconnectivity.

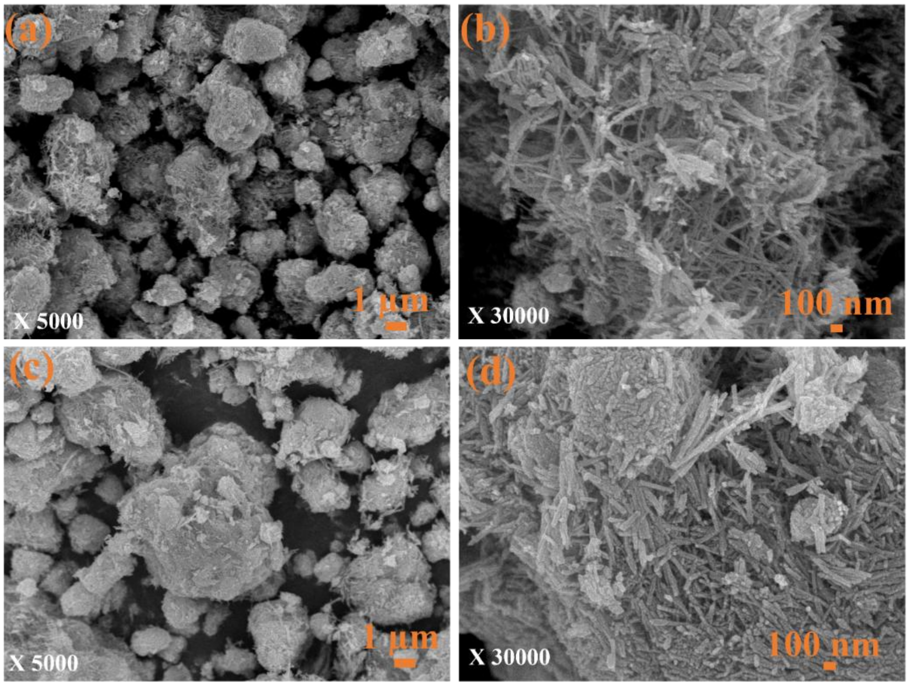

Figure 6.4. FESEM images of (a, b) WO_3 powder, and (c, d) $W_{18}O_{49}$ powder samples synthesized without support of FTO.

These morphological differences underline the importance of FTO substrate. The role of FTO substrate could be particularly significant in enhancing gas-sensing performance. The patterned FTO not only ensures effective electrical contact but also provides a textured surface that influences the growth of nanowires. This results in the unique interlinked uniform nanowires network observed in both WO_3 NWs/FTO and $W_{18}O_{49}$ NWs/FTO samples, which facilitates gas molecule diffusion and adsorption. Additionally, the presence of FTO may suppress undesirable recombination of charge carriers by providing a conductive pathway, enhancing the overall response of the sensors.

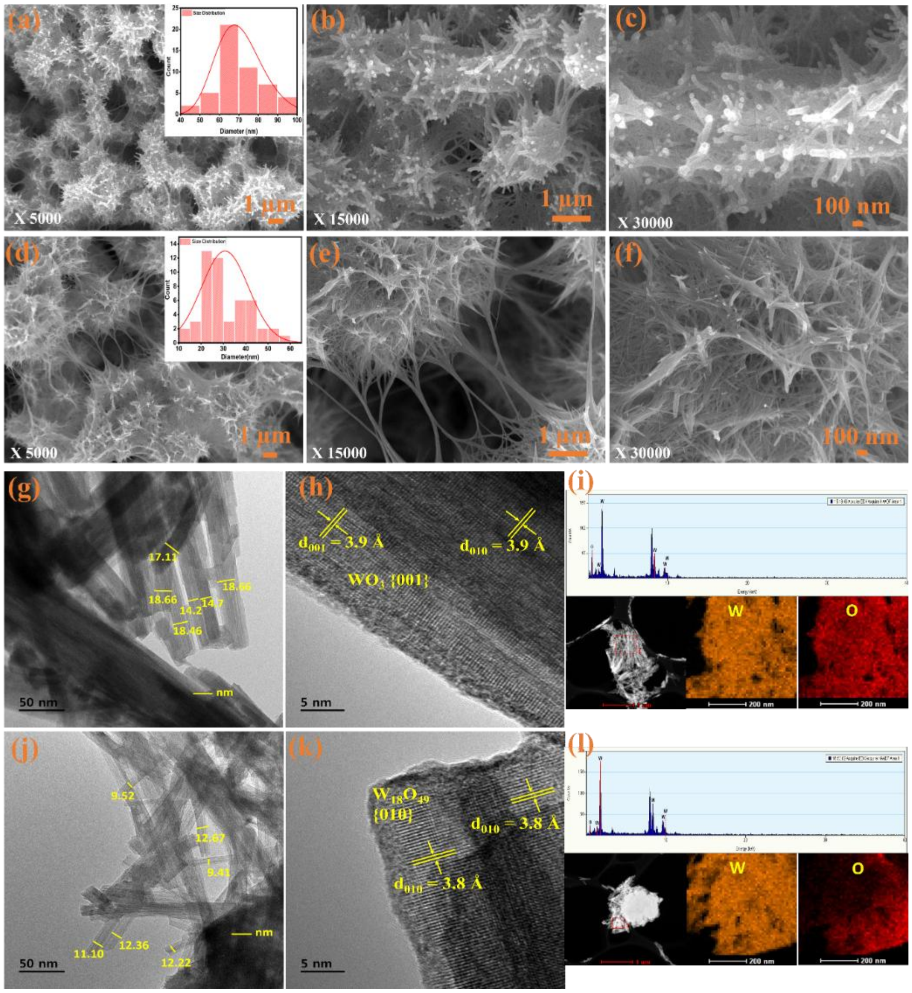

Figure 6.5. FESEM images of (a, b, c) WO_3 NWs/FTO, and (d, e, f) $W_{18}O_{49}$ NWs/FTO at various magnifications. HRTEM and EDS images of (g, h, i) WO_3-based samples, and (j, k, l) $W_{18}O_{49}$-based samples.

The HR-TEM analysis provides deeper insights into the crystallinity and lattice structure of the NWs. A close examination of the TEM images of WO_3 and $W_{18}O_{49}$-based samples (Figure 6.5(g, j)) revealed thinner nanowire diameters of 16.97 ± 2.77 nm and 11.21 ± 1.80 nm, respectively. The HR-TEM images of WO_3 NWs and $W_{18}O_{49}$ NWs (Figure 6.5(h, k)) exhibited a distinct lattice fringe spacing of 3.8 Å and 3.9 Å, respectively, corresponding to the (001) and (010) plane of hexagonal WO_3 and monoclinic $W_{18}O_{49}$, respectively. Furthermore, EDS images revealed stoichiometrically well-distributed W and O on the surface of WO_3 and $W_{18}O_{49}$ NWs (Figure 6.5(i, l)).

6.3.3 X-ray photoelectron spectroscopy Analysis

The XPS analysis was employed to evaluate the surface chemical composition and oxidation states of WO_3 and $W_{18}O_{49}$ nanowires. The Shirley background and C 1*s* line (284.5 eV) were used to calibrate the spectra. The survey spectra, Figure 6.6(a), confirmed the presence of W and O as the primary elements, with no detectable impurities. High-resolution W 4*f* spectra for WO_3-based samples exhibit two characteristic peaks at binding energies of 35.6 eV and 37.7 eV, corresponding to W $4f_{7/2}$ and W $4f_{5/2}$ of the W^{6+} oxidation states, indicative of the stoichiometric WO_3 phase [26,27]. In contrast, W 4f spectrum for $W_{18}O_{49}$-based samples, Figure 6.6(b), is deconvoluted into two additional peaks at 34.3 eV and 36.5 eV, associated with W $4f_{7/2}$ and W $4f_{5/2}$ of the W^{5+} states, confirming the oxygen-deficient nature of the $W_{18}O_{49}$ phase [28]. The O 1*s* spectra, Figure 6.6(c), for both samples were deconvoluted into three distinct peaks: lattice oxygen (O_L, 529.7-529.8 eV), oxygen vacancies (O_V, 530.4-530.6 eV), and chemisorbed oxygen species (O_C, 531.7-531.8 eV). In $W_{18}O_{49}$ NWs/FTO, the proportion of the O_L decreases, while the percentage content of the (O_V + O_C) increases, consistent with the oxygen-deficient nature of the $W_{18}O_{49}$ phase. These findings aligned with $W_{18}O_{49}$ NWs/FTO are critical for enhancing gas-sensing performance by facilitating increased adsorption and reaction of gas molecules on the nanowires surface.

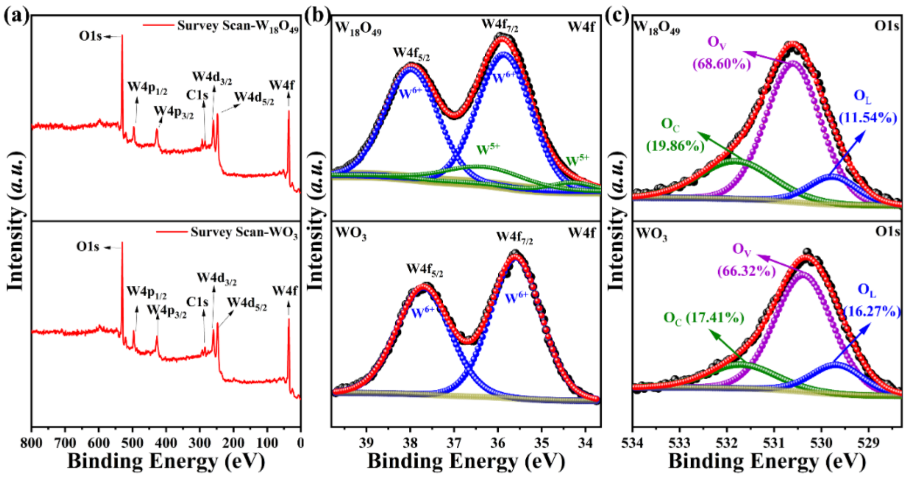

Figure 6.6. XPS spectra of (a) survey scan, (b) W 4*f*, and (c) O 1*s* regions for WO_3 NWs and $W_{18}O_{49}$ NWs.

6.3.4 BET Analysis

Figure 6.7 illustrates the nitrogen adsorption-desorption isotherm profiles for WO_3 and $W_{18}O_{49}$ NWs synthesized without the support of FTO substrates and Figure 6.8 is the isotherm profiles for WO_3 and $W_{18}O_{49}$ NWs prepared with the support of FTO.

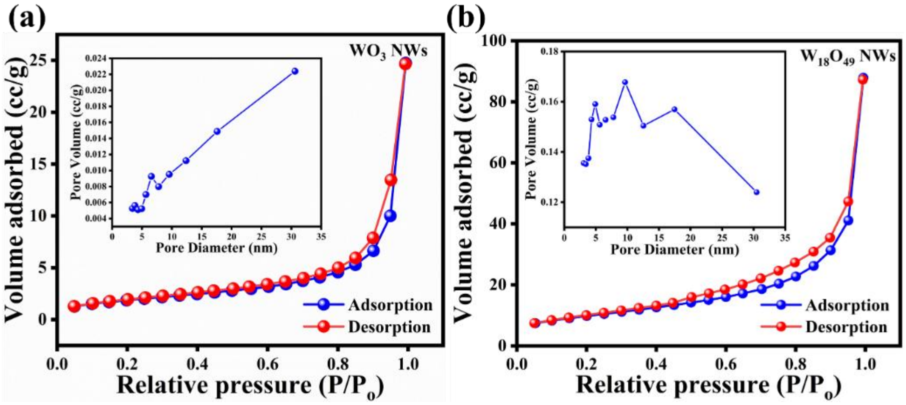

Figure 6.7. Nitrogen adsorption-desorption isotherms for (a) WO_3 NWs, (b) $W_{18}O_{49}$ NWs synthesized without the support of FTO.

The BET surface area, average pore size, and pore volume of the synthesized samples were computed, as summarized in Table 6.2. The $W_{18}O_{49}$ NWs, synthesized without the support of FTO, exhibits a significantly higher specific surface area and larger average pore size compared to WO_3 NWs powder, highlighting the porous and oxygen-deficient structure of $W_{18}O_{49}$. For the NWs grown on FTO substrates, the BET analysis reveals a substantial enhancement in specific surface area for both WO_3 and $W_{18}O_{49}$ NWs, with $W_{18}O_{49}$ NWs/FTO showing a markedly superior surface area and porosity. This increase in surface area for $W_{18}O_{49}$ NWs/FTO samples can be attributed to their highly interconnected architecture with the reduced NWs' diameter significantly, as well as the presence of structural defects such as increased O_C and O_V, which contribute to the formation of additional active sites. It can be inferred that the $W_{18}O_{49}$

NWs/FTO-based sensor device, that exhibits highest surface area of 104.273 ± 0.008 m^2/g with mesoporosity, prompted to have enhanced surface reactivity and adsorption capacity, key factors for improving gas-sensing performance.

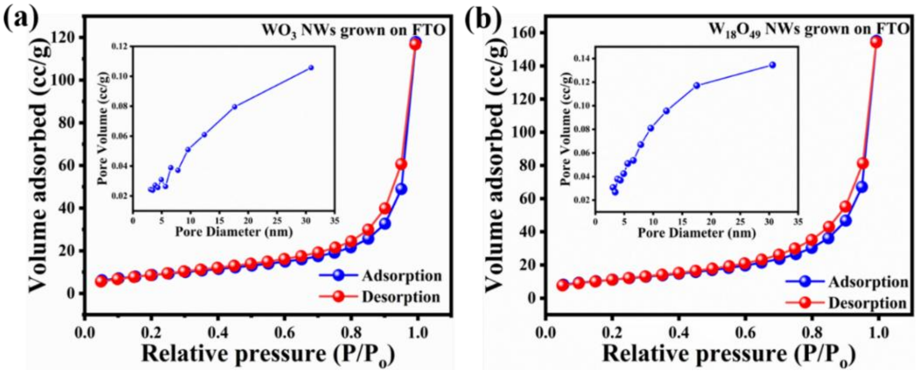

Figure 6.8. Nitrogen adsorption-desorption isotherms for (a) WO_3 NWs, (b) $W_{18}O_{49}$ NWs synthesized with the support of FTO.

Table 6.2. BET specific surface area, average pore size and pore volume calculation.

Samples	Specific Surface Area (m^2/g)	Average Pore Size (nm)	Pore Volume (cc/g)
WO_3	6.818 ± 0.004	3.406 ± 0.001	0.034 ± 0.002
$W_{18}O_{49}$	40.133 ± 0.002	5.422 ± 0.009	0.240 ± 0.006
WO_3 NWs/FTO	31.318 ± 0.005	3.238 ± 0.004	0.182 ± 0.007
$W_{18}O_{49}$ NWs/FTO	**104.273 ± 0.008**	**5.344 ± 0.005**	**0.241 ± 0.005**

6.3.5 Gas Sensing Analysis

The gas-sensing performance of the WO_3 NWs/FTO and $W_{18}O_{49}$ NWs/FTO sensors was systematically examined by positioning the sensors in a calibrated gas-sensing set-up. The investigation began with an electrical characterization *I-V* measurements over a DC bias voltage range of -5 V to +5 V to confirm the electrical connectivity and stability of the fabricated devices. The linear *I-V* characteristics, as shown in Figure 6.9(a), indicates the formation of stable ohmic contacts between the nanowires-based sensing materials and the FTO electrodes, ensures consistent resistance-based measurements. Following the *I-V* characterization, the gas-sensing performance of the sensors were observed under the exposure of several calibrated test gases (CO_2, ethanol, CO, NH_3, NO_2), commercially purchased.

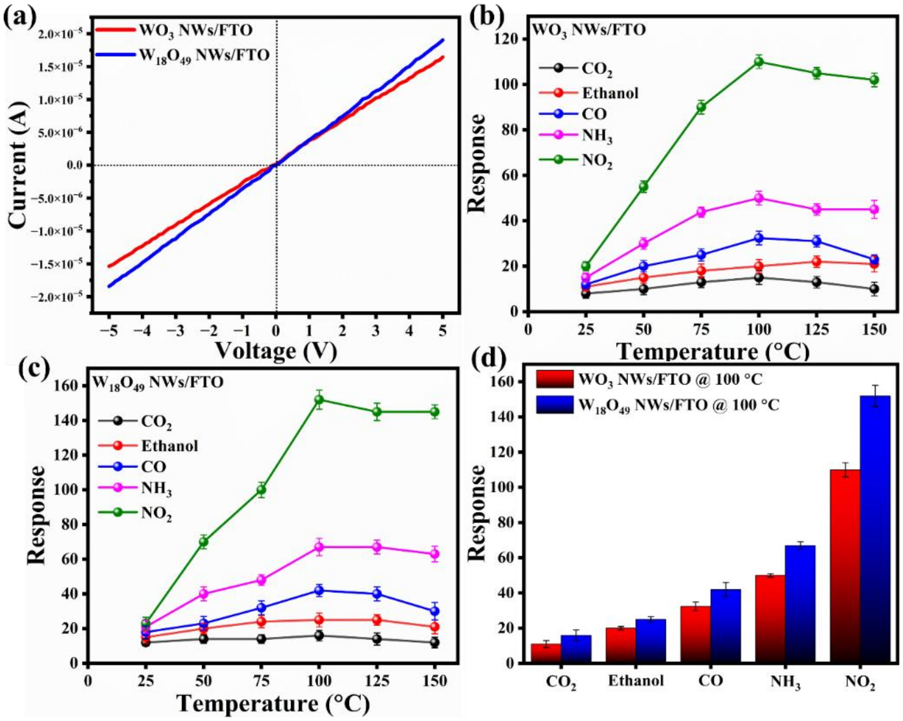

Figure 6.9. (a) Current-Voltage (*I-V*) analysis of WO_3 NWs/FTO and $W_{18}O_{49}$ NWs/FTO sensors; Response of (b) WO_3 NWs/FTO and (c) $W_{18}O_{49}$ NWs/FTO sensors toward 100 ppm analyte gases at 25-150 °C; (d) Cross-selectivity comparative analysis of the WO_3 NWs/FTO and $W_{18}O_{49}$ NWs/FTO sensors.

The responses of the WO_3 NWs/FTO and $W_{18}O_{49}$ NWs/FTO sensors to 100 ppm test gases were first investigated across a temperature range of RT-250 °C (Figure 6.9(b), Figure 6.9(c)), and the operating temperature and cross-selectivity were probed. The sensors exhibited *n*-type sensing behavior, in which the resistance increases upon exposure to oxidizing gas (NO_2) and decreases upon exposure to reducing gas (CO, NH_3, CO_2, ethanol), and returns to its initial resistance in the presence of air. Both the sensors demonstrated maximum response to NO_2 gas and at 100 °C, a temperature at which the adsorption-desorption kinetics of NO_2 molecules are most favorable.

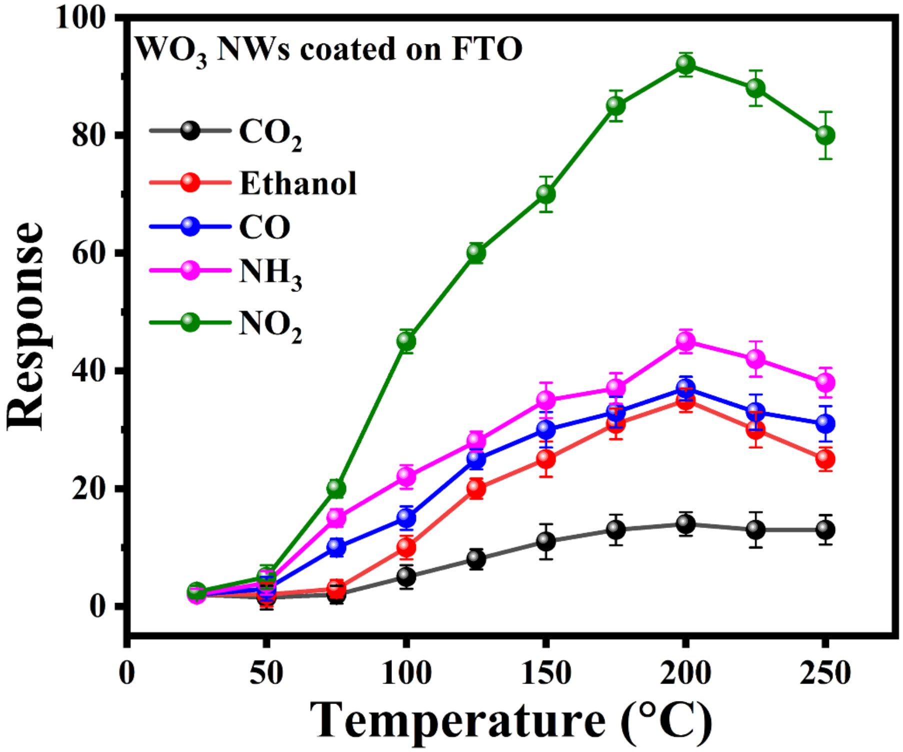

Figure 6.10. Response of WO_3 NWs coated on FTO, by doctor-blade coating method, toward 100 ppm analyte gases at 25-250 °C.

The lower operating temperature for these sensors, as compared to the WO_3 NWs coated on patterned FTO using doctor-blade coating method by forming paste (Operating temperature = 200 °C, Figure 6.10), can be attributed to the direct growth of NWs on FTO via hydrothermal synthesis. This enhances the interface between the sensing materials and the substrate, allowing for better charge transport and efficient gas molecule interaction, thereby reducing the energy requirements for sensor activation.

As shown in Figure 6.9(d), the cross-selectivity of both the sensors were illustrated by comparing the responses of both the WO_3 NWs/FTO and $W_{18}O_{49}$ NWs/FTO sensors towards 100 ppm interfering gases at operating temperature. The $W_{18}O_{49}$ NWs/FTO sensor shows the highest response of ~152 for 100 ppm NO_2, outperforming the WO_3 NWs/FTO sensor (R ~

110). The selectivity factors of the WO_3 NWs/FTO sensor for 100 ppm NO_2 were calculated to be R_{NO2}/R_{CO2} = 7.3, $R_{NO2}/R_{Ethanol}$ = 5.5, R_{NO2}/R_{CO} = 3.4, and R_{NO2}/R_{NH3} = 2.2. The selectivity factors of the $W_{18}O_{49}$ NWs/FTO sensor for 100 ppm NO_2 were calculated to be R_{NO2}/R_{CO2} = 9.5, $R_{NO2}/R_{Ethanol}$ = 6.1, R_{NO2}/R_{CO} = 3.6, and R_{NO2}/R_{NH3} = 2.3. Thus, it is evident that both the sensors exhibit significantly higher response to NO_2 compared to other interfering gases, and $W_{18}O_{49}$ NWs/FTO sensor exhibits 1.38 times improved gas-sensing performance compared to WO_3 NWs/FTO sensor.

Afterward, the dynamic gas-sensing response between the WO_3 NWs/FTO and $W_{18}O_{49}$ NWs/FTO sensors were compared at varying concentration of NO_2 gas ranging from 1 ppm to 500 ppm at the optimized operating temperature of 100 °C (Figure 6.11(a)). With the increase in NO_2 gas concentrations from 1 ppm to 500 ppm, the response values of WO_3 NWs/FTO and $W_{18}O_{49}$ NWs/FTO sensors increase from 12.22 to 142.71 and 18 to 216.40, respectively. The graph reveals a clear and systematic linear increase in response of both sensors with increasing NO_2 concentration. Notably, the $W_{18}O_{49}$ NWs/FTO sensor exhibits a superior response even at low concentrations, achieving R of ~18 at 1 ppm NO_2. The theoretical LoD for $W_{18}O_{49}$ NWs/FTO sensor was found to be 3 ppb, whereas for WO_3 NWs/FTO sensor, the LoD was found to be 9 ppb (Figure 6.11(b)). Both the sensors exhibit excellent reversibility behavior after each cycle, as evidenced by their complete recovery at all concentrations. Next, as shown in Figure 6.11(c), the dynamic response (T_{Res}) and recovery (T_{Rec}) times of both the sensors were also accessed for the 90% change in response during analyte gas adsorption and desorption, respectively. The transient profile of $W_{18}O_{49}$ NWs/FTO sensor towards 100 ppm NO_2 exposure at 100 °C demonstrates a rapid response time of 9 s and recovery time of 20 s, markedly faster than the corresponding values of 24 s and 31 s observed for the WO_3 NWs/FTO sensor. Consequently, the $W_{18}O_{49}$ NWs/FTO sensor consistently outperforms the WO_3 NWs/FTO sensor, exhibiting significantly higher responses at all concentrations of NO_2, impressive LoD, and remarkable quicker response and recovery time. This enhanced gas-sensing characteristics of the $W_{18}O_{49}$ NWs/FTO sensor reflects the critical influence of the unique $W_{18}O_{49}$ nanowires interlinked network, which provides efficient gas diffusion pathways and accelerate the adsorption-desorption kinetics. Additionally, the higher density of oxygen vacancies and chemisorbed oxygen species, significantly larger surface area and pore volume of $W_{18}O_{49}$ NWs over WO_3 NWs amplify its gas-sensing response by providing abundant active adsorption and interaction sites for analyte molecules.

To further validate the practical applicability of the $W_{18}O_{49}$ NWs/FTO sensor, the gas-sensing characteristics such as repeatability, long-term stability and performance under relative humidity, were assessed at 5 ppm NO_2, a concentration closer to real-world exposure levels in environment and industrial scenarios. The repeatability performance, conducted over 15 consecutive cycles as shown in Figure 6.11(d), demonstrated consistent sensor responses with negligible deviation, confirming the excellent reproducibility of the device. The long-term stability test of the $W_{18}O_{49}$ NWs/FTO sensors was assessed by monitoring its response values over a period of 60 days, every fifth day, towards 5 and 100 ppm NO_2 at 100 ℃ (Figure 6.11(e)). The sensor maintained its initial response (43.66 and 152, respectively) without any noticeable change, indicating its exceptional long-term stability, an essential characteristic for practical deployment.

Further, the influence of RH on NO_2-sensing performance was investigated at different RH levels of 47%, 75%, 87%, and 97.5% for three identical $W_{18}O_{49}$ NWs/FTO sensors (Sample A, B, and C), developed under identical conditions, maintaining consistent synthesis process and the analysis environments for gas-sensing performance, Figure 6.11(f). All the three sensors exhibited a response of 43.66 at 47% RH, with a negligible mean deviation in the performance, which showed a gradual decline to 43.2, 40, and 35 at 75%, 87%, and 97.5% RH, respectively. This decline can be attributed to the competitive adsorption of water molecules at higher RH levels, which partially obstruct active sites for NO_2 interaction. Despite this, the sensor maintained robust performance under high RH conditions, indicating its potential for real-world applications where humidity fluctuations are inevitable.

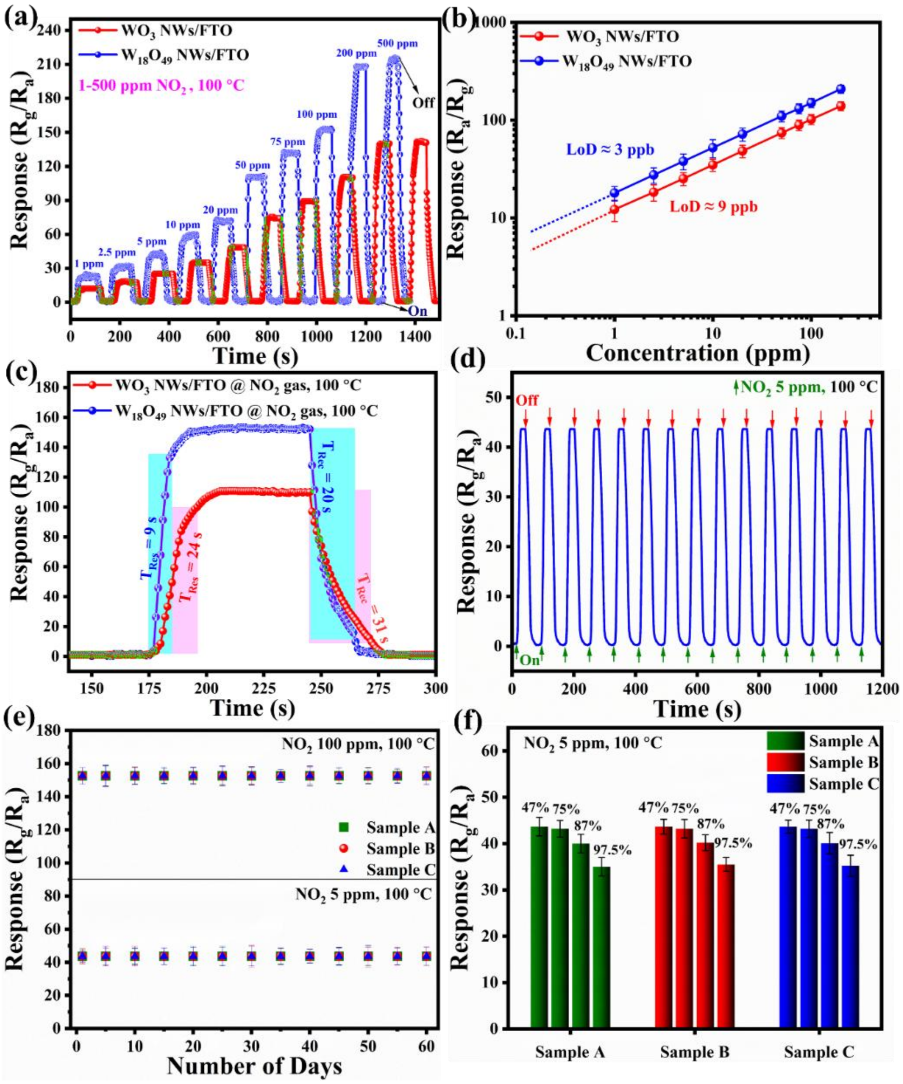

Figure 6.11. (a) Dynamic response for WO_3 NWs/FTO and $W_{18}O_{49}$ NWs/FTO sensors towards varying concentrations of NO_2 (1-500 ppm); (b) Calibration curve of WO_3 NWs/FTO and $W_{18}O_{49}$ NWs/FTO sensors for relation between response and NO_2 concentration (1-200 ppm); (c) Transient performance of the WO_3 NWs/FTO and $W_{18}O_{49}$ NWs/FTO sensors; (d) Repeatability of the $W_{18}O_{49}$ NWs/FTO sensor for 15 consecutive cycles; (e) Stability of the $W_{18}O_{49}$ NWs/FTO sensors over a

period of two months; (f) Performance of the three identical $W_{18}O_{49}$ NWs/FTO sensors under different RH levels.

Finally, the gas-sensing performance of $W_{18}O_{49}$ NWs/FTO sensor was compared with the previously reported sensing materials for the sensing of NO_2 gas. Table 6.3 clearly evidenced that $W_{18}O_{49}$ NWs/FTO sensor exhibits a considerably high response and is a highly effective sensing device for the selective detection of NO_2, with a rapid response/recovery time.

Table 6.3. Comparison of NO_2 gas sensors based on pristine WO_3 and $W_{18}O_{49}$ nanostructures synthesized by different technique.

Sensing Materials	**Operating Temperature (°C)**	**Concentration (ppm)**	**Response**	**T_{Res}/T_{Rec} (sec)**	**Ref.**
$W_{18}O_{49}$ nanowires	150	2.5	10.2	78/32	[29]
WO_3 nanofibers	200	1	12.52	11/26	[30]
WO_3 nanoflowers	200	1 (100)	6.78 (55.9)	(13/17)	[31]
WO_3 nanosheets	150	50	38	82/325	[32]
WO_3 3-D microflowers	150	100	55.5	9/225	[33]
WO_3 NWs/FTO	**100**	**100**	**110**	**24/31**	**This Work**
$W_{18}O_{49}$ NWs/FTO	**100**	**100**	**152**	**9/20**	**This Work**
		5	**43.66**	**7/19**	
		1	**18**		

6.3.6 Plausible Gas Sensing Mechanism

Figure 6.12 illustrates the plausible gas-sensing mechanism of the $W_{18}O_{49}$ NWs/FTO sensor, involving surface related redox reaction by the depletion region variation The gas-sensing mechanism of $W_{18}O_{49}$ nanowires grown on patterned FTO is governed by surface reactions and charge carrier modulation, facilitated by the unique properties of the nanowires and the conductive substrate. As an *n*-type semiconductor, $W_{18}O_{49}$ NWs primarily rely on the interaction of adsorbed gas molecules with free electrons in their conduction band. The gas-sensing process initiates with the adsorption of oxygen molecules from ambient air onto the $W_{18}O_{49}$ NWs surface at elevated temperatures. These oxygen molecules extract electrons from the conduction band of $W_{18}O_{49}$, forming negatively charged oxygen species, O_2^-, O^-, or O^{2-}, as described by the following equations:

$$O_2\,(g) \rightarrow O_2\,(ads) \qquad (6.1)$$

$$O_2\,(ads) + e^- \rightarrow O_2^-\,(ads) \quad (T < 150°C) \qquad (6.2)$$

$$O_2^-\,(ads) + e^- \rightarrow 2O^-\,(ads) \quad (150\,°C < T < 300\,°C) \qquad (6.3)$$

The formation of these oxygen species creates a depletion region near the surface of the NWs, reducing the electron density in the conduction band and increasing the material’s resistance. This behavior is characteristic of *n*-type semiconductors, where electron withdrawal decreases the overall conductivity.

Upon exposure to NO_2 gas, which is a strong oxidizing agent, NO_2 molecules interact with the adsorbed oxygen species or directly with the surface of the nanowires. These interactions further extract electrons from the conduction band, enhancing the surface depletion region and causing a significant increase in resistance.

$$NO_2\,(g) + e^- \rightarrow NO_2^-(ads) \qquad (6.4)$$

$$NO_2\,(g) + O^-\,(ads) \rightarrow NO_3^-(ads) \qquad (6.5)$$

The high density of O_V and O_C in $W_{18}O_{49}$ NWs play a crucial role in enhancing gas-sensing performance. These vacancies act as active sites for gas adsorption, improving the interaction with oxygen and NO_2 molecules. As a result, $W_{18}O_{49}$ NWs exhibit superior sensitivity and faster response compared to WO_3 NWs.

During the recovery phase, when the sensor is exposed to a clean-air environment, the adsorbed NO_2 molecules desorb from the surface, and the electron density is restored. This process can be expressed as:

$$NO_2^-(ads) \rightarrow NO_2\,(g) + e^- \qquad (6.6)$$

$$NO_3^-(ads) \rightarrow NO_2\,(g) + O^-\,(ads) \qquad (6.7)$$

The patterned FTO substrate plays a critical role in enhancing the sensing performance. It provides a highly conductive platform that facilitates efficient electron transport, minimizing interfacial resistance and improving the sensor's signal-to-noise ratio. Furthermore, the direct growth of NWs on FTO creates a porous, interconnected network structure that accelerates gas diffusion and surface reactions. This unique architecture also ensures consistent electrical contact and stability over repeated cycles.

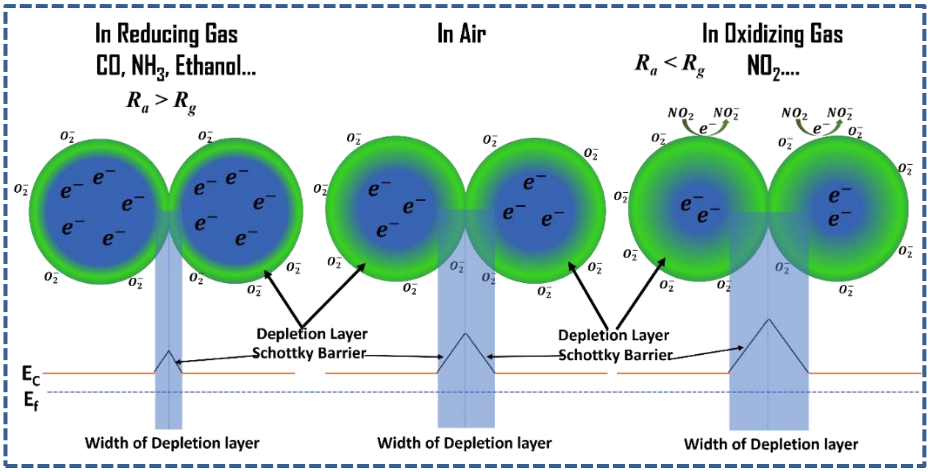

Figure 6.12. Plausible gas-sensing mechanism of $W_{18}O_{49}$ NWs/FTO sensor towards oxidizing and reducing gases.

6.4 Conclusions

In summary, the interlinked $W_{18}O_{49}$ nanowires network grown directly on patterned FTO substrates *via* a hydrothermal technique has been illustrated as a highly effective architecture for selective NO_2 gas sensing.

The $W_{18}O_{49}$ NWs/FTO sensor exhibited superior gas-sensing performance compared to WO_3-based counterparts, with a high response of 152 toward 100 ppm NO_2, 43.66 toward 5 ppm NO_2, at an optimized operating temperature of 100 ℃. The enhanced sensitivity, ultra-low limit of detection (3 ppb), and ultra-fast response-recovery time (9 s and 20 s, respectively) of the $W_{18}O_{49}$ NWs/FTO sensor are attributed to its high surface area, interconnected nanowire network, and increased content of oxygen vacancies and chemisorbed species, which facilitate efficient gas adsorption and charge transfer. The sensor's reliability was further validated through repeatability, long-term stability, and tolerance to different humidity levels, indicating its robustness for practical applications. Its ability to operate effectively at low NO_2 concentration and under humid conditions underscores its potential for environmental monitoring and industrial safety applications. The strategy illustrated in this work would benefit the way for design and preparation of similar architectures in next-generation gas-sensing technologies.

References

[1] N. Ha, K. Xu, Y. Cheng, R. Ou, Q. Ma, Y. Hu, V. Trinh, G. Ren, J. Zhang, J.Z. Ou, A Room Temperature High-Performance Visible-Light-Assisted NO_2 Gas Sensor Based on Ultrathin Zinc Oxysulfide, Advanced Sensor Research 3 (2024). https://doi.org/10.1002/adsr.202300007.

[2] X. Su, Z. Zhong, X. Yan, T. Zhang, C. Wang, Y.X. Wang, G. Xu, L. Chen, Facile Synthesis of Metallosalphen-Based 2D Conductive Metal-Organic Frameworks for NO_2 Sensing: Metal Coordination Induced Planarization, Angewandte Chemie - International Edition 62 (2023). https://doi.org/10.1002/anie.202302645.

[3] M.K. Tiwari, S. Chand Yadav, A. Kanwade, J.A. Kumar Satrughna, S.M. Rajore, P.M. Shirage, Advancements in lanthanide-based perovskite oxide semiconductors for gas sensing applications: a focus on doping effects and development, Analytical Methods 15 (2023) 5754–5787. https://doi.org/10.1039/d3ay01420g.

[4] Y. Gao, J. Wang, Y. Feng, N. Cao, H. Li, N.F. de Rooij, A. Umar, P.J. French, Y. Wang, G. Zhou, Carbon-Iron Electron Transport Channels in Porphyrin–Graphene Complex for ppb-Level Room Temperature NO Gas Sensing, Small 18 (2022). https://doi.org/10.1002/smll.202103259.

[5] J. Lee, H. Lee, T.H. Bae, D. Cho, M. Choi, G. Bae, Y.S. Shim, S. Jeon, 3D ZnO/ZIF-8 Hierarchical Nanostructure for Sensitive and Selective NO_2 Sensing at Room Temperature, Small Struct 5 (2024). https://doi.org/10.1002/sstr.202300503.

[6] M.K. Tiwari, A. Kanwade, S.C. Yadav, A. Srivastava, J.A.K. Satrughna, P.M. Shirage, NASICON-type $Na_3Fe_2(PO_4)_3$ material for an excellent room temperature CO sensor, J Mater Chem C Mater 11 (2023) 5469–5480. https://doi.org/10.1039/d3tc00300k.

[7] K.W. Huang, C. Sivakumar, C.H. Wu, C.W. Lee, W.E. Lee, F.Y. Tsai, M.S. Ho, Highly Efficient Room Temperature NO_2 Sensor Using Two-Phase TiO_x Heterogeneous Nanoparticles, ACS Appl Mater Interfaces 16 (2024) 10485–10495. https://doi.org/10.1021/acsami.3c15770.

[8] M.K. Tiwari, S.C. Yadav, A. Srivastava, A. Kanwade, J.A.K. Satrughna, S.S. Mali, J. V. Patil, C.K. Hong, P.M. Shirage, Enhancement of CO gas sensing performance by Mn-doped porous $ZnSnO_3$ microspheres, RSC Adv 12 (2022) 32249–32261. https://doi.org/10.1039/d2ra06785d.

[9] I. Tanyeli, I. Darmadi, M. Sech, C. Tiburski, J. Fritzsche, O. Andersson, C. Langhammer, Nanoplasmonic NO_2 Sensor with a Sub-10 Parts per Billion Limit of Detection in Urban Air, ACS Sens 7 (2022) 1008–1018. https://doi.org/10.1021/acssensors.1c02463.

[10] L. Sinha, H. Lee, Y. Ohshita, P.M. Shirage, Defect Mediated $W_{18}O_{49}$ Nanorods Bundle for Nonenzymatic Amperometric Glucose Sensing Application, ACS Biomater Sci Eng 6 (2020) 1909–1919. https://doi.org/10.1021/acsbiomaterials.9b01791.

[11] Lichchhavi, H. Lee, Y. Ohshita, A.K. Singh, P.M. Shirage, Transformation of Battery to High Performance Pseudocapacitor by the Hybridization of $W_{18}O_{49}$ with RuO_2 Nanostructures, Langmuir 37 (2021) 1141–1151. https://doi.org/10.1021/acs.langmuir.0c03056.

[12] M.K. Tiwari, A.R. Kanwade, S.M. Rajore, J.A.K. Satrughna, Y. Ito, H. Lee, Y. Ohshita, A. Ogura, S.S. Mali, J. V. Patil, C.K. Hong, P.M. Shirage, $W_{18}O_{49}$ Nanofibers Functionalized with Graphene as a Selective Sensing of NO_2 Gas at Room Temperature, ACS Appl Mater Interfaces (2024). https://doi.org/10.1021/acsami.4c10014.

[13] Y. Lu, M. Meyyappan, J. Li, Trace detection of hydrogen peroxide vapor using a carbon-nanotube-based chemical sensor, Small 7 (2011) 1714–1718. https://doi.org/10.1002/smll.201100406.

[14] Z. Zhang, T. Lu, D. Yang, S. Lu, R. Cai, W. Tan, A Dual-Function Sensor for Highly Sensitive Detection of Flame and Humidity, Small 18 (2022). https://doi.org/10.1002/smll.202203334.

[15] S.C. Yadav, M.K. Tiwari, A. Kanwade, H. Lee, A. Ogura, P.M. Shirage, Butea monosperma, crown of thorns, red lantana camara and royal poinciana flowers extract as natural dyes for dye sensitized solar cells with improved efficiency, Electrochim Acta 441 (2023). https://doi.org/10.1016/j.electacta.2022.141793.

[16] Kenry, J.C. Yeo, J. Yu, M. Shang, K.P. Loh, C.T. Lim, Highly Flexible Graphene Oxide Nanosuspension Liquid-Based Microfluidic Tactile Sensor, Small 12 (2016) 1593–1604. https://doi.org/10.1002/smll.201502911.

[17] A. Srivastava, J.A.K. Satrughna, M.K. Tiwari, A. Kanwade, S.C. Yadav, K. Bala, P.M. Shirage, Lead metal halide perovskite solar cells: Fabrication, advancement strategies, alternatives, and future perspectives, Mater Today Commun 35 (2023). https://doi.org/10.1016/j.mtcomm.2023.105686.

[18] W. Yan, M. Hu, P. Zeng, S. Ma, M. Li, Room temperature NO_2-sensing properties of WO_3 nanoparticles/porous silicon, Appl Surf Sci 292 (2014) 551–555. https://doi.org/10.1016/j.apsusc.2013.11.169.

[19] R. Jain, Y. Lei, R. Maric, Ultra-low NO2 detection by gamma WO_3 synthesized by Reactive Spray Deposition Technology, Sens Actuators B Chem 236 (2016) 163–172. https://doi.org/10.1016/j.snb.2016.05.134.

[20] A.S. Shaikh, S.C. Yadav, A. Srivastava, A.R. Kanwade, M.K. Tiwari, S.M. Rajore, J.A.K. Satrughna, M. Dhonde, P.M. Shirage,

Dynamic synergy of tin in the electron-transfer layer and absorber layer for advancing perovskite solar cells: a comprehensive review, Energy Advances 3 (2024) 1505–1552. https://doi.org/10.1039/d4ya00204k.

[21] S.M. Rajore, A.R. Kanwade, J.A.K. Satrughna, M.K. Tiwari, P.M. Shirage, A comprehensive review on advancements in catalysts for aluminum-air batteries, J Power Sources 616 (2024). https://doi.org/10.1016/j.jpowsour.2024.235101.

[22] J.A.K. Satrughna, A.R. Kanwade, S.M. Rajore, M.K. Tiwari, Y. Ito, A. Ogura, H. Lee, Y. Ohshita, P.M. Shirage, Sol-gel-based synthesis of high-capacity-$NaCoO_2$ cathode for advanced sodium-ion batteries, Electrochim Acta 507 (2024). https://doi.org/10.1016/j.electacta.2024.145201.

[23] S.S. Kalanur, Y.J. Hwang, S.Y. Chae, O.S. Joo, Facile growth of aligned WO_3 nanorods on FTO substrate for enhanced photoanodic water oxidation activity, J Mater Chem A Mater 1 (2013) 3479–3488. https://doi.org/10.1039/c3ta01175e.

[24] G. Zhao, J. Xuan, Q. Gong, L. Wang, J. Ren, M. Sun, F. Jia, G. Yin, B. Liu, In Situ Growing Double-Layer TiO_2 Nanorod Arrays on New-Type FTO Electrodes for Low-Concentration NH_3 Detection at Room Temperature, ACS Appl Mater Interfaces 12 (2020) 8573–8582. https://doi.org/10.1021/acsami.9b20337.

[25] J.A.K. Satrughna, A. Kanwade, A. Srivastava, M.K. Tiwari, S.C. Yadav, S. Teja Akula, P.M. Shirage, Experimental and computational advancement of cathode materials for futuristic sodium ion batteries, Materials Today (2023). https://doi.org/10.1016/j.mattod.2023.06.013.

[26] Y.Z. Zhang, J. Liang, Z. Huang, Q. Wang, G. Zhu, S. Dong, H. Liang, X. Dong, Ionically Conductive Tunnels in h-WO_3 Enable High-Rate NH^{4+} Storage, Advanced Science 9 (2022). https://doi.org/10.1002/advs.202105158.

[27] Y. Xiao, M. Wang, D. Liu, J. Gao, J. Ding, H. Wang, H. Bin Yang, F. Li, M. Chen, Y. Xu, D. Xu, Y.X. Zhang, S. Fang, X. Ao, J. Wang, C. Su, B. Liu, Selective Photoelectrochemical Oxidation of Glycerol to Glyceric Acid on (002) Facets Exposed WO_3 Nanosheets,

Angewandte Chemie - International Edition 63 (2024). https://doi.org/10.1002/anie.202319685.

[28] H. Guo, L. Pan, M. Gao, L. Kong, J. Zhang, A. Khan, N.A. Siddiqui, J. Lin, Electronic Structure Modulating of $W_{18}O_{49}$ Nanospheres by Niobium Doping for Efficient Hydrogen Evolution Reaction, Chemistry - A European Journal (2024). https://doi.org/10.1002/chem.202403043.

[29] Y. Qin, W. Xie, Y. Liu, Z. Ye, Thermal-oxidative growth of aligned W18O49 nanowire arrays for high performance gas sensor, Sens Actuators B Chem 223 (2016) 487–495. https://doi.org/10.1016/j.snb.2015.09.113.

[30] Y. Qiu, Y. Wang, Synthesis, growth kinetics and ultra-sensitive performance of electrospun WO_3 nanofibers for NO_2 detection, Appl Surf Sci 608 (2023). https://doi.org/10.1016/j.apsusc.2022.155112.

[31] G.M. Hingangavkar, Y.H. Navale, T.M. Nimbalkar, R.N. Mulik, V.B. Patil, Hydrothermally engineered WO_3 nanoflowers: A selective detection towards toxic NO_2 gas, Sens Actuators B Chem 371 (2022). https://doi.org/10.1016/j.snb.2022.132584.

[32] S. Rani, R. Dahiya, V. Kumar, P. Berwal, S. Sihag, Hydrothermally engineered WO_3 nanosheets as potential NO_2 gas sensor, Ionics (Kiel) (2024). https://doi.org/10.1007/s11581-024-05934-2.

[33] S.A. Beknalkar, V.L. Patil, N.S. Harale, M.P. Suryawanshi, A.P. Patil, V.B. Patil, J.H. Kim, P.S. Patil, 2-D to 3-D conversion of WO_3 nanostructures using structure directing agent for enhanced NO_2 gas sensing performance, Sens Actuators A Phys 304 (2020). https://doi.org/10.1016/j.sna.2020.111882.

Chapter 7

Conclusions and Scope for Future Work

The core focus of this thesis is the synthesis and characterization of advanced functional materials, specifically Mn-doped $ZnSnO_3$, $Na_3Fe_2(PO_4)_3$, $W_{18}O_{49}$*/graphene composites, and interlinked* $W_{18}O_{49}$ *nanowire networks, for their potential application in gas and humidity sensing. Emphasis has been placed on cost-effective wet chemical synthesis methods and the underlying growth mechanisms of these nanostructures. The developed sensors exhibit exceptional gas-sensing performance, including ultra-high sensitivity, rapid response and recovery, and room-temperature operation. Special attention has been given to the role of doping, nanostructuring, and composite engineering in enhancing sensing performance, making these materials promising candidates for next-generation chemical sensors.*

7.1 Dissertation Summary

In ***Chapter 1***, a comprehensive introduction to gas sensors was presented, covering their significance, working principles, types, and recent advancements. The discussion included the importance of gas sensors in various fields, such as environmental monitoring, industrial safety, healthcare, and automotive applications. Special emphasis was given to the advantages of MOS-based gas sensors due to their high sensitivity, low cost, and ease of fabrication. The selection of materials for gas sensing was justified based on their electronic properties, surface characteristics, and interaction mechanisms with target gases. The chapter concluded with the scope and objectives of the research, highlighting the need for developing high-performance gas sensors using advanced functional materials.

Chapter 2 detailed the experimental and characterization techniques employed in this research. The synthesis methods, including co-precipitation, sol-gel, and hydrothermal techniques, were discussed to emphasize their role in tailoring the morphology and structural properties of nanomaterials. The deposition techniques such as doctor-blade coating and DC magnetron sputtering were utilized for fabricating sensor devices. Various characterization techniques, including XRD for phase analysis, FESEM with EDS for morphological and elemental analysis, TEM for high-resolution imaging, XPS for surface chemical analysis, and N_2 adsorption-desorption analysis for surface area and porosity evaluation, were employed. Gas and humidity sensing measurement systems were also described in detail, along with the methodologies used to control gas concentration and humidity levels.

In ***Chapter 3***, Mn-doped $ZnSnO_3$ microspheres synthesized via a co-precipitation method were explored for CO gas sensing. The doping of Mn significantly enhanced the structural, morphological, and surface properties, leading to improved gas-sensing characteristics. XRD confirmed the cubic structure, BET analysis demonstrated an increased surface area, and XPS indicated defect modifications that influenced sensing properties. The optimized composition (x = 0.10) exhibited a remarkable response (311.37% increase) with a lower operating temperature of 200°C, rapid response (6.6 s), and recovery (34.1 s), making it a promising material for CO gas sensors.

Chapter 4 investigated $Na_3Fe_2(PO_4)_3$ (NFP), a NASICON-type material, synthesized via the sol-gel method for CO gas detection at room temperature. The sensor was fabricated using a thick-film deposition technique on Cu-interdigitated electrodes. The NFP sensor demonstrated excellent selectivity towards CO among various gases, with a rapid response (417.58 in 14 s) and quick recovery (3 s). The response was significantly higher than traditional resistive sensors, and the sensor showed exceptional stability over multiple cycles. The cost-effectiveness and earth-abundant nature of NFP further support its potential for real-world gas sensing applications.

In ***Chapter 5***, the gas-sensing performance of $W_{18}O_{49}$ nanowires hybridized with graphene was examined for NO_2 detection at room temperature. The composite sensor, specifically $W_{18}O_{49}$/Gr1.5%, exhibited ultra-high sensitivity (~150-160 times response), fast response (~3 s), and rapid recovery (~6 s). The hybrid structure facilitated charge transfer and enhanced adsorption-desorption dynamics, improving the sensor's selectivity and stability. The limit of detection was as low as ~0.3 ppm, and the device maintained stability across humidity levels (20%-97%) for three months. While $W_{18}O_{49}$/Gr3% displayed higher selectivity, it showed a slightly reduced sensitivity, emphasizing the importance of optimized graphene content for superior gas-sensing performance.

Chapter 6 focused on an interlinked $W_{18}O_{49}$ nanowire network deposited on an FTO substrate for selective NO_2 detection. The unique nanostructured network provided an interconnected electron transport pathway, significantly enhancing sensor performance. The sensor demonstrated excellent selectivity for NO_2 over other gases, along with superior stability, reproducibility, and long-term durability. The results highlighted the potential of nanowire-based sensor designs in developing highly efficient and reliable gas sensors for environmental safety applications.

Overall, this thesis work successfully demonstrates the development and optimization of novel gas sensors based on advanced functional materials. The studies demonstrated how material engineering, including doping strategies, hybridization with 2D nanomaterials, and nanostructured network formation, can significantly enhance gas-sensing performance. The findings contribute to the development of next-generation gas sensors with ultra-high sensitivity, rapid response/recovery, room-temperature operation, and long-term stability. These advancements pave the way for practical applications in air quality monitoring, industrial safety, and environmental pollution control, with the potential for large-scale commercialization.

7.2 Outlook and Future Prospects

The advancements in gas sensor technology presented in this thesis contribute significantly to the field of chemical sensing, particularly in the development of highly sensitive, selective, and low-power gas sensors. The synthesis and characterization of functional materials such as $W_{18}O_{49}$ nanowires, their composites, and other metal oxide nanostructures have provided a strong foundation for next-generation sensing applications. The room-temperature sensing capability demonstrated in this work opens new possibilities for ***energy-efficient and portable sensor devices***, which are crucial for environmental monitoring and industrial safety. Additionally, integrating these materials into ***flexible and wearable sensor*** platforms can enable real-time environmental monitoring and healthcare applications.

The ***selectivity of gas sensors*** remains a crucial challenge. Future studies can explore novel surface functionalization strategies, heterostructure engineering, and ***machine-learning-based data processing*** to improve selectivity toward target gases in complex environments. Furthermore, miniaturization and ***integration with wireless communication technologies*** can lead to the development of portable sensor devices for real-world applications.

Another promising avenue is the ***exploration of multi-gas sensing capabilities*** by designing hybrid sensing platforms that can simultaneously detect multiple gases. Additionally, extending the research to ***humidity and VOC sensing for indoor air quality monitoring and industrial safety applications*** would be beneficial. Investigating alternative, eco-friendly synthesis approaches and scalable fabrication techniques will further contribute to the commercialization of these materials.

Overall, the advanced functional materials developed in this thesis pave the way for innovative sensor technologies, and future advancements in material design, device engineering, and data analytics can further enhance their performance and applicability in environmental monitoring, healthcare, and industrial safety.